Effect of Arc Welding Processes on the Weld Attributes of Micro Alloyed HSLA Steel

By

RISHI PAMNANI

(Enrolment No:ENGG02201204013)

Indira Gandhi Centre for Atomic Research, Kalpakkam

A thesis submitted to the

Board of Studies in Engineering Sciences

In partial fulfillment of requirements
for the Degree of

DOCTOR OF PHILOSOPHY

of

HOMI BHABHA NATIONAL INSTITUTE

August, 2016

Reccomendation of Viva Voice

As members of the Viva Voce Board, we certify that we have read the dissertation prepared by **Rishi Pamnani** entitled **"Effect of Arc Welding Processes on the Weld Attributes of Micro Alloyed HSLA Steel"** and recommend that it may be accepted as fulfilling the thesis requirement for the award of Degree of Doctor of Philosophy.

Chairman - Dr. A.K.Bhaduri Date: 27/8/2016

Guide/Convener - Dr.T.Jayakumar Date: 27 Aug 2016

Member 1 - Dr.K.Velusamy Date: 27/8/2016

Member 2 - Dr.B.P.C.Rao Date: 27/8/2016

Techical Advisor - Dr.M.Vasudevan Date: 27/08/16.

External Examiner –Prof. P.K. Ghosh 27/8/16 Date:
(Deputy Director, IIT Roorkee)

Final approval and acceptance of this dissertation is contingent upon the candidate's submission of the final copies of the dissertaion to HBNI.

I hereby certify that I have read dissertation titled **"Effect of Arc Welding Processes on the Weld Attributes of Micro Alloyed HSLA Steel"** prepared under my direction and recommend that it may be accepted as fulfilling the disertation requirement.

27082016

Date:

Place: Kalpakkam

T.Jayakumar
(Guide/Convener)

STATEMENT BY AUTHOR

This dissertation has been submitted in partial fulfillment of requirements of an advanced degree at Homi Bhabha National Institute (HBNI) and is deposited in the Library to be made available to vorrowers under rules of the HBNI.

Brief quotations from this dissertation are allowable without special permission, provided that accurate acknowledgement of source is made. Requests for permission for extended quotation from or reproduction of this manuscript in whole or in part may be granted by Competent Authority of HBNI when in his or her judgement the propsed use of the material is in the interests of scholarship. In all other instances, however, permission must be obtained from the author.

Date:

Place: Kalpakkam (Rishi Pamnani)

DECLARATION

I, hereby declare that the investigation presented in the thesis entitled "**Effect of Arc Welding Processes on the Weld Attributes of Micro Alloyed HSLA Steel**" submitted to **Homi Bhabha National Institute (HBNI)**, Mumbai, India, for the award of **Doctor of Philosophy** in **Engineering Sciences** is a record of work carried out by me under the guidance of **Dr. T. Jayakumar**, former Director, Metallurgy and Materials Group, Indira Gandhi Centre for Atomic Research, Kalpakkam. The work is original and has not been submitted as a whole or in part for a degree/diploma at this or any other Institution/ University.

Date:

Place: Kalpakkam (Rishi Pamnani)

List of publications arising from the thesis

<u>Published</u>:

1. Rishi Pamnani, M Vasudevan, P Vasantharaja, T Jayakumar. Optimisation of A-GTAW Welding Parameters for Naval Steel (DMR-249 A) by Design of Experiments Approach: ***J. of Mat:Design and Application***. **DOI: 10.1177/1464420715596455**

2. Rishi Pamnani, R.P. George, B. Anandkumar, T. Jayakumar, M. Vasudevan, U. Kamachi Mudali. Electrochemical Corrosion Studies of Base Metals and Welds of Low Carbon Steels Used in Ship Building Industry: ***Innovations in Corrosion and Mat. Sc, Bentham Publication,*** **Vol 6, DOI: 10.2174/2352094906666151207195150**

3. Rishi Pamnani, Govind K. Sharma, S. Mahadevan, T. Jayakumar, M. Vasudevan, B.P.C. Rao. Residual Stress Studies on Arc Welding Joints of Naval Steel (DMR-249A): ***Journal of Manufacturing Processes, 20 (2015), 104-111.***

4. Rishi Pamnani, M Vasudevan, T Jayakumarand P Vasantharaja. Development of Activated Flux, Optimization of Welding Parameters and Characterization of Weld Joint for DMR-249A Shipbuilding Steel: ***Trans IIM, 2016, DOI: 10.1007/s12666-016-0857-0***

5. Rishi Pamnani, M Vasudevan, T Jayakumar, K C Ganesh, P Vasantharaja. Numerical Simulation and Experimental Validation of Arc Welding of DMR-249A Steel: ***Defence Technology, 12 (2016), 305–315***

6. Rishi Pamnani, T Jayakumar, M Vasudevan, T Sakthivel. Investigations on the Impact Toughness of HSLA Steel Arc Welded Joints. ***Journal of Manufacturing Processes, 21 (2016), 75–86***

7. Rishi Pamnani, V Karthik, T Jayakumar, M Vasudevan and T Sakthivel. Evaluation of Mechanical Properties across DMR-249A Steel Weld Joints using Automated Ball Indentation.***Materials Science&EngineeringA, 651(2016), 214–22.***

Under Review

8. Rishi Pamnani, T Jayakumar, M Vasudevan, V Shankar, P Vasantharaja. Effect of Arc welding Processes on the Microstructure and Mechanical Properties of Naval Steel (DMR-249A) Weld Joints: ***Defence Technology- DT-D-16-00017***

Conferences Attended (w/o proceedings):

1. Development of Improved Welding Technique for Naval Structural Material (DMR-249A). Rishi Pamnani, T Jayakumar, M Vasudevan, P Vasantharaja, ***IWCEM-2014***, Pune, 24-26 May 2014.

2. Optimising Welding of Naval Construction Steel by Design of Experiments. Rishi Pamnani, T Jayakumar, M Vasudevan, P Vasantharaja, ***IWCEM-2015***, Pune, 23-25 May 2015.

3. Studies on Corrosion Characteristics of High Strength Low Alloy Steels Used in Ship Building Industry. Rishi Pamnani, B Anandkumar, RP George, T Jayakumar,M Vasudevan,U Kamachi Mudali,***IWCEM-2015***, Pune, 23-25 May 2015.

4. Electrochemical Potentiodynamic Studies of High Strength Low Alloy (HSLA) Marine Steels. Rishi Pamnani, B Anandkumar, RP George, T Jayakumar,M Vasudevan,U Kamachi Mudali,***CORSYM-2015***, Chennai, 31 Jul-01 Aug 2015.

Solely dedicated to

Gurudutt, Kavita

and Rashmi

ACKNOWLEDGEMENTS

I owe my deep sense of gratitude to my mentor, philosopher and guide **Dr T Jayakumar**, former Director, Metallurgy and Materials Group (MMG), Indira Gandhi Centre for Atomic Research (IGCAR). Without his untiring mentorship, constant inspiration, valuable discussions and suggestions, this thesis would not have been possible. He patiently provided the vision, encouragement and advice necessary for me to proceed through the entire research program.

I am highly obliged to **Dr M Vasudevan**, Head, AWMPS/MTD, IGCAR for being a guiding force and all the technical and professional expertise he extended right from the first step towards initiation of present studies to the final fruitful conclusion. I appreciate him for critically going through the draft of my thesis and research papers.

I express my sincere gratitude to **Cmde KC Joshi**, Senior Officer Naval Detachment, Prototype Training Center (Kalapkkam) and the **Indian Navy** for extending due permission for pursuing this study. I express gratefulness to the **Naval Dockyard (Visakhapatnam)**, **Mazagaon Dockyard Limited**, Mumbai and **Cochin Shipyard Limited**, Kochi for their constant encouragement and support. I extend heartfelt gratitude to **Mr KV Ravi**, Head, **Mr N Rathinasamy**, Technical Services Superintendent, and the operations team and other colleagues of PRPD/BARCF for extending their assistance and co-operation. I feel indebted to Mr **SLN Swamy**, Section Head, PIS/RDG, IGCAR for being a constant source of support and motivation.

My sincere thanks to the doctoral committee **Dr. AK Bhaduri**, Chairman, **Dr K Velusamy** and **Dr BPC Rao** for evaluating the progress of the research work and offering useful suggestions and direction.

I take this opportunity to specially thank all the co-authors **Dr U Kamachi Mudali, Dr BPC Rao, Dr Rani P George,Dr V Karthik**, **Shri S. Mahadevan, Dr Vani Shankar, Dr Govind Sharma, Mr T Sakthivel, Dr B Anand Kumar, Mr P Vasantharaja** and **Mr KC Ganesh** of technical papers originated out of this research work, for extending professional supervision and impetus throughout my research work. I would like to thank **Shri V Maduraimuthu, Dr B Arivazhagan** and **Shri N Chandrashkar** for various useful discussions. I sincerely acknowledge the support received from my friend **T Sakthivel** for finding out unique solutions and justifiable technical reasonings whenever I felt stuck in engineering jagrons. I am highly obliged to **Mrs Indira Logu** for her concern and courtesies towards completion of my studies in time.I would also like to thank all the colleagues of **MTD, MMD, NDED** and **CSTG** for their help and support.

I am thankful to **Dr RV SubbaRao**, **Dr K Sankaran, Dr V Chandramouli, Shri R KrishnaPrabhu, Dr R Ramasheshan, Dr R Sudha, Dr Shamima Hussain, Mr Yatendra Kumar, Mr Chandraveer Singh, Mr Kalyan Phani** and **Ms Rasmi** for many useful discussions and support during the course of thesis work.

I would like to extend my regards to **Mr V Rajendran, Mr V Ganeshan, Ms Alka Kumari, Mr K Mohanraj, Mr Narayan P Rao, Mr Arun Kumar, Mr Swapan Kumar Mahato, Ms S Paneer Selvi, Ms N Sreevidya, Mr R Balakrishnan** and **Mr Krishna Chaitanya** for timely help and technical assistance extended by them. I express my special appreciation to **Shri D. Manokaran** and **Mrs Gauri** for their dedication towards carrying out welding and metallography sample preparations. I extend special appreciation and regards to the work force of Central Workshop, Zonal Workshop and all other technical laboratories without whose contribution towards various test specimen preparation and conduct of experiments/ analysis, present research studies would not have been possible.

I express my profound gratitude to my my father **Shri Gurudutt L Pamnani,** mother **Smt Kavita Pamnani**, my brother **Mr Vijay**, my sister **Mrs Namrata Dentan**, **Dr Shanti**, **Ms Radha**, my family members, in-laws, other near and dear ones for their personal support and encouragement.

Finally, I express my sincere thankfulness to my wife **Dr Rashmi Pamnani**, son **Raghav** and daughter **Rudrakshi** for their love, patience and sacrifices to make this achievement a reality. Above all, I owe it to **the Almighty** for granting me health, strength and wisdom to undertake this research work and enabling me to take it to successful completion.

Contents

Abstract

The primary aim of the investigations carried out in the PhD was to study feasibility of activated flux gas tungsten arc welding (A-GTAW) process as alternate welding technique for naval structural steel (DMR-249A) and compare the effect of different arc welding processes on weld attributes of DMR-249A steel weld joints.

The experiments were carried out with combinations of oxide fluxes to develop suitable activated flux for GTAW of DMR-249A steel. The bead width and depth of penetration obtained in the bead on plate experiments using various combinations of fluxes were measured. Mixture 1, with maximum depth to width ratio about 0.86, was used as optimum flux combination to carry out experiments for optimising welding parameters.

Design of Experiments (DOE) approach was employed using Response Surface Methodology (RSM) and Taguchi technique to optimize the welding parameters for achieving maximum Depth of Penetration (DOP) in a single pass. Design matrix was generated using DOE techniques and bead on plate experiments were carried out to generate data regarding influence of welding process variables on DOP. The input variables considered were current, torch speed and arc gap and the DOP was considered as the response variable. The equations correlating depth of penetration with the process parameters were developed for both the optimization techniques. The identified optimum process parameters were validated by carrying out bead on plate experiments. The root mean square (RMS) error between the predicted and measured DOP values for the validation experiments of the RSM (D-Optimal) and Taguchi optimization technique was found to be 0.57 and 0.86 respectively. Thus, RSM (D-Optimal) was observed to predict optimized welding process parameters for achieving maximum DOP with better accuracy during A-GTAW process. The welding parameters of 270 A current, 60 mm/min speed and 3 mm arc gap were finalised to carry out double sided A-GTAW weld joint.

Four weld joints were fabricated using shielded metal arc welding (SMAW),submerged arc welding (SAW), flux cored arc welding (FCAW) and activated flux gas tungsten arc welding (A-GTAW) processes.All the four weld joints passed radiographic examination.

The Finite Element Model (FEM) simulation of thermo-mechanical behavior of SMAW (the most common welding technique used for welding of microalloyed steels and construction of ships) and A-GTAW (welding technique being studied and developed as alternative welding technique for DMR-249A steel) joints was studied using SYSWELD software. The double ellipsoidal heat source distribution model was employed for the thermal and residual stress analysis. The numerically estimated temperature distribution was validated with online temperature measurements using K-type thermocouples. The predicted residual stress profiles across the weld joints were compared with the values experimentally measured using non-destructive techniques.

X-Ray Diffraction (XRD) and ultrasonic technique (UT) were used to experimentally estimate the residual stresses across the weld joints. The residual stresses profile of higher heat input A-GTAW process was observed to be comparable with SMAW process. A good agreement between measured and predicted thermal cycles and residual stress profile established FEM as a dependable technique to estimate residual stresses in arc welded joints of DMR-249A steel.

The microstructure study of the base metal DMR 249A and the four weld joints were undertaken using optical microscope, SEM and EBSD. The microstructure of DMR-249A steel exhibited predominantly fine grained equiaxed ferrite and some percentage of pearlite of banded type structure. For weld metals, the optical micrographs showed grain boundary ferrite, Widmanstatten ferrite with aligned second phase along with veins of ferrite, acicular ferrite, polygonal ferrite and microphases. The minor changes in percentage of volume fraction of the different ferrites (grain boundary, Widmanstatten, acicular and polygonal) were observed in the samples characteristic to the difference in heat input of the various arc welding processes. The inclusion rating and estimation of volume fraction of various ferritic morphologies was undertaken to correlate microstructural transformation during welding with mechanical properties of various arc welded joints.

The hardness values measured across the weld joints were found within the scatter band of 200 -290 $HV_{0.2}$ as compared to values of 196-210 $HV_{0.2}$ for base metal. The hardness of weld metal was observed to be higher than the base metal. The micro-hardness values gradually increases from base metal to HAZ and a minor decrease in the hardness value was observed near the fusion zone followed by higher hardness values in weld metal. Similar trends of hardness values have been reported in weld joint of HSLA steels.

The investigations were carried out to ascertain the mechanical properties of the weld joints. The tensile test performed on base metal and cross weld joint specimen showed higher yield strength about 460 - 480 MPa in the cross weld joints as compared to about 427 MPa of base metal. The percentage elongation of cross weld joint (19-20%) was lower than the base metal (30%). The UTSof both the base metal and weld joints were comparable (about 600 MPa). The tensile fracture of the cross weld joint occurred in the base metal region away from weld metal which confirmed the existence of adequate strength in weld metal. The A-GTAW process being the newly developed welding process for DMR-249A steel, 180° bend test was carried out only for A-GTAW joint. No cracks observed on application of dye penetration testing confirmed the integrity and adequate ductility of A-GTAW weld joint.

The impact toughness values of base metal (>350 J and 160 J respectively at room temperature and -60°C) was observed to be superior than the weld joints (160-200 J and 10-70 J respectively at room temperature and -60°C). The difference in impact toughness values is attributed to presence of impurities/inclusions in weld metal, coarse grain size due to welding heat input and traces of grain boundary and Widmanstatten ferrites in weld metal as compared to smaller equiaxed grains of base metal.

The mechanical properties across the SMAW, SAW, FCAW and A-GTAW weld joints in DMR-249A steel were evaluated using automatic ball indentation (ABI) technique. The tensile strength was observed to vary significantly across the weld joints. The strength values (YS and UTS) decreased systematically across the weld joint from weld metal to base metal. The strain hardening exponent was found to be comparable across the weld joints with marginal higher values for HAZ. The comparable values of strain hardening exponent for weld metal and base metal showed the balanced strength and ductility of the welds. The ABI was found to be a dependable technique for analysis and characterization of mechanical properties across weld joint by using a small amount of test materials.

The electrochemical properties of base metal (DMR-249A HSLA steel) and welded butt joints were compared by conducting potentiodynamic anodic polarization studies. Experiments were also carried out with base material samples of ABA and D40S steels for comparing and understanding corrosion behaviour of DMR-249A steel. The base metal and weld metals of arc welded joints displayed similar corrosion characteristics for general and pitting corrosion in sea water and fresh water. It was concluded that the qualified arc welding processes did not deteriorate the corrosion characteristics of the base metal, DMR-249A steel.

The values of hardness and strength exhibited by A-GTAW weld metal were comparable with weld metals of other arc welded joints. The A-GTAW weld joint indicated good impact toughness value of 200 J at room temperature. The sub zero (-60°C) impact toughness was found to be 10 J. The significant reduction in toughness of A-GTAW joint at sub-zero temperatures is attributable to more percentage of grain boundary ferrite and Widmanstatten ferrite in high heat input double pass A-GTAW welding process. The coarse grains of A-GTAW weld metal is also a significant factor leading to decrease in sub-zero impact toughness.The weld attributes of phase transformation, microstructure, inclusions and mechanical properties were found to be distinctive characteristic of the different arc welding processes studied. The hardness, tensile properties and corrosion properties were found to be comparable for all the weld joints. The FCAW and SMAW joints exhibited better sub-zero impact toughness followed by SAW and A-GTAW.The significant variation observed in sub-zero impact toughness was attributed to the microstructral transformation of equiaxed base metal to various ferrite morphologies, grain size, inclusions and variation in chemical composition of weld metals of different joints.

List of Figures

List of Tables

Symbols and abbreviations

Symbols		Abbreviations	
d/w	Depth to Width Ratio	**A-GTAW**	Activated Flux Gas Tungsten Arc Welding
σ	Stress	**ABI**	Automatic Ball Indentation
Ε	Strain	**AEC**	Acousto-Elastic Constant
E	Elastic Modulus	**ANOVA**	Analysis of Variance
V	Measured Ultrasonic Velocity	**BM**	Base Metal
$\mathbf{V_0}$	Velocity in the Stress-Free State	**CCD**	central composite design
A	Acousto-Elastic Constant	**CR**	Corrosion Rate
B	Acousto-Elastic Constant (ns/MPa)	**CGHAZ**	Coarse Grain Heat Affected Zone
t	Ultrasonic Transit Time	**DQ**	Direct Quenching
ν	Poisson Ratio	**DOE**	Design of Experiments
$\mathbf{d_o}$	Unstressed Lattice Spacing	**DBTT**	Ductile Brittle Transition Temperature
dt	Total Indentation Diameter	**EBSD**	Electron Back-Scatter Diffraction
dp	Plastic Indentation Diameter	**F/W**	Fresh Water
D	Indenter Diameter	**FGHAZ**	Fine Grain Heat Affected Zone
ε_p	True Plastic Strain	**FCAW**	Flux cored Arc Welding
σ_t	True Stress	**FEM**	Finite Elements Modelling
P	Applied Load	**HSLA**	High Strength Low Alloy
K	Strength Coefficient	**HAZ**	Heat Affected Zone
n	Strain Hardening Exponent	**NDE**	Non-Destructive Examination
$\mathbf{I_{corr}}$	Corrosion Current	$\mathbf{L_{CR}}$	Longitudinal Critically Refracted
$\mathbf{E_{corr}}$	Corrosion Potential	**QT**	Quenched and Tempered
ρ	Density	**RSM**	Response Surface Method
$\mathbf{b_c}$	Cathodic Slope	**RS**	Residual Stresses
$\mathbf{b_a}$	Anodic Slope	**SMAW**	Shielded Metal Arc Welding
$\mathbf{R_p}$	Polarization Resistance	**SAW**	Submerged Arc Welding
		S/W	Sea Water
		SEM	Scanning Electron Microscope
		TMCP	Thermomechanical Controlled Process
		UTS	Ultimate Tensile Strength
		UT	Ultrasonic Techniques
		WM	Weld Metal
		XRD	X-ray Diffraction
		X-Weld	Cross Weld
		YS	Yield Strength

Chapter 1. Introduction

The primary aim of the investigations carried out in this thesis is to study the feasibility of the activated flux gas tungsten arc welding (A-GTAW) process as alternative welding technique for high strength low alloy (HSLA) naval steel DMR-249A and to compare the effect of different arc welding processes on the attributes of DMR-249A welded joints. The feasibility of developing A-GTAW as an alternative welding technique for DMR-249A steel was examined by studying the thermomechanical behaviour, microstructure and mechanical properties of weld joints fabricated by A-GTAW process. The thermal gradients and residual stress profiles of shielded metal arc welding (SMAW) and A-GTAW process were simulated using FEM and compared with experimental results. The effect of different arc welding processes which include SMAW, FCAW, SAW and A-GTAW on weld attributes of DMR-249A welded joints was compared by studying the microstructure, mechanical properties, residual stresses and corrosion characteristics of the weld joints.

1.1 High Strength Low Alloy Steels

The HSLA steels are generally Mn alloy grades with approximately 0.2% C and grain-refining elements, such as V, Nb, and Ti contributing towards enhanced resistance to brittle fracture [1-2]. The required yield strength levels are obtained with alloying elements such as Si, Ni, Cu, Cr, and Mo etc. [1-5]. HSLA steelexhibits equiaxed fine grain ferritic steels with good yield strength and weldability [1-7]. High-strength, low alloy (HSLA) steels have been widely used in the construction of buildings, pipelines and ships [1-12]. The principal advantages of these materials are not only their good combination of strength and toughness, but also their good weldability. Therefore, the HSLA steel is suitable for applications in large-scale welded steel structures. Its good weldability and lack of preheat requirement provide a great convenience for the construction of large-scale structures, and significantly reduce the processing costs.

During the welding thermal cycle, base steel close to the fusion area will transform to austenite, martensite, ferrite and/or bainite, depending on the cooling rate and steel composition. These different phase microstructures correspond to different mechanical properties. For HSLA steels, the average width of the HAZ is about 2 to 6 mm. The base plate possesses an average grain size of 3 to 7 μm, which exhibits a equiaxed ferretic structure with small percentage of pearlite. The weld metal in the welding beads has a typical microstructure of proeutectoid ferrite, polygonal Widmanstatten and acicular ferrite, as well as micro phases of bainite and martensite. The proeutectoid ferrite has equiaxed form or thin veins delineating prior austenite grain boundaries. The sideplate Widmanstatten ferrite shows the parallel ferrite laths emanating from prior austenite grain boundaries. The acicular ferrite, considered a toughening phase that improves the strength and toughness of the weld metal, lies between the bodies of prior austenite grains. Acicular ferrite nucleates intragranularly on non-metallic inclusions producing a fine "basket-weave" microstructure that is very resistant to crack propagation. To control the complex process of acicular ferrite nucleation, selection of specific welding process parameters is of critical importance.

DMR-249A steel, a structural grade steel standardized by the American Bureau of Shipping for use in ship building, is used in the construction of the hull of various vessels with specific weight and resilience qualities [13-15]. The steel exhibits predominantly ferritic structure and less than 10% (Vol.) pearlite structure. The average grain size and hardness of the steel is 5.5 µm and 196-212 $HV_{0.2}$ respectively. The DMR-249A steel has comparable microstructure and mechanical properties to that of S355J2G3, AH 36, HSLA 80, ABA and D40S steels generally used for structures and ship construction [16-20].

1.2 Welding Processes

Conventional arc welding (fusion welding) is extensively used during construction and fabrication of bridges, nuclear reactors, ships,machineries and various types of structure including space vehicles. Submerged Arc Welding (SAW) and Flux cored Arc Welding (FCAW) are commercially preferred automated welding processes, Shielded Metal Arc Welding (SMAW) is used for on-site manual welding and repair works whereas Activated flux Tungsten Inert Gas (A-GTAW) is a cost effective non conventional automated welding process for enhancing productivity. In A-GTAW welding, a fine layer of activating flux, an inorganic powder, is coated on the steel plate before welding. The penetration depth was multiplied by a factor of 1.5 to 3 while changing from the GTAW process to A-GTAW, depending on the alloys being welded. Considering the theoretical basis, the one difference between the GTAW process and A-GTAW is the use of activating fluxes. In the last four decades, various theories explaining the mechanism of activating fluxes have been published viz Theory of Savitskii and Leskov 1980, Theory of Heiple and Roper 1982, Theory of Simonik 1976 and Theory of Lowke, Tanaka and Ushio 2005 [21-24]. It is believed that enhancement in depth of penetration occurs due to a reversed Marangoni-effect in conjunction with arc constriction.

1.3 Residual Stresses

Residual stresses (also called as locked-in stresses) are a system of self-equilibrating stresses which may exist in a body when it is free from external loads or forces. The welding process for each material and joint geomerty has a different residual stress distribution depending upon the extent of shrinkage, cooling rate and phase transformation. The residual stresses induced by the shrinkage of the molten region are usually tensile. When the effect of phase transformations is dominant, compressive residual stresses are formed in the transformed areas [25-26].

The measurement of residual stresses developed during welding of a ship's hull can helpto lower the risk of failure by predicting their influence on fatigue, corrosion and other detrimental surface phenomena. Tensile residual stresses are harmful as they assist crack propagation and also contribute to fatigue failure and stress corrosion cracking. Compressive residual stresses increase wear and corrosion resistance and are beneficial in preventing origination and propagation of fatigue cracks. Measurement of residual stresses is important to optimise the welding process for reducing detrimental effect of residual stresses. The techniques used to measure residual stresses are broadly categorized into destructive, semi-destructive and non-destructive techniques [27-28]. The non-destructive techniques considered in this study are X-ray diffraction (XRD) and ultrasonic techniques (UT).

The XRD technique uses the distance between crystallographic planes, i.e. the lattice d-spacing, as a strain gauge. The presence of residual stresses in the material produces a shift in the XRD peak angular position that is directly measured by the detector [28-30]. The depth of penetration of X-rays is of the order of 5 to 30 microns.

The calculation of residual stresses is based on the shift in the peak position of diffracted X-rays of a selected set of planes.

Stress measurements using UT are based on measuring the variation of ultrasonic wave velocity of a particular wave mode in a stressed material. Compared to other possible ultrasonic wave modes, longitudinal critically refracted (L_{CR})wave is most sensitive to the stress field [31]. The L_{CR} method uses longitudinal waves travelling just beneath the surface. The wave speed for L_{CR} waves is therefore affected by the average stress in a layer which may be a few millimetres depending on the ultrasonic wave frequency employed. The variation of sound velocity or transit time in stressed material is compared with velocity or transit time in a non-stressed specimen. Transit time varies from one place to another across the weld joint, corresponding to the existing compressive/tensile stresses.

1.4 Finite Element Modelling and Simulation

Extensive research has been undertaken to develop numerical models to understand the effect of welding process variables on the weld attributes [32-45].In order to simulate a welding process the welding heat source must be modified. One of the major characteristics of the heat source is its motion through time and space. Goldak et al. proposed an analytical heat source model, which is known as the “double ellipsoidal heat source model”. Duranton et al. explained the thermo-mechanical model used as well as the simulation methodology for multi pass welding [36]. Mollicone, et al. explained a number of finite-element (FE) models to illustrate the effect of using different modeling strategies for the simulation of the thermo-elasto-plastic stages of the welding process [37]. Various researchers have published on the thermo mechanical simulation of arc welding of naval structure materials [16-17, 38]. Available published literature on prediction of thermal and residual stress trends using welding process using SYSWELD software, and validation with experimental results, have established FEM analysis as a useful tool for thermo mechanical characterisation of welding processes [39-45].

1.5 Corrosion

For naval structural material, the deterioration of structural strength and structural integrity is a major factor in assets management. This type of deterioration is influenced by the loss of section thickness for structural elements and by the potential for loss of integrity through corrosion; specially, where protective measures such as paint coatings, galvanizing and cathodic protection can be ineffective. Various studies have been carried out to understand stress corrosion cracking, hydrogen induced cracking, microorganism induced corrosion, pitting, crevice and general corrosion behaviour of base metal and weld joints for HSLA steels [46-49]. A number of studies have been carried out to explain the extent of deterioration caused by pitting corrosion [50-53]. Corrosion is a chemical or electrochemical oxidation process, in which the metal transfers electrons to the environment and undergoes a valence change from zero to a positive value. Information on corrosion rates, passivity and pitting tendencies can be obtained by measurements of current-potential relations under carefully controlled conditions. The corrosion rate of steel in a medium/solvent of interest can be ascertained by anodic and cathodic polarization experiments (Tafel plot) as per ASTM Standards [54-57].

1.6 Scope of Investigation

The scope of this study involved the development of activated flux for A-GTAW of DMR-249A steel, optimisation of welding parameters over an operating range of process parameters and ascertaining parameters for achieving maximum depth of penetration. The investigation include measurement of residual stresses developed in arc welding of DMR-249A steel and comparison of residual stress profiles of SMAW and A-GTAW processes using FEM simulation and non destructive measurement techniques. The weld metal attributes of joints fabricated using SMAW, SAW, FCAW and A-GTAW processes were examined by carrying out testing of mechanical properties and optical/SEM/EBSD analysis of microstructure.The studies have also been carried out to characterise the corrosion behaviour of DMR-249A steel and compare the corrosion behaviour of base metal and weld metal of various arc welded joints using potentiodynamic electrochemical experiments.

The work detailed in this thesis has the following aims:

(i) Development of activated flux and optimisation of welding parameters of A-GTAW process for DMR-249A steel.

(ii) Residual stress measurements for DMR-249A steel weld joints using non destructive techniques and validation of thermo-mechanical behaviour of weld joints as simulated using FEM.

(iii) Microstructure characterisation and comparison of mechanical properties of DMR-249A steel and weld joints.

(iv) Determining and comparing corrosion characteristics of base metal DMR-249A and various weld metals of arc welded joints.

The above goals were achieved through the following approaches:

(i) Development of activated flux and optimisation of welding parameters for DMR-249A steel.

(a) Welding experiments with eight different combinations of inorganic oxide fluxes were used to finalise a suitable A-GTAW flux for DMR-249A steel to achieve maximum depth to width ratio of about 0.86.

(b) Understanding criticality of surface active/stable elements and sensitivity of heat input for A-GTAW mechanism.

(c) Experiments for design of experiments (DOE) using response surface method (RSM) and Taguchi techniques.

(d) Investigation into desirability and multi desirability approach for DOE.

(e) Comparison of RSM (D-Optimal) matrices D-22, D-34 and D-36 with Taguchi (T-9 and T-27) matrices.

(ii) Simulation of thermomechanical behaviour of DMR-249A steeljoints.

(a) FEM modelling and simulation using SYSWELD software.

(b) Measurement of residual stress across weld joints using XRD.

(c) Calculation of acousto-elastic constant for DMR-249A steel.

(d) Measurement of residual stress across weld joints using UT.

(e) Validation of simulated thermo-mechanical behaviour with experimental measurements.

(iii) Microstructure Characterisation and Mechanical Properties.

(a) Fabrication of weld joints using four different arc welding processes.

(b) Characterisation of base metal and weld metal microstructure using optical and scanning electron microscopes.

(c) Chemical composition including oxygen/nitrogen analysis of weld metal.

(d) Comparison of mechanical properties of arc welded joints by tensile, impact and micro hardness tests.

(e) Comparison of mechanical properties across weld joints using Automatic Ball Indentation technique.

(iv) Potentiodynamic corrosion studies.

(a) Electrochemical polarisation studies with anodic and Tafel plots.

(b) Understanding electrochemical corrosion behaviour of base metal and weld joints.

(c) Characterising DMR-249A steel corrosion characteristics with available commercial steels.

(d) Microstructure characterisation, SEM studies and surface profilometry for comprehending general corrosion characteristics of DMR-249A steel.

1.7 Outline of thesis

The thesis comprises of the following chapters:

1. Introduction
2. Literature Review, Motivation and Objectives
3. Finalisation of Flux and Optimisation of Welding Parameters
4. Modelling and Simulation using SYSWELD
5. Residual Stress Measurements
6. Microstructure Characterisation and Mechanical Properties
7. Evaluation of mechanical properties across weld joints using Automated Ball Indentation
8. Corrosion Studies
9. Summary of Research Findings and Future Work

The highlights of each chapter are given below:-

Chapter 1 gives a brief introduction to A-GTAW, other arc welding processes and phase transformation in weld metal; use of DOE in optimisation of welding parameters, development of residual stresses in welding and measurement of residual stresses, use of SYSWELD software for FEM simulation and corrosion characteristics of weld joints.

Chapter 2 provides a detailed literature survey on understanding of A-GTAW, factors affecting choice of activated flux, heat flow in weld pool and advantages of A-GTAW.It covers literature review of studies carried out for understanding and measurement of residual stresses in welded joints, understanding of heat source modelling and advantages of Finite Element Modelling and simulation. The motivation and objectives for development of A-GTAW as alternative welding technique for ship building steels and effects of arc welding processes on attributes of DMR-249A steel are also given.

Chapter 3 provides experimental details of development of activated flux and design of experiments carried out to optimise the weld process parameters for achieving desired depth of penetration. The various combinations of fluxes were prepared to decide suitable flux for DMR-249A steel. The design of experiments was carried out for optimization of welding parameters to achieve the desired depth of penetration. The square butt weld joints were fabricated with 10 mm thick plates employing A-GTAW welding using developed flux and optimized process parameters. The discussion of chapter includes challenges encountered for development of activated flux for naval structural steels (DMR-249A HSLA steel) due to:-

(a) Presence of Surface Stable elements like Al and Ca (greater than 150ppm) that reduce weld penetration

(b) Low content of Surface Active elements like S (lesser than 60 ppm) required for stable and reliable *dy/dT* (surface tension to temperature gradient)

(c) Sensitivity of weld penetration to critical heat input and critical concentration of surface active elements.

Chapter 4covers the description of heat source used for FEM simulation of welding, comparison of simulated thermal and residual stress profiles of A-GTAW and SMAW weld joints and validation with experimental results.There was good agreement between the measured and predicted thermal cycles for both the weld joints fabricated by SMAW and A-GTAW processes.The study established FEM based thermo-mechanical analysis as a reliable method for interpretation of residual stresses in DMR-249A steel weld joints.

Chapter 5deals with comparison of XRD and UT for residual stress measurements and evaluation of residual stresses developed in A-GTAW and SMAW weld joints. The RS developed in high productivity double sided A-GTAW and conventional five pass SMAW weld joints were observed to be similar. The appreciable similarity of UT measurements with XRD measurements establishes UT as a dependable technique for measurement of residual stresses in DMR-249A weld joints.

Chapter 6 presents the studies carried out to ascertain the mechanical properties of hardness, tensile strength and impact toughness of the various arc welding joints. The chapter also emphasises the characteristics of the inclusions and phase transformation in weld metal of various arc welding processes based on optical, scanning emission microscope (SEM) and electron back scatter diffraction (EBSD) studies.

Chapter 7 gives the comparison of strength and strain hardening exponent across the arc welded joints of DMR-249A using Automatic Ball Indentation technique. The ABI results were validated with the standard conventional tensile test results. It was found that ABI can be effectively used to determine the mechanical properties across weld jointquite rapidly and by using a small amount of test materials compared to conventional test.

Chapter 8 contains the details of electrochemical potentiodynamic studies carried out to compare the corrosion behaviour of different arc welded joints and also comparison of corrosion potential of DMR 249A with other commercially available ship building steels. The chapter also discusses microstructural characterization employed to establish reasons for comparable corrosion characteristics in base and weld metals. The base metal and weld metals of arc welded joints displayed similar corrosion characteristics for general and pitting corrosion in sea water and fresh water.

Chapter 9 includes the summary of research findings and scope of future studies.

Chapter 2. Review of Literature and Motivation

This chapter provides a review of high strength low alloy (HSLA) steels, the effect of micro-alloying elements, their properties and applications. The chapter also covers a brief on conventional arc welding techniques, their applications, advantages and disadvantages. A comprehensive literature review of activated flux gas tungsten arc welding (A-GTAW) comprising of factors affecting choice of fluxes, heat flow in A-GTAW weld pool and advantages-disadvantages of the process is presented. The concise overview of residual stresses (RS) in welding with their source of build up, RS trends across weld joints, techniques of RS measurement and use of finite element method (FEM) for modelling of welding to predict the thermal cycles and residual stresses is also discussed in the chapter. The motivation and objective of the present research studies is presented at the end of the chapter.

2.1 HSLA Steels

HSLA steelsrelate to weldable fine grained ferritic steels with yield strength of > 355 N/mm^2. They are generally Mn alloy grade steels containing approx 0.2% C. The grain-refining elements, such as V, Nb, and Ti, are added as micro alloying elements to enhance their resistance to brittle fracture [1-2]. To obtain various yield strength levels, alloying elements such as Si, Ni, Cu, Cr, and Mo etc are also added. The demands on high strength steels have increased for special reasons such as better yield strength for higher load bearing capacity of thin sections, higher resistance to brittle fracture with low impact transition temperature and a high degree of weldability. These are the main reasons for advancements of high strength steels [2-4]. The choice of specific high strength steel depends on a number of application requirements including thickness reduction, corrosion resistance, formability and weldability. For many applications, the most important factor in the steel selection process is the favourable strength-to-weight ratio of HSLA steels compared with conventional low-carbon steels. This characteristic of HSLA steels has lead to their increased use in marine industry [1-12].

There are generally three different ways to make HSLA steels [7-12]. First, the oldest method is the QT method (quenched and tempered method), followed by the TMCP (thermomechanical controlled process) and finally, the last method is direct quenching (DQ). The common goal of all of these above mentioned production methods is to create a steel of high yield strength and good ductility. All the steels that are produced using one of these three methods (QT, TMCP or DQ) exhibit fine grains of ferrite-bainite-martensite. The steel manufactured using TMCP method can also have a predominantly ferrite-bainite microstructure. Therefined microstructure is created through the alloying of various microelements such as niobium, titanium, vanadium, and boron, which in turn make inclusions like carbides and nitrides. Together with fast cooling and tempering, the resulting average grain size is finer and the hardness of structure is high despite the small content of carbon.

2.1.1 Effect of alloying elements in HSLA steels

It is a long-standing tradition to discuss the various alloying elements in terms of how they impact the properties of the steel. The characteristics of the transformation in the various iron binary equilibrium systems permit a classification indicating that alloying elements can influence the equilibrium diagram in two ways (Fig 2.1) [58-61]:-

(i) By expanding the γ-field, and encouraging the formation of austenite over wider compositional limits. These elements are called γ-stabilizer.

(ii) By contracting the γ-field, and encouraging the formation of ferrite over wider compositional limits. These elements are called α-stabilizers.

In commercial alloy steels, which are multicomponent systems, alloying elements can be found (i) in the free state; (ii) as intermetallic compound with iron or with each other; (iii) as oxides, sulfides, and other nonmetal inclusions; (iv) in the form of carbides; or (v) as a solution in iron [62]. As to the character of their distribution in steel, alloying elements may be divided into two groups:

(a) Elements that do not form carbides in steel (e.g. Ni, Si, Co, Al, Cu and N)

(b) Elements that form stable carbides in steel (e.g. Cr, Mn, Mo, W, V, Ti, Zr, and Nb)

The first group elements do not form chemical compounds with iron and carbon, and consequently the only possible form in which they can be present in steel is in solid solutions with iron. The only exceptions are Cu and N. Copper dissolves in γ-iron at normal temperatures in amounts of up to 1.0%. If the Cu content exceeds 7%, iron will contain copper in the free-state as metal inclusions. Nitrogen also has a limited solubility in ferrite. When the N content is higher than 0.015%, nitrogen is found in steel in the form of chemical compounds with iron or some alloying elements (V, Al, Ti, and Cr). These chemical compounds are called nitrides. Alloying elements whose affinity for oxygen is greater than that of iron are capable of forming oxides and other non-metal compounds. When added at the very end of the steel melting process, such elements (e.g., Al, Si, V, Ti) deoxidize steel by taking oxygen from iron. The deoxidizing reaction yields Al_2O_3, TiO_2, V_2O_5 and other oxides. Owing to the fact that deoxidizers are introduced at the final stages of the steel melting process, the majority of oxides have no time to coagulate or to pass to slag, and as a result they are retained in the solid steel as fine non-metal inclusions. In addition to a great affinity for oxygen, some alloying elements have a greater affinity for sulphur than iron does, and upon being introduced into steel, they form sulphides. Alloying elements that form stable carbides in steel can be found in the form of chemical compounds with carbon and iron or be present in the solid solution. The distribution of these elements depends on the carbon content of the steel and the concurrent presence of other carbide-forming elements. If steel contains a relatively small amount of carbon and a great quantity of an alloying element, then, carbon will be bound to carbides before the carbide-forming elements are completely used. For this reason excess carbide-forming elements will be found in the solid solution. If steel has a large amount of carbon and little of the alloying elements, the latter will be present in the steel mainly as carbides.

All alloying elements that form solid solutions in ferrite affect its hardness. The hardness increase caused by substitutional solution is shown in Fig. 2.2 [63]. Si and Mn, the most frequently occurring alloying elements, have a relatively potent effect on the hardness of ferrite.

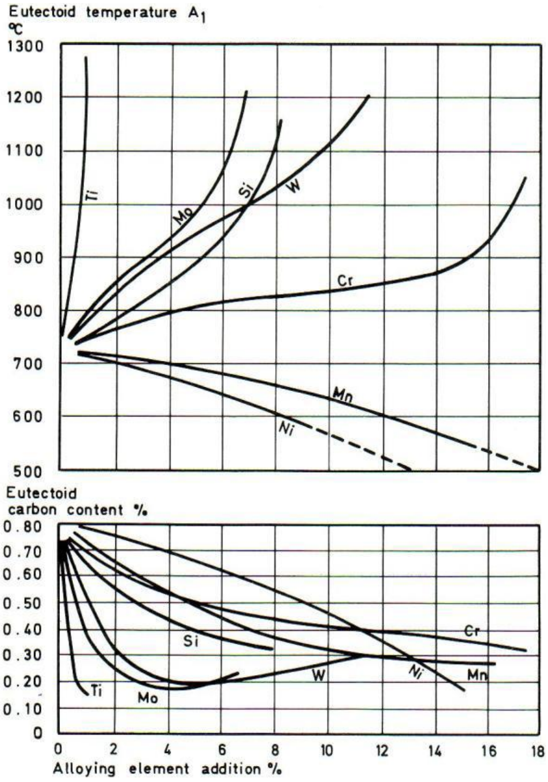

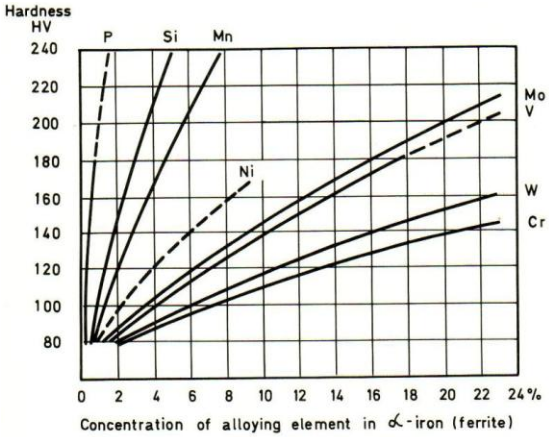

Fig. 2.1 Influence of alloying element additions Fig. 2.2 Effect of substitutional alloying on the eutectoid temperature andadditions on ferrite hardness [63]
the eutectoid carbon element content [61]

The elements Al, Nb, Ti and V in small amounts from 0.03 wt% to 0.10 wt% are important factors in inhibiting grain growth at the austenitizing temperature. This is because these elements are present as highly dispersed carbides, nitrides or carbo-nitrides (Al only as nitride) and that a high temperature is required to make them go into solution. Fig. 2.3 shows that in a steel containing about 0.05 wt% Nb or Ti and 0.20 wt% C, the niobium and titanium carbides are not dissolved until the temperature exceeds 1200°C [62]. For V and N contents of 0.1 wt% and 0.010 wt% respectively, the vanadium nitrides remain undissolved at temperatures up to and somewhat above 1000°C. Should the temperature rise so high that these phasesinhibiting grain growth go into solution, there will be a pronounced increase in grain size. The above-mentioned elements have found great use as microconstituents in the HSLA steels.

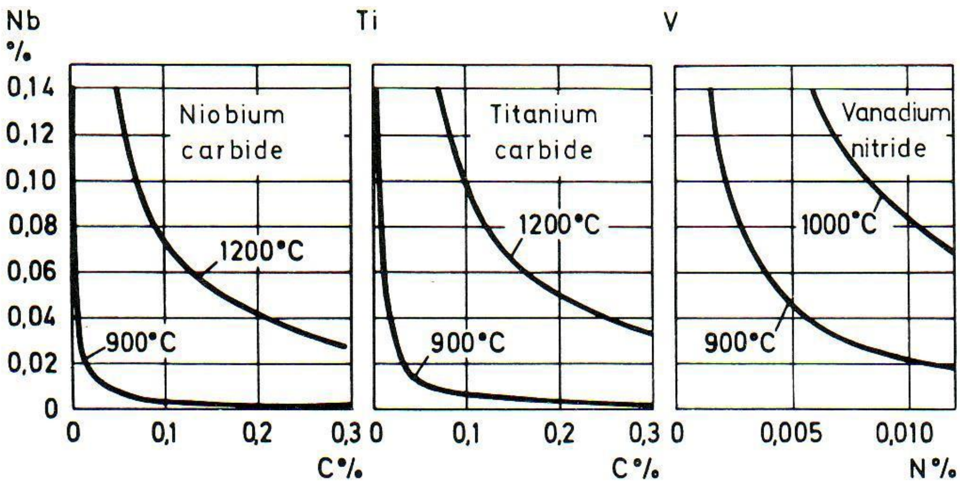

Fig. 2.3 Solubility isotherms of niobium carbide, titanium carbide and vanadium nitride in steel at different temperatures [63]

Ferrite grain refinement in ferrite-pearlite steels is accomplished through restricting the growth of austenite grains during hot rolling and/or by inhibiting the recrystalization of austenite during hot rolling so that the transformation occurs in unrecrastalized austenite. For example, in the hot rolling of semi-killed carbon steels, recrystalization of austenite occurs at temperature down to about 760°C. A 30% reduction at 815°C is sufficient for about 10% recrystalization. In a similar steel containing 0.03 wt% Nb, 10% recrystalization occurred after the steel was reduced 50% at 925°C. This explains why it is so difficult to refine grains in carbon steels until the rolling temperature drops below 815°C. It is usually less expensive to normalize a carbon steel than to obtain grain refinement by controlled rolling. In contrast, grain refinement in niobium steels can be obtained at finishing temperatures as high as 925°C.

In most instances, all Nb, C and N are in solution at the start of the hot rolling of austenite, but precipitation occurs during the rolling as the temperature of the steel drops. The precipitate particles hinder growth of austenite grains, and at still lower temperatures, the particles (or precipitation clusters) inhibit recrystalization of the deformed austenite grains. As indicated in Fig. 2.4, the effectiveness of microalloying elements in refining ferrite grains is in the same order as the solubility of their carbides in austenite (see Fig. 2.3).

It should be noted that the solubility of carbide particles in the austenite increases in the order NbC, TiC, VC, while the nitrides with normally lower solubility, increase in solubility in the order TiN, NbN, AlN, VN (see Fig. 2.5). It is thus apparent that NbC and TiN are the most stable particles and the most effective grain size refiners. However, Al, V, and Ti are more effective in high-nitrogen steels, by forming comparatively stable AlN, V(CN), and Ti(CN) in austenite, which may be potent in preventing grain coarsening on reheating but not effective in preventing recrystalization [63-65].

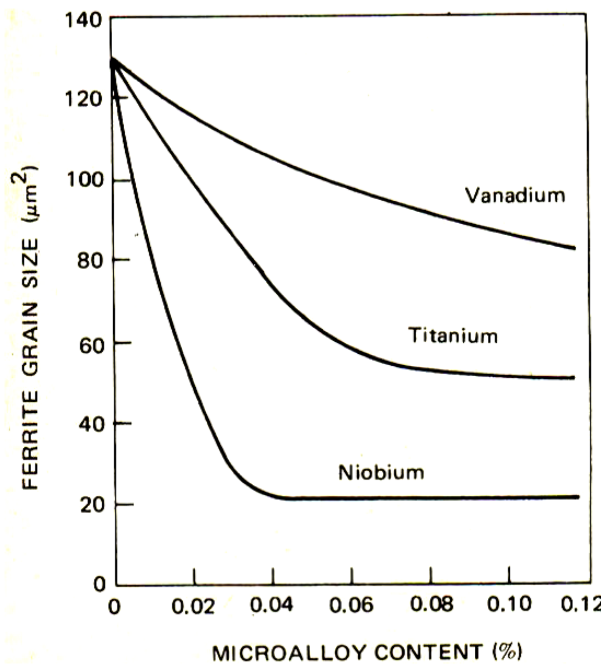

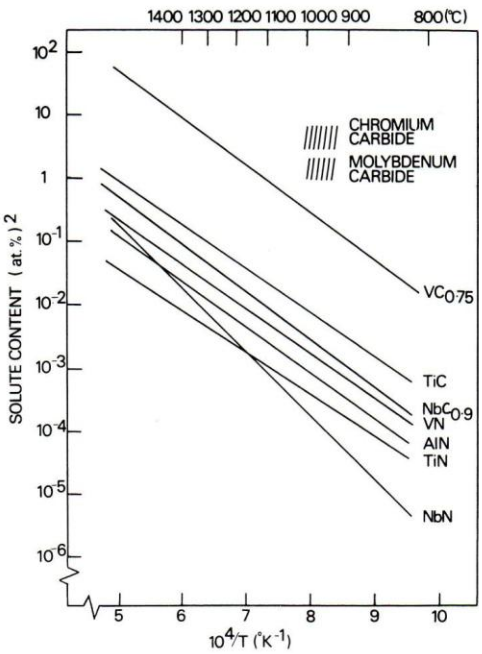

Fig. 2.4 Effect of microalloy content (Nb, Ti, V) on the ferrite grain size [64]

Fig. 2.5 Solubility product of carbides and andnitrides in austenite [65]

2.1.2 DMR-249A steel

Comprehensive research undertaken at the Defence Metallurgical Research Laboratory (DMRL), Hyderabad, India, resulted in development of DMR-249A steel [13]. DMR-249A is a low carbon (0.08 wt.% C) HSLA steel, with micro-alloying additions of 0.03–0.05 V, <0.05 Nb and 0.01–0.06 Ti. The steel is designed to have a predominantly ferritic microstructure, with pearlite less than 10% by volume. The average size of fine equiaxed ferrite grain is about 5.5 μm. The steel is characterized by higher strength and superior toughness at temperatures as low as minus 60 degree C [13-15]. This structural grade steel standardized by the American Bureau of Shipping for use in ship building is used in the construction of the hulls of various vessels with specific weight and resilience qualities. The chemical composition and mechanical properties of DMR249A are given in Table 2.1. The effects of alloying elements in DMR-249A steel are tabulated in Table 2.2. A typical microstructure of DMR-249A steel available in published literature [13-15] is given in Fig 2.6.

Table 2.1 Chemical Composition (wt.%) and mechanical properties of DMR-249A steel

C	Mn	Si	Ni	Al	Nb	V	S	P	Ti	Cu/Cr	N (ppm)	Fe
0.09	1.14	0.18	0.62	0.026	0.039	0.02	0.006	0.14	0.019	<0.020	56	Bal

Properties	YS (MPa)	UTS (MPa)	%Elongation	Charpy V-Notch Impact Toughness (J)		Hardness ($HV_{0.2}$)
				STP (25 °C) Sub	Zero (-60°)	
Value	430	620	30	>350	160	196-212

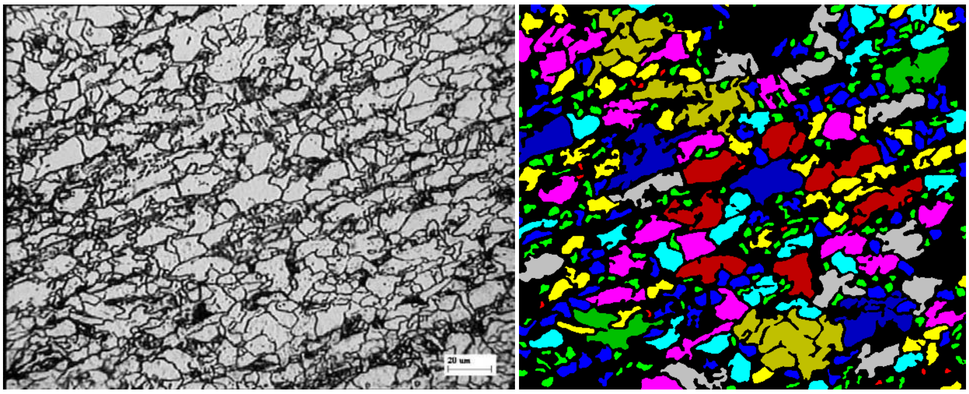

Fig 2.6 Microstructure of base material DMR-249A (GS: 5.5 + 3.8 μm)

Table 2.2 The effects of alloying elements in DMR-249A steel

	(%)	**Advantages / Improves**	**Disadvantages / Degrades**
C	0.08 – 0.11	Strength	Weldability, DBTT
Mn	1.150 – 1.65	Deoxidiser, Dissolves in Ferrite+$(Fe,Mn)_3C$ and improves (DBTT, Strength), MnS (Machinability, Prevents FeS) Cheaper substitute of (Ni,Cr)	Weldability, Hardenability, 2-10% (Brittle)
Si	0.150 – 0.40	Ferrite Stabiliser, Strength	Weldeability, DBTT
Ni	0.65 – 1.05	Toughness, Ductility with Strength and Hardness, DBTT, Fatigue, Heat Resist Properties	
Nb	0.05(max)	Grain Refinement, Precipitation Strengthening, Carbide/Nitride, DBTT, Increases re-crystallisation temp. (RCT)	
V	0.03 – 0.05		
Ti	0.01 – 0.06		
Al	0.03 (max)	Deoxidiser for acicular ferrite formation	
Cu	0.30(max)	Solid Solution Strengthening	
Cr	0.30(max)	Strength, Wear Resist, Corrosion Resistance	

Typically, plates of lower thickness are able to meet the specified properties in the as-rolled or normalized condition, but heavier gage (>18mm)plates require a water quenching and tempering (WQ+ T) treatment in order to meet both strength and toughness requirements consistently [14-15, 66]. Extensive literature exists on the production of normalized grades of microalloyed HSLA steel [2, 66-67]. These steels are typically normalized at 30–50 ◦C above the Ac_3 temperature. The actual normalizing temperature should be chosen such that it allows for complete re-austenitization of microstructure but also does not permit extensive austenite grain growth, as the average ferrite grain size in the product is significantly influenced by the grain size of the parent austenite.

The DMR-249A steel plates that are currently used meet specified properties in the as-rolled condition for thickness up to 16mm, but thicker plates require a water quenching and tempering treatment to meet property specifications. The production of steel is made cost effective by employing continuous casting, for higher yield, and controlled rolling, to overcome size limitation of plates and get required properties in as-rolled condition, obviating the need for heat treatment [13-15]. Typical flow chart of manufacturing process is shown in Fig 2.7 [13-15].

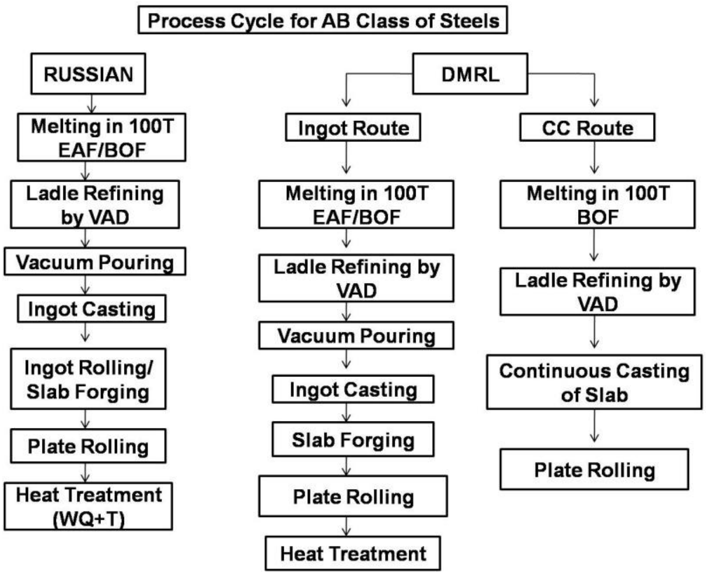

Fig 2.7 Flow chart of manufacturing process of DMR-249A steel[13-15]

2.2 Welding

Welding is the process of joining two metals with the use of heat and arc pressure. Arc welding is a fusion welding process that uses the heat generated by an electrical arc to melt the joining metals to create a strong joint.

2.2.1 Arc welding processes

The commonly used arc welding processes are enumerated below [68-69]:

2.2.1.1 Shielded metal arc welding (SMAW) - also known as "stick welding", uses an electrode that has flux, the protectant for the puddle, around it (Fig 2.8). The electrode holder holds the electrode as it slowly melts away. Slag protects the weld puddle from atmospheric contamination. SMAW produces heat from an electric arc that is maintained between the tip of a flux-covered electrode and the surface of the base metal. The electrode consists of a solid metal core covered by a mixture of mineral and metallic compounds. The composition of the coating depends on the type of electrode and welding polarity. Among its functions are shielding the weld pool, providing a fluxing action to remove impurities from the weld deposit and providing the desired weld mechanical properties by controlling the weld deposit chemistry. SMAW can be performed in areas of limited access and in all positions. It is a viable process for joining most metals and alloys, and the equipment needed is both portable and low in cost.

Advantages and disadvantages of SMAW - The welding equipment is relatively simple, portable, and inexpensive, as compared to other arc welding processes. For this reason, SMAW is often used for maintenance, repair, and field construction. However, the gas shield in SMAW is not clean enough for reactive metals such as aluminum . The deposition rate is limited by the fact that the electrode covering tends to overheatand fall off when excessively high welding currents are used.The limitedlength of the electrode (about 35 cm) requires electrode changing, and thisfurther reduces the overall production rate.

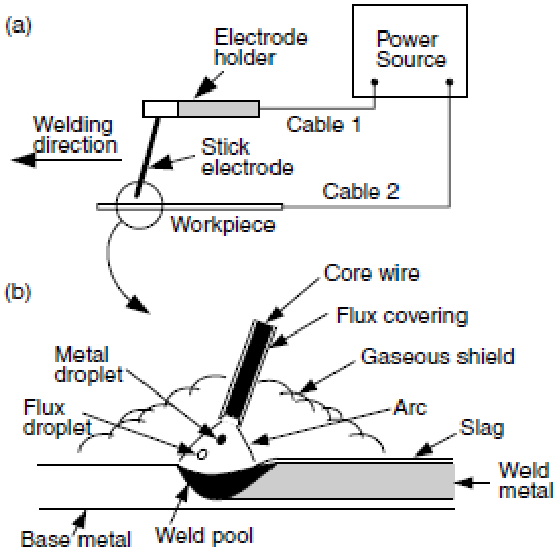

Fig2.8SMAW (*a*) overall process (*b*) welding area enlarged

2.2.1.2 Gas tungsten arc welding (GTAW) - also known as TIG (tungsten inert gas), uses a non-consumable tungsten electrode to produce the weld (Fig 2.9). The weld area is protected from atmospheric contamination by an inert shielding gas such as Argon or Helium. GTAW produces coalescence of metals by heating them with an electric arc between a tungsten electrode and the work-piece. Pressure and filler metal may or may not be used and shielding is obtained through the welding torch. The use of a non-consumable tungsten electrode and inert shielding gas produces the highest quality welds of any open arc welding process. Welds are bright and shiny, with no slag or spatter, and require little to no post-weld cleaning. GTAW can be used in all welding positions but requires a high level of operator skill, especially on thin and intricate parts. It has been used extensively in the aerospace & aircraft, energy, chemicals and oil & gas industries.

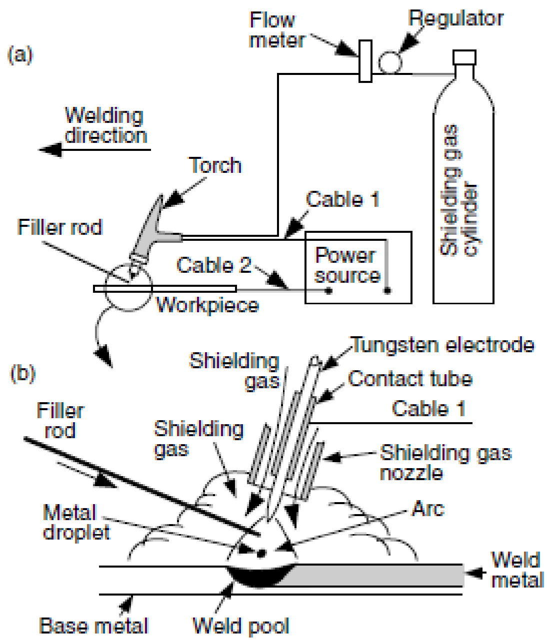

Fig 2.9GTAW (*a*) overall process (*b*) welding area enlarged

Advantages and disadvantages of GTAW – Gas tungsten arc welding is suitable for joining thin sections because of its lower heat input. The feeding rate of the filler metal is somewhat independentof the welding current, thus allowing a variation in the relative amountof the fusion of the base metal and the fusion of the filler metal. Therefore,the control of dilution and energy input to the weld can be achieved withoutchanging the size of the weld. It can also be used to weld butt joints of thinsheets by fusion alone, that is, without the addition of filler metals (*autogenous*welding). Since the GTAW process is a very clean welding process, it canbe used to weld reactive metals, such as titanium and zirconium, aluminum,and magnesium.

However, the deposition rate in GTAW is low. Excessive welding currentscan cause melting of the tungsten electrode and results in brittle tungsteninclusions in the weld metal. However, by using preheated filler metals, thedeposition rate can be improved. In the hot-wire GTAW process, the wire isfed into and in contact with the weld pool so that resistance heating can beobtained by passing an electric current through the wire.

2.2.1.3 Gas metal arc welding (GMAW) - commonly termed MIG (metal, inert gas), uses a wire feeding gun that feeds wire at an adjustable speed and an argon-based shielding gas or a mix of argon and carbon dioxide (CO_2) flows over the weld puddle to protect it from atmospheric contamination (Fig 2.10).GMAW is an arc welding process that incorporates the automatic feeding of a continuous, solid consumable electrode that is shielded by an externally supplied gas. The process is used to weld most commercial metals including steel, aluminium, stainless steel and copper and can be used to weld in any position when appropriate welding parameters and equipment are selected. GMAW uses direct current electrode positive (DCEP) polarity, and because the equipment offers automatic arc control, the only manual controls required by the welder are gun positioning, guiding and travel speed.Flux-cored arc welding (FCAW) - almost identical to MIG welding except it uses a special tubular wire filled with flux; it can be used with or without shielding gas, depending on the filler.

FCAW is an electric arc welding process designed for carbon steel, stainless steel and low-alloy steels. It uses an electric arc to produce coalescence between a continuous tubular filler metal electrode and the base material, and can be used with or without a shield gas. With gas shielded flux-cored wire, shielding agents are provided by a flux contained within the tubular electrode. An externally supplied gas augments the core elements of the electrode to prevent atmospheric contamination of the molten metal. With special voltage sensing feeders, it is possible to do high-quality flux-cored welding with a constant current welding power supply. The process is suitable for all position welding with the correct filler metal and parameters selection.When a shielding gas is used, the process equipment is virtually the same as used in GMAW.

Advantages and disadvantages of GMAW - Like GTAW,GMAW can be very clean when using an inert shielding gas.Themain advantage of GMAW over GTAW is the much higher deposition rate,which allows thicker workpiece to be welded at higher welding speeds. Thedual-torch and twin-wire processes further increase the deposition rate ofGMAW (12). The skill to maintain a very short and yet stable arc in GTAWis not required in GMAW. However, GMAW guns can be bulky and difficult-to-reachsmall areas or corners.

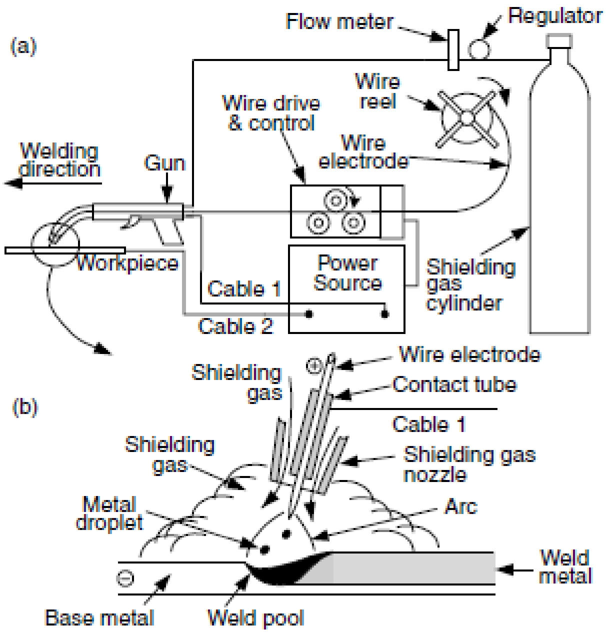

Fig 2.10GMAW (*a*) overall process (*b*) welding area enlarged

2.2.1.4Submerged arc welding (SAW) - uses an automatically fed consumable electrode and a blanket of granular fusible flux. The molten weld and the arc zone are protected from atmospheric contamination by being "submerged" under the flux blanket. SAW heats metals using an electric arc between a bare electrode and the base material, beneath a blanket of flux material. This process uses a continuous, solid wire electrode shielded by the flux. The flux acts to stabilize the arc during welding, shielding the molten pool from the atmosphere. It also covers and protects the weld during cooling and can affect weld composition and its properties. SAW is most commonly automated, but semi-automated systems are also available. The current can be either AC or DC and for automated systems, the electrodes can be a single wire or multiple solid or tubular wires, or strips. Welding can only be done in a flat or horizontal position due to the use of granular flux and the fluidity of the molten weld pool. High deposition rates can be achieved and very thick and thin materials can be welded with this process.

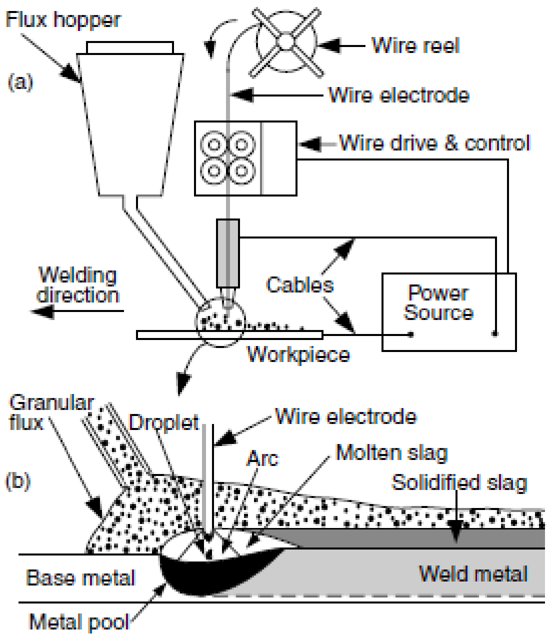

Fig 2.11SAW (*a*) overall process (*b*) welding area enlarged

Advantages and disadvantages of SAW - The protecting and refining action of the slag helps produce clean welds inSAW. Since the arc is submerged, spatter and heat losses to the surroundingair are eliminated even at high welding currents. Both alloying elements andmetal powders can be added to the granular flux to control the weld metalcomposition and increase the deposition rate, respectively. Use of two or moreelectrodes in tandem further increases the deposition rate. Because of its high deposition rate, workpieces much thicker than that in GTAW and GMAW canbe welded by SAW. However, the relatively large volumes of molten slag andmetal pool often limit SAW to flat-position welding and circumferentialwelding (of pipes). The relatively high heat input can reduce the weld quality and increase distortion.

2.2.2 Factors affecting depth of penetration

There are several welding variables which affect the degree of weld penetration. The following points, in no particular order, highlight the effects that welding process parameters have on penetration depth(assuming all other variables are held constant) [68-69].

Current: The welding variable that has the greatest effect on the degree of weld penetration is current (measured in amperage or amps). Quite simply, as welding current increases (i.e., more amperage), weld penetration increases.With arc welding processes which use constant current (CC) output, current is the main, presettable welding variable. However, with processes that use constant voltage (CV) output, voltage and wire feed speed (WFS) are the main, presettable welding variables, with current being a result of WFS. As WFS increases, the corresponding current level for that particular electrode type and diameter also increases.

Polarity: The type of welding polarity used affects penetration level. With most arc welding processes, DC+ (direct current electrode positive) polarity produces more weld penetration, because more arc energy is focused into the base plate. Conversely, DC- (direct current electrode negative) polarity produces less weld penetration, because more arc energy is focused into the electrode and not into the base plate. This is the case with the Shielded Metal Arc Welding (SMAW), Gas Metal Arc Welding

(GMAW), Flux Cored Arc Welding (FCAW) and SAW processes. The exception is the Gas Tungsten Arc Welding (GTAW) process, in which the effect of polarity on penetration is opposite. With GTAW, DC- polarity results in more weld penetration (with DC+ polarity generally not used).

Some advanced power sources use Waveform Control Technology and AC (alternating current) in order to provide excellent arc stability and control between weld deposition rates and weld penetration levels. They also have the ability to control the balance of the AC wave, offset of current and frequency for further control over the weld characteristics.

Welding Process: the various arc welding processes have associated weld penetration characteristics. For example, the SAW, FCAW and GMAW (in a globular, spray or pulse spray arc metal transfer mode) processes are known in general for higher levels of weld penetration. Whereas the GTAW, GMAW-C (metal core) and GMAW (in a short circuit metal transfer mode) processes are known in general for lower levels of penetration. Of course this correlation is also related to current. For example, the SAW process tends to be used at very high current levels while the short circuit GMAW process tends to be used at lower current levels. The SMAW process can have deeper or shallower penetration characteristics, depending on the specific type of electrode used.

Type of Electrode: Even within the same welding process, electrodes of different classifications can have different penetration characteristics. For example, with the SMAW process, an E6010 electrode typically has deeper penetration, while an E7024 electrode has shallower penetration. Another example can be seen with the FCAW process. An E70T-1 electrode typically has deeper penetration, while an E71T-1 electrode typically has shallower penetration.

Travel Angle: The degree of the travel angle, whether a push or drag travel angle, affects how much of the arc force is directed down into the base plate. A travel angle of 0° to 10° (i.e. the electrode perpendicular to the plate) will result in more weld penetration. As the travel angle becomes more severe, the level of weld penetration will decrease.

Shielding Gas Type: shielding gas types also have an effect on weld penetration. Shielding gases with a higher rate of thermal conductivity, such as 100% carbon dioxide (CO_2) or 100% helium (He), will produce welds with a broader, deeper penetration profile. While shielding gases with a lower rate of thermal conductivity, such as 100% argon (Ar), or an Ar / CO_2 or Ar / oxygen (O_2) blend, have a shallower penetration profile that is more tapered in the middle.

Electrode Diameter: When welding with two different diameters of the same electrode and at the same current level, generally more penetration is achieved with the smaller diameter electrode than with the larger diameter electrode. As the same amount of current flows through each electrode, the concentration or density of current is greater in the smaller diameter electrode than in the larger diameter electrode. As a result of this higher current density, the smaller diameter electrode will have greater weld penetration than the larger diameter electrode. Note however that every electrode diameter has a maximum current density before the welding arc becomes very unstable and erratic. So as current reaches a certain level, it will become necessary to increase the electrode diameter.

Travel Speed: How fast the electrode travels down the joint affects how much time the arc energy has to transfer into the base plate at any particular point along the joint. As travel speed increases, the amount of time that the arc is over a particular point along the joint is less and the resulting level of penetration decreases.

CTWD Variations: with the GMAW, FCAW and SAW processes on constant voltage (CV) power sources and running at a set wire feed speed and voltage, as the contact tip to work distance (CTWD) is increased, more resistance to the flow of electricity through the electrode occurs, because the electrode (i.e., the metal electrical conductor) is longer. At a constant voltage level, this increase in resistance causes current to decrease (i.e. Ohms Law), which results in a decrease in penetration level.

2.3 Overview of A-GTAW welding

ThepenetrationcapabilityofthearcinGTAWweldingcanbesignificantlyincreasedb y applicationofafluxcoatingcontainingcertaininorganiccompoundsonthejointsurface priortowelding[70-79].Theuseoffluxis alsoclaimedtoreducethesusceptibilitytochangesinpenetrationcausedbycast-to-cast variabilityinmaterialcompositionandreportedtoproduceconsistentpenetrationregardless ofheat-to-heatvariationsinbasemetalcompositions[74, 80].Inparticular, alotofresearchhasfocusedontheA-GTAWweldingprocessdeveloped bytheE.O.PatonElectricWeldingInstitute(PWI)[71]. Inthisprocess, the activated fluxes are prepared with combinations of SiO_2, TiO_2, NiO, CuO_2 and combinations of oxide powders.The prepared mixtures of oxide powders are mixed with acetone and binder material to form a paste. The flux in the form of paste is manually applied on the bead on plate surface using a brush prior to welding (Fig

2.12).Theacetoneisevaporatedleavingfluxonthe

surfaceandautogenousGTAWweldingiscarriedout.

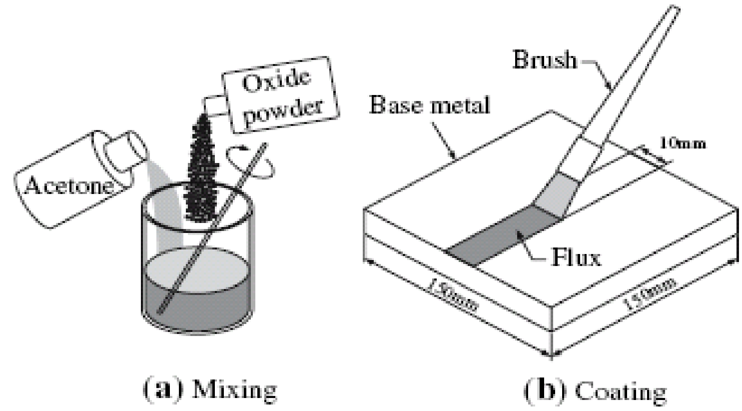

Fig 2.12 Preparation and application of flux on weld joint line

IthasbeenclaimedthattheA-GTAWprocesscanachieveinasinglepassafullpenetrationweldinsteelsandstainlesssteelsu pto 12mmthicknesswithoutusingabevelpreparationorfillerwire[80]. Furthermore,the weld jointmechanical properties and soundness are claimed to be unaffected.AseriesofGTAWfluxesthatproduceconsistentpenetrationregardlessofheat-to-heat variationsinbasemetalcompositionshavebeendeveloped,validatedandcommercialized. Thesefluxescanovercomethelowdepositionratesandshallowpenetrationcommoninmost GTAWprocessapplications.Specificfluxeshavebeendevelopedforstainlesssteels(types 304,316,347,409,410),nickel-basedalloys(alloys600,625,690,718,800),carbonandlow alloy steels, copper-nickelandtitanium(CPandTi-6AL-4V).

2.3.1 MechanismforIncreaseinPenetrationduetoFlux

Manyinvestigationshavebeenmadetounderstand themechanismofincreasedweldpenetrationinGTAweldingduetoflux[79-84]. Considering the theoretical basis, the only one difference between GTAW and A-

GTAW is the use of activating fluxes (Figure 2.13). In the last four decades, four different theories on the explanation of the mechanism of the activating fluxes were published [78,85].

Theory of Savitskii and Leskov 1980[21] : This theory indicates that the activating flux decrease the surface tension of the weld pool. This enhances the arc pressure to cause a deeper penetration into the pool and the arc pressure to reach a deeper penetration.

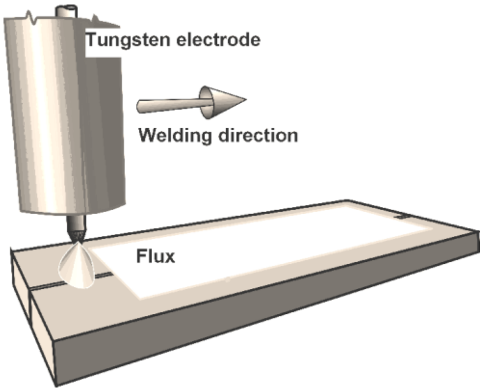

Fig 2.13Schematic of A-GTAW welding process

Theory of Heiple and Roper 1982[22]: The convective flowing of the molten metal from the centre towards the edge is the phenomenon that is called Marangoni-effect (gradient of the surface tension of the weld pool is negative). This theory explains the high penetration with the reversed Marangoni-convection. It says that the activating fluxes change the gradient of the surface tension from negative to positive that results in the flowing of the molten metal inwards towards the centre.

Theory of Simonik 1976[23] : Simonik says that oxide and fluorine molecules present in the activating fluxes have affinity to focus the free electrons at the edge of the plasma of the arc. The ions formed this way have substantially lower mobility than the free electrons. This leads to increased current density in the centre of the arc by means of the higher movement of the free electrons which leads to the deeper penetration.

Theory of Lowke, Tanaka and Ushio 2005[24]: They explain the deep penetration by means of the higher electric insulation of the activating fluxes. Because of the higher electric insulation, the arc is able to break through the surface (and the flux on it) at a narrower area. The focus of the arc increases which leads to higher current density in the arc spot and this causes the deep penetration.

Manyinvestigationsonthemechanismhavebeenmadeandthetworepresentativetheories areconstrictionofthearc[76-77, 86-87]andreversaloftheMarangoniconvectionintheweldpool[22,88-93]. AchangeinMarangoniflowhasbeenusedtoexplainvariablepenetrationinwelds(Fig. 2.14).Thischangeinfluidflowisrelated tothethermalcoefficientofsurfacetensionofthe moltenpool.Ifthethermalcoefficientofthesurfacetensionisnegative,thecoolerperipheral regionsofthepoolwillhavehighersurfacetensionthanthecentreoftheweldpoolandthe flowwillbeoutwardscreatingawideshallowweldpool(Fig.2.14a).Inmaterialswitha positivegradient,thisflowisreversedtowardsthecentreoftheweldpoolandinthecentre, themoltenmaterialflowsdownwards.Thiscreatesanarrowerdeeperweldpoolforexactly the same welding conditions (Fig. 2.14b).

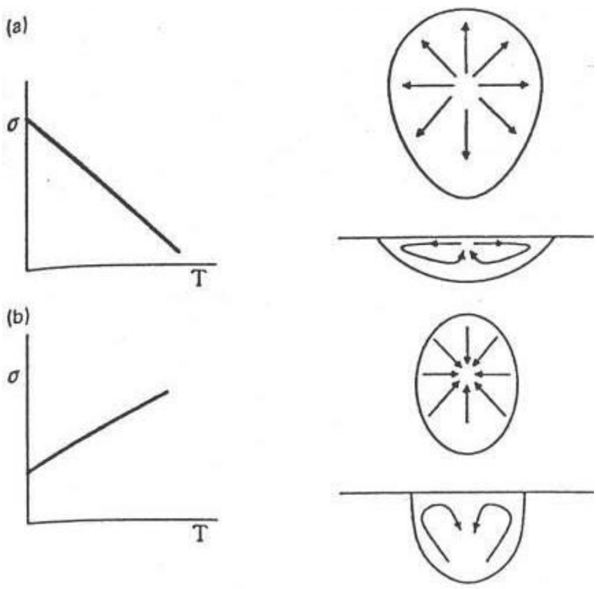

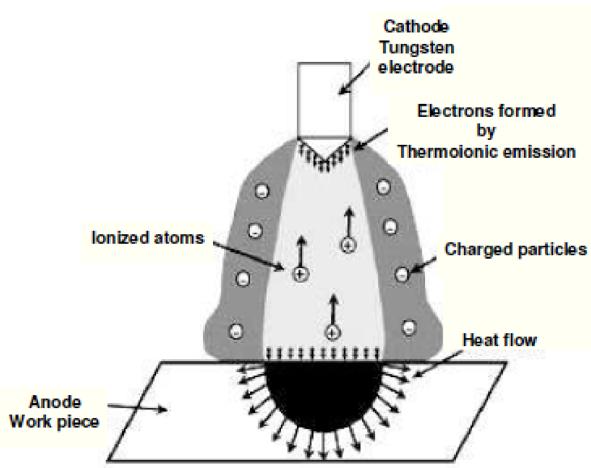

Fig.2.14Marangoniflow:σ□ issurfacetension,Fig.2.15Mechanismofarc

Tistemperature.onstrictionproposed
(a)Negativesurface tension temperaturecoefficientforA-GTAWprocess
(b)Positivesurfacetensiontemperature coefficient

Simonik[23]proposedatheoryfortheeffectivenessofthefluxesbaseduponanarc constrictionmechanism.AlthoughSimonik'stheoryappearsplausibleanddoesconcurwith hisexperimentalobservations,themodelproposedfortheGTAWarcdoesnotagreewith currenttheoryinwhicharciscomprisedofacentralizedionizedcolumnratherthanneutral atoms.LucasandHowse[79]haveproposedmechanismwhichisbasedontheconcept thattheGTAWarc is comprised of the following four regions as shown in Fig. 2.15.

PlasmaColumn	Current carried by the electronsand ions produced by the thermal ionizationoftheshieldinggas.
Anode/Cathode	Highpotentialdroptomaintainthecurrentflowasthegasiscooledby theelectrode
Cathode	Underthebombardmentbypositiveions,thehightemperatu recreates the condition for the thermionic emission of electrons
Anode	Under the influence of the anode potential drop, the electrons acceleratebutthenthekineticenergyistransferredtotheanode

Constrictionofthearcwillincreasethetemperatureattheanodebecauseoftheincreasei n currentdensityandthehigherarcvoltage.Itisconsideredthevaporizedfluxwillconstrict thearcbycapturingelectronsintheouterregionsofthearc.Electronattachmentcantake placeinthecoolerperipheralregionswheretheelectronshavelowenergyinaweakelectric field.Towardscentreofthearcwherethereisastrongelectricfield,hightemperaturesand veryhighenergyelectrons,ionizationwilldominate.Thusrestrictingcurrentflowtothe centralregionofthearcwillincreasethecurrentdensityintheplasmaandattheanode resultinginanarrowerarcandadeeperweldpool.Arcconstrictionwillbepromotedbyflux constituentswhosemoleculesoratomshavealargeelectronattachmentcrosssection. Halogencompoundshavelargeelectronattachmentcrosssectionwhendissociatedwillhave strongaffinityforelectrons.Othercompoundssuchasmetaloxideswhichhavealower electronattachmentdiameterbutahigherdissociationtemperatureareequallyeffectivein constrictingthearcastheycanprovideagreaternumberofvaporizedmoleculesandatoms intheouterregionsofthearc.

Themechanicalproperties,weldability,corrosionresistanceandsafeuseoftheseflux eshave beenextensivelytestedandfoundsuitableforawiderangeofapplications.Inmaterialsless than12.5 mmthickfullpenetrationmaybeachievedwithasquarebuttjoint,possiblyreducing weldbevelpreparationcosts.Inthickersections,thefluxcanbeusedonasquare-edgeland attheroot,andtheremainderoftheweldcanbecompletedusingaconventionalgroove preparation.Thismayeliminatetwoorthreepassesnecessarytocompletethejoint.Dueto theincreaseinpenetration,itispossibletoreduceheatinputs,ifnecessaryandstillachieve penetrationlevelstwicethatresultingfromconventionalGTAWwelding.StandardGTAW welding equipment,shieldingandbackinggasesandconsumablesaresufficientforcarryingoutflux assistedGTAWwelding.Usingflux,weldbeadwidthisonlyhalfortwothirdsofthatexpected withtraditionalGTAWweldingprocess.Thefluxeshavenotbeenfoundtosignificantlyalter theweldrootprofile.ThemechanicalpropertiesoftheGTAWweldmadewithfluxshouldbe nominallyidenticaltoaconventionalGTAWweldaslongastheconsumablesandshielding gasesaresame.Thereductioninweldingtimeissignificantwiththefluxandapplyingthe fluxisrelativelyeasyintheshoporfield.

2.3.2 Factors affecting weld pool flow in A-GTAW

The phenomenon of enhanced depth of penetration on application of activated flux involves many complex integrities. The nuances of established factors affecting weld pool flow in A-GTAW have been summarized in the following discussion [92-94].

Severalelementshavebeenreportedtoaffectweldpenetrationandbeadwidthincludi ng sulphur,oxygen,aluminiumandcalcium.Astheamountofsulphurandoxygeninthebase metalincreases,theamountofweldpenetrationincreasesandthebeadwidthdecreases.In addition,asthepercentagesofaluminiumandcalciumincrease,weldpenetrationdecreases andthebeadwidthincreases.Mostliteratureonvariableweldpenetrationagreesthatsulphur hasthedominanteffectonweldpenetration.Asageneralrule,sulphurbeginstohave detrimentaleffectonweldpenetrationinausteniticstainlesssteelatlevelslessthan0.01wt% (100ppm)withtheeffectdramaticallyincreasingwithlevelsbelow0.006wt%(60ppm).

However,itshouldbenotedthattheactualpenetrationwilldependonthecombinationo f otherelementsinaspecificmaterialheat.

The addition of sulfur, oxygen, selenium, and tellurium to stainless steel in low concentrations (less than 150 ppm) was shown to substantially increase GTA weld depth-to-width ratio (*d*/*w*). All these elements are known to be highly surface active in liquid iron. Measurements of the temperature dependence of the surface tension for steels with different GTA weld penetration characteristics produced an impressive correlation between a positive surface tension temperature coefficient arising from surface-active impurities and high *d*/*w* ratio welds (Fig. 2.16) [95].

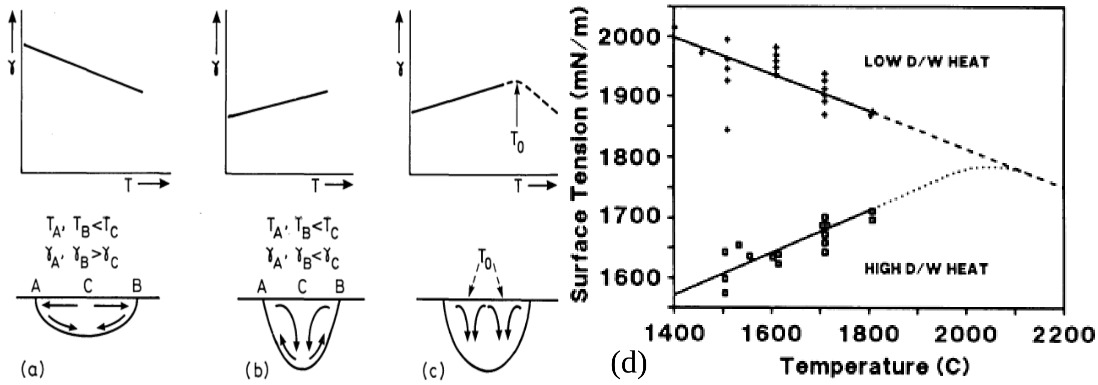

Fig 2.16 dγ*/dT Curves* (a) Low S concentration (b) High S concentration(c) Critical Temp To (reversal in the direction of thermo capillary flow) (d) For two steelsdata labeled"high *d*/*w* heat" are from material having approximately 160 ppm more sulfur than thematerial labeled "low *d*/*w* heat." the dashed lines indicate the expected behavior of thesurface tension above the maximum temperature studied [95]

When additions were made to the weld pool of elements known to react with surface-active elements already present in the steel to form compounds that are not surface active, the GTAW weld *d*/*w* ratio decreased. Aluminum reacts with oxygen and produced wider, shallower welds. (Fig 2.17) [96].The effect of alloying elements like Mn and Si is given in Fig 2.18 [91]. Cerium reacts with both sulfur and oxygen and also produced lower *d*/*w* ratio welds. The effect of doping with Sulfur and Selenium is given in Fig 2.19 [97].

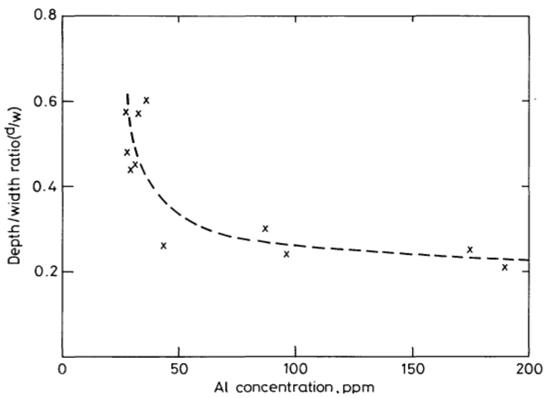

Fig 2.17 Variation of aspect ratio of weld pool *d/w* with Al content [98]

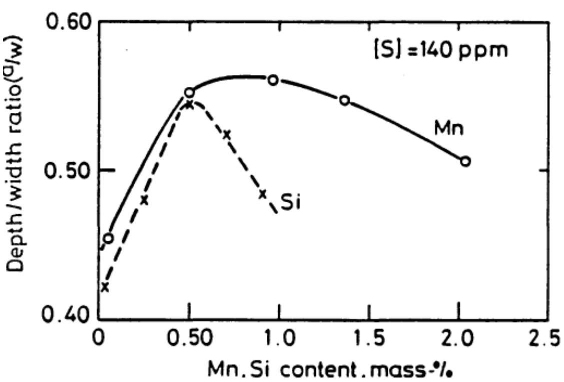

Fig 2.18 Effect of Mn and Si on d/w ratio [91]

An example of the success of the fluid flow model in explaining GTA welding phenomena is provided by butt welding together two steels with large differences in weld penetration characteristics. The weld pool is not centered over the joint; rather, it is displaced toward the material with low *d*/*w* behavior [97], as indicated schematically in Fig. 2.20. The low *d*/*w* material has a low concentration of surface-active impurities and therefore a high surface tension. Thus, there is a net surface tension gradient across the weld pool toward the low *d*/*w* material, producing the fluid flow pattern and weld cross section indicated in Fig. 2.20. Ishizaki et al[99] have reported that the variousweld profiles could be classified into six categorieswhich are shown in Fig. 2.21

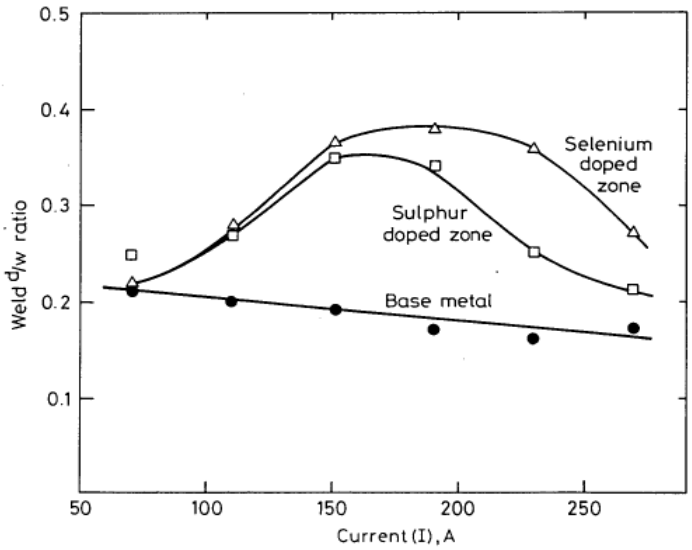

Fig 2.19Plot of weld *d/w* ratio for zones doped with sulfur and selenium [97]

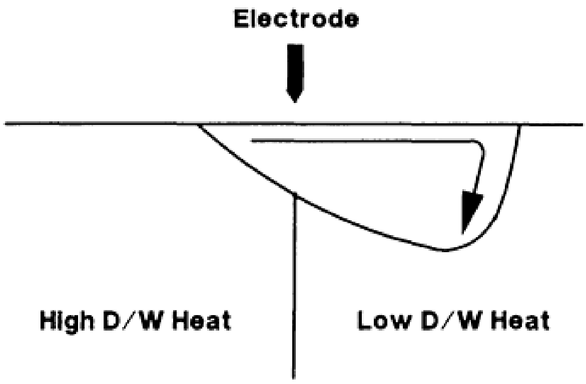

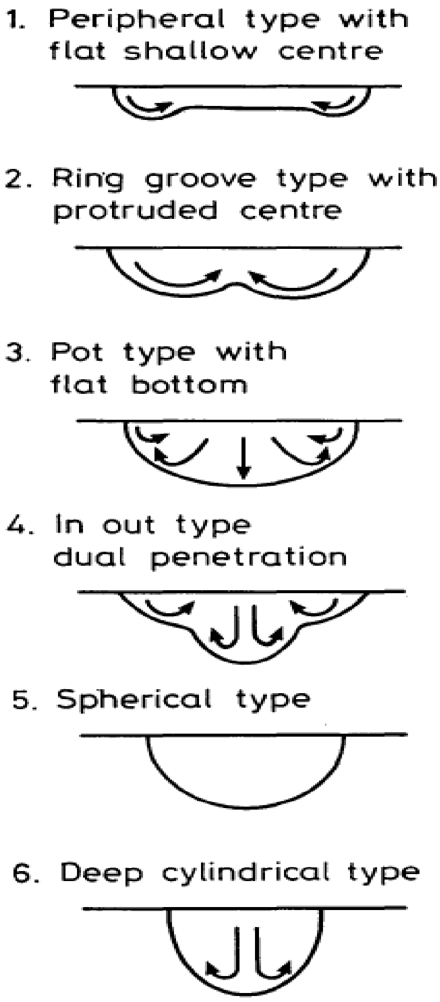

Fig. 2.20typical fluid flow generated when butt welding two heats of material with different penetration characteristics [97]

Fig 2.21Classification of weld profile types [99]

2.3.3 Benefitsofusingactivatedflux

Specificadvantagesclaimed[70]fortheactivatingfluxprocess, comparedwiththeconventionalGTAWprocessinclude:

(a) Increasesdepthofpenetration;upto12mmthickstainlesssteelcanbeweldedina singlepasscomparedwithtypically3mmwithconventionalGTAW.

(b) Overcomestheproblemofcast-to-castvariationinlowsulphur(lessthan0.002%) containingstainlesssteelwhichwouldnormallyformawideandshallowweldbead with conventional GTAW.

(c) Reducesweldshrinkageanddistortion.Straightsidedsquare-buttjointweldwill producelessdistortionthanamulti-passweldinthesamethicknessmaterialbutwith aV-joint.

(d) Reduction in bevel preparation requirements

(e) Decrease in the number of weld passes

(f) Shortening of weld times

(g) Reducedconsumptionofweldingfillerwire

(h) Elimination of back gouging and/or grinding

Theclaimfortheincreaseinproductivityisderivedfromthereductionintheweldingti me eitherthroughthereductioninthenumberofpassesortheincreaseinweldingspeed.Overall weldingcostscanbereducedbyupto50%ormorecomparedtoconventionalwelding. The disadvantagesofusingthefluxincludetheroughersurfaceappearanceoftheweldbeadand theneedtocleantheweldafterwelding.Itoftenrequiresrigorouswirebrushingtoremove the slag residue.

2.3.4 Success of A-GTAW with 304LN/316LN stainless steels and other alloys

Specific activated flux [100] has been developed for enhancing the penetration performance of the GTAW welding process for welding of type 304LN and type 316LN stainless steels. A significant increase in penetration of over 300% has been achieved in single pass GTAW welding [101-102]. The use of flux has caused no degradation in the microstructure and mechanical properties of the welds compared to those produced by conventional GTAW welding. The use of flux therefore would result in significant cost reduction as there is no requirement for edge preparation and filler metal addition. The improvement in creep-rupture properties of the A-GTAW weld joints of 316LN stainless steel has already been demonstrated [103]. The developed Activated flux has been successfully field-tested and demonstrated for all its advantages for welding of dummy core subassemblies of a sodium cooled fast reactor made of 304L SS [104]. Significant reduction in residual stresses and distortion in A-GTAW weld joints of austenitic stainless steels has been reported [105]. It is also reported that process parameters optimization would help in achieving the desired depth of penetration during A-GTAW welding [106].

In recent times, a lot of research has been undertaken on applicability and advantages of A-GTAW as alternate welding process for duplex stainless steels (DSS), ferritic stainless steels, Reduced Activation Ferritic/Martensitic (RAFM) steel, 9Cr-1Mo (P-91) steel, 2.25Cr-1Mo (P22) steel and other alloys [107-118]. Magudeeswaran et al. [107] studied A-GTAW process parameters such as current, travel speed, electrode gap and voltage, that influence and aid in controlling the aspect ratio of DSS joints. Badheka et al. [108] studied the effect of current, welding speed, joint gap and electrode diameter on weld bead dimensions on 6 mm thick dissimilar weld between carbon steel to stainless steel. Zou et al. [109] adopted the method of double-shielded advanced A-GTAW welding for the welding of the duplex stainless steel. Tseng et al. [110] investigated the influences of specific flux powders, including FeF_2, FeO, and FeS on the surface appearance, geometric shape, angular distortion, hot cracking susceptibility, and metallurgical properties of 5 mmthick 17Cr–10Ni–2Mo alloys. Huang et al. [111] examined the influence of oxide-based flux powder and carrier solvent composition on the surface appearance, geometric shape, angular distortion, and ferrite content of austenitic 316L stainless steel GTAW joints. Sakthivel et al. [112] joined 316 LN stainless steel plates using A-GTAW welding and conventional GTAW welding processes. Meng et al. [113] carried out experimental investigations toward the effect of A-GTAW process parameters on penetration in mild steel plates. Ruan et al. [114] reported microstructure and mechanical properties of 6082-T6 joints fabricated using A-GTAW technique. Vasantharaja et al. [115] carried out studies on A-GTAW welding of Reduced Activation Ferritic/Martensitic (RAFM) steel. Various studies on functional utility of A-GTAW on materials like 9Cr-1Mo (P-91) and 2.25Cr-1Mo (P22) steels have been reported by Maduraimuthu et al. [116]and Arivazhagan et al. [117-118] respectively.

2.4 Phase transformation during Welding in Ferritic Steels

Post-solidification phase transformations, when they occur, can change thesolidification microstructure and properties of the weld metal. It is, therefore,essential that post-solidification phase transformations be understoodin order to evaluate the weld metal microstructure and properties.The atomic arrangement in a crystal can be altered either by breaking all the bonds and rearranging the atomsinto an alternative pattern (reconstructive transformation),or by homogeneously deforming the original pattern intoa new crystal structure (displacive transformation) [119].In the displacive mechanism, the change in crystalstructure also alters the macroscopic shape of the samplewhen the latter is not constrained. The shape deformationduring constrained transformation is accommodated by acombination of elastic and plastic strains in the surroundingmatrix.It is the diffusion of atoms that leads to the new crystalstructure during a reconstructive transformation. The flowof matter is sufficient to avoid any shear components ofthe shape deformation, leaving only the effects of volumechange. Fig 2.22 is a summary of the maintransformations that occur in steels.

Acicular ferrite is a microstructure of ferrite that is characterized by needle shaped crystallites or grains when viewed in two dimensions. The grains are three dimensional in shape and have a thin, lenticular shape. This microstructure is advantageous over other microstructures because of its chaotic ordering, which increases toughness. Acicular ferrite is formed in the interior of the original austenitic grains by direct nucleation from the inclusions, resulting in randomly oriented short ferrite needles with a 'basket weave' appearance. This interlocking nature, together with its fine grain size (0.5 to 5 μm with aspect ratio from 3:1 to 10:1), provides maximum resistance to crack propagation by cleavage. Acicular ferrite is also characterized by high angle boundaries between the ferrite grains [120]. This further reduces the chance of cleavage, because these boundaries impede crack propagation. It is of considerable commercial importance because it provides a relatively tough and strong microstructure. It forms in a temperature range where reconstructive transformations become relatively sluggish and give way to displacive reactions such as Widmanstatten ferrite, bainite and martensite.

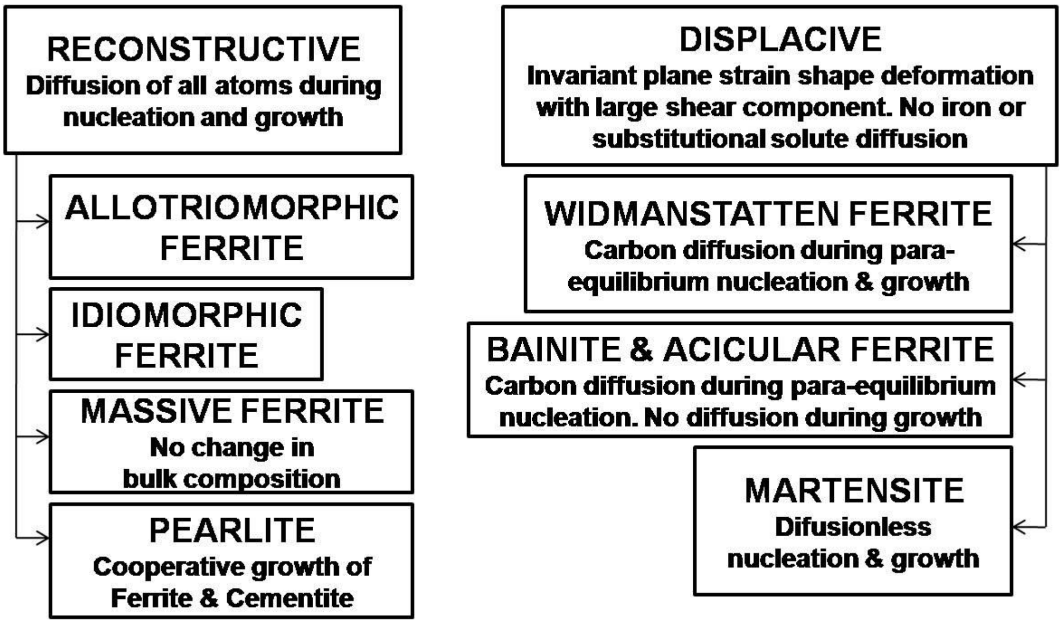

Fig. 2.22 Classification of the transformation products of austenite [119]

Widmanstatten ferrite develops when coarse austenite grained steel due to high temperature heating is cooled fast but less than critical cooling rate. In this structure, the proecutectoid phase separates not only along the grain boundaries of austenite, but also inside the grains after certain crystallographic planes and directiosn in the shape of plates or needles, forming mesh like arrangements. Widmanstatten structure is characterized by its low impact energy and low percentage elongations [121].

Grain boundary ferrite,also called pro-eutectoid ferrite, forms along the austenite grain boundary when the weld metal is cooled in the stage of austenite-ferrite transformation. Elongated or granulated, this grain boundary ferrite grows into the austenite grain on one side of the boundary. This reaction is known as ferrite veining due to its branching aspects throughout the weld metal [122].

Polygonal ferrite occurs in the form of coarse ferrite islands inside the prior austenite grains. Its presence reduces the toughness of the weld metal. Its amount increases with the increase in heat input during welding and decreases with the increase in carbon and chromium content of the weld metal [122].

The amount of grain boundary ferrite and polygonal ferrite increases and amount of acicular ferrite decreases with the increase in the heat-input. It can be attributed to the coarsening of the ferrite at the higher heat-input. Available literature suggests that a reduction in austenite grain size leads to a replacement of acicular ferrite with bainite [122].

Bainite forms during thermal treatment at cooling rates too fast for pearlite to form,yet not rapid enough to produce martensite. Two main forms can be identified:upper and lower bainite. This latter distinction is valuable because there are cleardifferences in the mechanical properties of upper and lower bainite [123].*Upper bainite* consists of fine plates of ferrite, each of which is about 0.2 μm thickand about 10 μm long. The plates grow in clusters called sheaves. Upper bainiteevolves in distinct stages beginning with the nucleation of ferrite plates at theaustenite grain boundary.*Lower bainite* is obtained by transformation at relatively low temperatures. Lowerbainite has a microstructure and crystallographic features which are very similar tothose of upper bainite. The major difference is in the nature of the carbideprecipitates in that carbides also precipitate inside the ferrite plates of lower bainite.The transition between upper and lower bainites is believed to occur over a narrowrange of temperature. It is possible for both forms to occur simultaneously duringisothermal transformation near the transition temperature, as depicted in Fig. 2.23 [124].

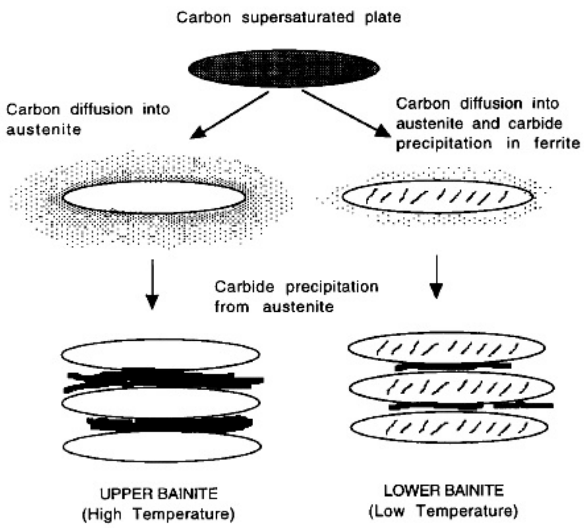

Fig. 2.23Schematic representation of transition from upper to lower bainite [124]

The main difference between bainite (bainitic ferrite) and acicular ferrite is related tothe nucleation and growth mechanism. In bainite, ferrite constituent initiates on theaustenite grain boundaries, forming sheaves of parallel plates with nearly the samecrystallographic orientation. However, acicular ferrite nucleates intragranularly atnonmetalic inclusions, within large austenite grains and on the surfaces of existingacicular ferrite laths, Fig 2.24 [125-126].

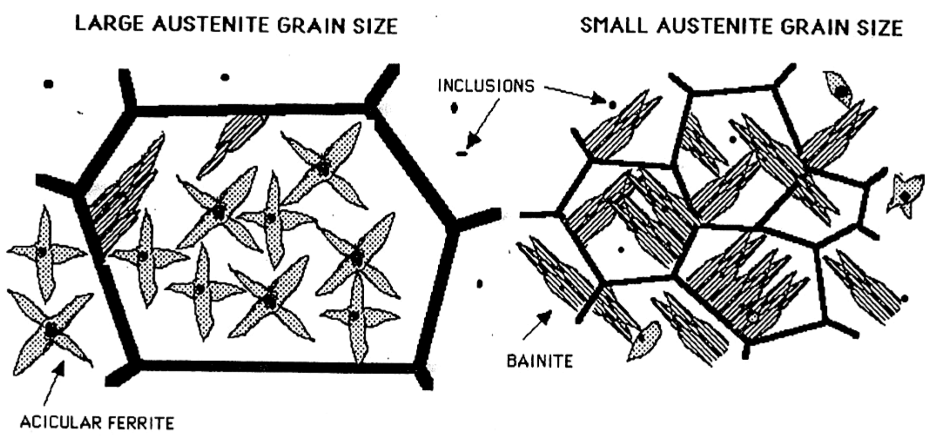

Fig 2.24 Schematic illustration of the nucleation and growth mechanism of acicular ferrite and bainite [124]

The grain structure of the transformed phase depends on the heat input, cooling rate and solidification mode. The equaixed grains form a band along the weld centerlinewhich in turn block off the columnar grains as heat inputand welding speed are increased. The variation in grainmorphologies from the fusion boundary to weld centerlinecan be explained using cooling rate and constitutionalsupercooling principles. According to the Kou, as the weldingspeed is increased, solidification (growth) rate of the weldmetal (R) is also increased [69]. High cooling rate reduces theratio of G/R where G is the temperature gradient.Therefore, constitutional supercooling ahead of solid-liquidmetal interface is increased. High constitutional supercoolingand low G/R ratio are known to promote theequiaxed grains compared to columnar grains [69]. Influence of temperature gradient , growth rate and coolingrate on solidification modes and grain structure is shown inFig. 2.25. It is evident from the figure that the high coolingrate and low G/R ratio promotes the fine equiaxed grainstructure. Formation of fine equiaxed grains in weld metaloffers two advantages: (a) better mechanical properties suchas toughness, strength and ductility and (b) reduced solidificationcracking tendency. Higher heat input for agiven welding speed lowers the temperature gradient which in turn lowers the G/R ratio which leads to increasein the cellular or equiaxed structure. Value of G/R ratio isfound different for different zones of weld metal. It is evidentfrom the macrographs that weld bead near the upper surfaceor reinforcement zone has coarse columnar grains. It mayprimarily be attributed to high value of G/R ratio becausecooling rate would be low near the weld surface.

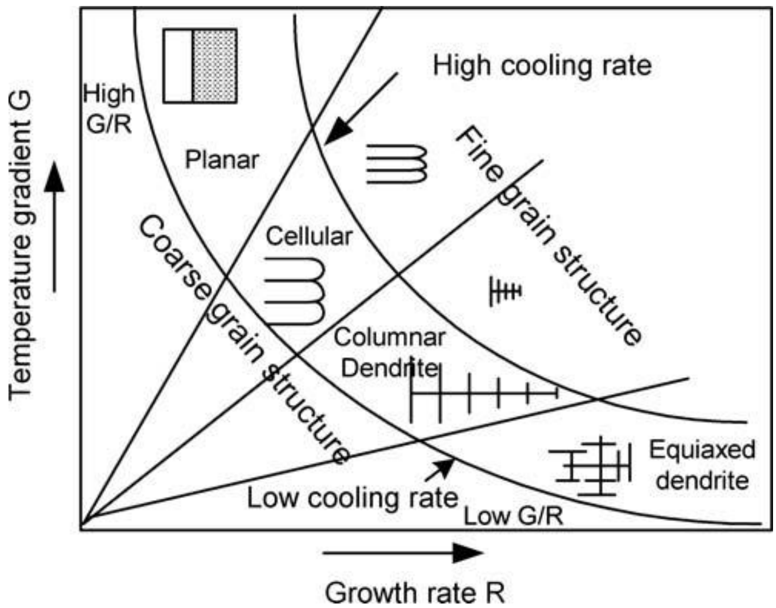

Fig. 2.25 Effect of temperature gradient (G), growth rate (R) and coolingrate on solidification modes and grain structure [69]

Several *continuous-cooling transformation (CCT) diagrams* have beensketched schematically to explain the development of the weld metalmicrostructure of low-carbon, low-alloy steels [127–132]. The one shown in Fig.2.26 is based on that of Onsoien et al. [133].The hexagons represent thetransverse cross sections of columnar austenite grains in the weld metal. Asaustenite (γ) is cooled down from high temperature, ferrite (α) nucleates atthe grain boundary and grows inward.The grain boundary ferrite is also called“allotriomorphic” ferrite, meaning that it is a ferrite without a regular facetedshape reflecting its internal crystalline structure. At lower temperatures, themobility of the planar growth front of the grain boundary ferrite decreasesand Widmanstatten ferrite, also called side-plate ferrite, forms instead. Theseside plates can grow faster because carbon, instead of piling up at the planargrowth front, is pushed to the sides of the growing tips. Substitutional atomsdo not diffuse during the growth of Widmanstatten ferrite. At even lower temperatures, it is too slow for Widmanstatten ferrite to grow to the grain interiorand it is faster if new ferrite nucleates ahead of the growing ferrite. This newferrite, that is, acicular ferrite, nucleates at inclusion particles and has randomlyoriented short ferrite needles with a basket weave feature.

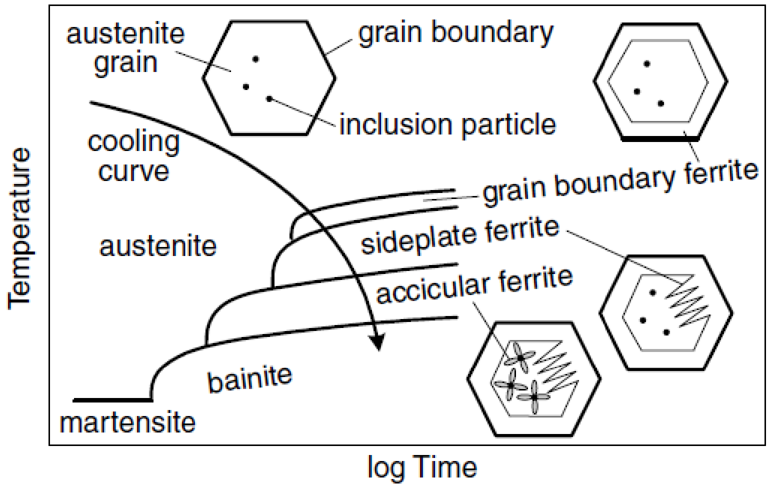

Fig 2.26 Continuous cooling transformation diagram for weld metal of lowcarbon steel

2.4.1 Factors Affecting Microstructure

Bhadeshia and Suensson [134] showed the effect of severalfactors on the development of microstructure of the weld metal(Fig 2.27): the weldmetal composition, the cooling time from 800 to 500°C , the weld metaloxygen content, and the austenite grain size. The vertical arrows indicate thedirections in which these factors increase in strength. This is explainedwith the help of CCT curves.

Cooling Time Consider the left CCT curves (broken lines) in Fig 2.28.As cooling slows down (D*t*8–5 increases) from curve 1 to curve 2 and curve 3,the transformation product can change from predominately bainite, to predominately acicular ferrite to predominatelygrain boundary and Widmanstatten ferrite.

Alloying Additions An increase in alloying additions (higher hardenability)will shift the CCT curves toward longer times and lower temperatures.Consider now cooling curve 3 in Figure 2.28. The transformation product canchange from predominately grain boundary and Widmanstatten ferrite (leftCCT curves) to predominately acicular ferrite (middle CCT curves) to predominately bainite (right CCT curves) (Fig 2.28).

Grain Size Similar to the effect of alloying additions, an increase in theaustenite grain size (less grain boundary area for ferrite nucleation) will alsoshift the CCT curves toward longer times and lower temperatures.

Weld Metal Oxygen Content The effect of the weld metal oxygencontent on the weld metal microstructure is explained as follows. First, asshown in Fig 2.27, Fleck et al. [135] observed in submerged arc welds thatthe austenite grain size before transformation decreases with increasingweld metal oxygen content. Liu and Olson [136] observed that increasing theweld metal oxygen content increased the inclusion volume fraction anddecreased the average inclusion size. In fact, a large number of smaller sizeinclusions of diameter less than 0.1mm was found. Since fine second-phaseparticles are known to increasingly inhibit grain growth by pinning the grainboundaries as the particles get smaller and more abundant [137], increasing the weld metal oxygen content should decrease the prior austenite grain size.Therefore, the effect of decreasing the weld metal oxygen content is similar tothat of increasing the prior austenite grain size (as seen in Fig 2.27). Secondly, larger inclusions, which are favored by lower weld metal oxygen content, can act as favorable nucleation sites for acicular ferrite [138]. Appropriateinclusions appear to be in the size range 0.2–2.0mm, and the mean sizeof about 0.4mm has been suggested to be the optimum value. Fox et al. [139] suggested in submerged arc welds of HY-100 steel that insufficientinclusion numbers are generated for the nucleation of acicular ferrite if theoxygen content is too low (<200ppm). On the other hand, many small oxideinclusions (<0.2mm) can be generated if the oxygen content is too high(>300ppm). These inclusions, though too small to be effective nuclei for acicular ferrite, reduce the grain size and thus provide much grain boundary areafor nucleation of grain boundary ferrite. As such, optimum oxygen contentcan be expected for acicular ferrite to form (as shown in Fig2.27b).Other factors have also been reported to affect amount of acicular ferritein the weld metal. For example, it has been reported that acicular ferriteincreases with increasing basicity index of the flux for submerged arc welding [140], Ti [140-141], and Mn and Ni [142].

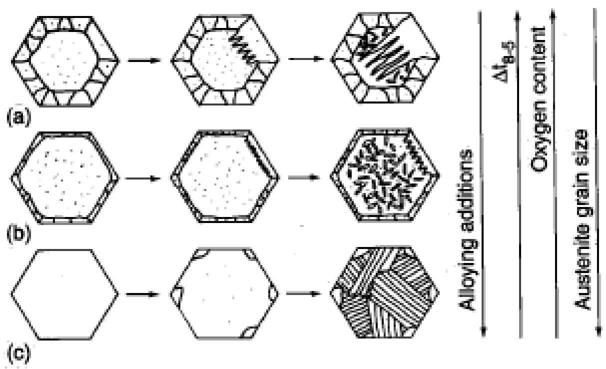

Fig 2.27 Schematic showing effect of alloy additions, cooling time from 800 to 500°C, weld oxygen content, and austenite grain size[134]

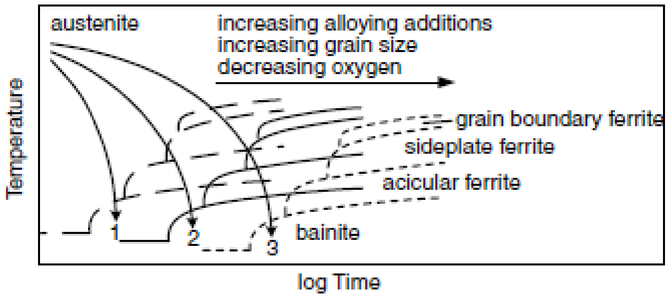

Fig 2.28Effect of alloying elements, grain size, and oxygen on CCT diagrams for weld metal of low-carbon steel [69]

There seems to be general agreement that microstructures primarily consisting of acicular ferrite provide optimum weld metal mechanical properties, both from strength and toughness points of view, by virtue of its small grain size and high angle grain boundaries. The formation of large proportions of upper bainite, ferrite side plates, or grain boundary ferrite, on the other hand, are considered detrimental to toughness, since these structures provide preferential crack propagation paths, especially when continuous films of carbides are present between the ferrite laths or plates. Attempts to control the weld metal acicular ferrite content have led to the introduction of welding consumables containing complex deoxidizers (Si, Mn, AI, Ti) and balanced additions of various alloying elements (Nb, V, Cu, Ni, Cr, Mo, B). The final weld metal microstructure will depend on complex interactions between several important variables such as:

(i) Total alloy content

(ii) Concentration, chemical composition, sizedistribution of non-metallic inclusions

(iii) Solidification microstructure

(iv) Prior austenite grain size

(v) Weld thermal cycle.

2.5 Residual Stresses and Distortions

The residual stresses in a component or structure are stresses caused by incompatible internal permanent strains. They may be generated or modified at every stage in the component life cycle, from original material production to final disposal. Welding is one of the most significant causes of residual stresses. It typically produces large tensile stresses whose maximum value is approximately equal to the yield strength of the materials being joined, and balanced by lower compressive residual stresses elsewhere in the component. The distortion causes the degradation of the product performance and the increase of the manufacturing cost due to the poor fit-up, so that it needs to be eliminated or minimized below a critical level.

Tensile residual stresses may reduce the performance and ultimately cause failure of manufactured products. They may increase the rate of damage by fatigue due to the increase of the average stress applied or environmental degradation. They may reduce the load bearing capacity by contributing to failure by brittle fracture, or cause other forms of damage such as shape change. Compressive residual stresses are generally beneficial, but cause a decrease in the buckling load.

2.5.1 Mechanism

There are four types of distortions in welding. The first two are longitudinal shrinkage and transverse shrinkage that occur in plane. The other two are angular distortion and longitudinal distortion (bowing), which appear out of plane. The angular distortion is mainly caused by the non-uniform extension and contraction through thickness direction due to the temperature gradient. The longitudinal distortion (also called buckling distortion)is generated by the longitudinal tensile residual stress [143].

Distortions due to heat are mainly due to fast temperature variations that generates non-uniform expansion and contraction. The localized heating and non-uniform cooling during welding result in a complex distribution of the residual stresses in the joint region, which often leads to undesirable deformation or distortion of the welded structure.

2.5.2 Residual stress consequences and parameters

One of the main consequences of residual stresses is warping of thin components upon welding. There are a number of distortion control strategies. They can be mainly classified into two:

(a) Design-related and process-related variables, that include weld joint details, plate thickness and thickness transition if the joint consists of plates of different thicknesses, stiffeners spacing and number of attachments, corrugated construction, mechanical restraint conditions, assembly sequence and overall construction planning.

(b) Welding process, there are important variables including method, travel speed and welding sequence.

Distortion mitigation techniques are implemented to counteract the effects of shrinkage during cooling, which distorts the fabricated structure. One common problem associated with welding is the finished products dimensional tolerance and stability. Fig 2.29 below shows the typical profiles of residual stresses induced during a welding process [144-145].

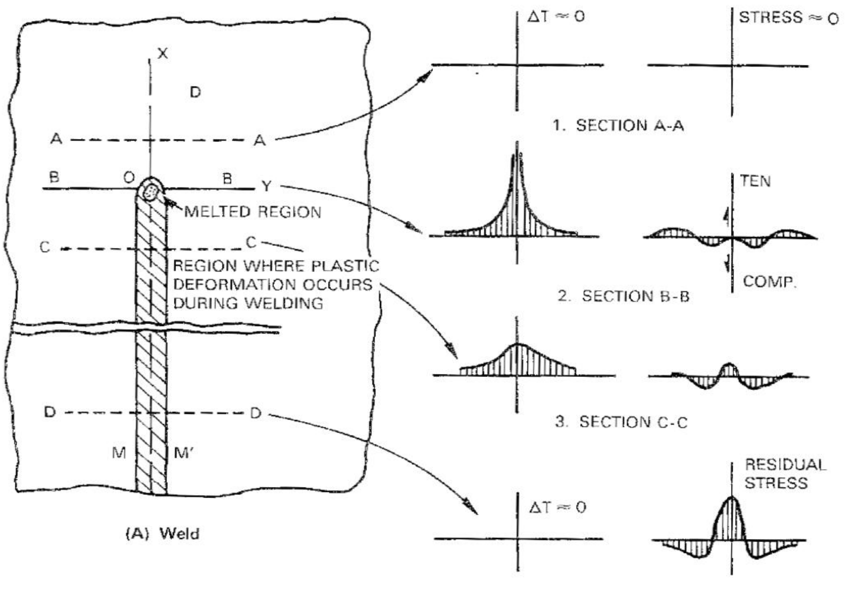

Fig 2.29(a) Thermal stress distribution before, during and after welding [144]

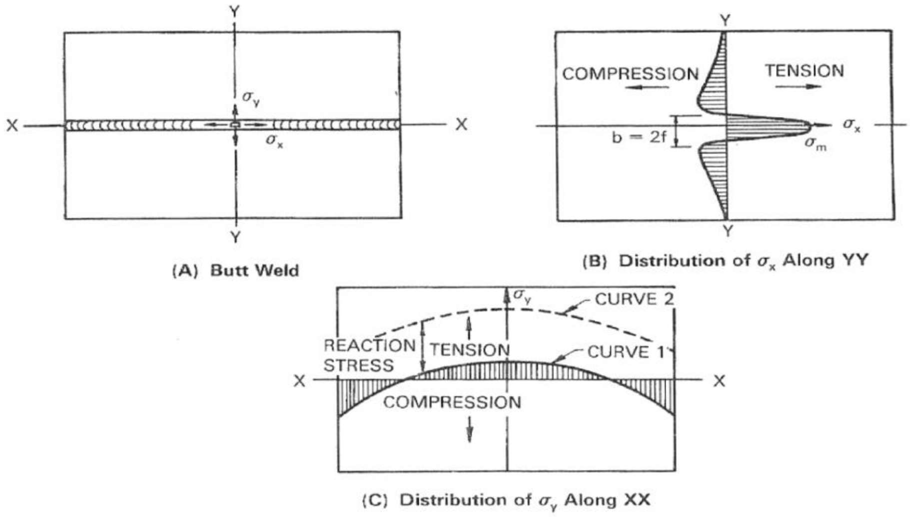

Fig 2.29(b)Thermal stress after the welding [144]

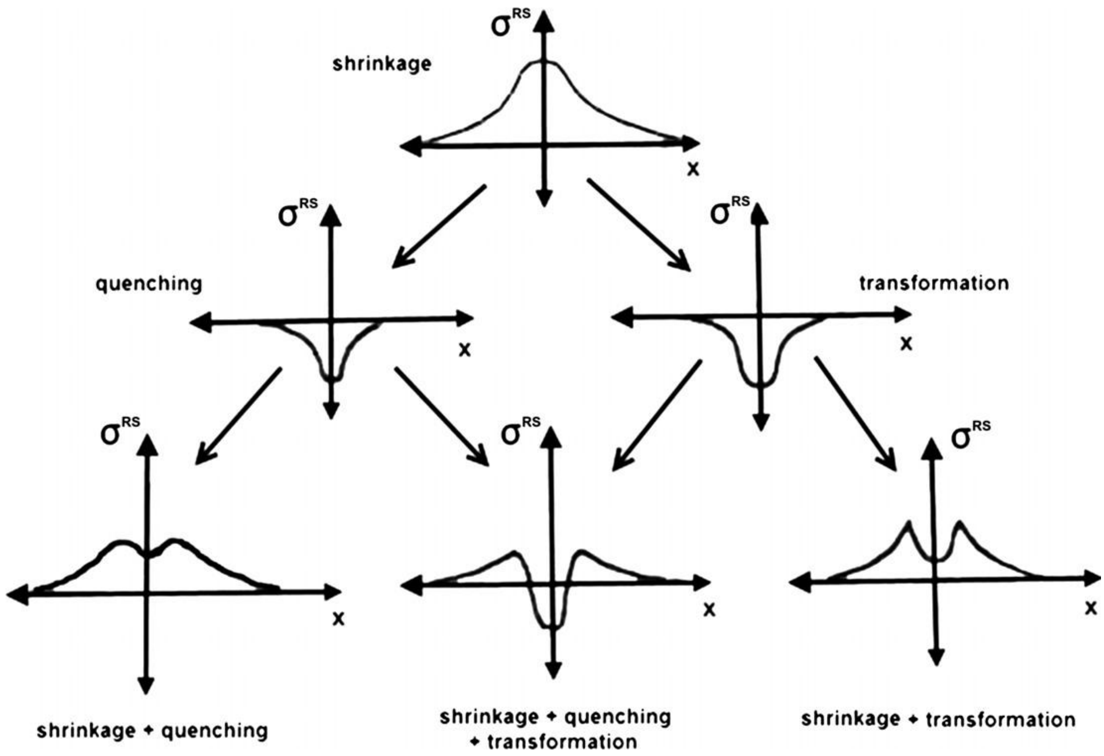

Fig 2.29(c) Change of residual stress due to metallurgical processes during welding [145]

2.5.4 Residual stress measuring techniques

Residual stresses may be measured by non-destructive techniques; or by locally destructive techniques and by sectioning methods. The selection of the measurement technique should take into account volumetric resolution, material, geometry, accessibility and if the component needs to be used after the testing or not. The various measurement techniques can be classified into non-destructive, semi-destructive and destructive techniques [25-27] as shown in Fig 2.30.

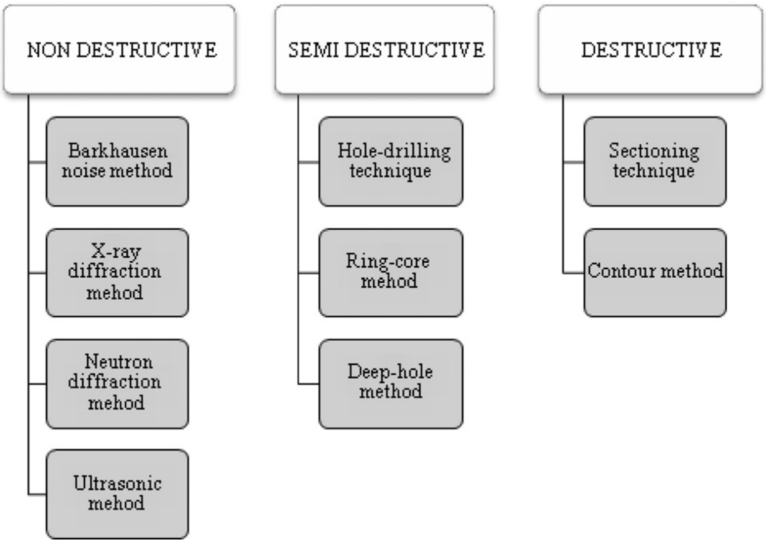

Fig. 2.30 Residual stresses measuring techniques [27]

2.5.5 X-Ray Diffraction (XRD) technique for residual stress measurement

The XRD technique uses the distance between crystallographic planes, i.e. the d-spacing, as a strain gage.The presence of residual stresses in the material produces a shift in the XRD peak angular position that is directly measured by the detector [25-27, 146]. The depth of penetration of X-rays is of the order of 5 to 30 microns.Diffraction occurs at an angle 2θ, defined by Bragg's Law : $n\lambda = 2d \sin \theta$, where n is an integer denoting the order of diffraction, λ is the X-ray wavelength, d is the lattice spacing of crystal planes, and θ is the diffraction angle. Any change in the lattice spacing, d, results in a corresponding shift in the diffraction angle 2θ. Measuring the change in the angular position of the diffraction peak for at least two orientations of the sample defined by the angle enables calculation of the stress present in the sample surface lying in the plane of diffraction, which contains the incident and diffracted X-ray beams. To measure the stress in different directions at the same point, the sample is rotated about its surface normal to coincide the direction of interest with the diffraction plane.

Fig. 2.31(a), shows the sample in the ψ = 0 orientation. The presence of a tensile stress in the sample results in a Poisson's ratio contraction, reducing the lattice spacing and slightly increasing the diffraction angle, 2θ. If the sample is then rotated through some known angle ψ (Fig. 2.31(b)), the tensile stress present in the surface increases the lattice spacing over the stress-free state and decreases 2θ.

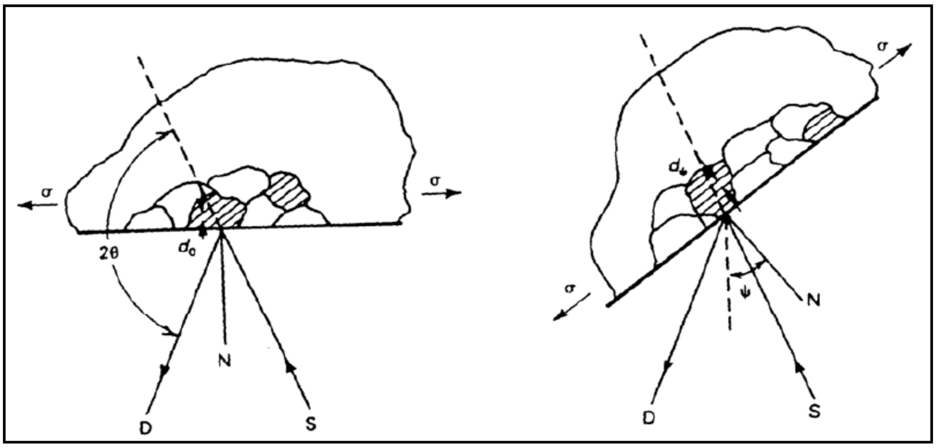

Fig 2.31(a) Fig 2.31(b)

Fig2.31 Principles of X-ray diffraction stress measurement [27]
(a) ψ = 0. (b) ψ = ψ (sample rotated through some known angle ψ)
D-X-ray detector; S- X-ray source; N-normal to the surface

2.5.6 Ultrasonic method for residual stress measurement

For the determination of mechanical stress states in materials, the dependence of the elastic wave velocity (acoustoelastic effect) on the amount of stress is exploited. This dependence has been well characterized and an accurate theoretical description is available [147]. However, the practical realization of the technique needs considerations of the following problems:

(a) The variation of ultrasonic velocity with stress is very small so that accurate time of flight and path length measurements is needed.

(b) The velocity of elastic waves is also influenced by microstructure, texture etc. To determine the stress states by ultrasonic techniques, it is therefore necessary to separate these different influences.

TheL$_{CR}$ technique is a special case of angle beam inspection, and normal wave is excited when the angle of incidence is slightly greater than the critically refracted angle. The angle of incidence giving a 90° refracted angle for the normal wave is called the "first critical angle[148] as shown in Fig. 2.32." Refraction at interfaces is governed by Snell's Law, as given by Equation.

$$\frac{\mathrm{Sin}\,\theta 1}{\mathrm{V1}} = \frac{\mathrm{Sin}\,\theta 2}{\mathrm{V2}} \text{-------------- (2.1)}$$

For Plexiglas wedge and steel interface,

V_1 = Velocity of Ultrasonic wave in Perspex (2730 m/s).
V_2 = Velocity of Ultrasonic wave in Steel (5890 m/s).
θ_1 = Incident angle of the Ultrasonic beam (Degrees).
θ_2 = Refracted angle of the Ultrasonic beam (Degrees).

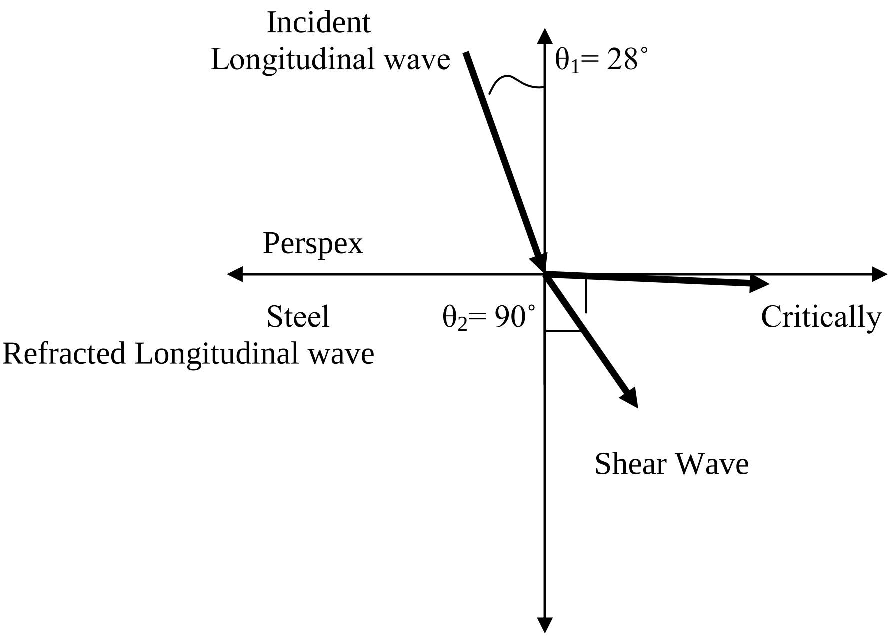

Figure 2.32 Critically refracted longitudinal wave as per Snell's Law

First critical angle for Plexiglas (Lucite (or) Perspex) to steel is about 28°. Egle and Bray [149] established the sensitivity of this critically refracted longitudinal ultrasonic wave velocity to the strain on rail steel specimens.

Based on C.O. Ruud [150], it has been pointed out by Planichamy, Joseph, Vasudevan et al. [151-153] that the measurement of transit time is straight forward and less error prone for the estimation of residual stresses in weld joints. For a given fixed path length, they have defined the AEC in terms of transit time for the first time as follows;

Hook's law of elasticity is $\sigma = E\varepsilon$ ------------------- (2.2)

where σ is stress, ε is strain and E is elastic modulus. By including the anharmonic properties in the presence of applied(or)residual stresses, the above equation may be rewritten in the power series as

$$\sigma = \varepsilon E + C\varepsilon^2 + D\varepsilon^3 \qquad \text{--------------------(2.3)}$$

where C is third order anharmonic constant, D is fourth order anharmonic constant and so on. Limiting to the second order strain, a very simplified form of the anharmonic stress-strain law can be written as

$\sigma = \varepsilon E + C\varepsilon^2$ and rewritten as

$$\sigma = \varepsilon(E + C\varepsilon) \qquad \text{-------------------------(2.4)}$$

The term in the parenthesis is approximately related to the velocity of ultrasonic wave in the presence of stress (applied(or)residual). By further simplifying the above equation (2.4), the AEC for a given material is defined in its simplest form as follows

$$V = V_0 + A\sigma \qquad \text{-------------------------(2.5)}$$

Where, V is the measured ultrasonic velocity, V_0 is the velocity in the stress-free state, A is AEC and σ is applied(or)residual stress. For a given path length, ultrasonic velocity is inversely proportional to transit time. In the fabricated L_{CR} wave transmitter-receiver assembly, the distance between the transmitter and the receiver is maintained constant. Hence, it is possible to define the AEC in terms of transit time in the following way:

$$t = t_0 + B\sigma \qquad \text{---------------------------(2.6)}$$

where, t is the measured ultrasonic transit time at different locations of the weld joint, t_0 is the transit time measured along the gauge length with zero load condition B is AEC defined in terms of transit time and σ is applied(or)residual stress. Thus, the measured transit time difference (Δt, the time difference between transit times measured at zero load and applied loads) is directly converted into residual stresses by dividing it with AEC.

$$t = t_0 + B\sigma \qquad B = (t - t_0)/\sigma \qquad \text{------------------------(2.7)}$$

where 't' is the measured ultrasonic transit time at different loading conditions, t_0 is the transit time measured under no load, B is the AEC defined in terms of transit time and σ is the applied/residual stress present in the material/component. Thus from the above equation, one needs only to measure the transit times at different locations to evaluate the residual stress at a given location.

2.5.7 Advantages of prediction of residual stresses

Controlling the fabrication-induced residual stress state can significantly enhance the structure service life. The advantages of prediction of residual stresses [25-27] are enumerated below:

(a) Understand consequences of fabrication/manufacturing process.

(b) It can lead to quality enhancement.

(c) It can minimize costly service problems.

(d) It can help to improve and optimise welding process parameters and techniques employed for reduction in residual stress build up.

(e) To enhance the service life of welded components and lowering risk of failure by predicting the influence of residual stresses on fatigue, corrosion and other detrimental surface related phenomena.

2.6 Finite Element Method in welding

Finite element method is a method used to solve complex mathematical problems by the process of discretization of the model in to small elements. An element is formed by identifying a finite number of points called nodal points. The domain of the function will be an assemblage of finite elements connected together appropriately on their boundaries. Now the function is defined as a continuous function that is uniquely described in terms of the nodal point in that particular element.

Residual stresses in welded structures are unavoidable. The key to understanding of residual stress and distortion in a welding process is resolution of temperature distribution with respect to time. These temperature distribution problems are basically heat transfer problems. These include analytical models from simple 1D solution to complicated 3D models which accounts for 3D heat source distribution with heat losses from work piece to surroundings. Last so many years, a number of mathematical approaches had been followed for solving this problem. The analytical solutions were introduced over 70 years ago. Numerical methods like finite difference method and finite element analysis were introduced about 30 years ago.

To investigate residual stress distribution and magnitude for stiffened plates, numerical analysis is still the best and cheaper option if time is not an important factor. For many years, researchers have studied the predictive methods for welding-induced distortions using the finite element method (FEM). Many complex models contributed to the knowledge of distortion, but due to computational intensity, some are very difficult to solve.

Welding simulation of large assemblies imposes tremendous computational demands. Welding simulation normally requires transient analysis to capture the component response during the welding, such as the welding sequence, welding direction, cooling and fixture. Welding simulation is nonlinear and often difficult to converge because of the material behaviour at the elevated temperature.

Welding simulation needs good finite-element meshing with sufficient mesh density along the welds and the heat-affected zone. Usually in weld simulation, a varying size mesh is used such that in HAZ meshing will be very fine whereas zones away from HAZ are of very coarse mesh. Despite the fast-growing computer technology, the complexity of an industrial problem could easily make the simulation model not feasible to complete in an acceptable turnaround time. According to the applications, either accuracy or time may have to be compromised for an efficient analysis.

Prediction of residual stresses by numerical modelling of welding and other manufacturing processes has increased rapidly in recent years. Modelling of welding is technically and computationally demanding, and simplification and idealization of the material behaviour, process parameters and geometry is inevitable, apart from the computational usage intensity, the biggest problem is to create a valid physic model of the component. Numerical modelling is a powerful tool for the behaviour of the materials, but validation with reference to experimental results is still essential. A Finite Element model has been used to analyze the thermal and mechanical phenomena in welding processes. In that, study a standard FE formulation limited to solid domain was adopted for mechanical analysis, proving to be effective.

2.6.1 Numerical Simulation of Welding

Over the past decade, a number of researchers have been working in the areas of analytical as well as FE-based numerical simulation techniques in order to temperature, residual stress and distortion during welding using the moving heat source.

Gery et al. [154] explained a moving heat source model based on Goldak's double-ellipsoid heat flux distribution. A C++ programme was developed in order to implement heat inputs into finite element thermal simulation of the plate butt joint welding. The transient temperature distributions and temperature variations of the welded plates during welding were predicted and the fusion zone and heat affected zone were obtained. Effects of the heat source distribution, energy input and welding speed on temperature changes were further investigated.Dean Deng et al. [155]explained numerical simulation of temperature field and residual stress in multi-pass welds in stainless steel pipe and made a comparison with experimental measurements.Shaodong Wang et al. [156] developing an algorithm that tries to simulate the thermal cycle during welding efficiently and accurately. A space–time finite element method (FEM) is proposed to solve the transient convection–diffusion thermal equation. The method has been applied to the steady-state thermal analysis of welds. A moving coordinate frame (Eulerian frame), in which the heat source is stationary, is used to improve the spatial resolution of numerical analysis for the thermal cycle of welds effectively, as well as to incorporate the addition of the filler metal naturally.Hidekazu Murakawa et al. [157] based on inherent strain theory and interface element formulation, developed a practical prediction system to compute the accumulated distortion during the welding assembly process in the current study. Using the developed prediction method, calculated the welding distortion in a thin plate structure by considering both the shrinkage due to heat input and the gap/misalignment generated during assembly process. H. Long et al. [158]investigated distortions and residual stresses induced in butt joint of thin plates using Metal Inert Gas welding. A moving distributed heat source model based on Goldak’s double-ellipsoid heat flux distribution is implemented in Finite Element (FE) simulation of the welding process. Thermo-elastic– plastic FE methods are applied to modelling thermal and mechanical behaviour of the welded plate during the welding process.

Barroso et al. [159]explained Prediction of welding residual stresses and displacements by simplified models, experimental validation. Dean Deng et al. [160] developed a computational approach to predict welding residual stress in low temperature transformation steel, taking into account the phase transformation. The main objective is to examine the influence of transformation induced plasticity on the welding residual stress by means of the developed numerical method. Liam Gannon et al. [161] predicted and compared the temperature field during welding and the welding induced residual stress and distortion fieldswith experimental results. The effect of four welding sequences on the stiffener is investigated and their effects on the ultimate strength of the stiffened plate under uniaxial compression are discussed. Appropriate conclusions and recommendations regarding the welding sequence are presented. Coz Diaz et al. [162]thermal stress analyses were performed in GTAW welding process of two different stainless steel specimens in order to compare their distortion mode and magnitude. To develop suitable welding numerical models, one must consider the welding process parameters, geometrical constraints, material non-linearity's and all physical phenomena involved in welding, both thermal and structural. In this sense, four different premises are taken into account.

Lindgren [163] explained the finite element method to predict the thermal, material and mechanical effects of welding. The numerical approach used in Computational Welding Mechanics (CWM) was also discussed in brief. Aarbogh et al. [164] explained controlled experimental data for single pass metal inert gas welding of austenitic steel plate to validate welding stresses using numerical codes.Zhu et al. [165]explained the effect of thermal conductivity on the distribution of transient temperature fields during welding.The yield stress was found to have significant effect and Young’s Modulus to have small effect, respectively, on the residual stress and distortion.The model using material properties at the room temperature gave reasonable predictions for the transient temperature fields, residual stress and distortion.Olivier Asserin et al. [166] applied the sensitivity analysis methodology to numerical welding simulation in order to rank the importance of welding process variables on the distortion and residual stresses. The numerical welding simulation used the finite element method with thermal and mechanical computation. Due to local sensitivity of analysis, the validity of the results was limited to the neighbourhood of a nominal point, and cross effects could not be detected.

Azar et al. [167]explained that the dimensions of a heat source model in welding can be calculated based on experimentally observed weld pool size. An analytical approach called 'discretely distributed point heat source model' was used for this purpose as an intermediate stage between the experiments and the numerical model.

Attarhaet al.[168] measured the welding temperature distributions in the HAZ using K-type thermocouples in similar and dissimilar thin butt-welded joints which experienced one-pass GTAW welding process. Three dimensional finite element simulations were also implemented to predict the temperature distributions throughout the plates using ABAQUS software.

2.7 Motivation and appraisal of problem

Welding as a fabrication technique presents challenging problems to designers and manufacturers. A variety of welding parameters must be taken into account to produce sound welded structures. Considering the constraints involved in arc welding processes, the SMAW process is restricted by low depth of penetration and limited productivity due to regular replacement of electrodes. The FCAW process involves high cost of flux and excessive fumes. The SAW process has disadvantages of applicability to 1G welding only, use of combination of flux and filler material, susceptibility to hydrogen cracking, higher entrapped inclusions, and higher associated distortion and residual stresses. The SMAW, SAW and FCAW processes involve cost of edge preparation and rough bead profile [68-69]. A lot of research has been undertaken to establish the advantages of A-GTAW process for fabricating weld joints with better mechanical properties [100-118]. The A-GTAW process has been examined to be a low cost and high productivity process obviating major disadvantages of conventional arc welding processes [70, 100-118]. The A-GTAW process does not require any filler material. The reduced weld metal volume results in less distortion and reduced residual stresses. The process also provides a smooth weld bead finish and does not produce hazardous fumes. Though a lot of investigations have been undertaken on the applicability and advantages of A-GTAW as an alternative welding process for duplex stainless steels, ferritic stainless steels, Reduced Activation Ferritic/Martensitic (RAFM) steel, 9Cr-1Mo (P-91) steel, 2.25Cr-1Mo (P22) steel and other alloys [107-118], besides a few quoted fluxes [70], there is very little literature available on development of activated flux for GTAW of HSLA steels. The review of published work on innovations/phenomenon in A-GTAW technique reveals that development of A-GTAW could provide an alternative cost effective welding technique for HSLA steel (DMR-249A) for enhancing productivity and expedite ship construction at naval shipyards.

The motive of the research was to develop an activated flux for DMR-249A steel to achieve enhanced depth of penetration over a conventional GTAW process. The feasibility of developing A-GTAW as an alternative welding technique for DMR-249A steel was examined by studying the thermomechanical behaviour, microstructure and mechanical properties of weld joint fabricated by an A-GTAW process. The thermal gradients and residual stress profiles of SMAW and A-GTAW process were simulated and compared with experimental results. The effect of different arc welding processes on weld attributes of DMR-249A steel welded joints was compared by studying the microstructure, mechanical properties and corrosion characteristics of the weld joints.

Chapter 3. Finalisation of flux and optimisation of A-GTAW parameters

This chapter provides experimental details of development of activated flux and design of experiments carried out to optimize the weld process parameters for achieving the desired depth of penetration. Various combinations of fluxes were prepared to decide a suitable flux for DMR-249A steel. The design of experiments was carried out for optimization of welding parameters to achieve the desired depth of penetration. Square butt weld joints were fabricated with 10 mm thick plates employing A-GTAW welding using the developed flux and optimized process parameters. The challenges encountered for development of activated flux for naval structural HSLA steel,DMR-249A are highlighted.

3.1 Design of Experiments

The weld bead geometry and the weld quality of A-GTAW joints significantly depend on the selection of input process parameters. To predict the exact optimal input welding parameters without consuming excess time and raw materials in experimentation trials; there are different methods of optimization for obtaining the required output values through development of models. The DOE approach is the most significant and efficient way for optimization of process variables. The use of DOE methods over the last two decades has grown significantly and has been adapted in science and engineering experiments to optimize process parameters[169].

3.1.1 Response Surface Method (RSM)

The RSM has been demonstrated to be a powerful tool for determining the effects of each factor and the interactions among them. This allows process optimization to be conducted effectively [170]. The response surface procedures involve experimental strategy, mathematical methods and statistical inference, which enable users to make an efficient empirical exploration of the system in which they are interested [171]. RSM significantly reduces the number of experiments required for evaluation, analysis and optimization of process parameters. Fitting a second-order model to the response variable(s) of interest is an integral aspect of RSM [172].Consequently, the development of appropriate second-order designs is extremely important. There are many standard second-order RSM designs, including the central composite design (CCD) and its variations (rotatable CCD, spherical CCD, small composite design etc.), the Box-Behnken design and the hybrid family of designs (Fig 3.1). There are situations where standard designs are not always appropriate, such as unusual sample size requirements, non-standard blocking conditions and variations from the standard model. For these scenarios, optimal designs have been suggested and the same are frequently used in practice. *D*-optimal design for a second-order response model is considered as one of the superior models [173-175].

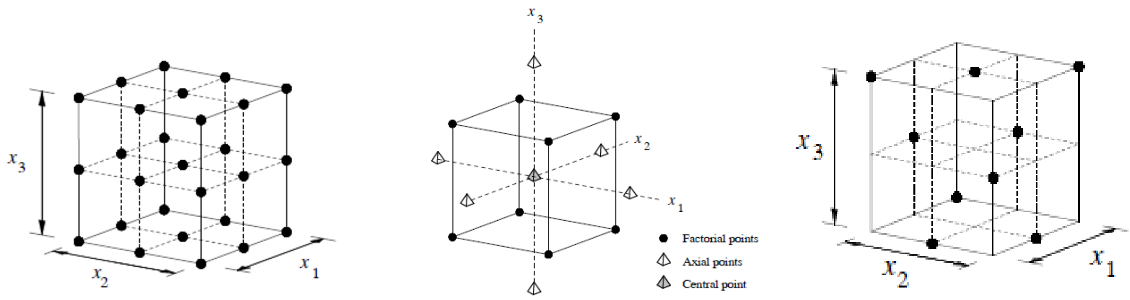

(a) (b) (c)

Fig 3.1 (a) Full Factorial Design (b) CCD (c) Fractional Factorial Design (D-Optimal)

The corresponding D-optimal design also consists of three portions as CCD (the cube design, the axial design and center points) but with different weights and may be considered as differential weighted fractional factorial design. A graphical representation of full factorial design, CCD and Fractional Factorial Design (D-Optimal) is shown in Figures 1(a), (b) and (c) respectively.

The models fit and discrimination is better understood with the use of statistical terms R-squared and Adequate Precision Ratio [176-177]. The coefficient of determination, denoted R^2 (R-squared), is a number that indicates how well data fit a statistical model. R-squared is a statistical measure of how close the data are to the fitted regression line. R-squared does not indicate whether a regression model is adequate. There can be a low R-squared value for a good model, or a high R-squared value for a model that does not fit the data. The adjusted R-squared is a modified version of R-squared that has been adjusted for the number of predictors in the model.The adjusted R-squared compares the explanatory power of regression models that contain different numbers of predictors. The adjusted R-squared increases only if the new term improves the model more than would be expected by chance. The predicted R-squared indicates how well a regression model predicts responses for new observations. The adjusted R-square is used to compare models with different numbers of predictors and the predicted R-square used to determine how well the model predicts new observations and whether the model is too complicated. If the model is significant, lack of fit insignificant, there is good agreement between adjusted and predicted R-square [176-177].

Adequate Precision is a measure of the experimental signal to-noise ratio. It compares the range of the predicted values at the design points to the average prediction error. It is a function of model parameters, p, the number of points, n, and the variance, σ^2, estimated by the root mean square residual from ANOVA) [176-177]. For a given set of input parameters, adequate precision increases with increase in number of experiments and decreases with increase root mean square residual. As a thumb rule, the ratios greater than 4 indicate adequate model discrimination.

3.1.2 Taguchi

Taguchi strategy is focused upon finding the best design that minimizes the expected loss (or mean square deviation) over an uncontrollable noise space. Taguchi's methods [172]studies the parameter space based on the fractional factorial arrays from DOE, called *orthogonal arrays*. Taguchi argued that it is not necessary to consider the interaction between two design variables explicitly, so he developed a system of tabulated designs which reduce the number of experiments as compared to a full factorial design. An advantage is the ability to handle discrete variables. A disadvantage is that Taguchi ignores parameter interactions. Juang and Tarng [178] have adopted a modified Taguchi method to analyze the effect of each welding process parameter (arc gap, flow rate, welding current and speed) on the weld pool geometry. Lee et al. [179] have used the Taguchi method and regression analysis in order to optimize Nd-YAG laser welding parameters (nozzle type, rotating speed, title angle, focal position, pumping voltage, pulse frequency and pulse width) to seal an iodine-125 radioisotope seed into a titanium capsule. The Taguchi method has been successfully applied to a number of industrial processes, including automotive industry [180-181], robotics processing [1820-183], plastics industries [184] and computer-aided design/electrical engineering tasks [185-186].

The RSM and Taguchi belong to factorial design. A factorial experiment can be analyzed using ANOVA or regression analysis [185]. It is relatively easy to estimate the main effect for a factor. Optimization of factors that could have higher order effects is the primary goal of RSM. Besides deducing optimal welding process parameters, the motive was also to evaluate the possible difference between the fit of empirical models to the experimental data obtained in relation to experimental design achieved by D-Optimal RSM [186] and optimized output with respect to signal to noise ratio based on Taguchi orthogonal arrays [187].

3.2 Experimental details

Activated fluxes were prepared with combinations of SiO_2, TiO_2, NiO, CuO_2 and combinations of oxide powdersbased on the professional knowledgebase experience and technical expertise at IGCAR [100-102]. The combination of oxide fluxes were named as SiO_2, $TiO_2$and Mix 1 to 6. The prepared mixtures of oxide powders were mixed with acetone and binder material to form a paste. The DMR-249A steel plate was machined into rectangular plates of dimensions 300x120x8 mm^3. The flux in the form of paste was manually applied on the “bead on plate” surface using a brush prior to welding(Fig 2.12). The bead on plate experimentswere carried out to make 8 beads having a length of 110 mm per plate.The welding was carried out using an automatic GTAW welding machine(Fig 3.2)with a direct current electrode negative (DCEN) Lincoln electric power source (Model: Precision TIG 375).A 2% thoriated tungsten electrode of diameter 3.2 mm with 60^o tip angle and argon as shielding gas with a flow rate of 10 liter/min was used. Experiments were carried out at 270 and 280 amperes current and weld torch speed of 60 and 75 mm/min. Table 3.1 shows the welding parameters used for bead on plate experiments.

The design of experiments (DOE) was conducted for optimisation of maximum penetration with prepared activated flux (Mix 1) by using MINITAB 16 and Design Expert7 software. MINITAB 16 was used to generate a Taguchi design matrix. MINITAB only provides for CCD and Ben Behnken Options for RSM designs so Design Expert7 was used to generate a generation of D-Optimal (RSM) matrix. The three welding process parameters (welding, current speed and arc gap) were taken as input factors to study the effect on the response factor DOP. The aim was to understand the variation in DOP with variation of welding parameters and to optimize parameters for maximizing DOP.

Fig 3.2GTAW machine

D-Optimal : In D-Optimal, the optimization design matrix for quadratic solution is generated by using the vertices, centre of edges, constraint plane centroids, axial check points, interior points and overall centroid. The design matrix generates varying model runs depending on the number of process parameters and five runs each for replicates and lack of fit respectively. The model runs remain constant for a specified number of process input parameters. The number of runs for lack of fit and replicates can be increased, as per requirements of the user, for minimising error and improving statistical fit of the matrix.

The three welding process parameters viz Current, Torch Speed and Arc Gap were considered over a predetermined range as shown in Table 3.1.Three matrices were generated with different numbers of replicate and lack of fit points as given in Table 3.2 to attain a better statistical fit of the design matrix.

Table 3.1Three Welding Process Parameters

SNo.	Process Parameters	Unit	Range
1	Current	Amps	120 to 300
2	Torch Speed	mm/min	60 to 120
3	Arc Gap	mm	1 to 4

Table 3.2D-Optimal Experiment Matrix generated with additional Lack of Fit and Replicates

SNo	Design Matrix	Model Points	Lack of Fit Points	Replicates	Total Runs
1	D-Optimal 22	10	5	7	22
2	D-Optimal 34	10	12	12	34
3	D-Optimal 36	10	14	12	36

Taguchi : Taguchi technique generates predetermined DOE matrix depending on the levels of factors. The range of the three factors (welding process parameters viz Current, Torch Speed and Arc Gap) was divided into three levels (Table 3.3). L9 and L27 design matrices were generated to carry out statistical analysis by the Taguchi technique. The L27 matrix was taken as reference matrix as the L9 matrix does not give interaction effects of the process parameters.

Table 3.3 Factors for Taguchi DOE

SNo.	Process Parameters	Unit	Level 1	Level 2	Level 3
1	Current	Amps	120	180	300
2	Torch Speed	mm/min	60	90	120
3	Arc Gap	mm	1	2.5	4

The bead on plate experimental runs,using developed flux, were performed according to the design matrix generated by the optimization techniques. The weld bead profiles (Fig 3.3) were measured using an optical microscope at 10X resolution. The measured experimental results of the DOP were used for the statistical analysis.

Fig 3.3 Weld Bead Profiles of Experimental Runs

3.3 Results and discussions

3.3.1 Development of activated flux

The bead width and depth of penetration obtained in the bead on plate experiments using various combinations of fluxes are summarised in Table 3.4. The mixture 1,2,5 and 6 were observed to give a depth of penetration of 8.1 mm, 8.02 mm, 7.15 mm and 7.4 mm respectively, which is an appreciable enhancement as compared to the depth of penetration of 3.19 mm achieved by autogenous welding without application of flux. The average hardness value of the weld metal for different mixtures was between 252 to 279 VHN, as compared to the base metal hardness value of 196-210 VHN. The maximum depth to width ratio of about 0.86 has been obtained from Mixture-1 (Table 3.4). Mixture 1 has been used as the optimum flux combination to carry out welding experiments. It has been reported that several elements including Sulphur, Oxygen, Silicon, Aluminium and Calcium have significant effect on weld penetration and bead width for activated flux GTAW welding [91-98, 190-191]. The surface active elements like S, O, Se etc. (upto a critical concentration-approx 150 ppm) are found to increase penetration whereas surface stable (reactive elements/ deoxidisers) elements like Al, Ca etc. are observed to reduce weld penetration.

As the developed flux composition was based on optimising the percentage concentration of surface active elements, the concentration of Si and O in the weld metal was analysed (Table 3.5). It was observed that the percentage of Si and O, in weld metal, individually and in combination influence the DOP [91-93]. For similar oxygen content (Mix 1 and 2), Mix 1 with higher Si % showed higher DOP. For similar silicon content (Mix 2 and 3), Mix 2 with higher O% displayed higher DOP. Mix 5 and 6 having similar Si and O % showed similar trend of DOP. Though SiO_2 (without mixing with other oxide fluxes) had high Si % and was also observed to have high (Si+O)%, the low DOP is attributed to low O% in weld metal. The relationship of concentration % of Si and O with DOP (Fig 3.4) confirmed that though combined concentration percentage of (Si+O) is a significant indicator of DOP.An optimised combination of Si and O isneeded to achieve higher DOP*.

* DOE was undertaken using welding parameters as variables as change in welding parameters affect DOP in predictable range. Though optimised combination of Si and O provides significant increase in DOP, the chemical combination was not studied for DOE as even minor variations in chemical composition leads to unpredictable and incoherent patterns over large range of resulting DOP.

Table 3.4 Weld Penetration and Bead Profile with Different Flux Mixtures

FLUX	CURRENT SPEED-1 (280 Amps 75 mm/min)			CURRENT SPEED-2 (270 Amps 60 mm/min)			Avg VHN	Bead Picture CURRENT SPEED2
	DOP	BWD/W		DOP	BWD/W			
Autogenous	2.91	14.6	0.199	3.19	15.8	0.20	268	
TiO_2	3.48	11.16	0.311	3.69	15.9	0.23	273	
SiO_2	3.26	12.91	0.252	3.8	14.23	0.27	252	
Mix 1	**7.98**	**9.72**	0.820	**8.1**	**9.67**	0.86	**269**	
Mix 2	**7.12**	**11.69**	0.609	**8.02**	**14.81**	0.54	**261**	
Mix 3	4.74	12.64	0.375	5.82	15.43	0.38	279	
Mix 4	3.54	14.49	0.244	4.96	13.09	0.38	277	
Mix 5	**6.01**	**13.82**	0.434	**7.15**	**13.28**	0.54	**292**	
Mix 6	**7.23**	**13.79**	0.524	**7.40**	**15.9**	0.46	**269**	

Table 3.5 Relationship of concentration% of Si and O on DOP

ACTIVATED FLUX	CONCENTRATION (%)			DEPTH OF PENETRATION (mm)
	Si	O	(Si+O)	
TiO_2	0.18	0.076	0.256	3.7
SiO_2	0.26	0.078	0.338	3.8
Mix 1	0.24	0.126	0.366	8.3
Mix 2	0.22	0.125	0.345	8
Mix 3	0.22	0.095	0.315	5.8
Mix 4	0.19	0.11	0.3	4.9
Mix 5	0.2	0.125	0.325	7.1
Mix 6	0.2	0.124	0.324	7.4

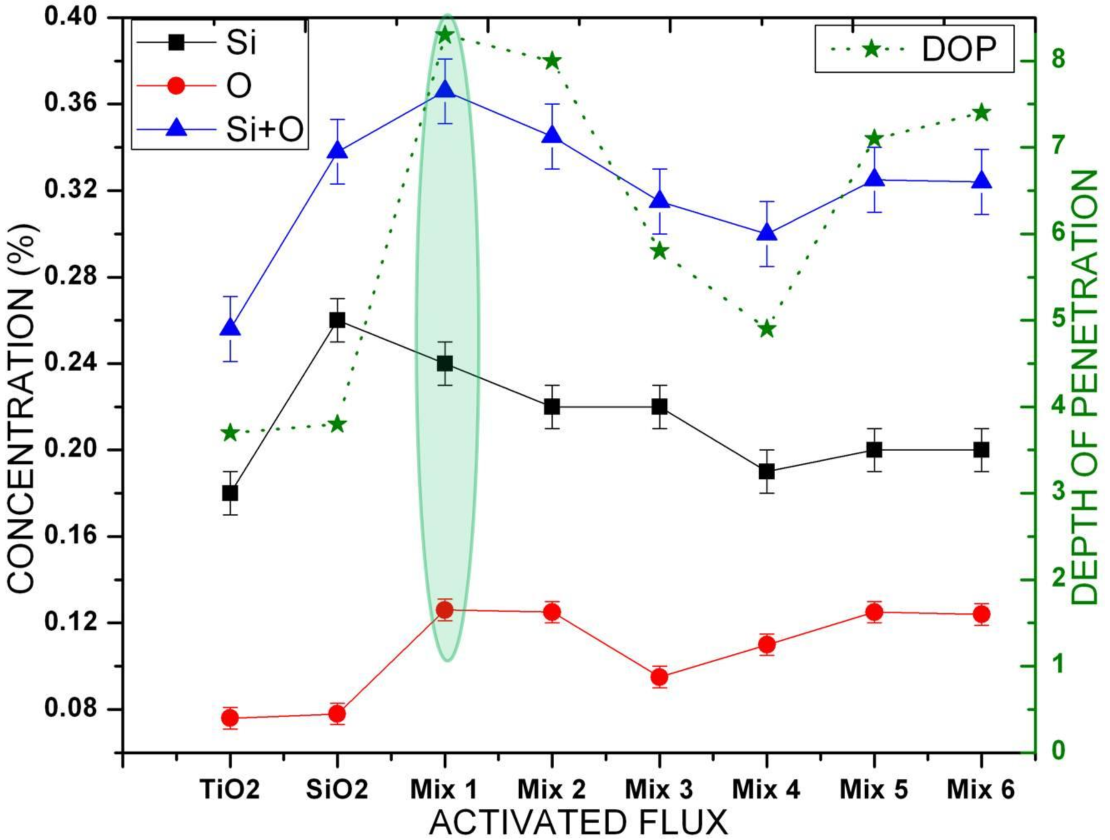

Fig 3.4 Relationship of concentration% of Si and O on DOP (a) % Si and O (b) DOP

3.3.2 Design of Experiments

D-Optimal : Three D-Optimal matrices were generated for analysis. The reduced quadratic model was used to derive the factor equation for DOP. The D-Optimal with 36 data set is given in Table 3.5 was taken as reference design matrix.

Table 3.5 D-Optimal 36 Design Matrix

Run	**Current** (Amperes)	**Torch Speed** (mm/min)	**Arc Gap** (mm)	**DOP** (mm)
1	120.00	120.00	1.00	1.91
2	300.00	60.00	1.00	5.15
3	210.00	90.00	2.50	3.57
4	300.00	60.00	4.00	4.45
5	210.00	90.00	2.50	3.53
6	300.00	60.00	1.00	3.18
7	300.00	90.00	4.00	3.46
8	210.00	90.00	2.50	3.38
9	300.00	120.00	4.00	2.83
10	120.00	60.00	4.00	1.77
11	210.00	120.00	1.00	2.93
12	300.00	60.00	2.50	6.18
13	120.00	60.00	1.00	1.62
14	255.00	90.00	2.50	4.32
15	120.00	120.00	2.50	0.75
16	300.00	120.00	1.00	2.89
17	120.00	90.00	4.00	1.6
18	120.00	120.00	1.00	2.07
19	120.00	60.00	4.00	2.05
20	210.00	60.00	2.50	2.48
21	120.00	120.00	4.00	0.87
22	210.00	60.00	1.00	3.96
23	300.00	90.00	1.00	2.73
24	300.00	60.00	4.00	6.08
25	210.00	60.00	4.00	4.76
26	120.00	90.00	2.50	1.58
27	300.00	120.00	1.00	3.08
28	210.00	90.00	4.00	3.4
29	120.00	90.00	1.00	2.03
30	210.00	90.00	2.50	1.79
31	120.00	60.00	2.50	1.48
32	120.00	120.00	4.00	1.51
33	300.00	120.00	2.50	3.75
34	300.00	120.00	4.00	3.71
35	165.00	105.00	2.50	2.64
36	300.00	90.00	2.50	3.93

The criteria chosen for selection are given in Table 3.6. D-Optimal 36 matrix is considered better for statistical analysis as the convergence of Adjusted and Predicted R-Squared is superior and Adequate Precision is highest amongst the matrices under consideration.

The experimental data were used to calculate the coefficients of the reduced quadratic equation. Table 3.7summarizes the ANOVA results for the significance of the coefficients of the models and regression coefficient. For any of the terms in the model, a large regression co-efficient and a small p-value would indicate a more significant effect on the respective response variables. The Response Surface Graphs are shown in Fig 3.5.

ANOVA (Table 3.7) and Response Surface Graphs (Fig 3.5(a-d))show that DOP is primarily influenced by Current and Welding Speed. The significance of the model by ANOVA is estimated at 95% significance level. Significance probability value (p value) of less than 0.05 portrays the process parameters to be significant. The significance probability values of less than 0.05 for process parameters Current (A), Speed (B) and Current-Speed interaction (AB) in Table 7 show significant effect of these parameters on DOP. It is also observed that the effect of Arc Gap is of less consequence as compared to Current or Welding Speed.

The deviation between Adjusted R-Squared (0.7277) and Predicted R-Squared (0.6505) is observed to be approx 0.07 which is less than the criterion value of 0.2. The reasonable agreement between values shows adequacy of the model. The Adequate Precision Ratio (Signal to Noise Ratio in terms of process parameters, number of experimental runs and variance from mean) of 13.235 exhibits adequate model discrimination. Fig 3.5 shows that higher DOP is achieved at higher current and lower speed. DOP is highly influenced by current at slower speeds. At higher speeds, the DOP increases with higher current but the influence of higher current on DOP in less significant as compared to that at lower speeds.

Table 3.6 Criterion for selection of Reduced Quadratic Model Equations

DESIGN MATRIX	Adj R-Sq	Pred R-Sd	Adeq Precision	
D-Optimal 22	0.7819	0.6962	12.039	The "Pred R-Squared" should be in reasonable agreement with the "Adj R-Squared" with maximum deviation of 0.2.
D-Optimal 34	0.7149	0.6247	11.565	"Adeq Precision" measures the signal to noise ratio. A ratio greater than 4 is desirable.
D-Optimal 36	0.7277	0.6505	13.235	

Table 3.7 ANOVA for D-Optimal 36 DOE Matrix

Source	Sum of Squares	df*	Mean Square	F Value	p-value Prob> F	Contribution Percentage
Model	48.94	7	6.99	14.36	< 0.0001	significant
A-CURRENT	*35.01*	*1*	*35.01*	*71.93*	*< 0.0001*	*74.27(significant)*
B-SPEED	*5.65*	*1*	*5.65*	*11.60*	*0.0020*	*11.98(significant)*
C-ARC GAP	*0.26*	*1*	*0.26*	*0.53*	*0.4737*	*0.55*
AB	*2.56*	*1*	*2.56*	*5.26*	*0.0295*	*5.43(significant)*
AC	*1.15*	*1*	*1.15*	*2.36*	*0.1357*	*2.44*
BC	*1.07*	*1*	*1.07*	*2.20*	*0.1490*	*2.27*
A^2	*1.44*	*1*	*1.44*	*2.95*	*0.0968*	*3.05*
Residual	13.63	28	0.49			
Lack of Fit	*7.50*	*18*	*0.42*	*0.68*	*0.7711*	*not-significant*
Pure Error	*6.13*	*10*	*0.61*			
Cor Total	62.57	35				

Std. Dev.	0.70	R-Squared	0.7822
Mean	2.98	Adj R-Squared	0.7277
C.V. #%	23.38	Pred R-Squared	0.6505
PRESS^	21.87	Adeq Precision	13.235

**Degree of Freedom, # Coefficient of Variation, ^ Predicted Residual Sum of Squares*

The final reduced quadratic equation in terms of the actual factors, developed post ANOVA analysis of the D-Optimal model, is:-

$$\mathbf{DOP = -3.52298+(0.044470*CURRENT)+(0.02576*SPEED)+(0.17737*ARC\ GAP)-(1.37062E\text{-}004*CURRENT*SPEED)+(1.83825E\text{-}003*CURRENT*ARC\ GAP)-(5.46989E\text{-}003*SPEED*ARC\ GAP)-(5.61985E\text{-}005*CURRENT^2)}$$

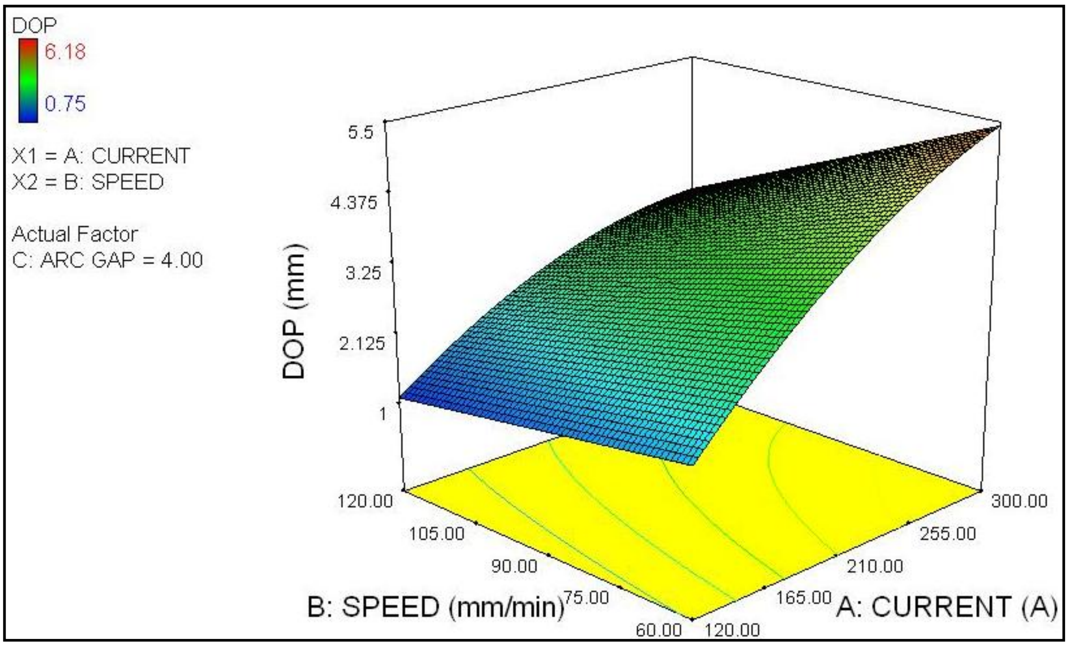

Fig 3.5(a) Surface Response of Current and Speed on DOP

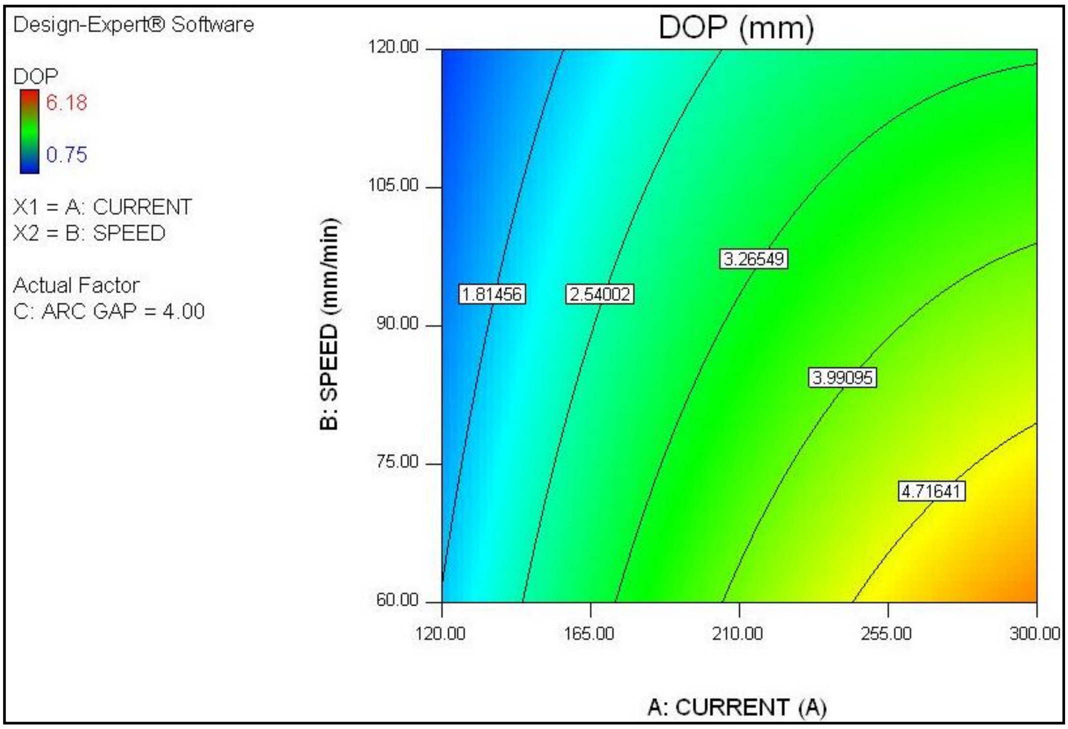

Fig 3.5(b) Response of Current and Speed on DOP

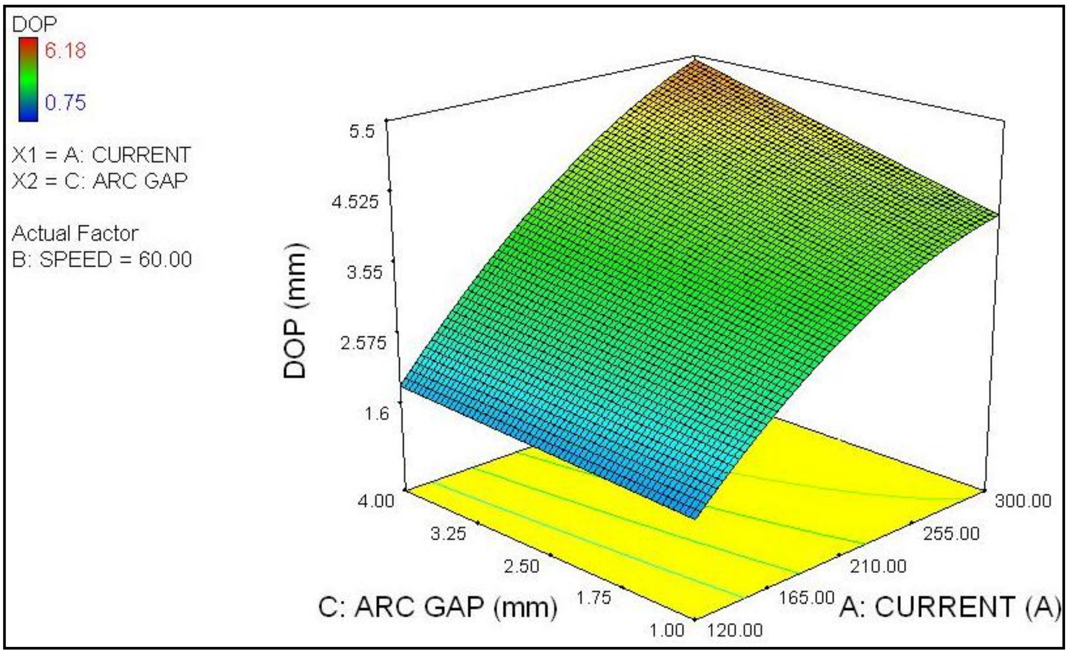

Fig 3.5(c) Surface Response of Current and Arc Gap on DOP

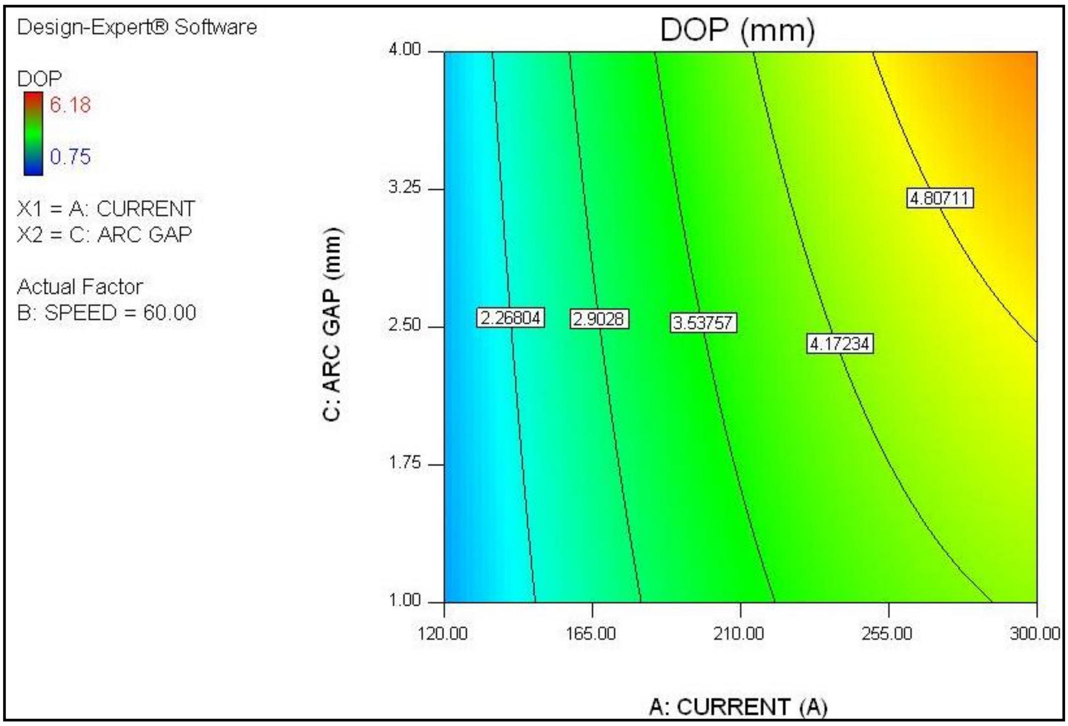

Fig 3.5(d) Response of Current and Arc Gap on DOP

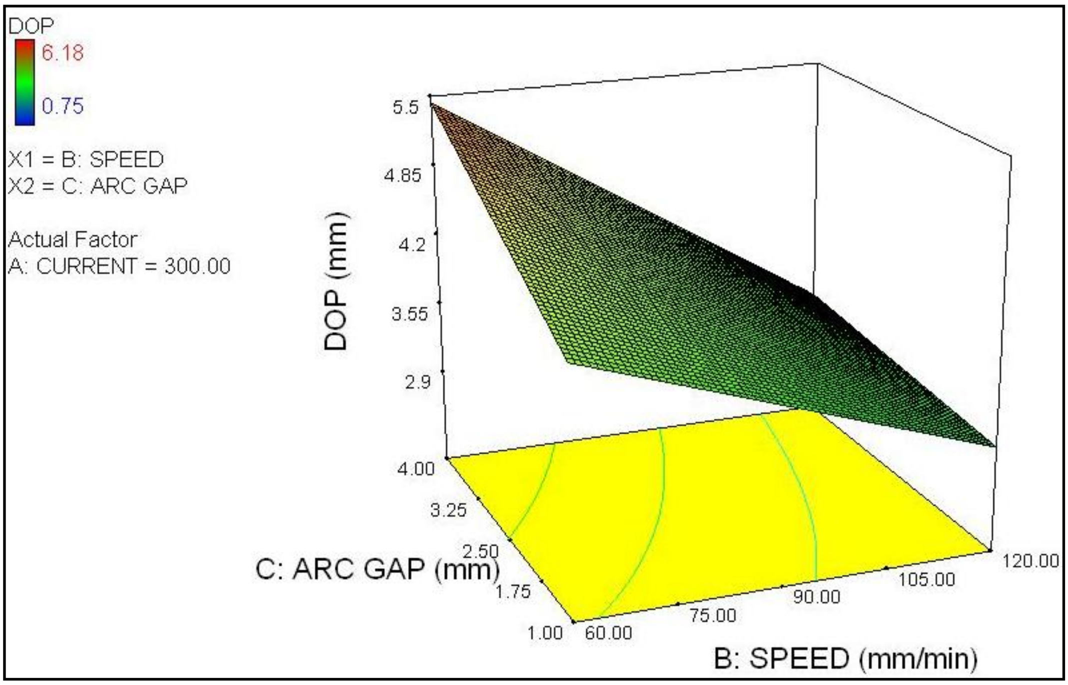

Fig 3.5(e) Surface Response of Speed and Arc Gap on DOP

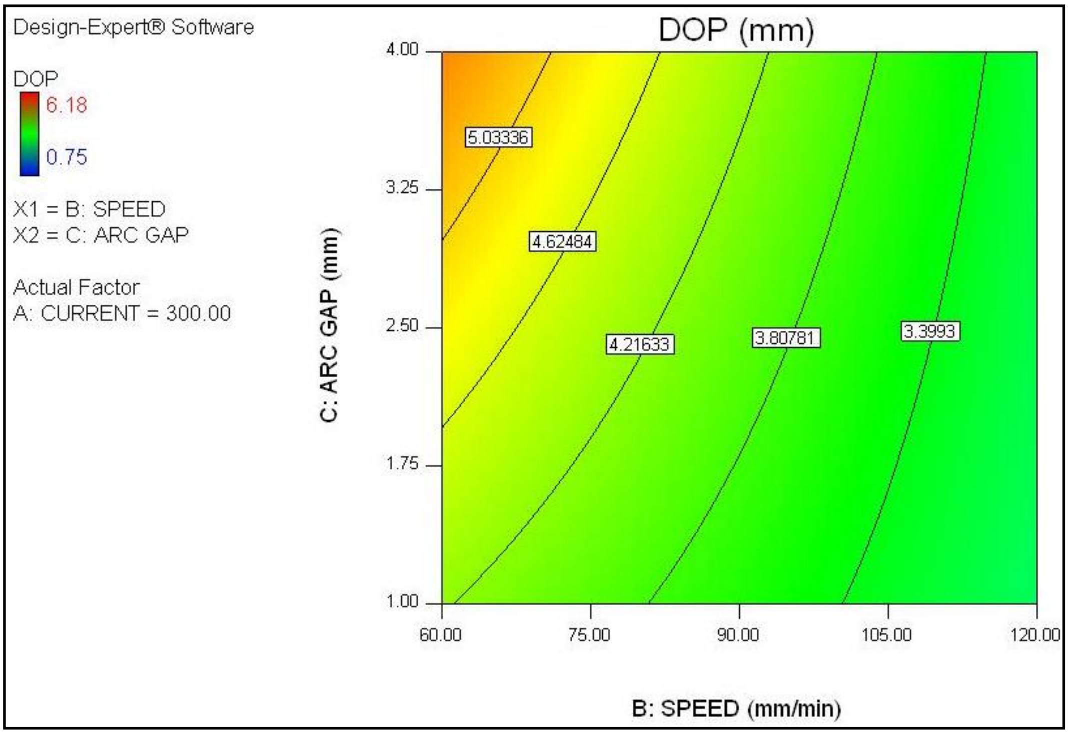

Fig 3.5(f) Response of Speed and Arc Gap on DOP

Fig 3.5 Response Surface and Overlay plots for effect of Current, Welding Speed and Arc Gap on DOP (D-Optimal 36)

The desirability matrix for maximising DOP as response for three different constraints was derived by using D-Optimal 36. The desirability criterion and two sets of process parameters chosen for validation of experiment from the predicted matrix are given in Table 3.8. Experiments were performed to validate the desirability approach. The predicted and experimental values were found to be in close agreement.

Table 3.8 Desirability criterion and matrix for D-Optimal 36

Criterion						
Name	**Goal**	**Lower Limit**		**Upper Limit**		
CURRENT	is in range	120		300		
SPEED	is in range	60		120		
ARC GAP	is in range	1		4		
DOP	maximize	NA		6.18		
Matrix						
No	**CURRENT**	**SPEED**	**ARC GAP**	**Desirability**	**DOP (Model)**	**DOP (Experiment)**
1	300.00	60.00	4.00	0.864	5.44187	5.61
2	300.00	60.06	3.98	0.863	5.43343	5.58

Taguchi: The design matrix generated by MINITAB 16 is shown in Table 3.9. In order to evaluate the influence of each selected factor on the responses; the signal-to-noise ratios S/N for each control factor have to be calculated. For achieving maximum DOP, the criterion of larger the better was used [$S/N= - 10 \log (1/n)(\Sigma 1/y^2)$, where n is the number of observations and y is the observed data]. The total number of bead on plate experiments were undertaken to include all the experimental runs required for both D-Optimal and Taguchi matrices. The experiments were conducted as per D-Optimal matrix. Additional experiments required for the Taguchi design matrix were conducted to complete the response parameter of Taguchi design matrix. The Taguchi experimental results obtained by means of MINITAB 16 statistical software are summarized in Tables 3.10 &3.11. The graphical representation of the results is shown in Figs. 3.6&3.7. The p-values for current, speed and current-speed interaction in ANOVA Table 11 show significant effects of these parameters on DOP for the model estimated at 95% significance level. The main effects plot (Fig.3.6) shows the influence of process parameters depending on the range of influence of each parameter. It can be noticed that the current is the most important factor affecting the responses. Torch speed has a lower relevant effect. The arc gap plots show the lowest effect among the factors. Interaction Plot given in Fig. 3.7 shows that DOP increases with higher current but the influence of higher current on DOP in less significant as compared to that at lower speeds. It is also observed that the interaction of speed and arc gap has the least influence on DOP. Fig. 3.7 shows that, higher DOP is achieved at higher current and lower speed.

The final regression equation in terms of the actual factors, as developed by post analysis of the Taguchi model is:-

DOP = 1.94 - 0.0226 Torch Speed + 0.0140 Current + 0.019 Arc Gap

Table 3.9 TAGUCHI L27 DOE Matrix

Run	**Current** (Amperes)	**Torch Speed** (mm/min)	**Arc Gap** (mm)	**DOP** (mm)
1	120	60	1.0	1.616
2	120	60	2.5	1.480
3	120	60	4.0	1.770
4	210	60	1.0	3.960
5	210	60	2.5	2.480
6	210	60	4.0	4.760
7	300	60	1.0	5.150
8	300	60	2.5	6.180
9	300	60	4.0	6.080
10	120	90	1.0	2.030
11	120	90	2.5	1.580
12	120	90	4.0	1.600
13	210	90	1.0	3.200
14	210	90	2.5	1.790
15	210	90	4.0	3.400
16	300	90	1.0	2.730
17	300	90	2.5	3.930
18	300	90	4.0	3.460
19	120	120	1.0	1.910
20	120	120	2.5	0.750
21	120	120	4.0	1.510
22	210	120	1.0	2.930
23	210	120	2.5	3.210
24	210	120	4.0	1.510
25	300	120	1.0	2.890
26	300	120	2.5	3.750
27	300	120	4.0	2.830

Table 3.10 Response Table for Signal to Noise Ratios (Larger is better)

Level	Torch Speed	Current	Arc Gap
1	10.185	3.716	8.835
2	7.932	9.137	7.460
3	6.609	11.873	8.431
Delta	3.576	8.153	1.374
Rank	2	1	3

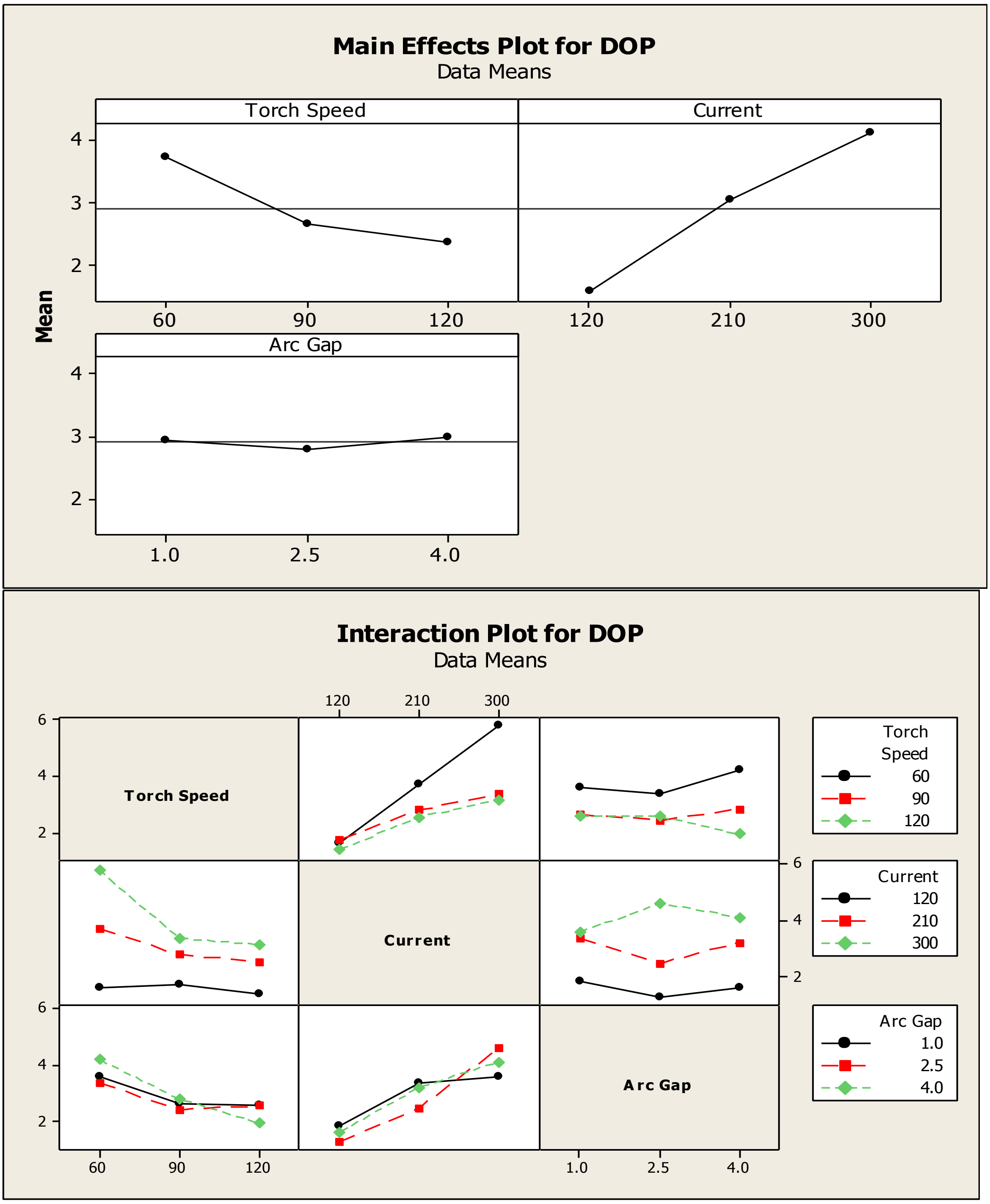

Fig 3.6 Main Effects and Interaction Plot of DOP for L27 Taguchi Matrix

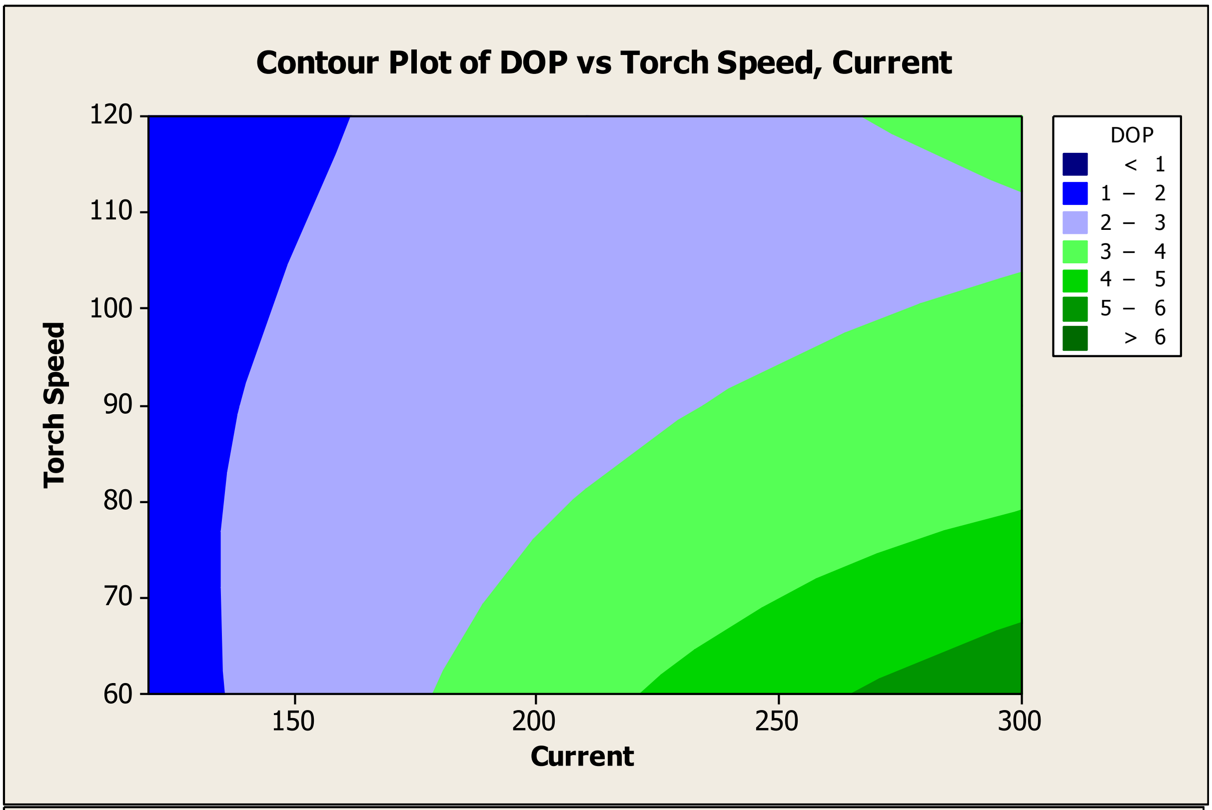

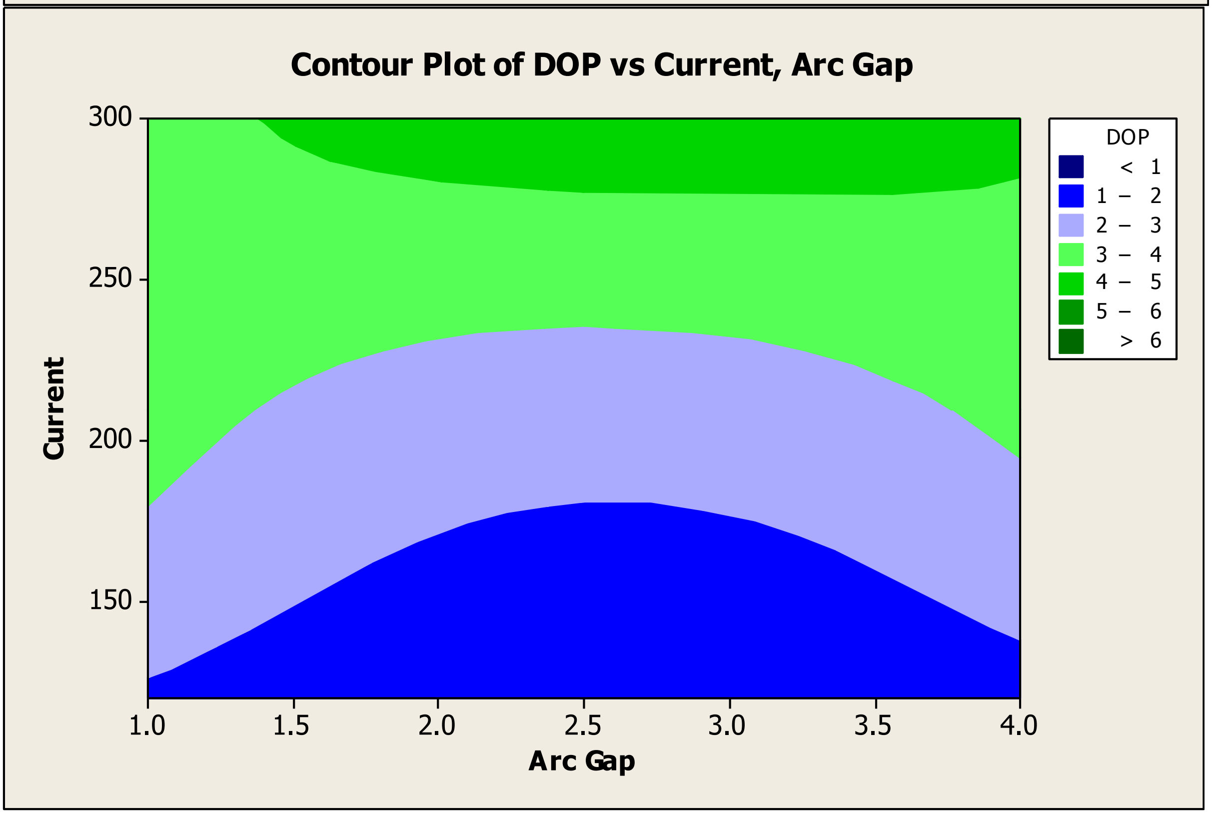

Fig 3.7 Overlay plots for Effect of Current (Amperes), Welding Speed (mm/min) and Arc Gap (mm) on DOP (mm) (L27 Taguchi)

Optimum parametric settings were found from the main effect plots at highest mean ratio values (Table 3.12). The experimental value of DOP obtained for the optimal parameters obtained by Taguchi is found to have some variation with the DOP value predicted by the model.

Table 3.11 Analysis of variance of means for L27 Taguchi matrix

Source	DF	Seq SS	Adj SS	Adj MS	F	P	
TSpeed	2	9.2438	9.2438	4.6219	11.19	0.005	(significant)
Current	2	28.9573	28.9573	14.4786	35.06	0.000	(significant)
ARCGAP	2	0.1848	0.1848	0.0924	0.22	0.804	
TSpeed*Current	4	6.2385	6.2385	1.5596	3.78	0.052	(significant)
TSpeed*ARCGAP	4	1.9285	1.9285	0.4821	1.17	0.393	
Current*ARCGAP	4	3.2333	3.2333	0.8083	1.96	0.194	
Residual Error	8	3.3035	3.3035	0.4129			
Total	26	53.0897					

Table 3.12 Optimum Parametric Conditions by Taguchi

Optimum Parametric Conditions by Taguchi		DOP Obtained (mm)	
Current (A)	300	Model Equation	Experiment
Torch Speed (mm/min)	60	4.876	5.61
Arc Gap (mm)	4		

In Taguchi design, interactions between control factors are aliased with their main effects and so the Taguchi technique gives the results in the form of linear interactions. Thesignificance of interactions and square terms of parameters are more clearly predicted in D-Optimal (RSM). The D-Optimal (RSM) shows the significance of all possible combinations of interactions and square terms. It was observed that for the Taguchi technique, data analysis and optimization of operating parameters were possible with thelowest number of experiments involving fewer computational complexities, whereas 3D surfaces generated by D-Optimal (RSM) can help in visualizing the effect of parameters on the response over the entire range specified. Taguchi L7 and D-Optimal D22 provide accurateestimationsfor restriction in number of experiments. Taguchi L27 and D-Optimal D36 prove to be better by increasing the number of experimental runs to achieve higher precision in evaluation.

3.3.3 Validation

Six experiments were undertaken to validate the DOP equations derived by D-Optimal and Taguchi design matrix. The validation results are given in Table 3.13.

Table 3.13 Results of Validation Experiments

S.No	Current	Speed	Arc Gap	Expt. DOP	D-Optimal		Taguchi	
					DOP	Error	DOP	Error
	Amps	mm/min	mm	mm	mm	%	mm	%
1	225	60	3	3.69	4.12	-0.12	3.80	-0.03
2	250	60	3	3.73	4.49	-0.21	4.15	-0.11
3	300	60	3	5.15	5.04	0.02	4.86	0.05
4	300	60	1.8	4.21	4.55	-0.08	4.83	-0.15
5	300	60	2.4	5.12	4.80	0.11	4.85	0.10
6	300	60	3	5.21	5.04	0.06	4.86	0.09

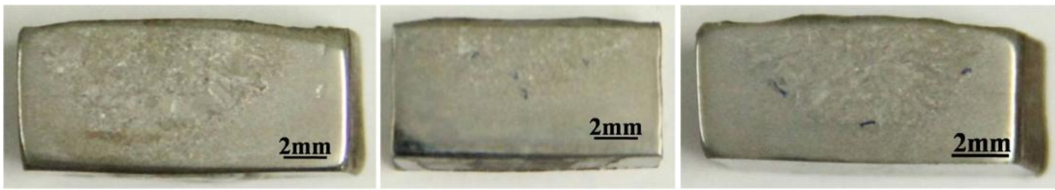

(a) Run 3, DOP 5.15 mm (b) Run 4, DOP 4.21 mm (c) Run 5, DOP 5.12 mm

Fig.3.8 Micrograph of Validation Experiments (a) Run 3 (b) Run 4 (c) Run 5

The validation experiments show that the corresponding DOP for pre determined input parameters can be achieved with good approximation.The micrograph showing the DOP for validation runs 3,4 and 5 are shown in Fig 3.8.The derived relation for DOP within the specified range of welding parameters (Current, Speed and Arc Gap) is within acceptable error limits of the 2.1 to 17.4%. D-Optimal is found to identify the process parameters more accurately than Taguchi technique. This is due to the fact that Taguchi derived equation is a linear fit within the scatter of experimental results, whereas the D-Optimal provides the flexibility of refiningthe regression fit equation depending on the significance of the input and interaction factors. The RMS error of the predicted and measured DOP values for RSM (D-Optimal) and Taguchi optimization techniquesare found to be 0.575 and 0.860 respectively. Thus, RSM (D-Optimal) is observed to predict optimized welding process parameters for achieving maximum DOP with better accuracy during the A-GTAW process.

The experiments carried out at 270 A current and 60 mm/min speed showed maximum weld penetration greater than thatpredicted by thedesign of experiments, as shown in Table 3.14. The abrupt increase in depth of penetration is attributed to the surface tension gradient change with respect to temperature that leads to enhanced reverse Marangoni flow [22, 95, 100] (Fig 2.16).

Table 3.14 Increase in DOP

S.No	Current	Speed	ArcGap	DoP	DoP	Error	DoP	Error
	Amps	mm/min	mm	mm	mm	%	mm	%
				Actual	RSM		Taguchi	
1	270	60	3	7.8	4.38	0.4384	4.4838	0.4251
2	275	60	3	7.6	4.60	0.3947	4.495	0.4085

For preparation of sound weld joint and ensure sufficient overlap of two passes, the welding parameters of 270 A current, 60 mm/min speed and 3 mm arc gap were chosen to make double sided A-GTAW weld joints.No cracks were observed on application of dye penetration testing which confirmed that the A-GTAW weld joint had adequate ductility.

Details of U-Bend test are given in Appendix A1.

3.4 Conclusions

Development of activated flux for naval structural steels (DMR-249A HSLA steel) was found to be a challenging task due to:-

(a) Presence of surface stable elements like Al and Ca (greater than 150ppm) that reduce weld penetration.

(b) Low content of surface active elements like S (less than 60 ppm) required for stable and reliable *dy/dT* (surface tension to temperature gradient).

(c) Sensitivity of weld penetration to critical heat input and critical concentration of surface active elements.

The following conclusions were derived from the experiments undertaken and observations from the experimental results:-

(a) An activated flux for joining DMR-249A, a low carbon HSLA, naval structural material has been developed successfully.

(b) The increase in the weld penetration achieved by using activated flux with aGTAW process is250% more than aconventional autogenous GTAW process without flux.

(c) It is confirmed that though combined concentration percentage of (Si+O) is a significant indicator of DOP, an optimised combination of Si and O isneeded to achieve higher DOP.

(d) Both the D-Optimal (RSM) and Taguchi optimization techniques identified the optimum process parameters of A-GTAW process for achieving maximum depth of penetration in single pass welding. However, the relation between DOP and the process parameters varied between the two optimization techniques. RSM based D-Optimal considered the interaction between the process parameters while the Taguchi technique ignored the interaction between the process parameters.

(e) Both the optimization techniques confirmed the significance of current, torch speed and arc gap (in decreasing order of significance) on DOP.

(f) Taguchi L7 and D-Optimal D22 provide considerable accurateestimationsfor restriction in the number of experiments. Taguchi L27 and D-Optimal D36 prove to be better by increasing the number of experimental runs to achieve higher precision in evaluation.

(g) In comparison with Taguchi, RSM (D-Optimal) is observed to predict optimized welding process parameters for achieving maximum DOP with better accuracy during A-GTAW process.

Chapter 4. Modelling and simulation using SYSWELD

The Finite Element Model (FEM) simulation of thermo-mechanical behaviour of SMAW (the most common welding technique used for welding of steels and construction of ships) and A-GTAW (welding technique being studied and developed as alternative welding technique for DMR-249A steel) joints was studied using SYSWELD software. The chapter covers the description of heat source used for FEM simulation of welding, comparison of simulated thermal and residual stress profiles of A-GTAW and SMAW weld joints and validation with experimental results. The double ellipsoidal heat source distribution model was employed for the thermal and residual stress analysis using SYSWELD software. The numerically estimated temperature distribution was validated with online temperature measurements using K-type thermocouples. The predicted residual stress profile across the weld joints was compared with the values experimentally measured using non-destructive techniques. A good agreement between measured and predicted thermal cycles and residual stress profile was observed. The present investigations suggest the applicability of numerical modeling as an effective approach for predicting the thermo-mechanical properties influenced by welding techniques for DMR-249A steel weld joints.

4.1 Experimental details

4.1.1 Fabrication of weld joints

For each weld joint, two plates of dimensions 300x120x10 mm^3 were used. Post edge preparation of the two plates (Square Butt for A-GTAW and 70° V-Groove for SMAW), specimens of 300x240x10 mm^3 with 300 mm weld length (Fig.4.1) were fabricated using A-GTAW and SMAW processes. The weld joints fabricated at the laboratory had similar process conditions. The welding parameters used for fabrication of the weld joints are given in Table 4.1.

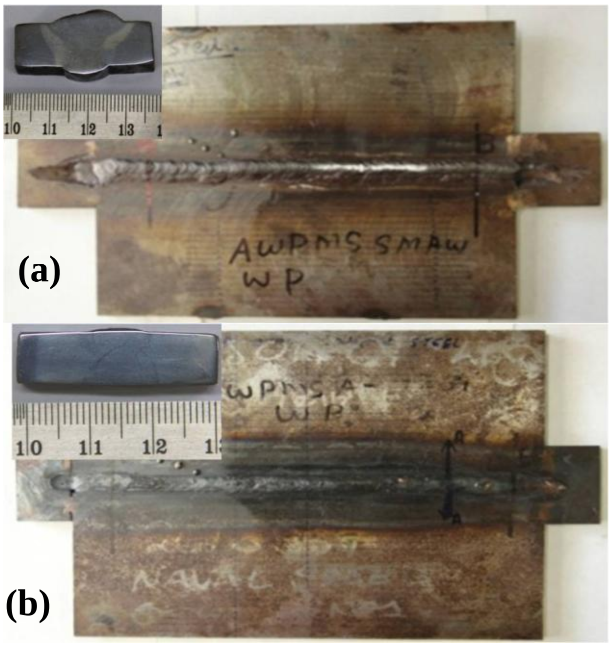

Fig 4.1 Photographs of the weld joints fabricated using (a) SMAW (b) A-GTAW processes

Table 4.1 Welding parameters for fabrication of weld joints

Welding process	Current (A)	Voltage (V)	Speed (mm/sec)	No. of passes	Heat input for weld length (kJ/mm)	Heat input for final pass (kJ/mm)
SMAW	120	25	1.5	5	10	2
A-GTAW	270	20	1	2	10.8	5.4

Temperature measurements during welding of the butt joints were done with the help of K-type thermocouples. The K-type thermocouples were spot welded on the plate before welding at a distance of 10 to 20mm away from the weld region as shown in Figure 4.2. For the double pass A-GTAW, both passes being similar, the thermocouples were used to measure temperature profiles for one pass only. For the multi pass SMAW, with limited storage capacity for thermocouple data, the time duration between changing of electrodes and removal of slag was not logged.

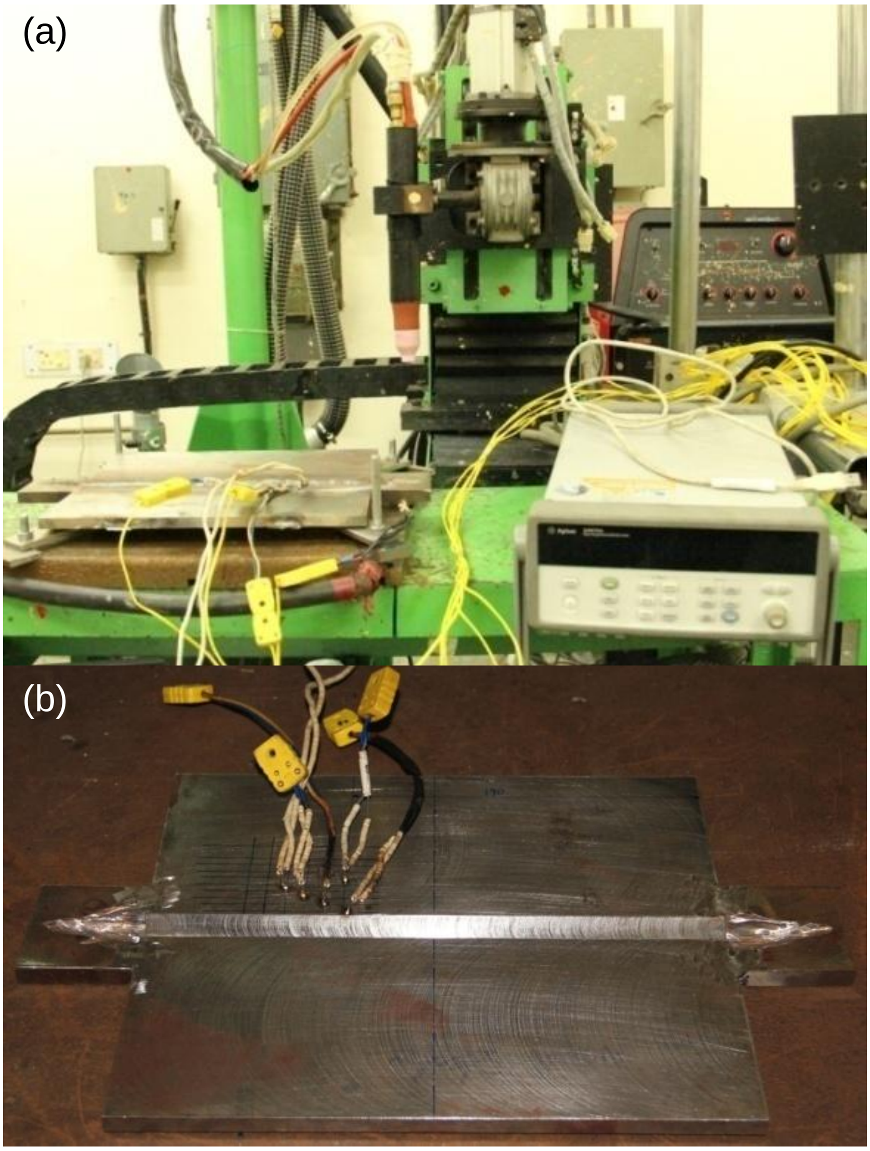

Fig.4.2 Spot welded thermocouple (a) A-GTAW joint (b) SMAW joint

The residual stress values measured experimentally using XRD and UT were used for validation of the simulated results. (The experimental details of residual stresses measurements XRD and UT are given in Chapter 5)

4.1.2 Numerical Modelling

In order to simulate a welding process the welding heat generation source must be modelled. One of the major characteristics of the heat source is its motion through time and space. The first efforts of analyzing and simulating moving heat sources were made by Rosenthal [299] and Rykalin [300]. Goldak et al. [301] proposed an analytical heat source model, which is known as the "double ellipsoidal heat source model", shown in Figure 4.3.

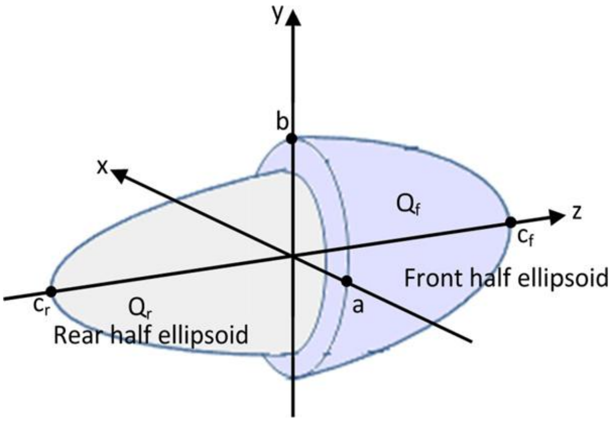

Fig.4.3 Heat source model [301]

The volumetric heat flux within two different ellipsoid (for any point x,y,z) is described by Eq. (3) and (4). The semi-ellipsoids of different heat flux are combined to give the heat source.

$$Q_f(x,y,z) = \frac{6\sqrt{3}r_f Q}{abc_f\pi\sqrt{\pi}} \exp\left(-\frac{3z^2}{c_f^2} - \frac{3x^2}{a^2} - \frac{3y^2}{b^2}\right) \ldots\ldots\ldots\ldots\ldots (4.1)$$

$$Q_r(x,y,z) = \frac{6\sqrt{3}r_r Q}{abc_r\pi\sqrt{\pi}} \exp\left(-\frac{3z^2}{c_r^2} - \frac{3x^2}{a^2} - \frac{3y^2}{b^2}\right) \ldots\ldots\ldots\ldots\ldots (4.2)$$

Arc Heat Input, $Q = V \times I \times n$ ……………..... (4.3)

where ***a***, ***b***, ***cf*** and ***cr*** are the ellipsoidal heat source geometric parameters, shown in Figure 4.3, Q = Heat input in Watts, V = Voltage in Volts and I = Current in Amperes.

The parameters ***rf*** and ***rr*** are proportion coefficients representing heat apportionment in front and back of the heat source respectively,where ***rf*** + ***rr*** = 2 . It is of great importance to note that, the values of Q(x, y, z) given by equations (3-4) must be equal at the $\boldsymbol{x = 0}$ plane to satisfy the condition of continuity of the overall volumetric heat source. This leads to definition of two constraints $\boldsymbol{rf = 2cf/(cf + cr)}$ and $\boldsymbol{rr = 2cr/(cf + cr)}$ suchthat $\boldsymbol{rf/cf = rr/cr}$. However, the double ellipsoidal heat source is described by arc efficiency $\boldsymbol{\eta}$, and four geometric parameters $\boldsymbol{a}$, $\boldsymbol{b}$, $\boldsymbol{cf}$ and $\boldsymbol{cr}$.

A numerical model was developed using the finite element module SYSWELD. The software is designed to carry out thermo-mechanical analysis of welding as a sequentially coupled analysis. The mesh model can have 1D (LINK) element, 2D (triangular or quadrilateral) elements or 3D (tetrahedral, hexahedral) elements. The present 3D simulation used hexahedral and wedge elements. Hexahedral elements for the square butt A-GTAW simulation and mixed type of elements for the V-joint SMAW were used. The sensitivity of the aanalysis to the mesh design was analyzed by trial and error. Mesh was analyzed using variable mesh size with the minimum size near the fusion zone and coarse mesh away from the fusion zone corresponding to the temperature gradient in the welded plates. A double ellipsoidal heat source model was used for simulation. A double ellipsoidal heat source is a volumetric source which can approximate the dimensions of the molten weld pool [203-205]. Two different FE models were generated with the welding path parallel to the Y axis and the model on the XY plane. For the A-GTAW square butt joint, FE models for 300 x 120 x 10 mm^3 size plate were generated with 76440 elements/82830 nodes. The symmetric model was mirrored. For the SMAW 70^o V-Groove butt joint,the 300 x 240 x 10 mm^3 plates with an included V-Groove at the centreline was modelled with 103350 elements/113099 nodes. The FE models are shown in Fig 4.4.

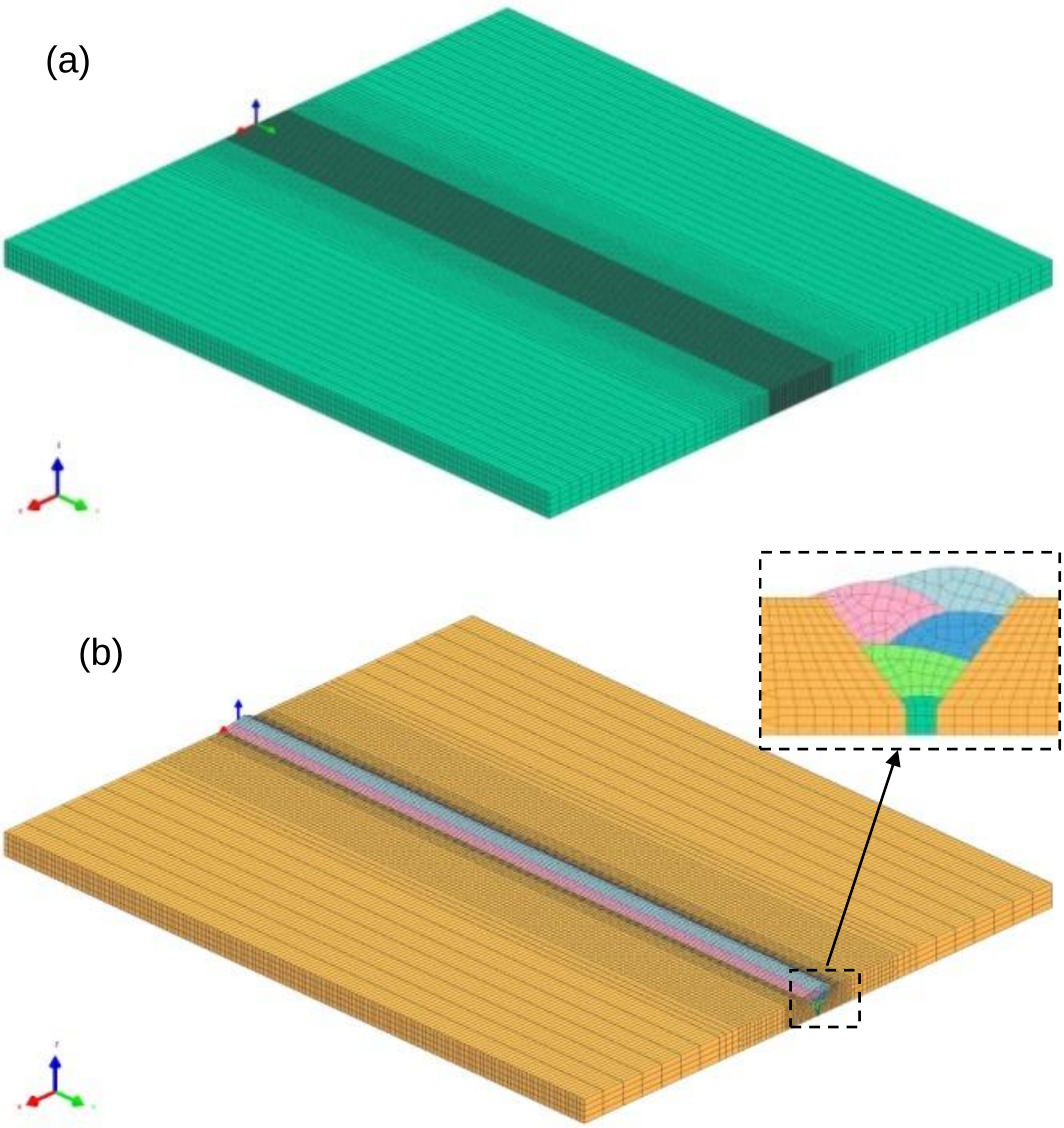

Fig. 4.4 FE model of weld joint (a) A-GTAW (b) SMAW

The simulation consisting of thermo-metallurgical analysis and mechanical analysis requires temperature and phase dependent material properties. For thermal analysis; thermal conductivity, specific heat, coefficient of thermal expansion and density with respect to temperature is considered. For mechanical analysis; Young's Modulus, ultimate tensile Strength, Poisson's ratio with respect to temperature are considered. *Thermal and mechanical properties are given in Appendix A2*. The available properties of equivalent HSLA steel with comparable chemical composition and mechanical propertieswere used to carry out simulations [16-17].

4.1.3 Assumptions for SYSWELD simulation

During welding, most of the heat energy dispersed into the component by conduction mode heat transfer. In this model, molten pool stirring was suppressed and the problem was considered as conduction heat transfer analysis. The thermal conductivity of the molten pool after melting point was artificially doubled to consider the molten pool stirring effect. Since conduction based model is used in this simulation, the enthalpy of material determines the liquid or solid phase. The enthalpy is calculated in terms of specific heat. The temperature dependent Cp value determines that the model is in solid or liquid phase at a specific temperature induced during welding simulation. Inthe absence of convection, temperature is not transferred whereas it is stagnating at specific zone that increases the local thermal gradients. Due to this heating rate and cooling rate varies andhas influence on distortion thereby the derivative of distortions like residual stress is influenced. The scenario of FEM model and experimental measurement is not same. The boundary conditions used as constant in FEM and in reality it varies with respect to temperature; so the gradual temperature measurement by thermocouple is expected.The convective heat transfer coefficient was taken as 25Wm^{-2}. Elastic constraints are applied for elements or nodes with a stiffness of 1000 N/mm.

4.2 Results and Discussions

4.2.1 Thermal Analysis

Experimentally measured macro bead profile and simulated bead profile for A-GTAW and SMAW weld joints are shown in Fig 4.5 and 4.6 respectively. The heat source was calibrated to achieve the bead profile as observed in macro cut section of the welded joints. Heat source parameters were measured from experimentally observed weld attributes and used in the calibration process. Dimensions of heat source were adjusted till it matches with the experimentally observed weld bead. The heat source fitting parameters used for FEM simulation of A-GTAW and SMAW joints are given in Table 4.2. It shows very close agreement with the experimental weld bead profiles.

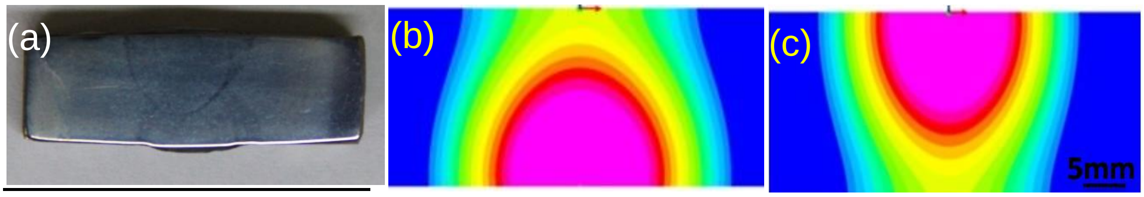

Fig. 4.5 A-GTAW Bead Profile (a) Macro (b) First pass (c) Second pass

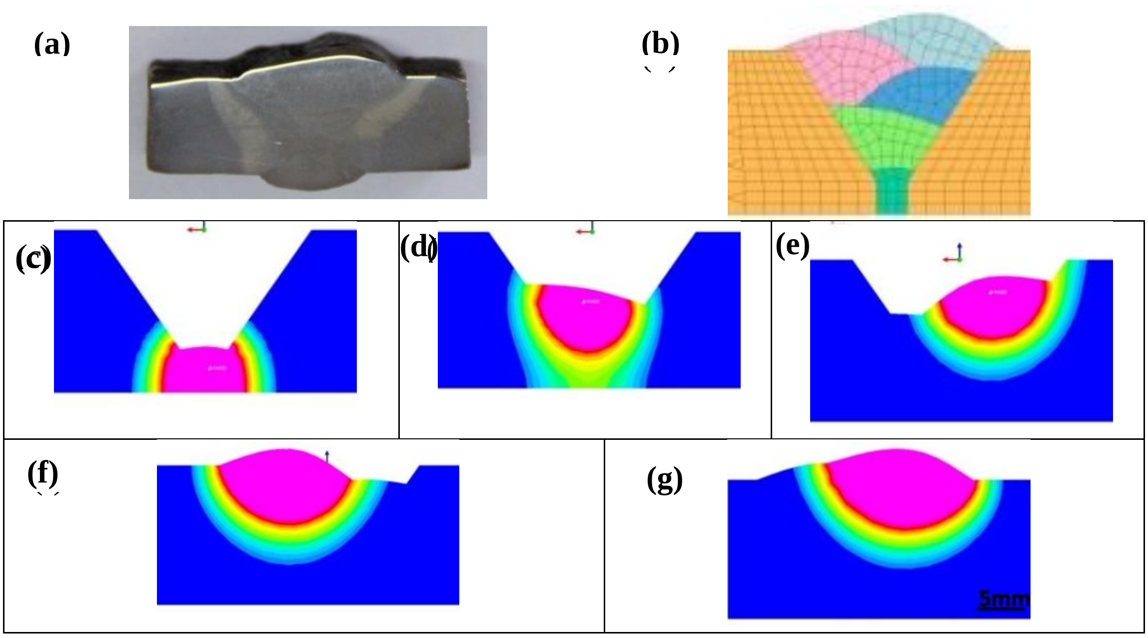

Fig. 4.6 SMAW Bead Profiles (a) Macro (b) 5 passes meshing (c)-(g) Passes 1 to 5

Table 4.2 Values of heat source calibrated function

Parameter	A-GTAW	SMAW
Front length of the molten zone, Af (mm)	4.5	5.5
Rear length of the molten zone, Ar (mm)	9.0	5.0
Half of the width of the bead, B (mm)	5.0	3.0
Penetration of the bead, C (mm)	6.0	3.0
X,Y,Z	0,0,0	0,0,0
Power (kW)	5.4	2.0
Efficiency	0.75	0.65
Velocity (mm/sec)	1	1.5

The experimental validation of temperature distribution was carried out by physically measuring temperature on plate surface using thermocouples placed at 10mm, 15mm and 20 mm away from the weld bead. Figure 4.7 and 4.8 shows the validation of predicted thermal cycles in A-GTAW and SMAW process respectively. Figure 4.7 and 4.8 indicate higher temperature gradients at areas closer to the welding heat input and lower temperatures away from the weld centre. The maximum heating and cooling rate is observed at the weld centre point. The thermal cycle has a sudden rise in the curve gradient and the slope of curve is lesser for cooling after the heat source passes, validating higher heating rate than the cooling rate.

The heating rate for both experimental and simulated results was observed to be similar. Figure 4.7 and 4.8 shows that the experimental cooling rate was lesser than the simulated cooling rate. It was also observed from Table 4.3 that thermocouple reading as compared to FEM show lower temperatures near to weld centreline but higher temperatures as distance from centreline increases, showing higher cooling rate in FEM. The simulated thermal profile showed steeper slope and higher cooling rate as the heat transfer mode was assumed to be primarily conduction with modified higher thermal conductivity for molten weld pool.

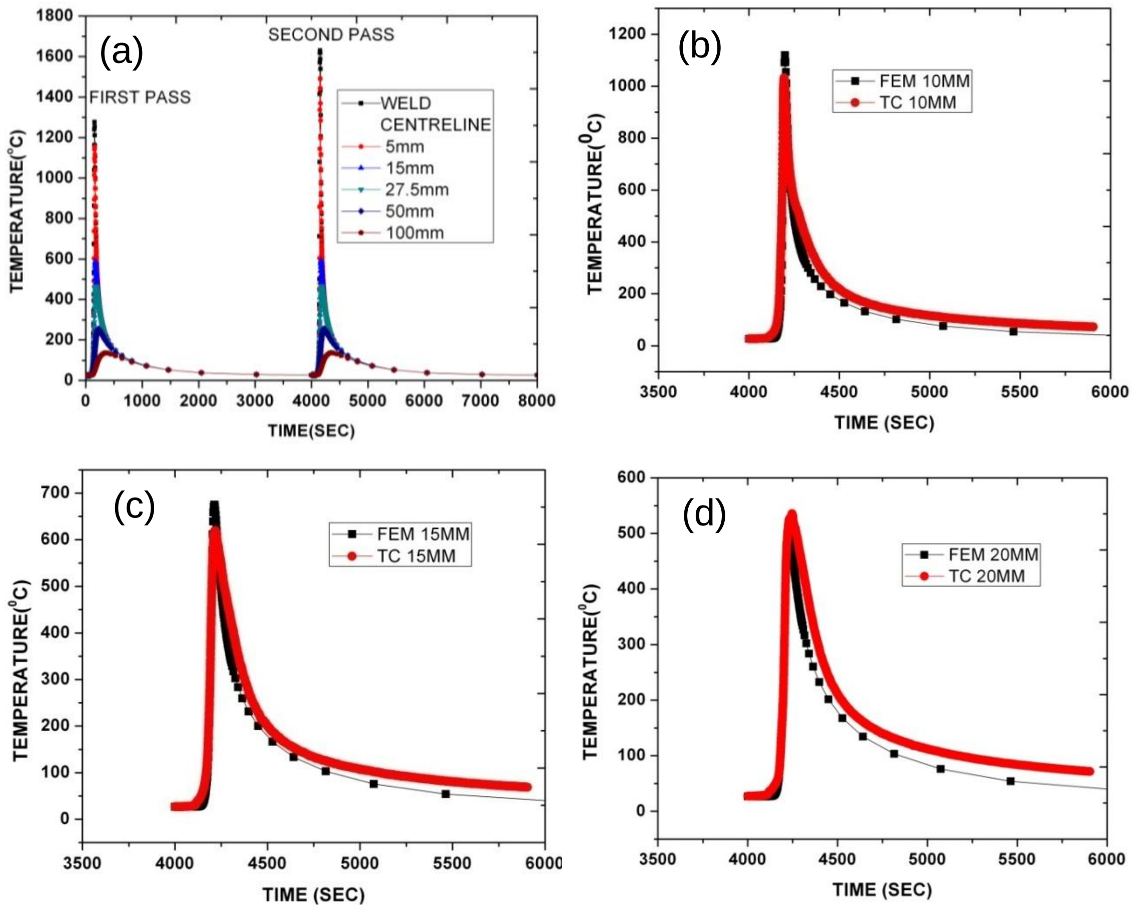

Fig 4.7 A-GTAW Thermal cycle (a) transverse direction, (b) at 10mm, (c) at 15mm, (d) at 20mm

The comparison of peak temperature values for each pass measured at the predetermined locations of thermocouple and as deduced from the FEM of A-GTAW and SMAW processes is given in Table 4.3.The higher heat input of 5 kJ/mm for A-GTAW compared with 2 kJ/mm for SMAW process resulted in higher temperatures in the A-GTAW weld joint. Also the arc constriction in A-GTAW induces concentrated temperature at the welding centre line which attributes higher temperature.

Table 4.3 Comparison of Peak Temperatures Measured by Thermocouple and predicted by FEM

Distance from Weld Centre	Centre Line	10mm	15mm	20mm
A-GTAW				
Thermocouple (^{0}C)	-	1080	631	541
FEM (^{0}C)	1630	1120	683	507
SMAW				
Thermocouple (^{0}C)	-	551	381	349
FEM (^{0}C)	1579	557	379	318

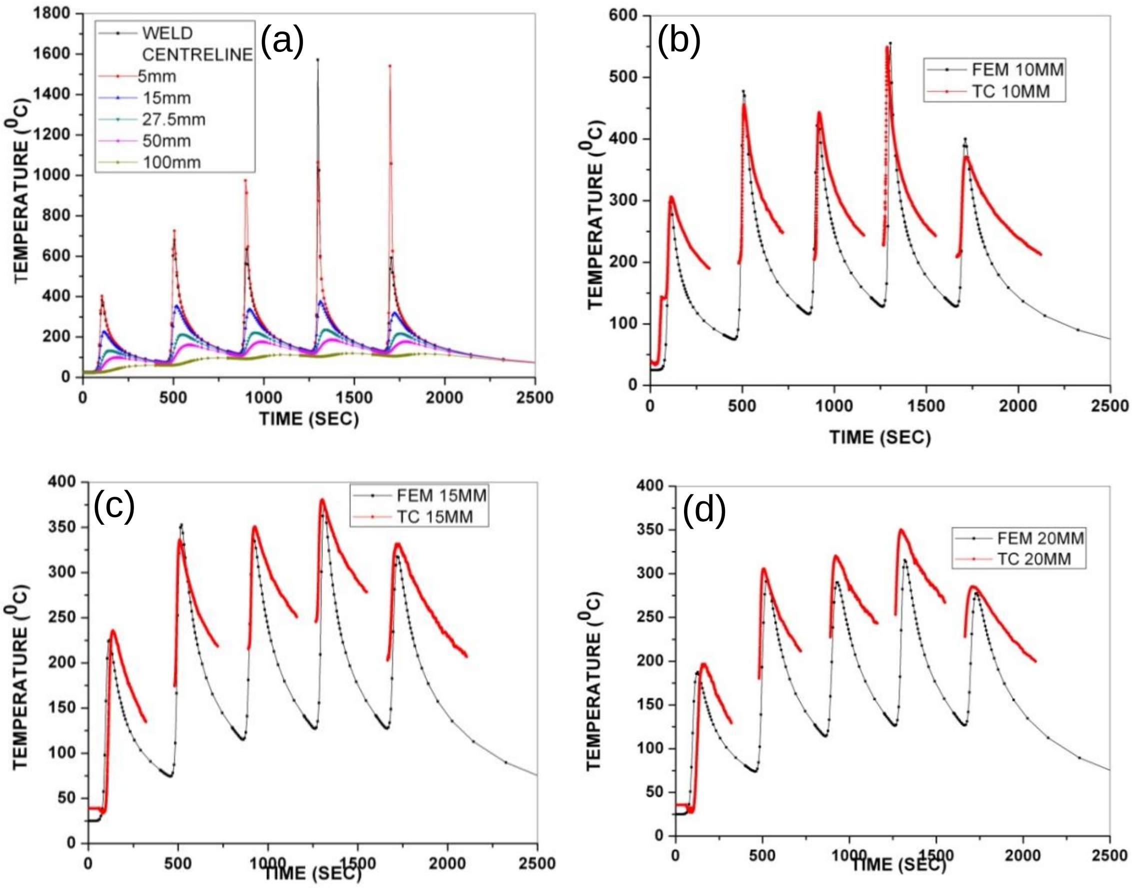

Fig 4.8 SMAW Thermal cycle (a) transverse direction, (b) at 10mm, (c) at 15mm, (d) at 20mm

The maximum peak temperature measured at molten weld centre in FEM for A-GTAW and SMAW depict the melting temperature and was found to be similar as mentioned in Table 4.3. The difference between maximum temperatures observed at different distances from weld centre for A-GTAW and SMAW is attributed to the difference in heat input for the two welding techniques. The higher heat input of 5 kJ/mm for A-GTAW compared with 2 kJ/mm for SMAW process resulted in higher temperatures in the A-GTAW welded plate.

4.2.2 Residual Stress Analysis

The predicted residual stress profiles in the A-GTAW and SMAW weld plates are given in Figure 4.9 (a-b). The residual stresses as measured experimentally using

XRD, UT (Lcr) techniques and FEM simulation for the plates using the A-GTAW and SMAW processes are shown in Fig 4.10.

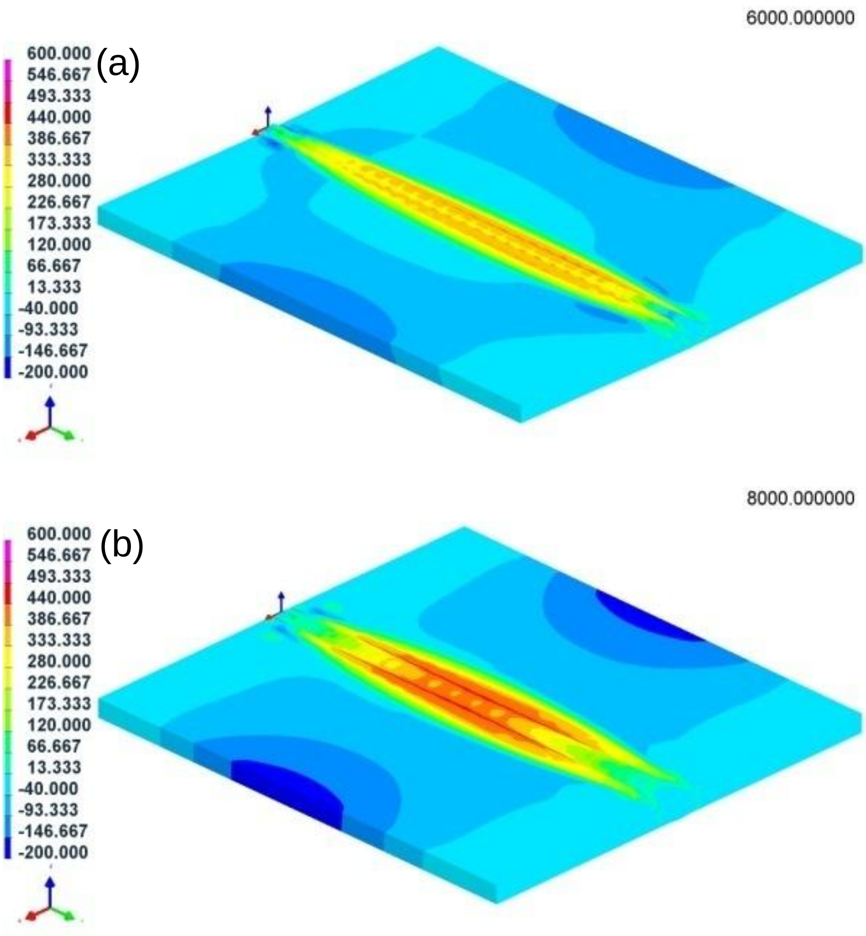

Fig. 4.9 Simulated longitudinal stress distributions using FEM

(a) A-GTAW (b) SMAW

Maximum tensile RS generally upto yield stress of the base material have been reported in weld joints made by advancedarc welding processes [206-207]. In Fig 4.10(a-b), tensile RS are shown to be present upto 20 mm to 40 mm on either side of the weld line.

Fig 4.10 shows that experimental stress measurements closely agreed with the numerical prediction. The comparison of residual stresses as measured and numerically predicted for the A-GTAW and SMAW processes is given in Table 4.4.

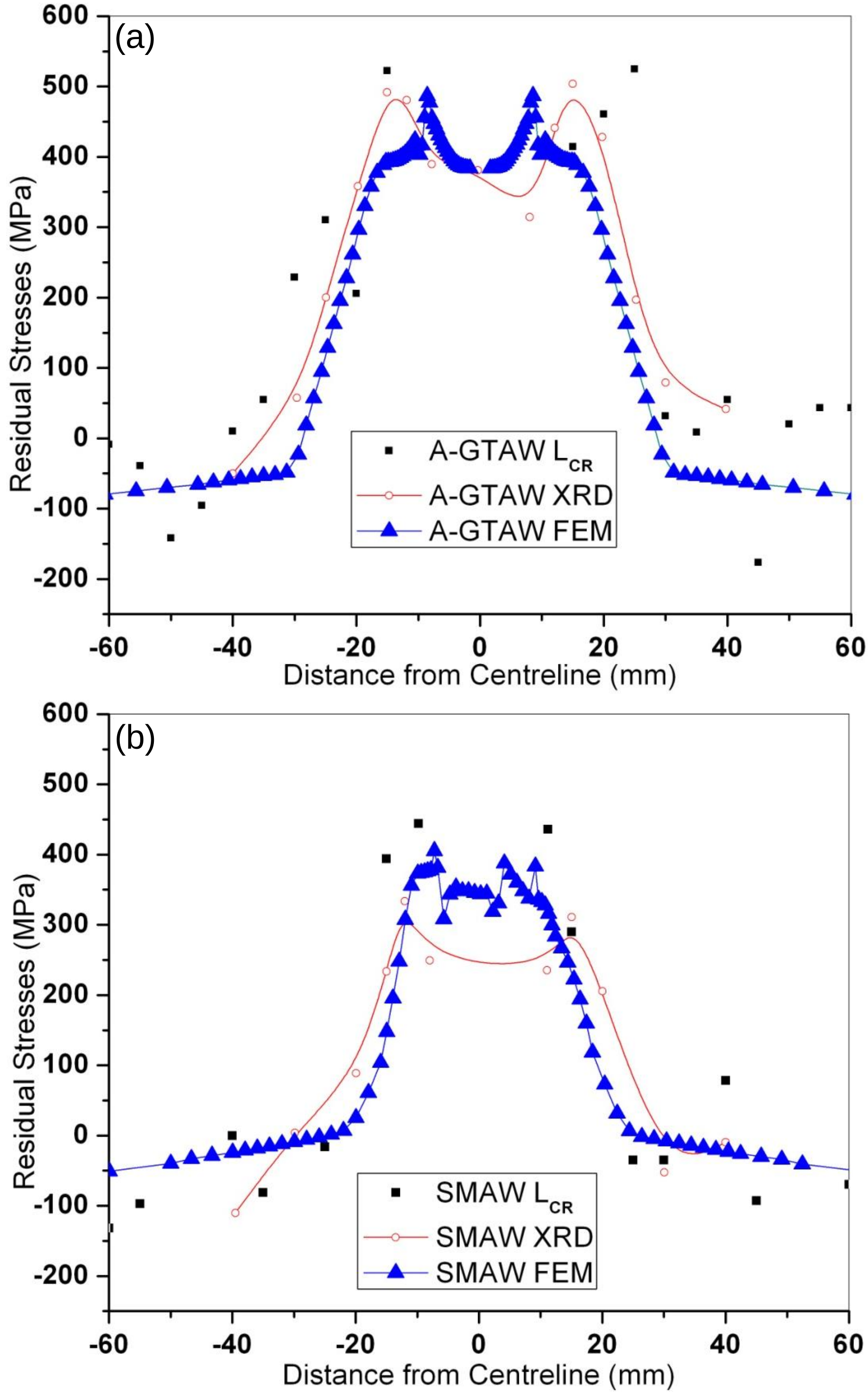

Fig. 4.10Longitudinal Residual stress comparison of FEM with XRD and L_{CR} methods
(a) A-GTAW (b) SMAW

Fig. 4.10 shows that experimental stress measurements are comparable with the numerical prediction. The profiles of the residual stresses measured by XRD, UT and FEM were observed to be similar. The minor variations in absolute values of stresses is attributable to the difference in residual stress gradients for different welding techniques and inherent volume of inspection of surface and bulk residual stresses of each respective technique [39-44, 151-153, 194-195]. The XRD measurements are sensitive to surface conditions with assumed depth of penetration in the order of 5 to 30 microns. For the L_{CR} measurements, residual stress is the average value over an effective penetration of 3 mm. The FEM simulated values are average stress values over 3 mm as interpreted from the SYSWELD model.

Table 4.4 Comparison of Maximum Residual Stress (MPa)

	XRD	UT	FEM
A-GTAW	505	526	496
SMAW	316	450	407

RS induced by shrinkage of the molten region is usually tensile. When the effect of phase transformations is dominant, compressive residual stresses are formed in the transformed areas. The microstructure studies of base metal DMR-249A and arc welded joints were undertaken using optical microscope and are discussed in subsequent chapters. The M-Shape profile for measured RS may be attributed to phase transformation occurring during solid state transformation of equiaxial ferrite in base material to grain boundary ferrite, accicular ferrite, windmanstatten ferrite, bainite and micro alloying phases(detailed explanation of microstructure is given in Chapter 6)which causes volume changes in weld metal [27, 208]. The volume expansion due to phase transformation counters the volume contraction due to shrinkage, releasing the tensile RS.

A-GTAW being automated process, the variation in experimentally measured residual stresses and derived from FEM were observed to be minimal (Fig 4.10a). Minor variation in residual stress values of experimental measurements and FEM for SMAW (Fig 4.10b) is due to manual process being used. For SMAW, there is minor variation in the location of passes in experiment and FEM. Also the energy absorbed during SMAW not being uniform might have impacted the field under stress.

4.3 Conclusions

Based on the research work the conclusions are summarized as follows:-

(a) A numerical model predicting residual stresses in the A-GTAW and SMAW weld joints was developed for DMR-249A steel and the results compared with non destructive measurements.

(b) The higher heat input of 5 kJ/mm for A-GTAW compared with 2 kJ/mm for SMAW process resulted in higher temperatures in the A-GTAW weld joint.

(c) There was similarity between the measured and predicted thermal cycles for both the weld joints fabricated by SMAW and A-GTAW processes.

(d) The model presented results consistent with the practical measurements by XRD and UT which has reasonable accuracy. The M-Shape profile for measured RS is attributed to the volume fraction changes due to transformation of phases in weld metal.

(e) The study establishes FEM based thermo-mechanical analysis as a tool for predicting residual stress in DMR-249Asteel weld joints.

Chapter 5. Residual stress measurement

This chapter presents a comparison of X-Ray Diffraction (XRD) and Ultrasonic Technique (UT) residual stress measurement techniques and an evaluation of residual stresses (RS) developed in A-GTAW and SMAW weld joints. The acoustoelastic constant for DMR-249A steel was deduced experimentally for carrying out RS measurements by UT. The RS developed in high productivity double sided A-GTAW and conventional five pass SMAW weld joints were observed to be similar with a minor increase of residual stresses in A-GTAW process due to high heat input per pass of welding. The similarity of UT measurements and XRD measurements establishes UT as a dependable technique for RS measurements.

5.1 Experimental details

5.1.1 Fabrication of weld joints

The weld joints fabricated for validation of FEM simulation (refer Chapter 4) were used as reference specimens for residual stresses measurements.

5.1.2 Determination of acousto-elastic constant (AEC) and RS measurements using UT

Acoustoelastic effect or acoustoelasticity is the dependency of ultrasonic wave speed and polarization on stress. The estimation of residual stress by L_{CR}technique requires determination of the AEC value, which represents the change in transit time of a L_{CR} wave with respect to the applied stress for a particular material [151-153]. Tensile testing specimens of DMR-249A steel were fabricated(rectangular cross section 20 width, 6 mm thickness and 65mm gauge length) as shown in Fig. 5.1.

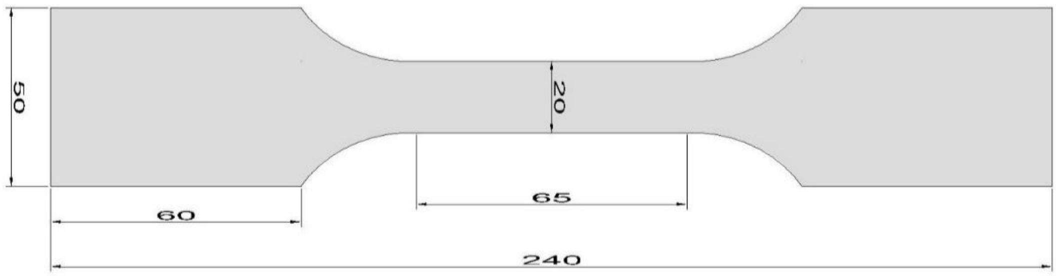

Fig. 5.1 Flat tensile sample for AEC measurement (all dimensions in mm)

The tensile specimens were stress relieved (vacuum annealed at 923K for 1 hour) and loaded in an universal tensile testing machine. The yield stress value of DMR-249A steel was taken as 490 MPa. An Ultrasonic L_{CR} probe assembly was fixed to the specimen with machine oil (OM 100) as the couplant. An Ultrasonic pulser receiver (35 MHz) with suitable filter setting (300 kHz - 20MHz) was used to excite the transducer and receive the signal. The signal was digitized with a digital oscilloscope (5 GHz) and was saved in a personal computer for post processing. All the signals were digitized at 1.25 GHz, which gives a precision of ~0.8 ns for transit time measurements. The Ultrasonic signal acquired for a no load condition was used as a reference. Tensile loads were applied up to yield stress; ultrasonic L_{CR} signalswere acquired at each load value and processed for estimation of transit time by specially developed software[151-153]. The experimental set up employed for determination of AEC is shown in Fig.5.2.

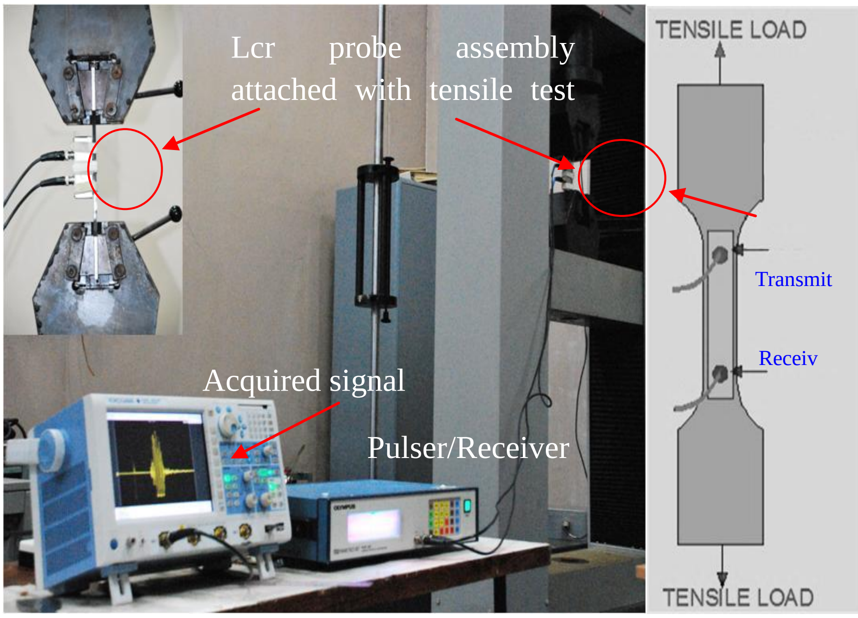

Fig. 5.2 Acquisition of L_{CR}signal during tensile testing

An integral ultrasonic L_{CR} wave probe assembly was used to generate and receive signals [192-193]. Ultrasonic transducers of 2 MHz frequency were mounted on Perspex wedges and molded in a housing so that the travel distance of ultrasonic wave is constant. The photograph of the probe assembly is given in Fig. 5.3; the typical dimensions of the assembly are 88x30x15 mm^3. The schematic of the probe assembly is shown in Fig. 5.4.The schematic of the L_{CR}technique setup used for signal acquisition is shown in Fig 5.5.

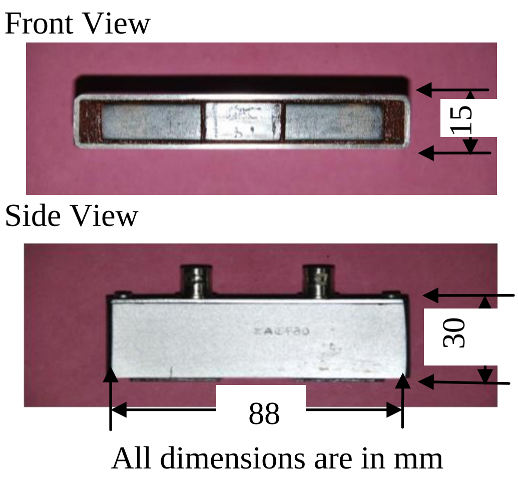

Fig.5.3Photograph of L_{CR}probe assembly

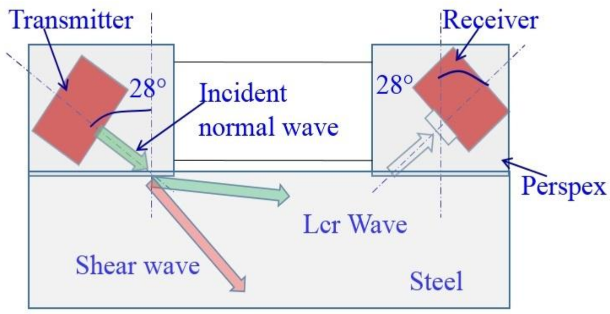

Fig. 5.4Schematic of L_{CR}probe assembly

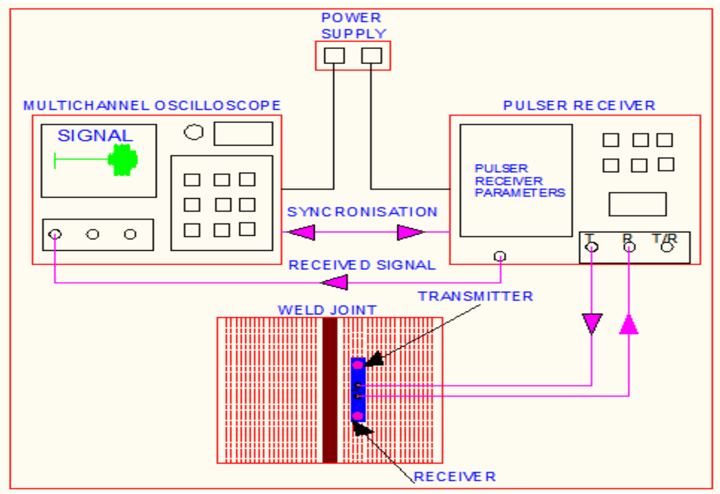

Fig.5.5Experimental setup used for acquisition of L_{CR}signals at different locations of weld joints

In order to make the transit time measurements on the surface of the weld joint using the L_{CR} probe, grid lines were marked on the surface of the weld joint.The lines were drawn parallel to the weld seam at regular intervals of 5 mm starting from the weld centre line at each side (left &right) of the weld joint. TheL_{CR} probe was placed and centered on the grid lines along the weld direction and ultrasonic signals were acquired and stored for further processing. The probe was hand pressed at the marked locations on the weld plate to achieve a similar signal strength for all the measurements.At the weld zone (~15 mm width), reliable transit time could not be obtained due to weld overlay variations, and hence residual stressmeasurements were not carried out.The data were acquired from 15 mm to 80 mm on either side of the weld centre.

The transit time of L_{CR}waves in the stress-relievedtensile specimen was designated as t_0. Transit time varied from one place to another across the weld joint corresponding to the existing compressive/tensile stresses. The change in the transit time at each grid line location compared to $t_0$is used to calculate the residual stress by using the AEC value (Eq. 2.7). The positive and negative changes in the transit time from 't_0' indicate the existence of tensile and compressive stresses, respectively.

5.1.3 X-Ray diffraction method

The XRD measurements were carried out using Chromium-Kα radiation using an X-ray tube operating at 30 kV with a target current of 7 mA (Model: Rigaku MSF 2M). Scanning was performed in the angular range of 150° to 162° in steps of 0.2° with a dwell time of 3 sec at each step to obtain quality data. The values were obtained over an area of 4x2 mm^2 and average value was used. The stress (σ) estimated by using XRD is based on the following equation [28, 194]:

$$\sigma = \left(\frac{E}{1+\nu}\right)_{(hkl)} \frac{1}{d_0} \left(\frac{\partial d_{\Psi}}{\partial \sin^2 \Psi}\right) \qquad (5.1)$$

E, ν and d_o correspond to the Young's modulus, Poisson ratio and unstressed lattice spacing respectively. From the plot of d measured at various ψ angles with $\sin^2\psi$, the slope is determined. The intercept of the plot is equal to d_o, which has a contraction due to the Poisson's ratio caused by the sum of the principal stresses. The stress is determined from the slope and from the known variables. The peak shift at various ψ angles (ranging from 0° to 45° in steps of 9°) and d-spacing relationship of lattice plane (211) were used for estimating the residual stresses. Because the value of the lattice spacing measured at $\psi = 0$ differs by not more than 0.1% from the stress-free lattice spacing, the intercept can be substituted for d_o [28, 194-195]. The residual stress can then be calculated without reference to a stress-free standard. Also, it is not sufficiently accurate to measure a d-spacing value at the presumed unstressed location due to the presence of impurities [194]. The $\sin^2\psi$ versus $d_{(211)}$ spacing plot for DMR-249A weld joint is given in Fig 5.6. A value of 210 GPa was used as the Young's modulus of the DMR-249A steel [13-15] to estimate the residual stress values. The values were estimated by XRD at intervals of 2 mm to 10 mm upto 40 mm on either side of the weld centreline. The d_o for DMR-249A steel ferritic bcc structure was found to be 1.1702 Å (Fig 5.6).

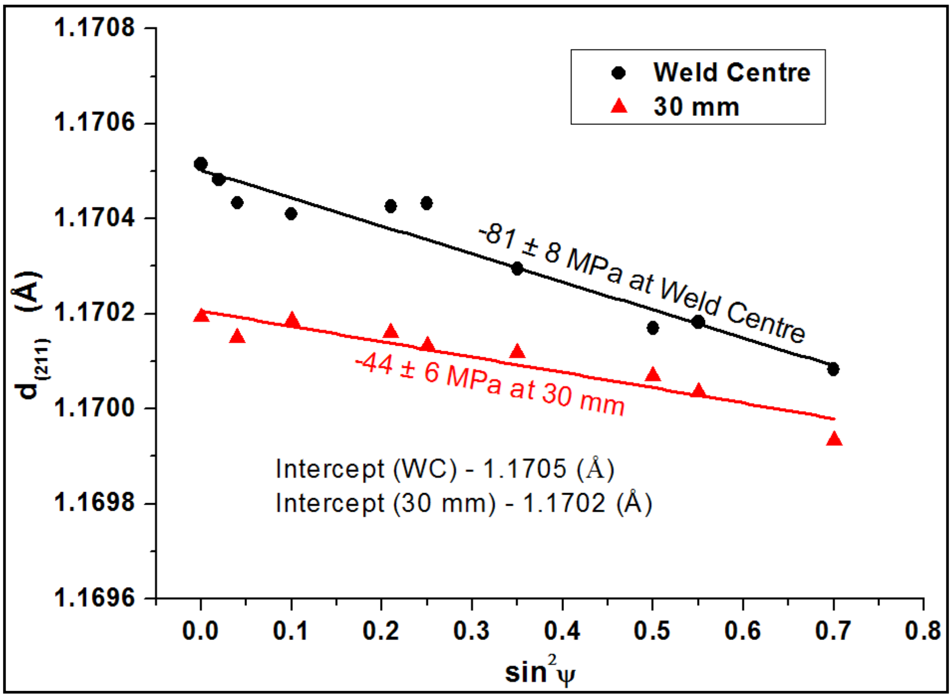

Fig. 5.6 $\sin^2\psi$ versus $d_{(211)}$ spacing plot for DMR-249A weld joint

Factors like alloy chemistry etc. can give rise to changes in lattice parameter. Changes in solute content can be brought about by the precipitation or dissolution of second phases during heat treatment, for example during welding. Such effects are particularly difficult to account for without direct measurements if they cause the strain-free lattice spacing to vary from point to point throughout the body of interest [196]. Ideally, E/(1+ν) would be different for the base metal and the weld zone. However considering the experimentally measured variation in d_o between the base metal (1.1702 Å) and weld metal (1.1705 Å) as shown in Fig. 5.6, the error in E was not considered to be substantial.

5.2 Results and discussions

5.2.1 Determination of acousto-elastic constant

The AEC denotes the change in ultrasonic velocity or transit time with respect to the applied stress. The variation of transit time of L_{CR} waves with applied stress is showed in Fig. 5.7. The change in transit time with respect to applied stress shows linear behaviour. The AEC, slope of the linear fit,was found to be 0.069 ns/MPa (thischanges about 14 MPa stress for every nano-second of transit time).

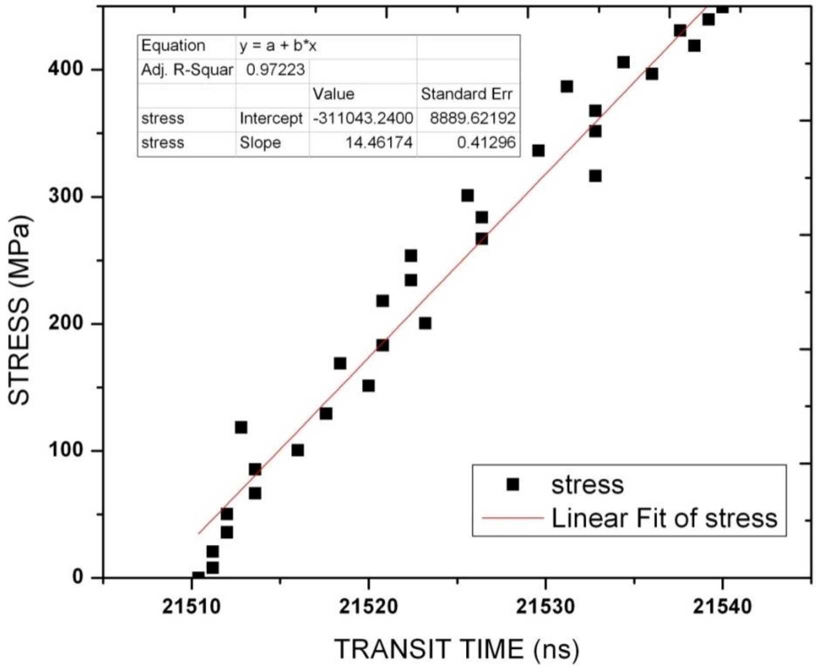

Fig. 5.7 Change in transit time of L_{CR}waves with applied stress during tensile testing

The measurements using L_{CR} waves depend on the AEC value which is specific to the material being examined and probe assembly.The magnitude of the AEC plays an important role in accurate determination of residual stress values and also in the associated error. The various reported research studies on measurement of RS by UT for low carbon steels, quenched and tempered steels, martensitic steels, austenitic steels, stainless steels and aluminium reported dimensions of AEC in ns/MPa [151-153] or as dimensionless quantity [197-198]. The acoustoelastic constant is reported to decrease linearly as the amount of carbide (cementite) phase is increased in the steel alloys. The value of AEC (0.069 ns/MPa)for DMR-249A steel being lower than commonly used 304L stainless steel (0.588 ns/MPa) [151-153] shows that the AEC is less sensitive for BCC structure as compared to FCC crystalline structure. This is attributed to higher atomic packing factor of FCC (austenitic steels) than BCC (ferritic steels).

5.2.2 Comparison of residual stress measurements for SMAW and G-TAW processes using ultrasonic L_{CR} wave mode

The surface longitudinal stress distribution across the weld joints fabricated by SMAW and A-GTAW processes are shown in Figs. 5.8(a) and (b), respectively. The residual stresses varied significantly in both the weld joints with maximum tensile residual stresses near the fusion boundary.

For the SMAW weld joint, the maximum tensile stress of 450 MPa is observed at a distance of 20 mm away from the weld centre. The maximum compressive stress measured is 150-180 MPa at 45-50 mm away from the weld centre. There is a changeover from tensile to compressive stress at about 25 mm away from the weld centre on both sides of the weld. In the A-GTAW joint, a maximum tensile stress of 510-520 MPa is observed at 15-25 mm away from the weld centre. The transition from tensile to compressive stress is observed at about 40 mm away from the weld centre on both sides of the weld joint. The maximum compressive stress obtained is 140-170 MPa at 45-50 mm away from the weld centre.The measured tensile and compressive residual stresses and the distance from weld line for changeover from tensile to compressive stresses are given in Table 5.1.

The location and magnitude of maximum compressive stress in both the SMAW and A-GTAW joints was found to be similar.Despite the variation in heat input and number of passes in the two different welding processes, the residual stress profiles across the weld joints were observed to be similar. The distance of changeover of residual stresses from tensile to compressive for A-GTAW was observed to be more as compared to the SMAW weld joint.

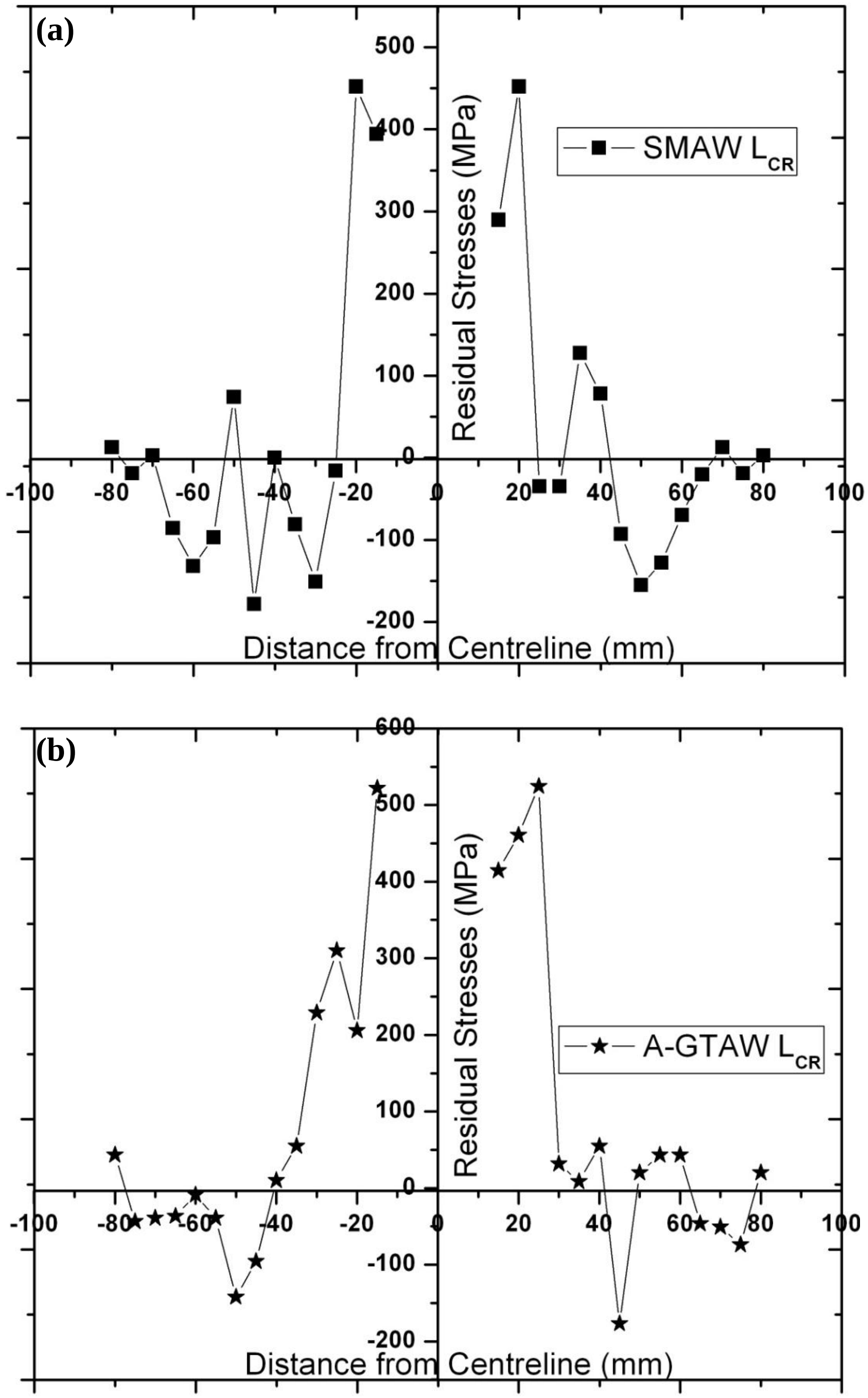

Fig. 5.8 Residual stress profiles measured using ultrasonic L_{CR} technique for the weld joints fabricated using (a) SMAW and (b) A-GTAW

Table 5.1 Residual stress values obtained using XRD and L_{CR} techniques

SNo	Residual Stresses on Either Side of Weld Center (WC)	SMAW		A-GTAW	
		XRD	L_{CR}	XRD	L_{CR}
1	Maximum Tensile RS (MPa)	285-315	450	430-490	510-520
2	Location of Max Tensile RS from Weld Center (mm)	15	20	15-20	15-25
3	Maximum Compressive RS (MPa)	160	150-180	40	140-170
4	Location of Max Compressive RS from Weld Center (mm)	40	45-50	40	45-50
5	Changeover from Tensile to Compressive from Weld Center (mm)	30	25	35	40

5.2.3 Comparison of residual stress measurements for SMAW and A-GTAW processes using XRD technique

The change in residual stress distribution across the SMAW and A-GTAW joints with distance from weld centre line as measured by XRD are shown in Figs. 5.9 (a) and (b), respectively. The maximum tensile stress measured by XRD for SMAW joint is observed to be 285-315 MPa at 15mm away from the weld centre. The transition from tensile to compressive stress is observed at about 30 mm away from the weld centre on both sides of the weld joint. The maximum compressive stress obtained is 160 MPa at 40 mm away from the weld centre. In A-GTAW Joint, the maximum tensile stress of 430-490 MPa is observed at 15-20 mm away from the weld centre. The transition from tensile to compressive stress is observed at about 35 mm away from the weld centre on both sides of the weld joint. The maximum compressive stress obtained is 40 MPa at 40 mm away from the weld centre.The location of maximum tensile/ compressive residual stresses and the changeover from tensile to compressive stresses was found to be similar for both welding processes. The differences in maximum tensile and residual stresses generated for SMAW and A-GTAW processes is attributable to the difference in heat input and manual/auto operation in the processes.The comparison of residual stresses as measured by XRD technique is given in Table 5.1 above.

5.2.4 Comparison of residual stress measurements by XRD and UT

The comparative graphs of the residual stress profiles obtained from XRD andUT techniques of SMAW and A-GTAW joints are shown in Fig. 5.9(a-b). The measured values for variation in residual stress built up by both methods showed similar stress profiles.

The residual stress measurements reported by various researchers in available published literature confirm the existence of maximum tensile stress upto yield stress magnitude of the base material. The tensile residual stresses of 250 MPa for 2219 Al, 300 MPa in 316LN steel, 320 MPa in 316L and 750 MPa in Z8CD12 steels have been reported [198-201]. The maximum tensile residual stress found in the present investigations is comparable to the yield stress of DMR-249A steel.

The correlation of measured values by XRD and L_{CR}methods plotted for the points of measurement in the two joints i.e. for distance of 15 mm to 40 mm on both sides of weld centreline is shown in Fig. 5.10 and Table 5.2. The observed slopes of 1.17 and 0.77 for SMAW and A-GTAW weld joints respectively show that the residual stress values as measured by XRD and L_{CR} method have similar profile and are comparable. The minor variations exist due to the difference in residual stress gradients for different welding techniques and inherent volume of inspection of surface and bulk residual stresses of respective technique. The minor deviation in the values measured by XRD and L_{CR} for A-GTAW is due to the high heat input per weld pass for the process. The high heat input leads to composite factors of peak temperatures, heat dissipation, cooling rate and thermal gradients resulting in complex residual stress patterns.

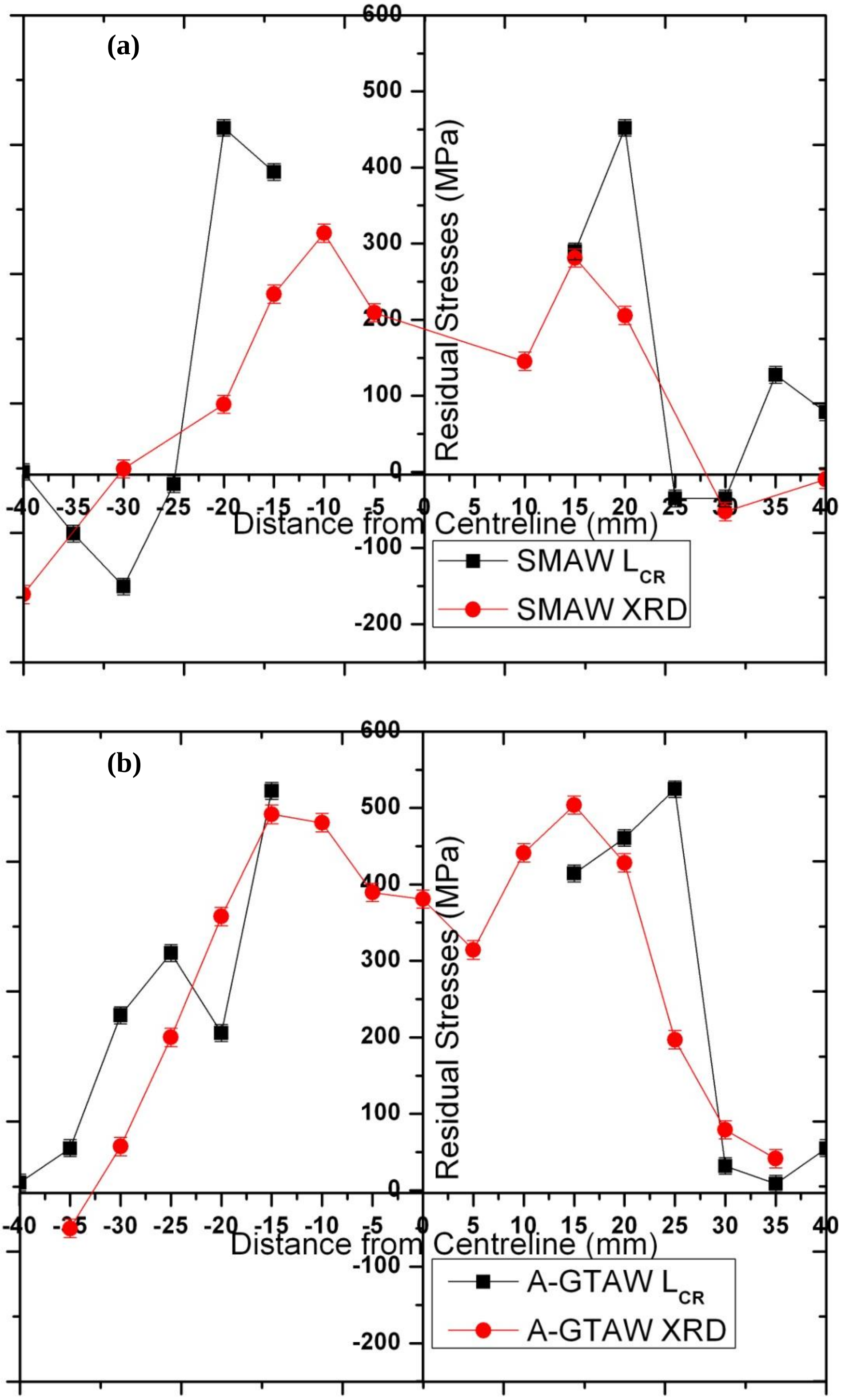

Fig. 5.9 Comparison of residual stress profiles measured using XRD and ultrasonic L_{CR} techniques for the weld joints fabricated using (a) SMAW and (b) A-GTAW process

The assumed depth of penetration of XRD is ofthe order of 5 to 30 microns.The errors associated in residual stress measurements by XRD method are ± 20 MPa. For the L_{CR} measurements, residual stress is the average value over the wavelength of material in which L_{CR} wave penetrated. For 2 MHz frequency, effective depth of penetration for L_{CR} wave is approximately 3 mm[202]. The corresponding error for L_{CR} was calculated to be 11MPa approximately.

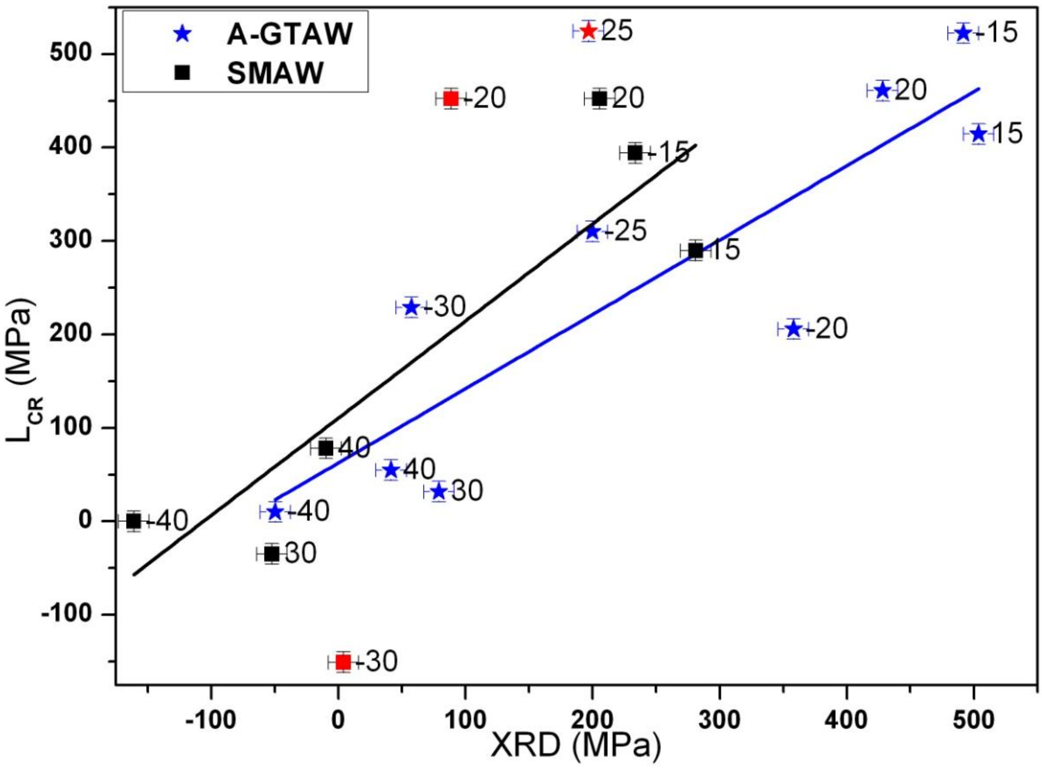

Fig. 5.10 Correlation of residual stress values obtained by XRD andL_{CR}techniques

Table 5.2 Correlation of residual stress values obtained by XRD andL_{CR}techniques

	SMAW	A-GTAW
Resi. Sum of Sq.	353.59589	524.34686
Adj. R-Sq	0.75608	0.754
Intercept	110.49838	62.57185
Slope	1.03918	0.79472

5.3 Conclusion

To the best of the author's knowledge, this is a first of its kind approach to compare the residual stresses estimated by ultrasonic L_{CR} and XRD techniques in welded joints of indigenously developed DMR-249A steel.The conclusions based on investigations conducted to compare the residual stresses and mechanical properties of SMAW and A-GTAW joints of DMR-249A steelare summarized as follows:-

(a) The AEC for DMR-249A steel was about0.069 ns/MPa.With application of the derived AEC,the use of L_{CR} waves for assessment of longitudinal residual stresses in DMR-249A naval steel weld joints made by SMAW and A-GTAW processes has been demonstrated.

(b) The residual stress developed in SMAW and A-GTAW jointswere observed to be similar.

(c)The stress values as measured by XRD and L_{CR}methods were found to be comparable.

.

Chapter 6. Microstructure characteristics and mechanical properties

The objective of the investigations discussed in this chapter is to compare the effect of SMAW, SAW, FCAW and A-GTAW processes on weld metal microstructure and mechanical properties in DMR-249A weld joints. Weld joints made from DMR-249A steel were fabricated using four different arc welding techniques viz. SMAW, SAW, FCAW and A-GTAW. The research includes the microstructural studies and analysis of micro-hardness, tensile and impact tests to evaluate weld metal in SMAW, SAW, FCAW and A-GTAW processes for DMR-249A steel. The microhardness, impact and tensile tests of the welded joints were conducted as per ASTM Standards [54-57]. The microstructural studies were undertaken using an optical microscope and fractography was carried out with a SEM. The optical, SEM and EBSD micrographs showed that the microstructures of the arc welded joints consisted of grain boundary ferrite, Widmanstatten ferrite with aligned second phase along with veins of ferrite, acicular ferrite, polygonal ferrite and microphases as compared tothe predominantly fine grained equiaxed ferrite microstructure of DMR 249A steel. Inclusion studies were undertaken to ascertain the types and numbers of inclusions associated with the different arc welding processes and the role of inclusions on impact toughness of weld metal. The tensile properties of DMR-249A steel and arc welded joints (cross weld samples) were comparable. The weld joints were found to have a minor increase in yield strength with corresponding decrease in ductility. The welded samples were observed to have low toughness at sub-zero temperatures. The factors contributing towards reduction in impact toughness at sub-zero temperatures compared to room temperature have alsobeen discussed.

6.1 Experimental details

6.1.1 Fabrication of weld joints

The chemical composition of the filler material electrodes used in the SMAW/SAW/FCAW processes is given in Tables 6.1. For each weld joint, two plates of dimensions 300x120x10 mm^3 were used. After carrying out the weld joint edge preparation (Square Butt for A-GTAW and 70^o V-Grove for SMAW/SAW/FCAW) (Fig 6.1), the plates were tack welded at ends with run-off plates at ends.Welding was done to make weld joint of 300x240x10 mm^3 for each process (Fig 6.2) (welding parameters are given in Table 6.2).

Table 6.1 Chemical composition (wt.%) of consumables/electrode for SMAW/SAW/FCAW processes

C	Mn	Si	Ni	Al	Nb	V	Ti	S/P/Sn/Cr/Mo/W/V	N (ppm)
0.02-0.04	1.10-1.50	0.1-0.25	2.2-2.5	0.01-0.02	<0.002	0.02	0.02	<0.010	15

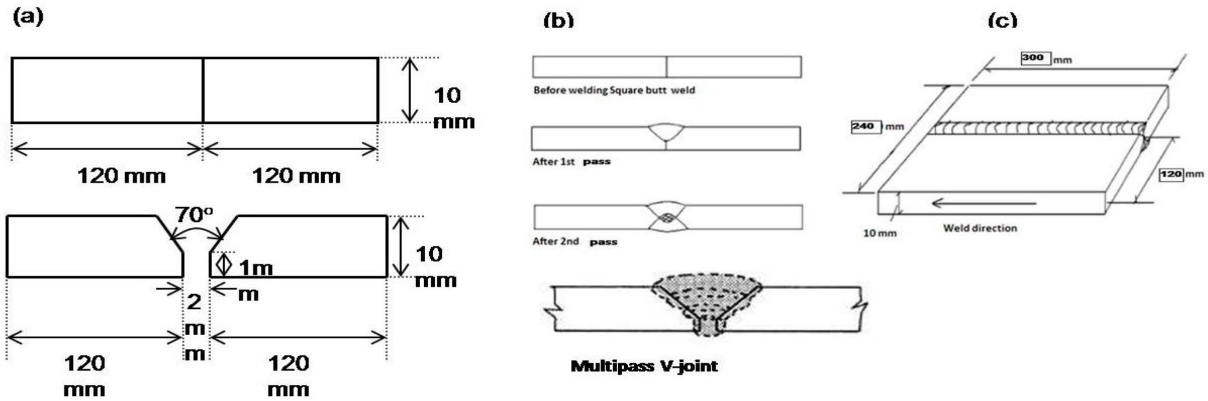

Fig 6.1 Weld joints (a) Square and V edge preparation (b) square-double pass and V-multi pass (c) Welded Specimen (schematic)

Table 6.2 Welding parameters for weld joints

Welding Process	Current (A)	Voltage (V)	Speed (mm/sec)	No. of Passes	Heat Input for Weld Length (kJ/mm)	Heat Input for Final Pass (kJ/mm)
SMAW	120	25	1.5	5	10	2
SAW	485	30	7.5	4	7.76	1.94
FCAW	155	25	3.33	6	7.0	1.16
A-GTAW	270	20	1	2	10.8	5.4

Fig 6.2(a) SMAW Joint Prepared at Lab

Fig 6.2(b) SAW Joint Prepared at Shipyard

Fig 6.2(c) FCAW Joint Prepared at Shipyard

Fig 6.2(d) A-GTAW Joint Prepared at Lab

Fig 6.2 SMAW, SAW, FCAW and A-GTAW Process Weld Joints
(300x240x10 mm^3each)

6.1.2 Microstructure and mechanical tests

Metallographic samples of size 20x10x10 mm^3 were cut (transverse to welding line) to carry out microstructural studies of the weld joint. Samples were polished from 80 to 2400 grit SiC paper followed by 1 μm diamond paste to obtain mirror finish. The inclusion studies of unetched specimens were carried out at 100x magnification using an optical microscope, followed by SEM and EDS. The specimens were etched using 2% Nital solution, and optical microscopy was carried out to ascertain the weld bead profiles and changes in microstructure of the base, HAZ and weld metal. The macrostructure of the SMAW, SAW, FCAW and A-GTAW arc welded joints at are given in Fig 6.3. For EBSD, the specimens were mechanically ground by using 80 - 4000 grade SiC paper, polished with 0.5 μm diamond suspension and then 60 nm colloidal silica suspension. The EBSD maps were collected using a Zeiss Ultra Plus field emission gun (FEG) SEM, equipped with an Oxford Instruments CHANNEL5 EBSD system. The parameters used for indexing were 8 bands of detection and 0.50 μm step size.

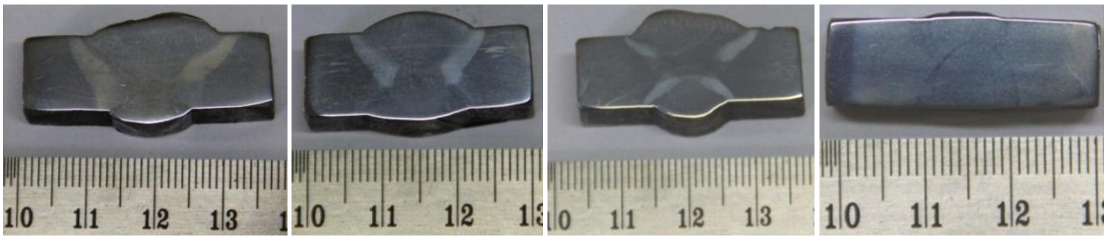

(a) SMAW (b) SAW (c) FCAW (d) A-GTAW

Fig 6.3 Macrostructure photos of DMR-249Asteel arc welded joints

The microhardness, Charpy impact (55x10x10 mm^3) and tensile (gauge length 260 mm, gauge diameter 4 mm) tests of the welded joint were conducted as per ASTM Standards E384, E23 and E8 respectively [208-209, 197]. The schematic of tensile and impact samples is given in Fig 6.4.

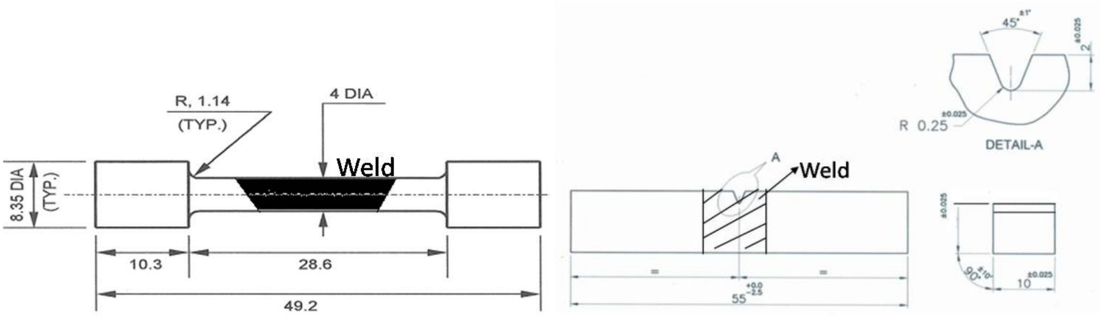

(a) Tensile test specimen (b) V-notch Charpy impact test specimen

Fig 6.4 Schematic diagram of tensile and impact test specimen

The chemical analysis of the weld joints was carried out using Jobin Yuon Make (JY 132F) spart atomic emission spectrometer. The conductive specimen was used as cathode with counter electrode as tungsten with a gap of 3 to 4 mm. 10kV voltage was used to ionize and bombarding argon gas. Photons transmitted from ejected atoms during transformation from an excited to ground state were passed through a quartz grating for refraction/dispersion analysis. The simultaneous multi elemental analysis was carried out post calibration, re-calibration, mini-calibration and analysis. The oxygen and nitrogen percentages were analyzed by using a Non Dispersive Infra Red (NDIR) analyzer.

6.2 Results and Discussion

6.2.1 Chemical composition analysis

The chemical composition of the weld metal for each of the weld joints is given in Table 6.3.The oxygen levels of the weld metals are influenced by many factors such as the amount of deoxidizers present (silicon, manganese, aluminum, etc.), the types of welding materials used, the welding process and the welding conditions [60, 210]. Weld metal deposited with flux shielded processes or with active gas shielded processes generally contains more oxygen than welds deposited with inert gas shielded processes. Oxygen percentage was found to be in the range of 0.06 to 0.07 for SMAW, SAW and FCAW joints and for the A-GTAW weld joint the oxygen percentage was observed to be 0.126. The higher oxygen content in A-GTAW joint is attributed to the activated flux which enhances the concentration of surface active elements that produce the required reverse Marangoni flow for achieving higher depth of penetration in A-GTAW[22,211-212].

Table 6.3 Chemical Composition (wt.%) of weld metal

Process	C	S	P	Mn	Si	Al	Ni	Nb	V	Ti	Cu/Cr	O%	N%
SMAW	0.053	0.01	0.016	0.84	0.15	0.01	2.27	0.02	0.02	0.02	<0.02	0.06	0.005
SAW	0.066	0.01	0.013	1.22	0.20	0.01	1.22	0.02	0.02	0.02	<0.02	0.06	0.004
FCAW	0.050	0.01	0.012	0.63	0.09	0.01	2.06	0.02	0.02	0.02	<0.02	0.07	0.003
A-GTAW	0.088	0.01	0.016	1.40	0.24	0.03	0.74	0.03	0.02	0.02	<0.02	0.126	0.002

In general, a welding process can be classified as low, medium, or high nitrogen if the amount of nitrogen in the weld metal deposit is less than 70 ppm, between 70 to 120 ppm, or greater than 120 ppm, respectively. Generally, self shielded welding processes are observed to have higher nitrogen pickup of 70 to 370 ppm whereas gas shielded processes have lower nitrogen pickup of range 30 to 140 ppm [213-215]. Nitrogen percentage was found to be similar, with a small range of 0.002 to 0.005%, for all weld joints (SMAW, SAW, FCAW and A-GTAW). The reduced nitrogen pickup in the self shielded (SMAW, SAW, FCAW) and gas shielded (A-GTAW) weld joints is a consequence of adherence to standard welding procedures and maintaining proper shielding during fabrication of joints.

6.2.2 Inclusion analysis

Non metallic oxides like AI_2O_3, SiO_2,MnO, TiO, Ti_2O_3, $CaCO_3$etc. are known to exist in weld metal in the form of inclusions. The inclusions in weld metals can be due to the entrapment of slag or flux in the weld metal (can be termed as primary inclusions) or due to the formation or entrapment of deoxidisers like aluminum, silicon,manganese, and titanium present in base metal or added for deoxidation and alloying of weld metal (can be termed as secondary inclusions). The primary inclusions can be associated with the welding technique and process employed for welding and usually occur as defects in welding processes that use flux, such as shielded metal arc welding, flux-cored arc welding, and submerged arc welding, but can also occur in gas metal arc welding.The secondary inclusions exist as an integral part of weld metal irrespective of the welding process and depend on the weld chemistry, heat input, number of passes and weld metal solidification rate. The consecutive stages in formation and segregation of secondary inclusions are shown in Fig 6.5.

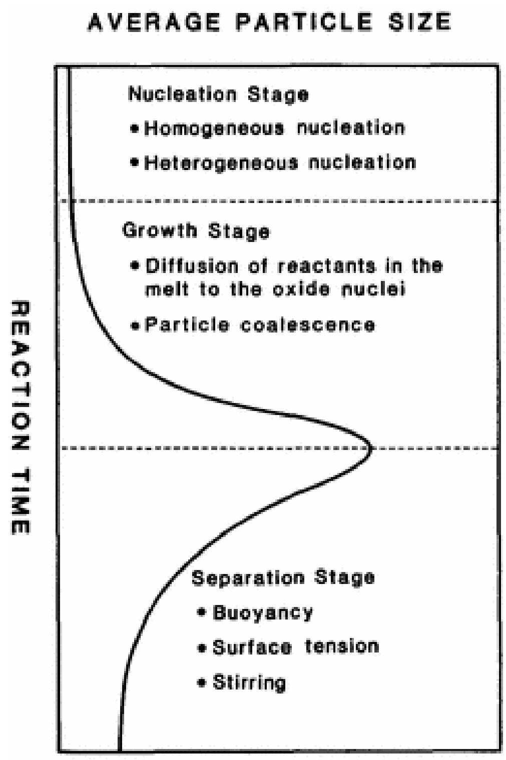

Fig 6.5Three consecutive steps in formation of deoxidising oxides

Austenite grain size, cooling rate and the distribution of nonmetallicinclusions are the dominant factors in acicular ferritenucleation, which has a significant influence on the impacttoughness of weld metals [216-219]. Amongst these factors, the intragranularnucleation of acicular ferrite on the non-metallic inclusionsis extensively reported. Also, the potential nucleation sitesfor the formation of acicular ferrite are strongly controlled by theinclusion size distribution, density and chemistry.Ito and Nakanishi [220], Koukabi, *et al.* [221], and Kanazawa, *et al.* [222], suggested that TiN was an effective nucleating agent for acicular ferrite during the austenite decomposition. Heintze and McPherson [223] reported the same findings, that TiN acted as a weld metal grain refining agent and that the effectiveness of titanium addition is enhanced in the presence of aluminum and boron. Mori, et*al.* [224], showed that an increase in nitrogen in the weld metal did not bring any microstructuralchange except for an increase in proeutectoid ferrite. Instead, they demonstrated that titanium containing oxides can nucleate acicular ferrite within the austenite grains. Pargeter [225]and Devillers ef *al.* [226] observed that grain boundary ferrite and ferrite sideplates are usually associated with inclusions with manganese and silicon, with or without sulfur. Acicular ferrite appeared to be associated with aluminum-bearing particles.Cochrane et al.[227] and Sagesse, etal.[228] suggested that the effectiveness of inclusions on phase transformation behavior may depend ontramp elements (either in the form of surface coating or other ways) rather than on the macroanalysis of the inclusions.The removal of inclusions from a weld deposit, with other features constant, causes a change in the microstructure from acicular ferrite to bainite [229].An increase in the number density of austenite grain surface nucleation sites (relative to intragranular sites) causes a transition from acicular ferrite to bainite [230]. But the number of inclusions in a weld joint is not conclusive evidence of higher acicular ferrite content. Depending on the sizedistribution, the partition of the inclusionsto the boundary and to the interior of thegrains may be different. An optimuminclusion size distribution to obtain a largevolume fraction of acicular ferrite is theone that contains a low percentage offine size particles, with the inclusion populationsizes resembling a normal, orclose to normal, distribution. The combinationof large austenite grains and highintragranular inclusion density is the keyto obtaining a refined microstructure.

The micrographs of DMR-249A base steel and weld metals of different welding techniques in the unetched condition are shown in Fig 6.6. The number of inclusions in the base metal were noticeably fewer than in the weld metals. It is imperative to note that the inclusion content in the weld metals was found to vary appreciably with the welding techniques. The distribution of inclusions in the weld metals was uniform in all the welding techniques employed, except that the SAW weld metal exhibited a greater number of inclusions and agglomeration behavior. The inclusion size, area fraction and number density were analysed using image analysis software (ImageJ) and the results are summarized in Table 6.4, and represented by bar charts in Fig 6.7 and Fig 6.8.

The examination of inclusions in weld metal associated with SMAW, SAW, FCAW and A-GTAW processes indicated the least number of inclusions in the SMAW joint of about 16.1 numbers per mm^2 and area fraction of 0.186. The SAW joint was evaluated to have numerous small and large inclusions, predominantly spherical, in clusters which are characteristic of the SAW welding process due to fast solidification of the weld pool leading to entrapment of more inclusions. The FCAW joint was observed to have more finer inclusions of spherical and elongated shapes. The inclusions found in the A-GTAW joint were largely scattered and spherical in shape.

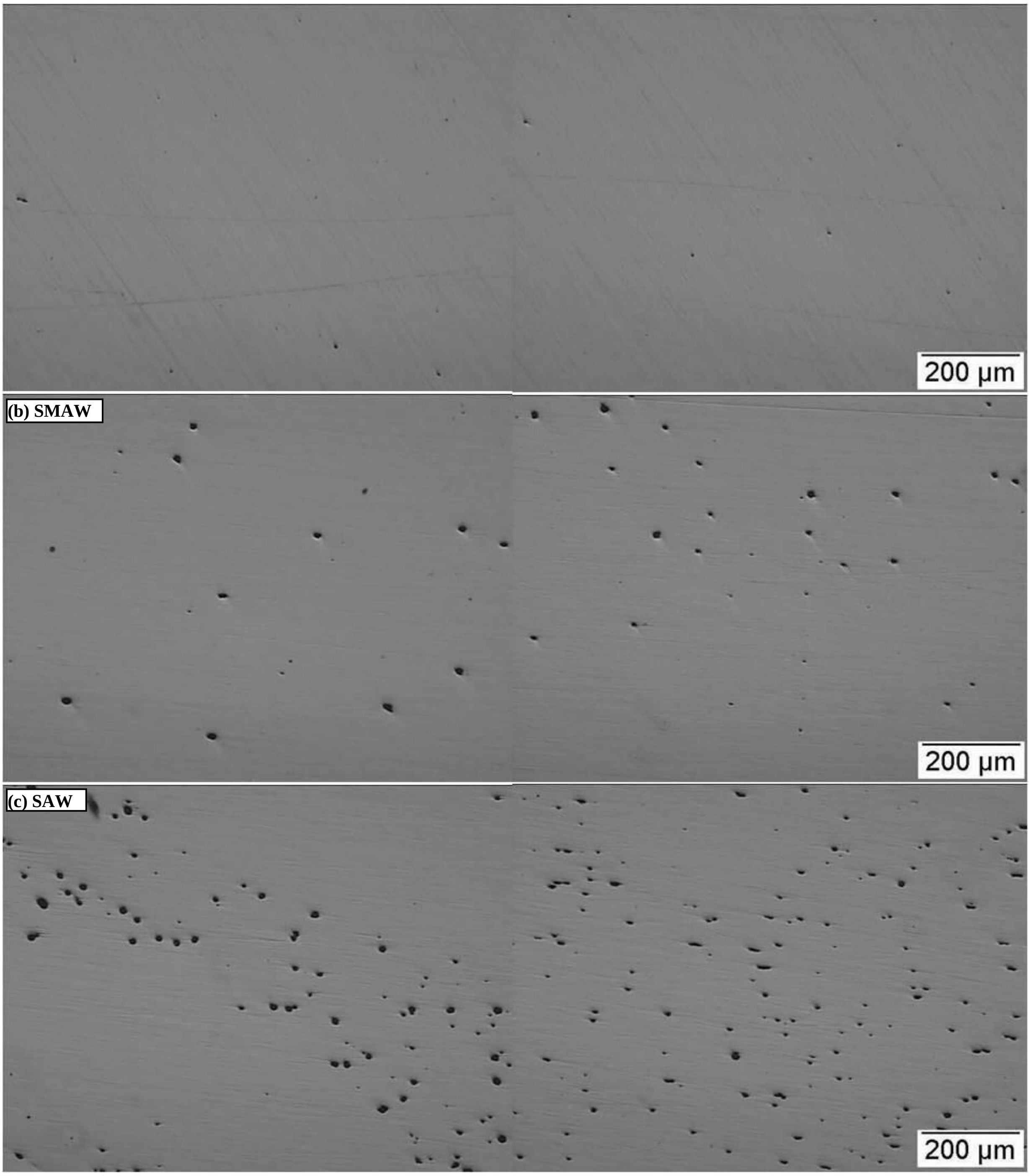
200 µm
(b) SMAW
200 µm
(c) SAW
200 µm

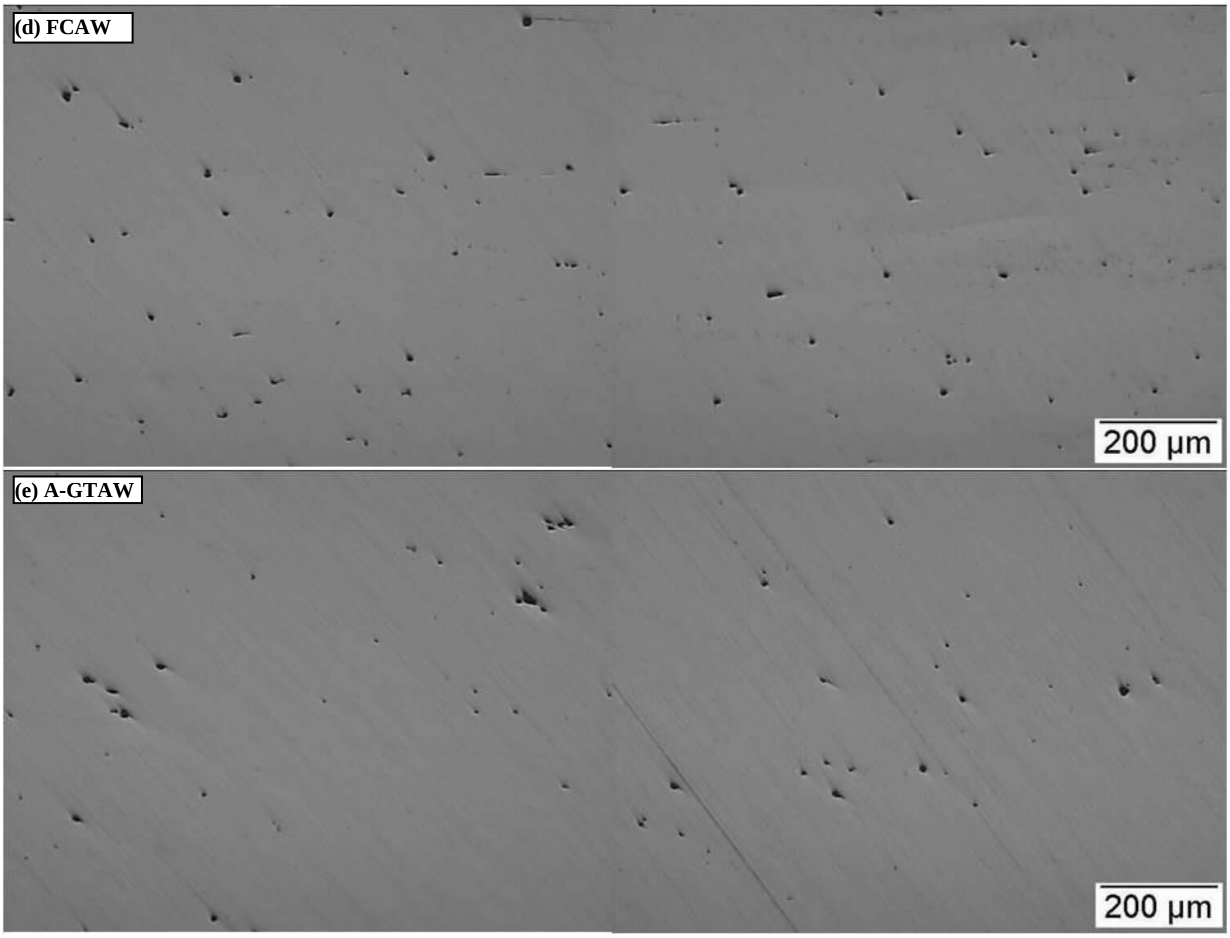

Fig 6.5 Optical micrographs (100X) of inclusions in as-polished samples of DMR-249A base steel and weld metals of SMAW, SAW, FCAW and A-GTAW weld joints

Table 6.4 Inclusion characteristics in SMAW, SAW, FCAW and A-GTAW joints

	Mean Size (µm)	Numbers per mm^2	Area Fraction	Distribution
SMAW	11.16	16.1	0.186	Large spherical
SAW	9.66	54.23	0.529	Small and large predominantly spherical, clustered
FCAW	4.48	41.8	0.271	Large, spherical and elongated, scattered
A-GTAW	6.67	26.87	0.257	Small and large, spherical, scattered

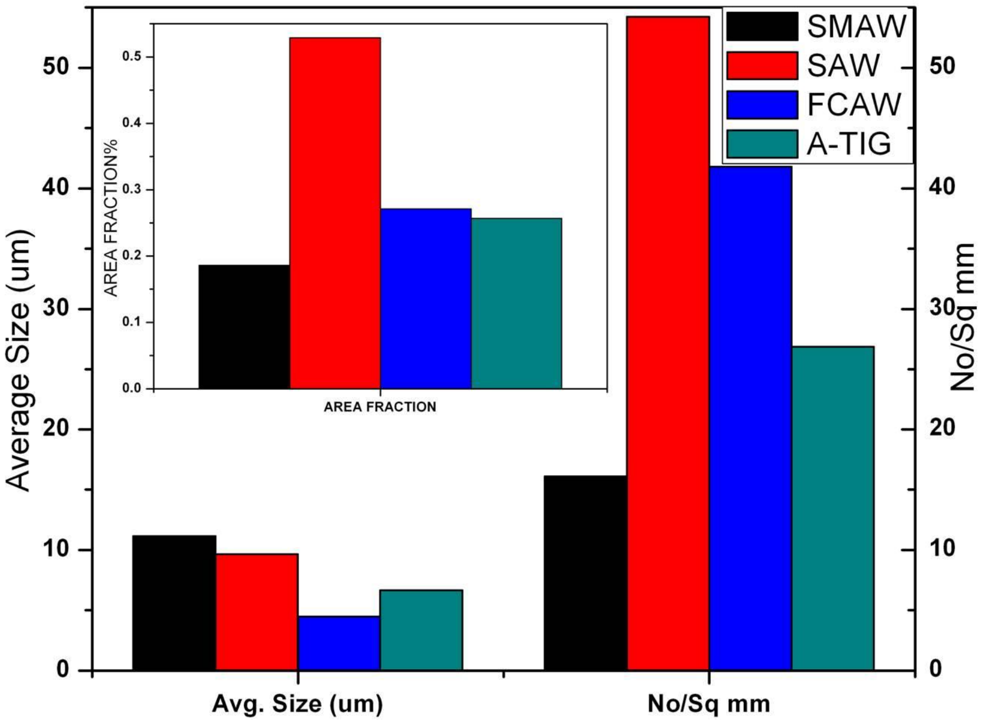

Fig 6.6 Bar chart for mean size, area fraction and number of inclusions per mm in arc welded joints of DMR-249A steel

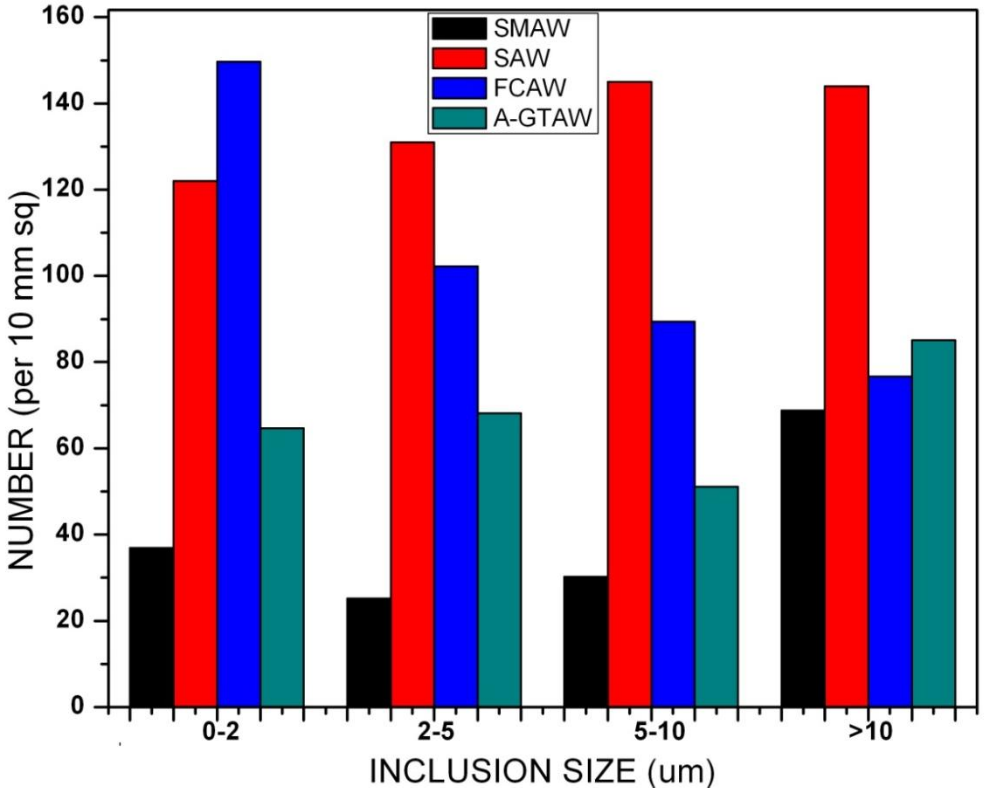

Fig 6.7 Histogram of numbers of inclusions of varying sizes in different arc welded joints of DMR-249A

The area fraction and the number of inclusions per mm^2 indicated maximum inclusions in SAW followed by FCAW, A-GTAW and SMAW. In SAW weld deposits, the volume fraction of non-metallic inclusions is considerably higher than that in other weld processes. The contribution of primary inclusions is likely to be more in SAW in comparison with other welding techniques due to contact of excess amount of flux with the weld metal. The solidification of submerged arc weld metal is extremely fast and because of the limited time available for growth and separation of the deoxidizing particles, the secondary inclusions may become trapped during segregation stage (Fig 6.5). The contribution of primary inclusions contained in FCAW weld metal is lower than SAW weld metal as the amount of flux interacting with the weld metal is comparatively less but higher than that in SMAW weld metal. The contribution of primary inclusions in SMAW weld metal is considered to be least compared to SAW and FCAW weld metals due to the welding arc force leading to minimal interaction of weld metal with the flux that exists on external surface of the filler material. The A-GTAW welding technique is considered to be the cleanest process amongst all the arc processes presently being studied. The flux is applied in A-GTAW process for enhancing the depth of penetration and does not contribute much towards formation of primary inclusions. The examination of inclusions in weld metals associated with SMAW, SAW, FCAW and A-GTAW processes indicated presence of scattered inclusions of bigger size in SMAW weld metal. The SAW weld metal was evaluated to have numerous small and large inclusions, predominantly spherical, in clusters which are characteristic of SAW welding process due to fast solidification of weld pool leading to entrapment of more inclusions. The FCAW weld metal was observed to have more of finer inclusions of spherical and elongated shapes. The inclusions found in A-GTAW weld metal were largely scattered and spherical in shape. The lowest number of inclusions was found in SMAW weld metal of about 16 numbers per mm^2 and area fraction of 0.186. The number density and area fraction of inclusions were higher in the SAW amongst all the arc processes being considered. Though the number density of inclusions in FCAW was found to be more than A-GTAW weld metal, the area fraction of inclusions in FCAW and A-GTAW were found to be comparable as the inclusions in FCAW weld metal were finer than the inclusions in A-GTAW weld metal.

The mean size (average size) of inclusions in weld metals shows the maximum value in SMAW weld metal followed by SAW, A-GTAW and FCAW (Table 6.4 and Fig 6.6). The number per unit area and the area fraction of SMAW inclusions is observed to be the least and the higher mean inclusion size is due to the substantial variation in size of inclusions present in SMAW and presence of more number of bigger inclusions compared to inclusions of smaller sizes (Fig 6.7). The mean size of the inclusions in SAW weld metal was measured to be higher than in FCAW and A-GTAW. The inclusions present in FCAW weld metal being finer, had smaller mean size than A-GTAW weld metal inclusions.

The analysis of chemical composition of weld metals revealed higher percentage of deoxidising agents Al, Si and Mn in A-GTAW weld metal (Table 6.3). The oxygen percentage was also measured to be the highest for A-GTAW weld metal, primarily due to the application of activated flux as discussed in Chapter 3. The more numbers and higher area fraction of the inclusions in A-GTAW weld metal as compared to SMAW weld metal can be associated with the presence of additional deoxidising agents and oxygen in the A-GTAW weld metal. It has been reported thatmore oxygen should relate to a higher volume fraction of inclusions [231] and also that oxides inclusions may be detrimental to weld metal toughness through the initiation of brittle fracture [232-233]. The numbers of inclusions and area fraction for FCAW weld metal was observed to be marginally higher than A-GTAW weld metal.

This can be attributed to the fact that the inclusions in A-GTAW process are primarily secondary inclusions whereas in FCAW process there is probability of entrapment of primary inclusions alongwith secondary inclusions due to the use of flux and also because of faster cooling associated with higher speed of welding. But the number of entrapped inclusions in FCAW is much lesser than that in SAW process. The correlation of percent concentration of Al, Si, Mn and O with the inclusion numbers and area fraction in SMAW, SAW, FCAW and A-GTAW weld metals has been shown in Fig 6.8.

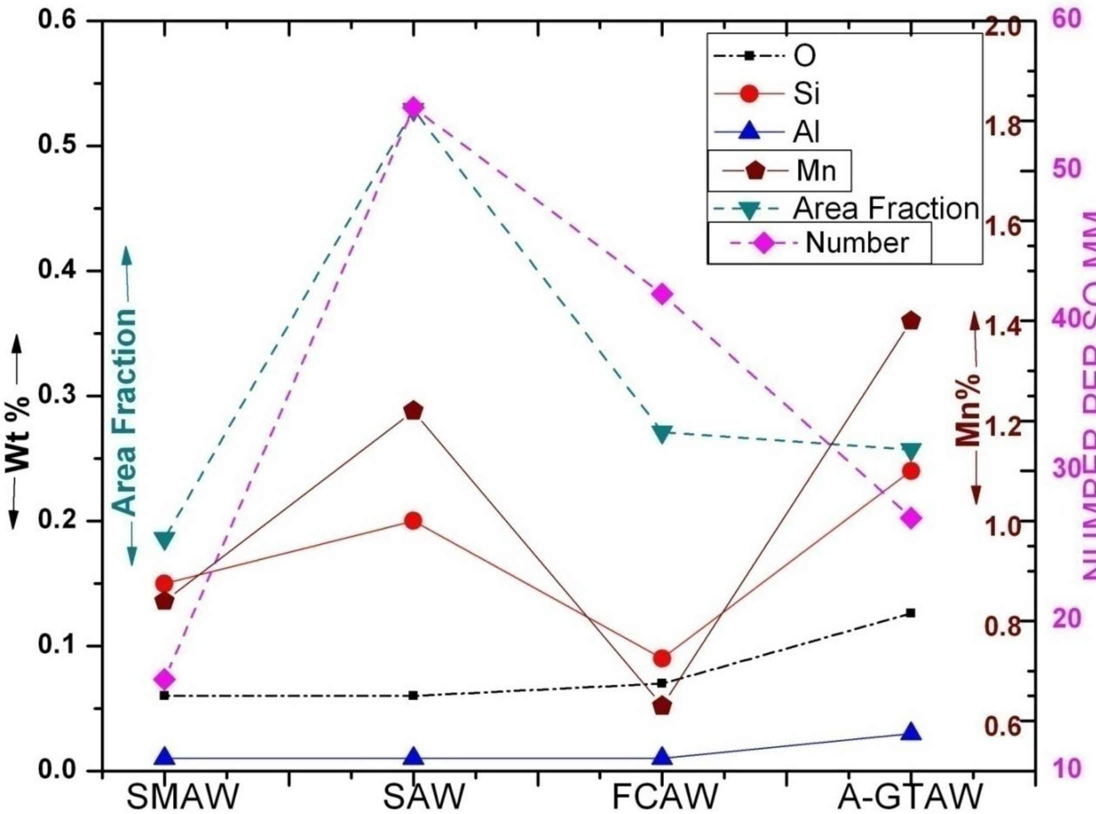

Fig 6.8 correlation of percent concentration of Al, Si, Mn and O with the inclusion numbers and area fraction in SMAW, SAW, FCAW and A-GTAW weld metals

The SEM and EDS analysis of the inclusions was carried out to confirm the chemical composition of the inclusions. The SEM micrographs and EDS patterns are given in Fig 6.9

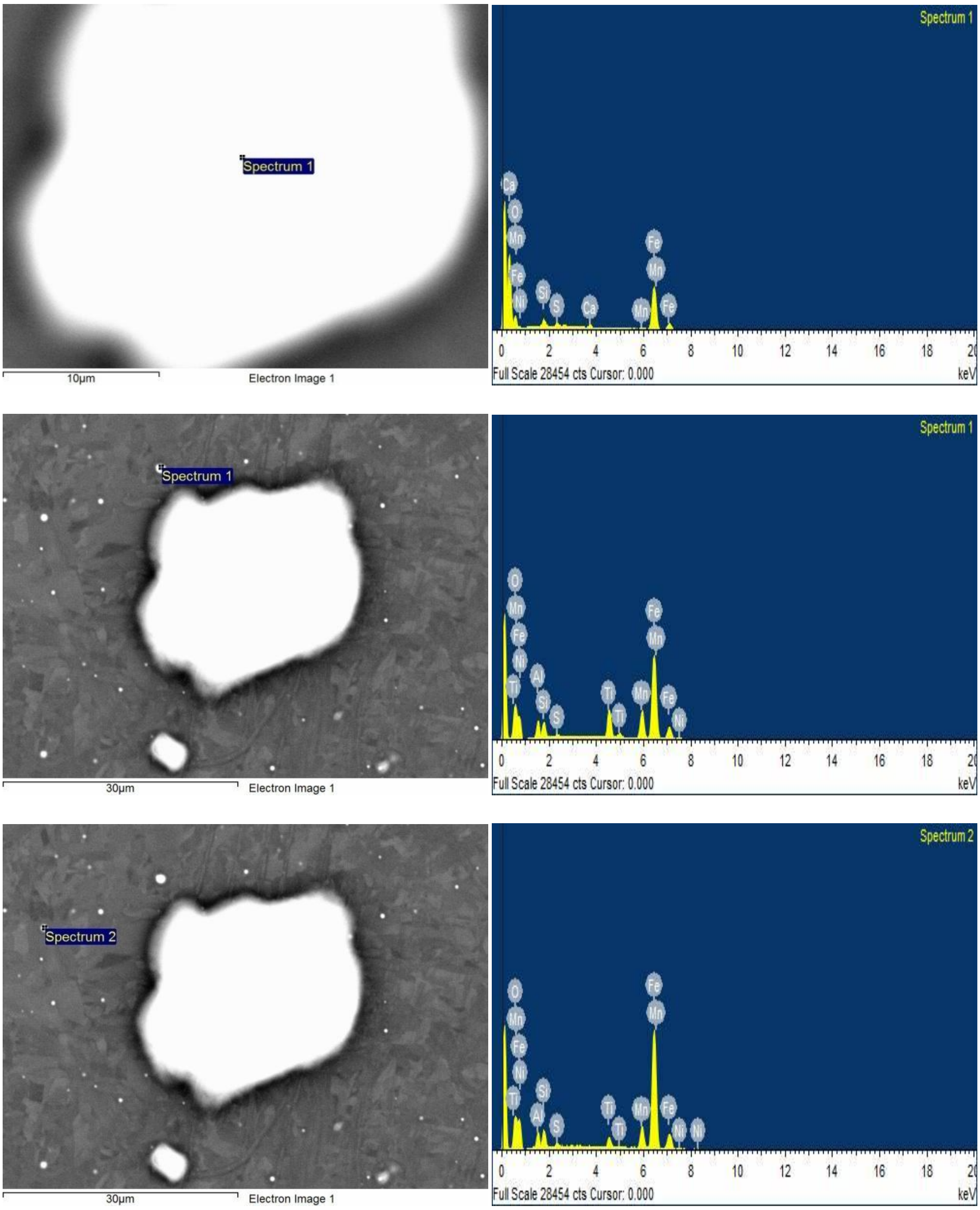

Fig 6.9 (a) SEM and EDS of inclusions in SMAW weld metal

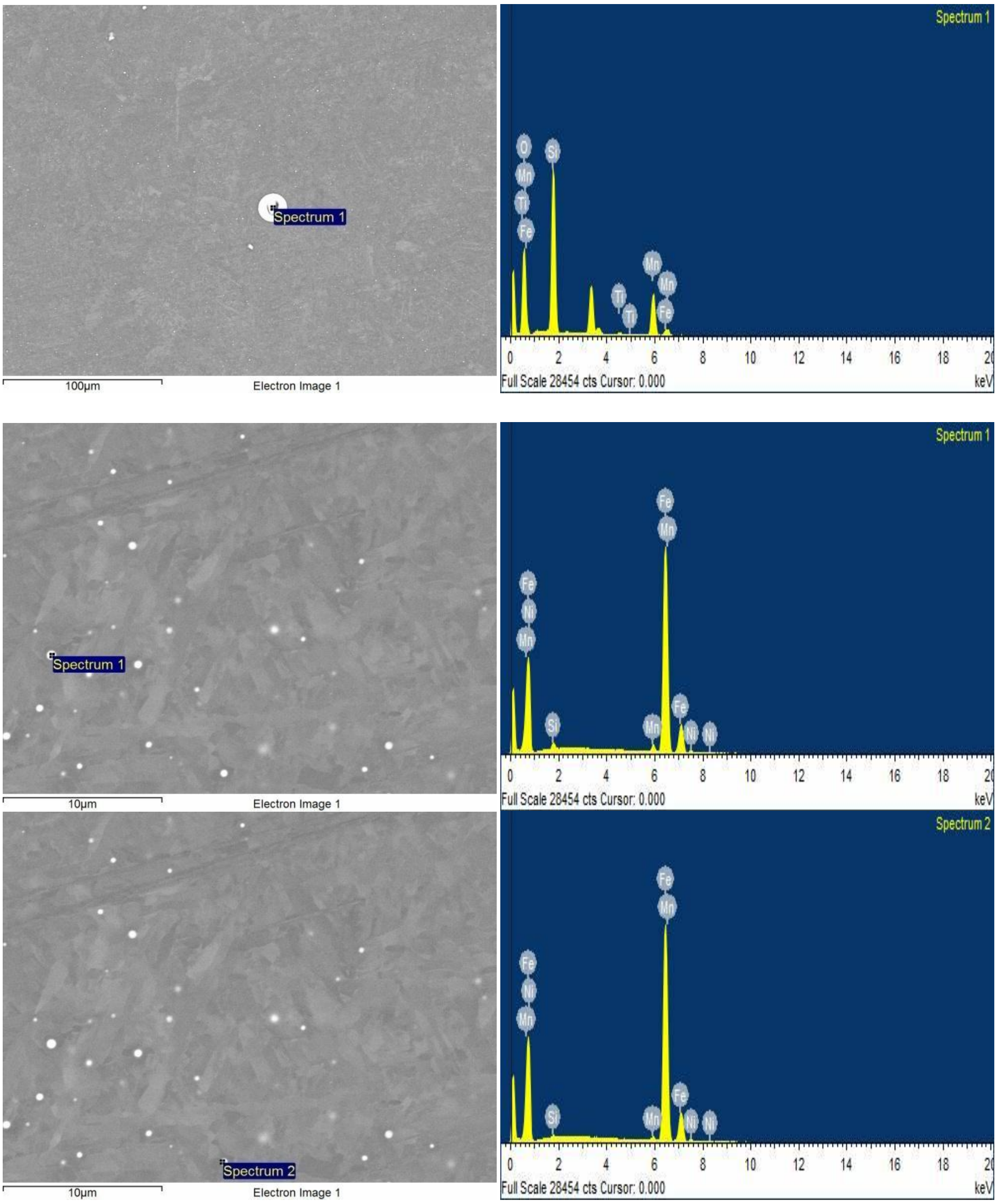

Fig 6.9 (b) SEM and EDS of inclusions in SAW weld metal

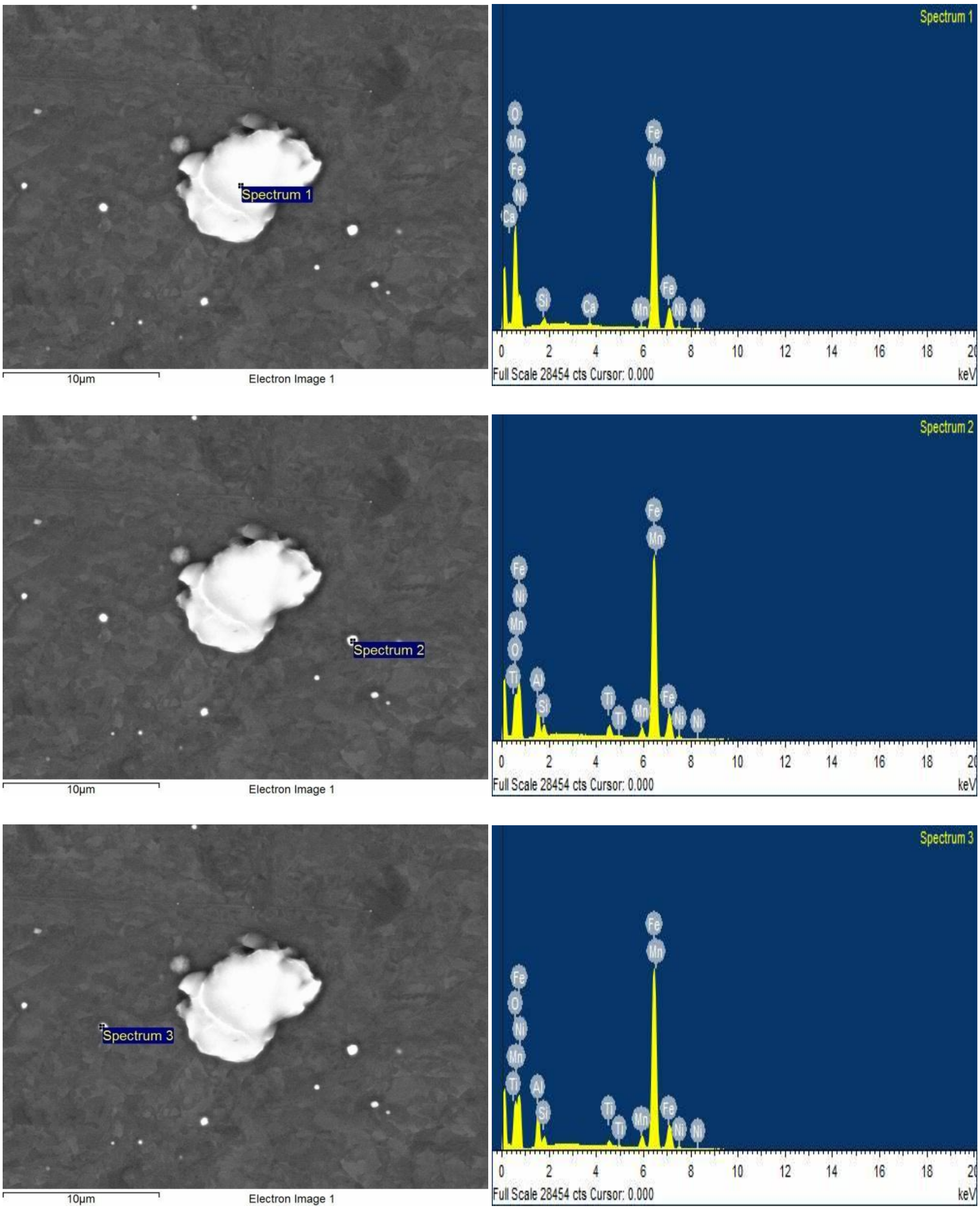

Fig 6.9 (c) SEM and EDS of inclusions in FCAW weld metal

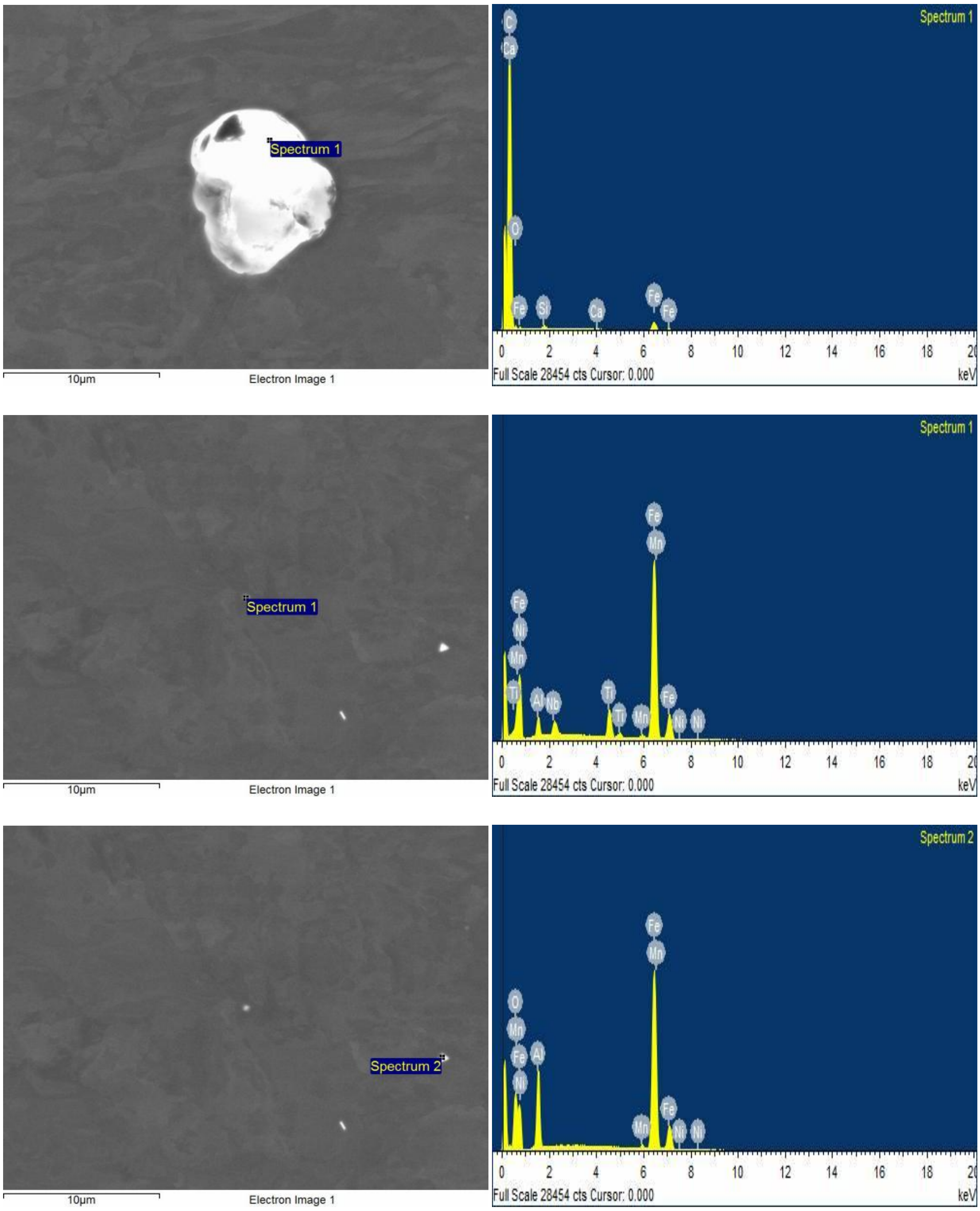

Fig 6.9 (d) SEM and EDS of inclusions in A-GTAW weld metal

The SEM micrographs of inclusions in weld metal of different arc welded joints showed that the maximum number of micro inclusions of size from 0.1 µm to 0.6 µm existed in SMAW and SAW weld metals. The inclusion density in FCAW weld metal was found to be lower and in A-GTAW was observed to be the least amongst all the welding processes. The micro inclusions of SMAW, FCAW and A-GTAW were found to contain Al, Si, Mn and Ti oxides whereas micro inclusions in SAW weld metal were observed to be predominantly Si and Mn oxides and traces of Al or Ti were not observed. The inclusions with size greater than 2 μm in SMAW, SAW, FCAW and A-GTAW were found to be consisting of Si, Mn and Ca oxides, with inclusions in A-GTAW showing predominantly Si oxides and inclusions in SAW showing some traces of Ti oxides also. *The high magnification SEM micrographs of inclusions and EDS analysis is given in Appendix A3*.

6.2.3 Microstructure analysis

The optical and SEM micrographs of the etched samples of base metal and weld metal of the SMAW, SAW, FCAW and A-GTAW arc welded joints are given in Fig 6.10. The microstructure of DMR 249A base steel shows predominantly fine grained equiaxed ferrite and some percentage of pearlite of banded type structure.Each of the ferrite micro-constituents has distinctive characteristics in terms of grain size, different degrees of lattice imperfections (i.e. dislocation or subgrain boundary density), grain boundary mis-orientation, and grain morphology. For weld metals, the optical micrographs showed grain boundary ferrite, Widmanstatten ferrite with aligned second phase along with veins of ferrite, acicular ferrite, polygonal ferrite and microphases. Minor changes in the percentage of volume fraction of the different ferrites (grain boundary, Widmanstatten, acicular and polygonal) were observed in the samples characteristic to the differences in heat input of the various arc welding processes. The grain boundary ferrite has equiaxed form or thin veins delineating prior austenite grain boundaries. The side plate Widmanstatten ferrite is seen as the parallel ferrite laths emanating from prior austenite grain boundaries. The acicular ferrite lies between the bodies of prior austenite grains and is considered a toughening phase due to the interlocking arrangement [69, 122]. Acicular ferrite only forms below the bainite–start temperature. Acicular ferrite and bainite seem to have similar transformation mechanisms. The microstructures might differ in detail because bainite sheaves grow as a series of parallel platelets emanating from austenite grain surfaces, whereas acicular ferrite platelets nucleate intragranularly at point sites so that parallel formations of plates cannot develop.

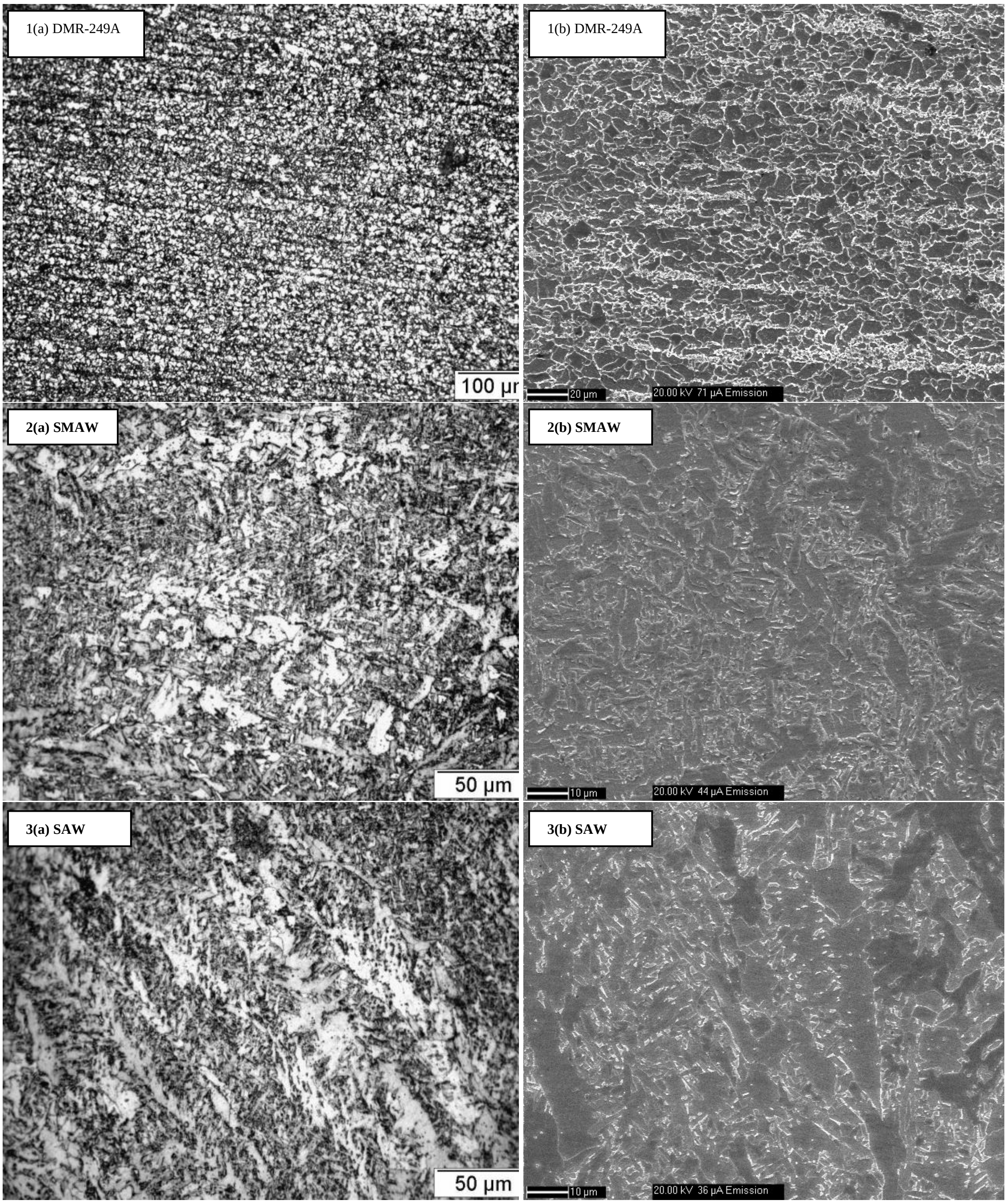

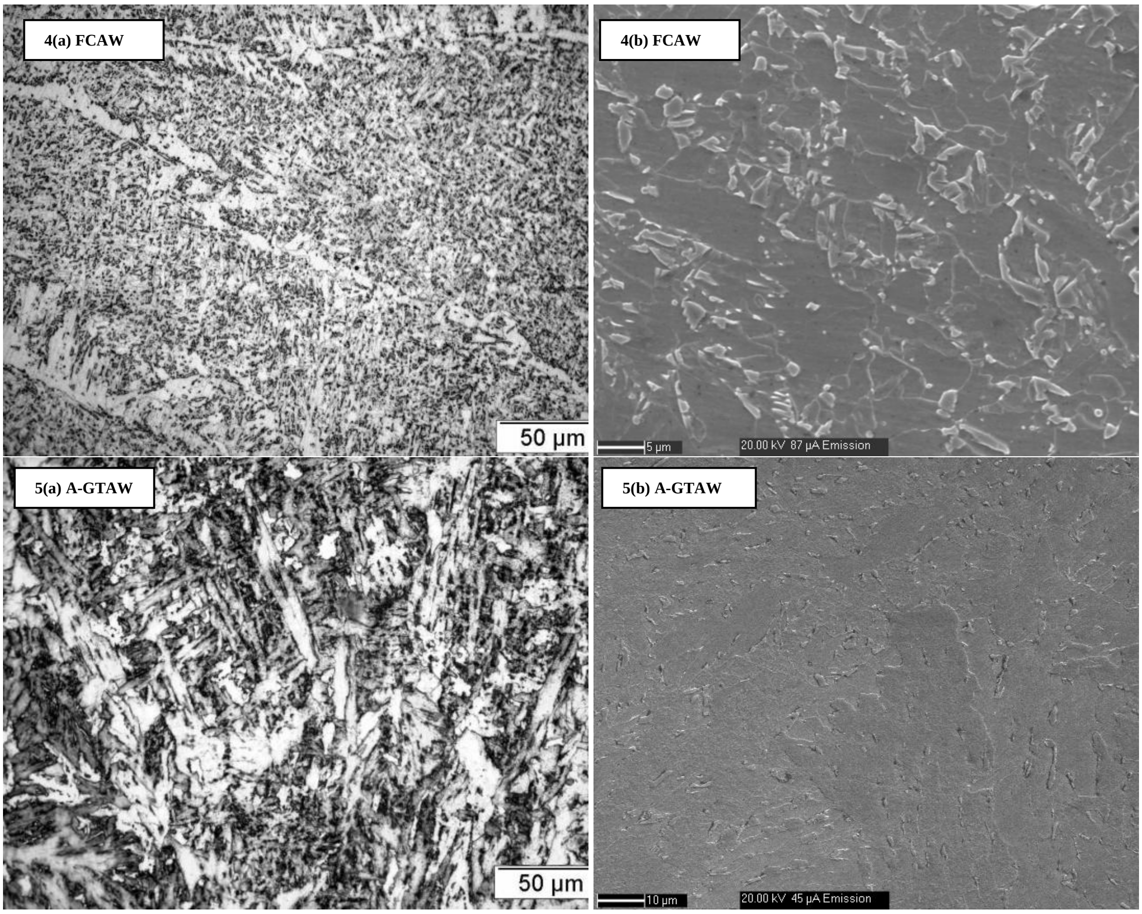

Fig 6.10 DMR-249A base steel and weld metal microstructures (a) Optical (b) SEM

When steels are welded, the degree of prior austenite grain coarsening depends on the amount of heat input during welding. It follows that when steels containing appropriate inclusions are welded, the amount of acicular ferrite increases at the expense of bainite, as the heat input and hence the austenite grain size is increased. Eventually, at very large heat inputs, the cooling rate decreases so much that larger quantities of Widmanstatten ferrite are obtained and there is a corresponding reduction in the amount of acicular ferrite. Widmanstatten structure is characterized by its low impact values and low percentage elongations. The area fractions of various ferritic phases seen in optical micrographs were ascertained with systematic manual point counting as per ASTM E 562 using the micrographs given in Fig 6.11.The A-GTAW associated with high heat input was observed to contain about 24 percentage of

Widmastatten ferrite, the highest amount compared to other three welding processes. The volume fractions of grain boundary ferrite, Widmanstatten ferrite, polygonal ferrite and microphases for the SMAW, SAW, FCAW and A-GTAW weld metals are given in Table 6.5.

Table 6.5 The volume fraction of grain boundary ferrite, Widmanstatten ferrite, polygonal ferrite and microphases using manual point counting

Volume Fraction	Grain Boundary Ferrite (G)	Widmanstatten Ferrite (W)	Polygonal Ferrite (P)	Microphases
SMAW	20	09	15	56
SAW	24	14	11	51
FCAW	24	16	08	52
A-GTAW	19	24	09	48

The transformation of austenite to these ferriticmorphologies is distinguished by the atomic mechanism oftransformation as reconstructive (grain boundary/polygonal ferrite)and displacive (Widmanstatten, acicular and bainitic ferrites).While reconstructive transformation is associated with volumechange, the displacive transformation is accompanied by invariantplane strain (IPS) [302-304]. The M-Shape profile for measuredresidual stress is attributed to the phase transformation occurringduring solid state transformation of equiaxial ferrite in basematerial to grain boundary ferrite, accicular ferrite, Windmanstattenferrite, bainite and micro alloying phases which cause volumechanges in weld metal. The acicular and Widmanstatten ferritesgrow by the displacive mechanism, so that their growth causesthe shape of the transformed region to change, the change beingan IPS with a large shear [119].

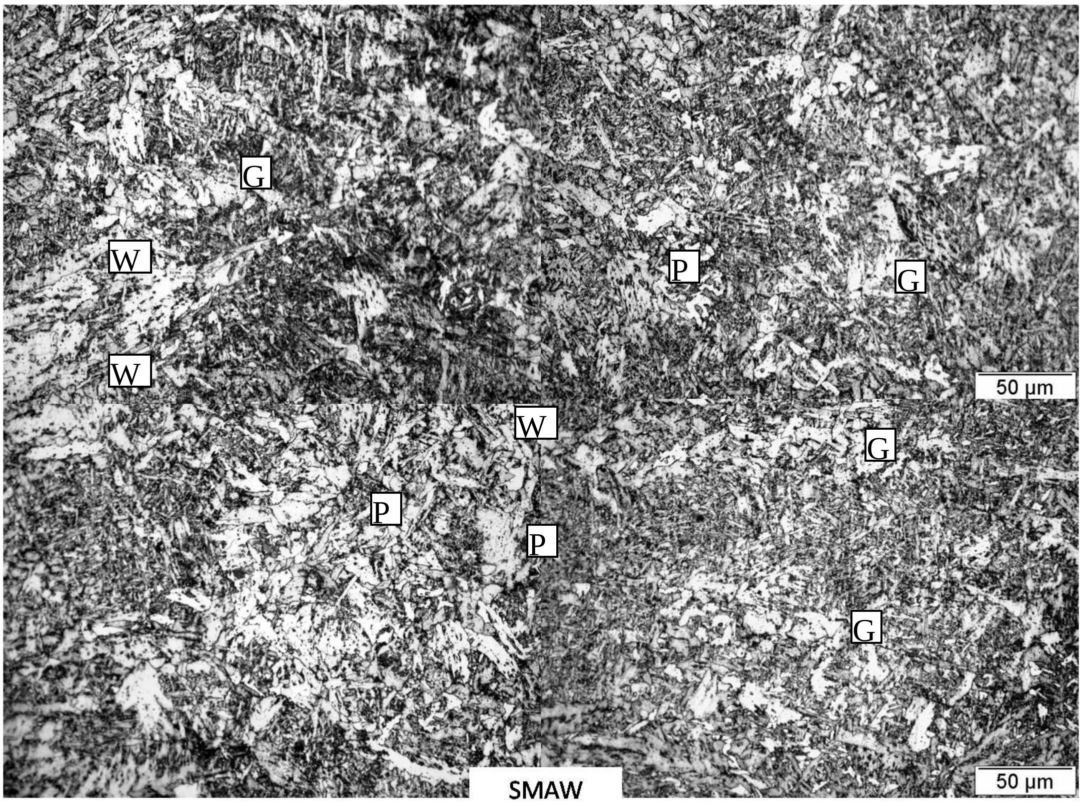
G
W
W
P
G
50 µm
W
G
P
P
G
50 µm
SMAW

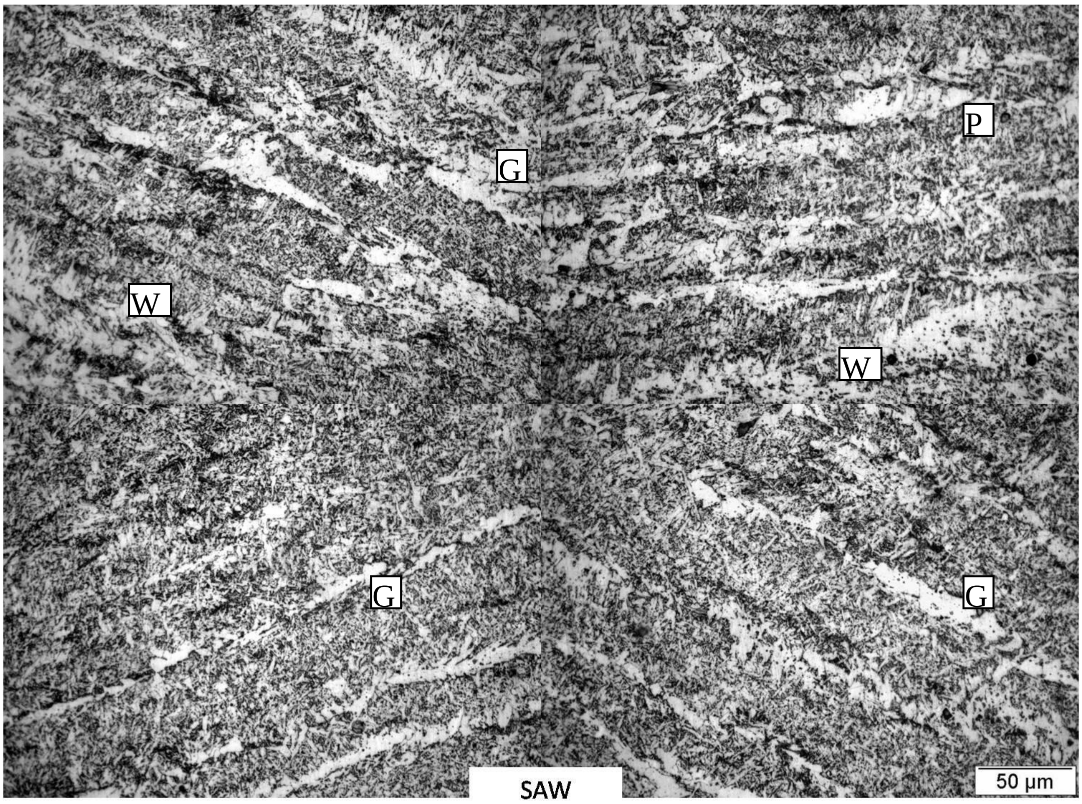
P
G
W
W
G
G
50 µm
SAW

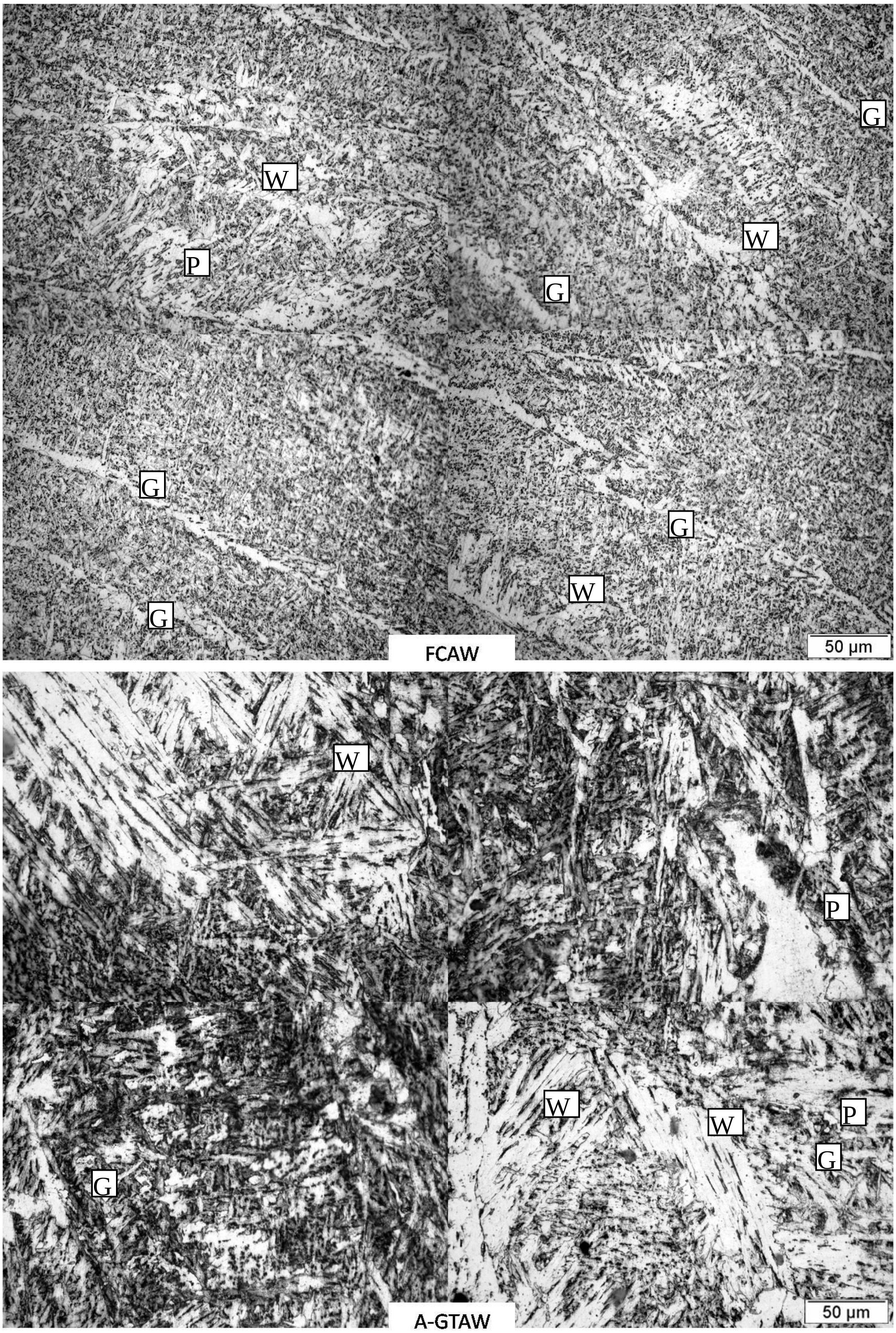

G: Grain Boiundary Ferrite, P:Polygonal Ferrite, W: Widmanstatten Ferrite

Fig 6.11Optical micrographs of SMAW, SAW, FCAW and A-GTAW used for systematic manual point counting as per ASTM E 562

Polygonal ferrite is characterised by mainly equi-axed grains containing a few low angle grain boundaries [60, 211-230]. The small grain size and high angle grain boundaries of acicular ferrite inhibit cleavage propagation and can increase toughness and strength. Bainite is in the form of very fine lenticular plates or laths that manifest as sheaves of ferrite plates usually separated by low-angle grain boundaries [60]. The high density of dislocations in bainite results in higher strength and lower ductility. The EBSD inverse pole figure maps and band contrast maps for different weld metals are given in Fig. 6.12. The grain boundaries have been colored according to the misorientation (black: 2-10, maroon: 10-30, green 30-50 and red >50) in Fig. 6.12(b) corresponding EBSD band contrast maps. The grain boundary misorientation profiles of SMAW, SAW, FCAW and A-GTAW weld metals are given in Fig 6.13. The volume fraction of different ferrite phases were calculated taking the characteristics aspect ratio, grain boundary angle, mean misorientation and grain size of each phase [212].

The volume fractions of acicular ferrite, polygonal ferrite and bainite for the SMAW, SAW, FCAW and A-GTAW weld metals are given in Table 6.6. The acicular ferrite percentage was calculated to be 29 for SMAW weld metal and lower acicular percentage of 19 for A-GTAW specimen. The acicular ferrite percentage was found to be corresponding to the associated large grain boundary angles as seen in Figs. 6.12 and 6.13.The average grain size and average grain area of all weld metals as measured from EBSD images is given in Table 6.7. The average grain size denotes the diameter of biggest circle fitting into the grain area.

Table 6.6 The volume fraction of acicular ferrite, polygonal ferrite and bainite for the SMAW, SAW, FCAW and A-GTAW weld metals using EBSD

Volume Fraction	Acicular Ferrite	Polygonal Ferrite	Bainite
SMAW	29	45	26
SAW	26	49	25
FCAW	22	43	35
A-GTAW	19	52	29

Table 6.7 Average grain size and grain area of weld metal

	Avg Size (μm)	Avg Area (μm^2)
SMAW	2.252972	8.459507
SAW	2.926955	14.51323
FCAW	2.475783	11.51611
A-GTAW	3.125473	24.06726

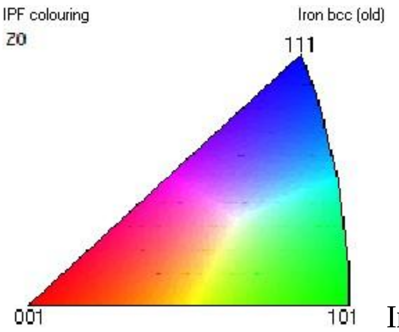

Inverse pole map for Fig5

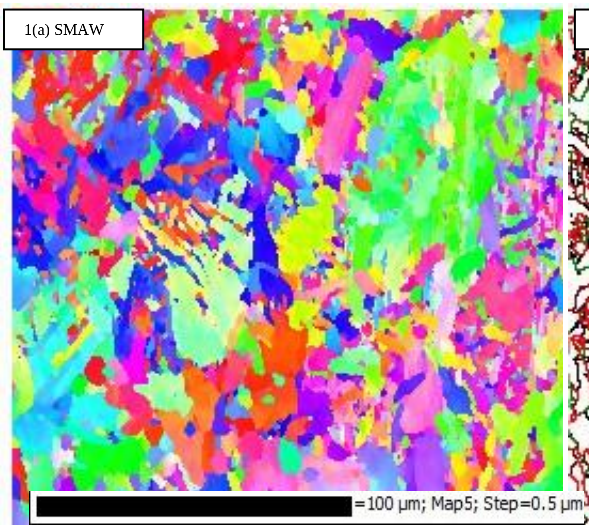

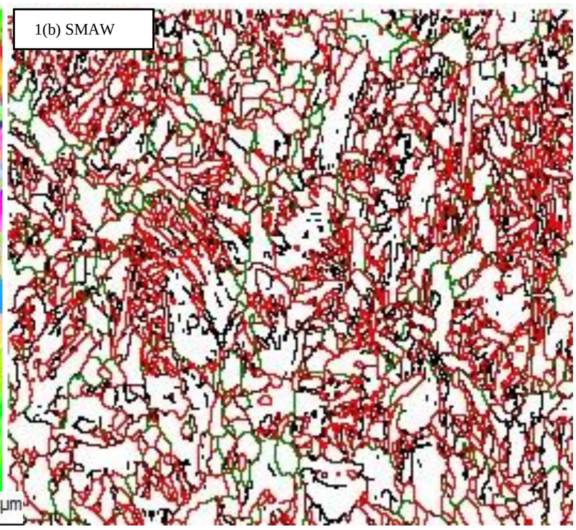

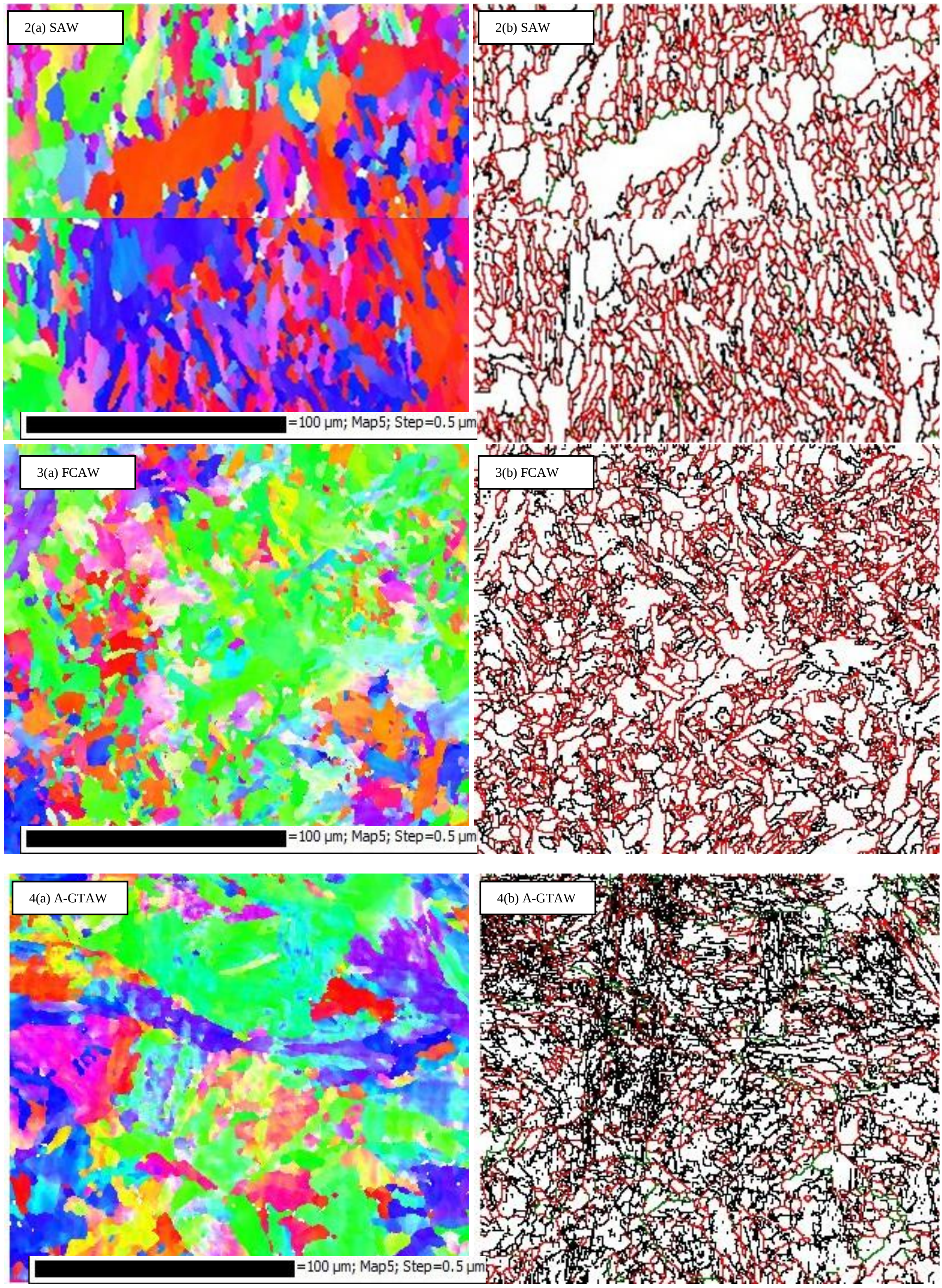

Fig 6.12 The EBSD inverse pole figure maps and band contrast maps for the weld metal specimens (Mis-orientation Angle- (black: 2-10, maroon: 10-30, green 30-50 and red >50))

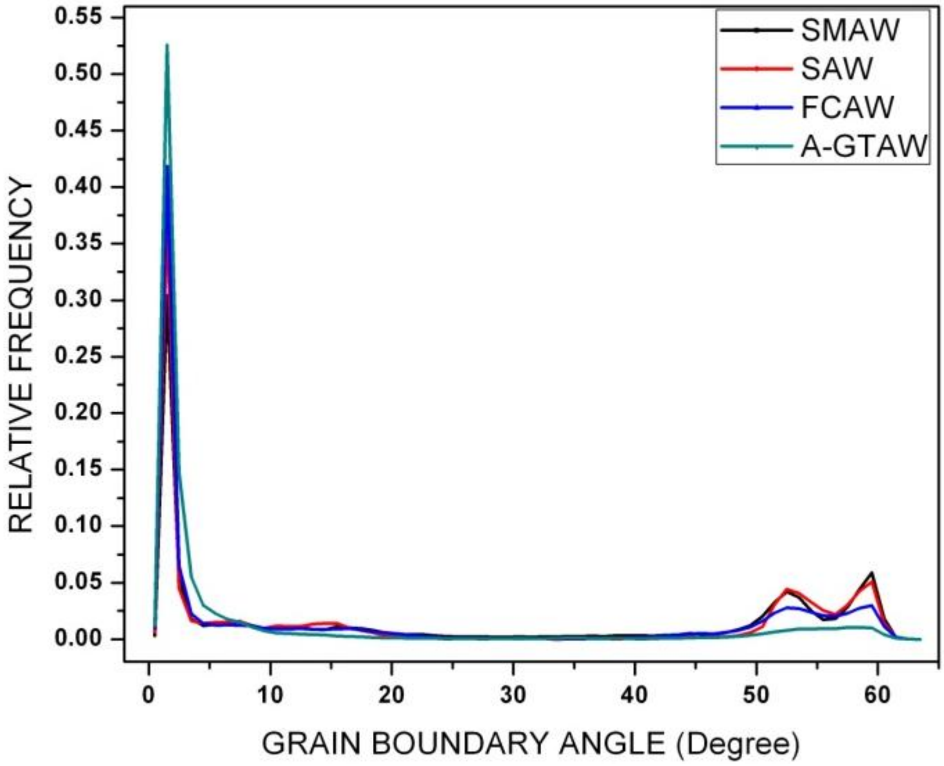

Fig 6.13 Grain boundary misorientation profiles of weld metal grains

The optical and SEM micrographs across the weld joints for SMAW, SAW, FCAW and A-GTAW joints are given in Fig 6.14. The pre austenitic grain size in the weld metal could not be ascertained as the weld metal is observed to be columnar and equiaxed structure. The width of columns shows maximum width for FCAW weld metal followed by A-GTAW, SAW and SMAW. The columnar structure is lengthier and similar in FCAW and SAW weld metal. The SMAW weld metal shows shorter length of columnar structure with refined grains. The microstructure present in the fine grain heat affected zone (FGHAZ) is a mixture of equiaxed ferrite plus microphases. Details of these regions show that microphases are decorating the grain boundaries, and are also in the form of small islands; these microphases are mainly degenerated ferrite/pearlite and become mainly ferrite constituents(mixture of acicular ferrite, bainite and constituents as microphases). In the coarse grain heat affected zone (CGHAZ), the microstructure is similar to the as-deposited regions; however, it has less acicular ferrite and more polygonal ferrite and bainite. This is due to the smaller grain size of the prior austenite grains observed in the CGHAZ (compared with the large columnar grains found in the as-deposited regions), which favours nucleation of bainite in the form of sheaves of small platelets, over intragranular acicular ferrite. The variation in columnar width and size observed in weld metal constituents post solidification, CGHAZ and FGHAZ is given in Table 6.8.

Table 6.8 variation in columnar width and size observed in weld metal constituents post solidification, CGHAZ and FGHAZ

Avg Grain Size (μm)	Columnar Width	WM	CGHAZ	FGHAZ
SMAW	35	2.25	45	4
SAW	55	2.92	50	3.5
FCAW	80	2.47	55	4
A-GTAW	57	3.12	60	5

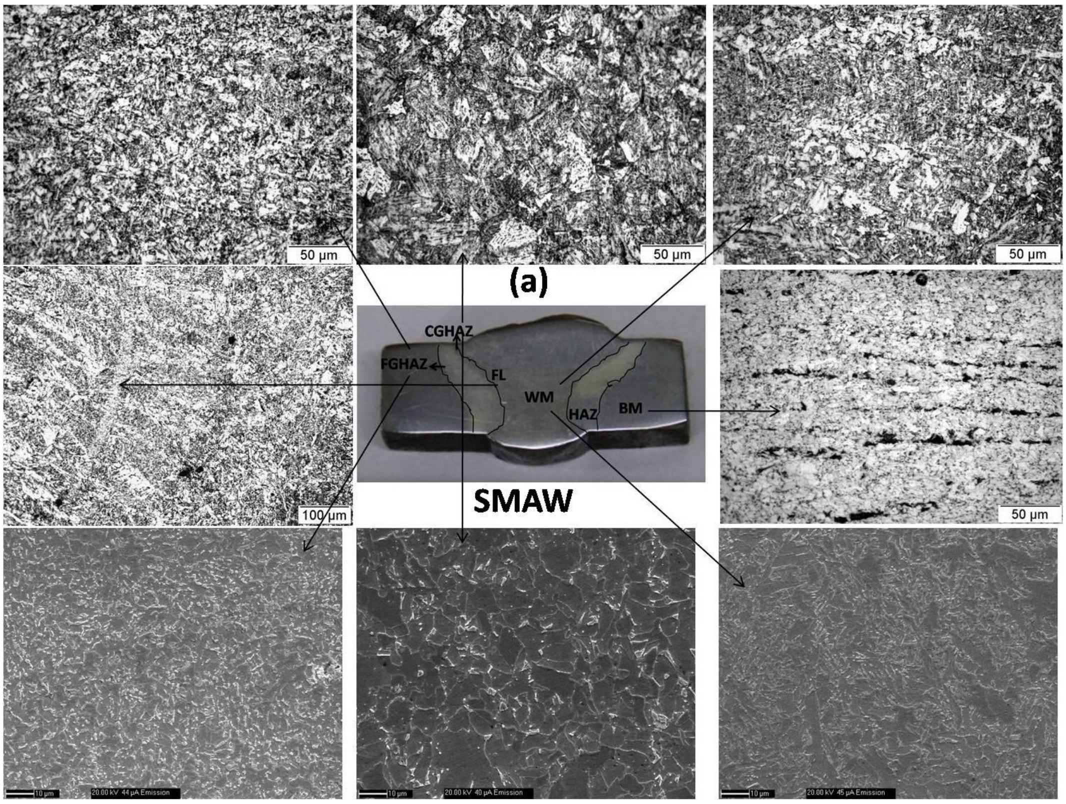

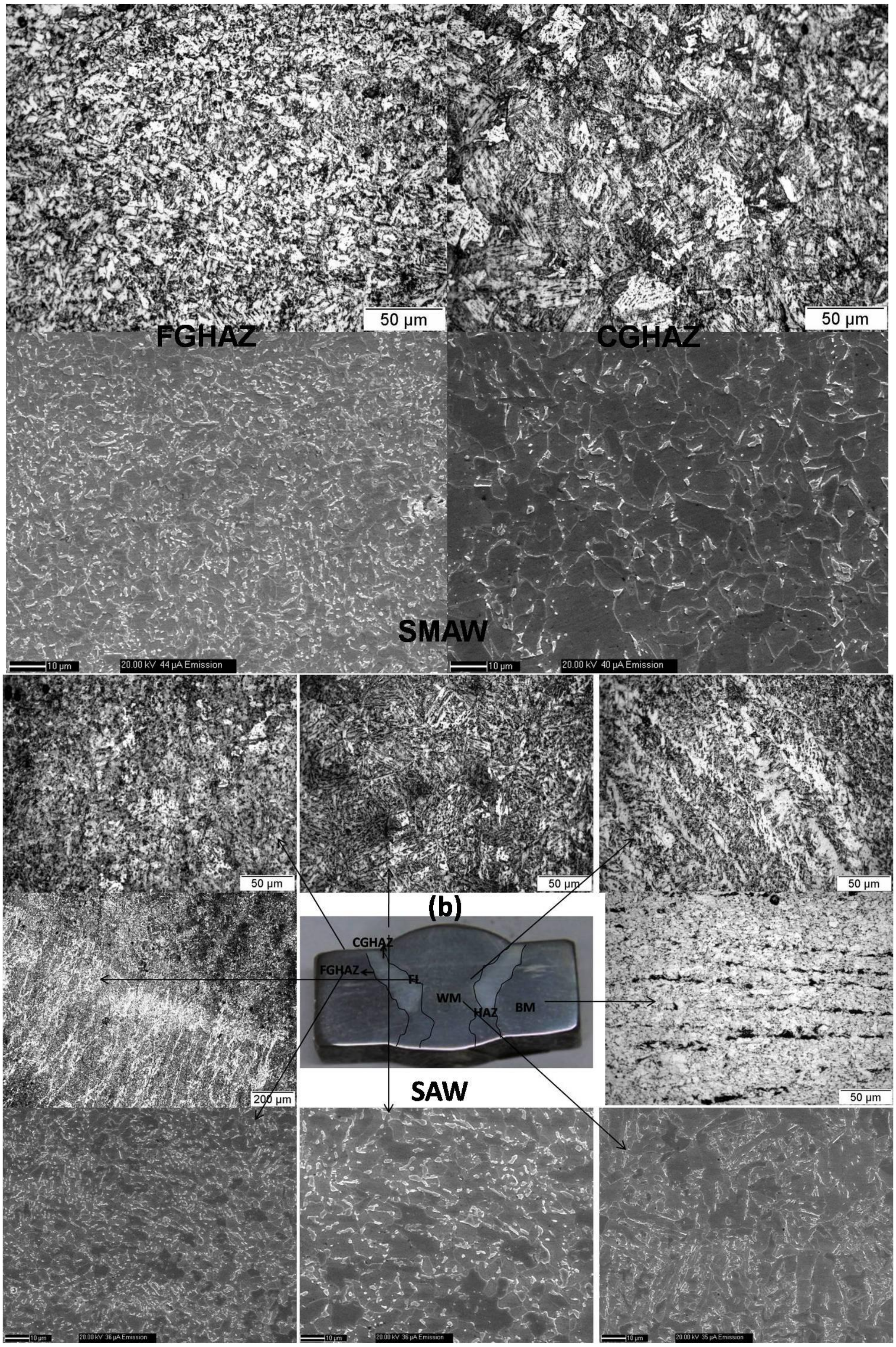
50 µm
50 µm
FGHAZ
CGHAZ
SMAW
10 µm
20.00 kV 44 µA Emission
10 µm
20.00 kV 40 µA Emission
50 µm
50 µm
50 µm
(b)
CGHAZ
FGHAZ
FL
WM
HAZ
BM
200 µm
SAW
50 µm

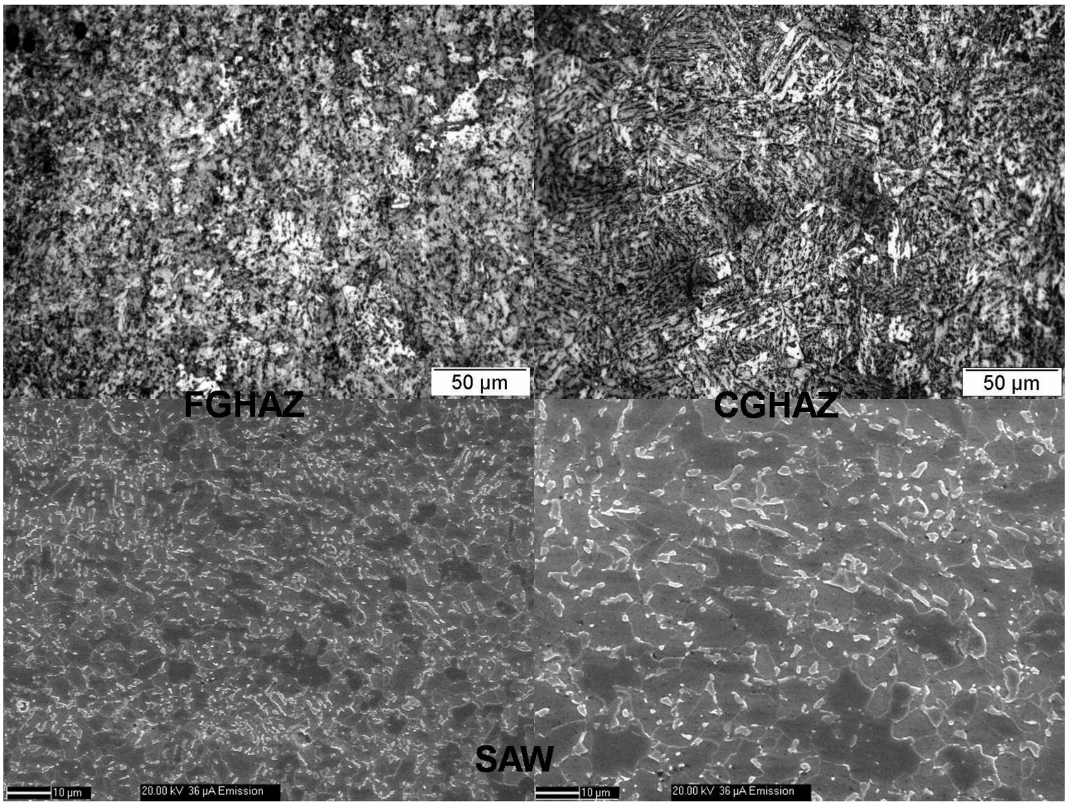
50 µm
FGHAZ
50 µm
CGHAZ
SAW
10 µm
20.00 kV 36 µA Emission
10 µm
20.00 kV 36 µA Emission

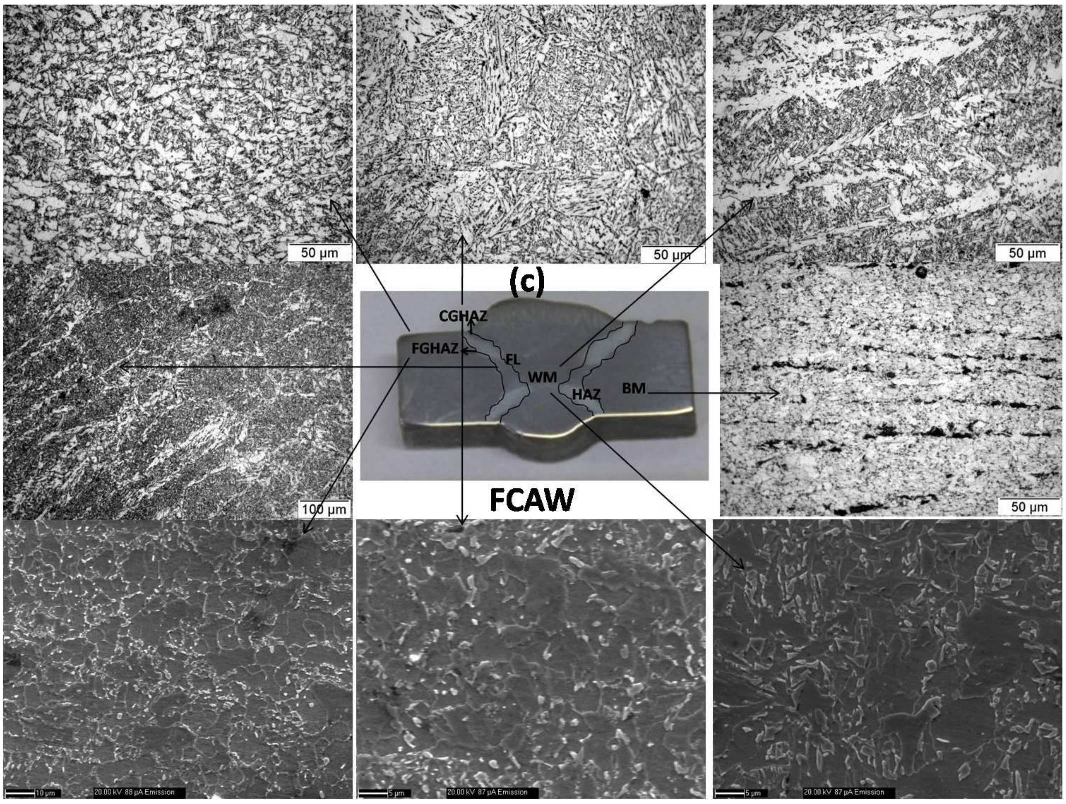
50 µm
50 µm
50 µm
(c)
CGHAZ
FGHAZ
FL
WM
HAZ
BM
100 µm
FCAW
50 µm

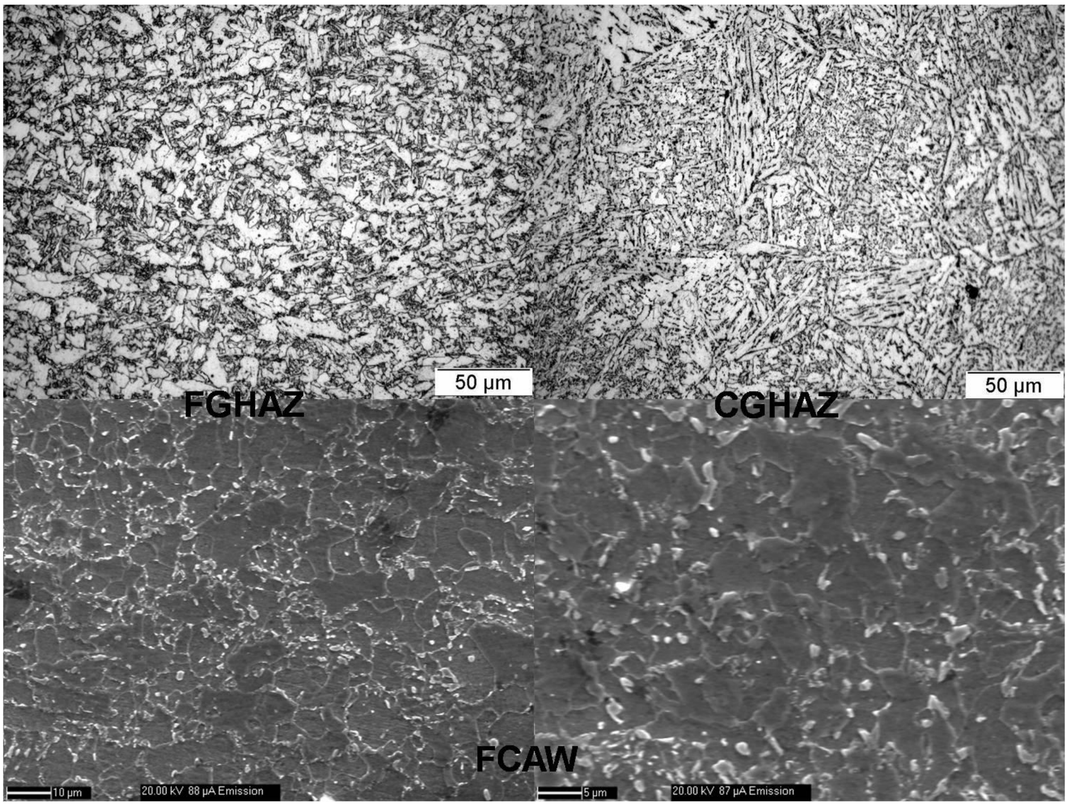
50 µm
FGHAZ
50 µm
CGHAZ
FCAW
10 µm
20.00 kV 88 µA Emission
5 µm
20.00 kV 87 µA Emission

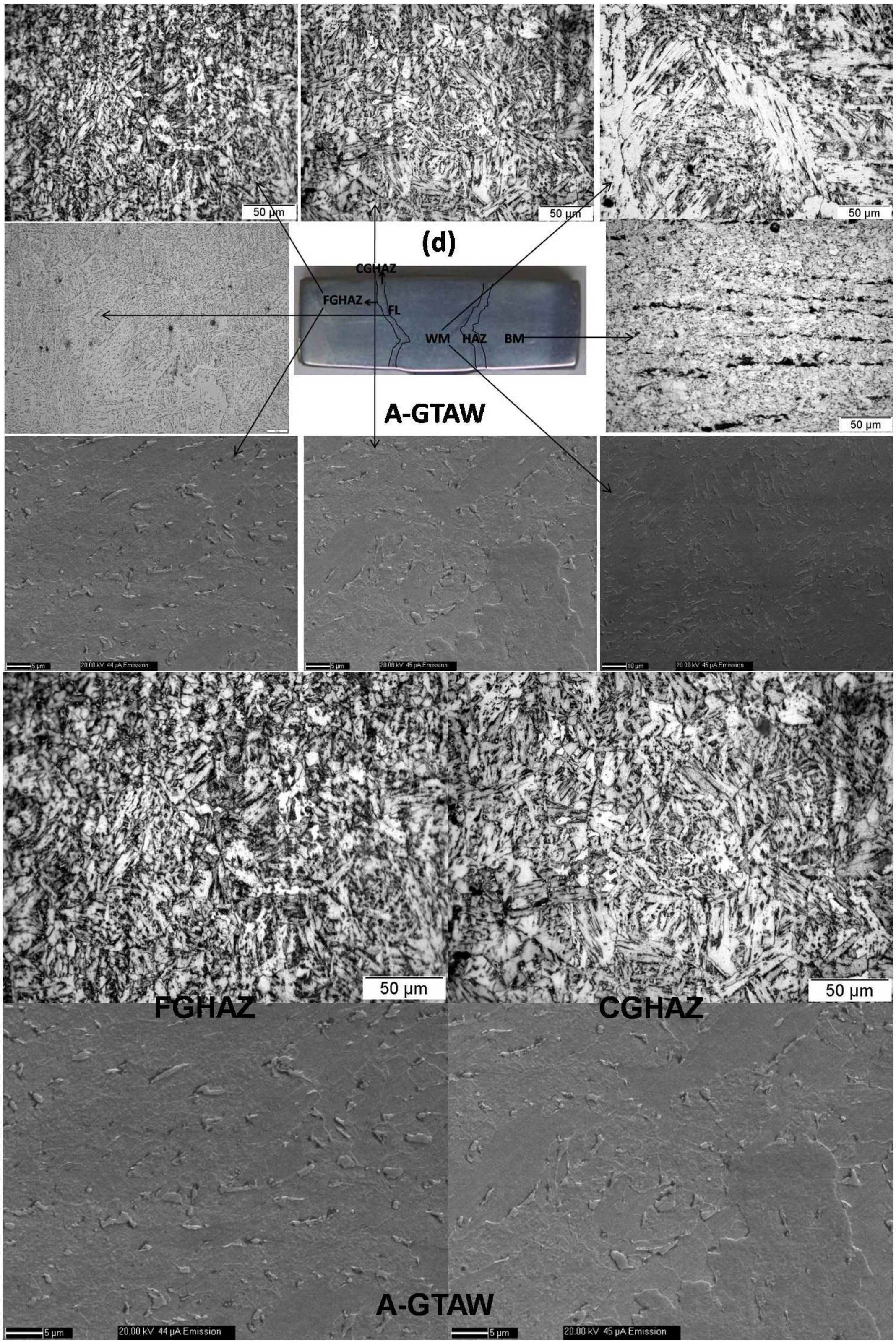

Fig 6.14 Optical and SEM micrographs across the weld joints for SMAW, SAW, FCAW and A-GTAW joints

6.2.4 Mechanical properties

A maximum hardness value for low carbon martensite is 340-400 HV,bainite is approximately 325 HV and of the acicular ferrite is approximately 267 HV [234-235]. The hardness value range of 250 to 300 HV in weld metal is attributed to predominant presence of acicular ferrites and other ferrite morphologies. The cooling rate in the HAZ is lower than that in the as-deposited region; therefore, more bainite is formed and consequently more carbon is rejected into the remaining austenite, giving an appreciable hardness. Also in this region, the prior grain size of austenite is smaller and may decrease the packet size of a lath-like microstructure, contributing to a further increase in hardness [236]. The hardness values measured across the weld joints correspond to the hardness values of bainitic and ferritic morphologies confirming the analysis of optical and SEM micrographs regarding presence of different ferrite phases across the weld joint.

The micro hardness values measured across the weld joint at 2 mm and 5 mm below the surface for all the weld joints are shown in Fig 6.15. The hardness values for all the weld joints were found between 200 and 330 $HV_{0.2}$. The profile of hardness across the weld joint for all the joints was observed to be similar. The hardness of weld metal was measured to be higher than the base metal. The micro-hardness values gradually increase from base metal to HAZ and a minor decrease in the hardness value was observed near the fusion zone followed by higher hardness values in weld metal. The hardness values measured across the weld joints correspond to the hardness values of bainite and ferrite confirming the analysis of optical and SEM micrographs regarding presence of different ferrite phases across the weld joint.

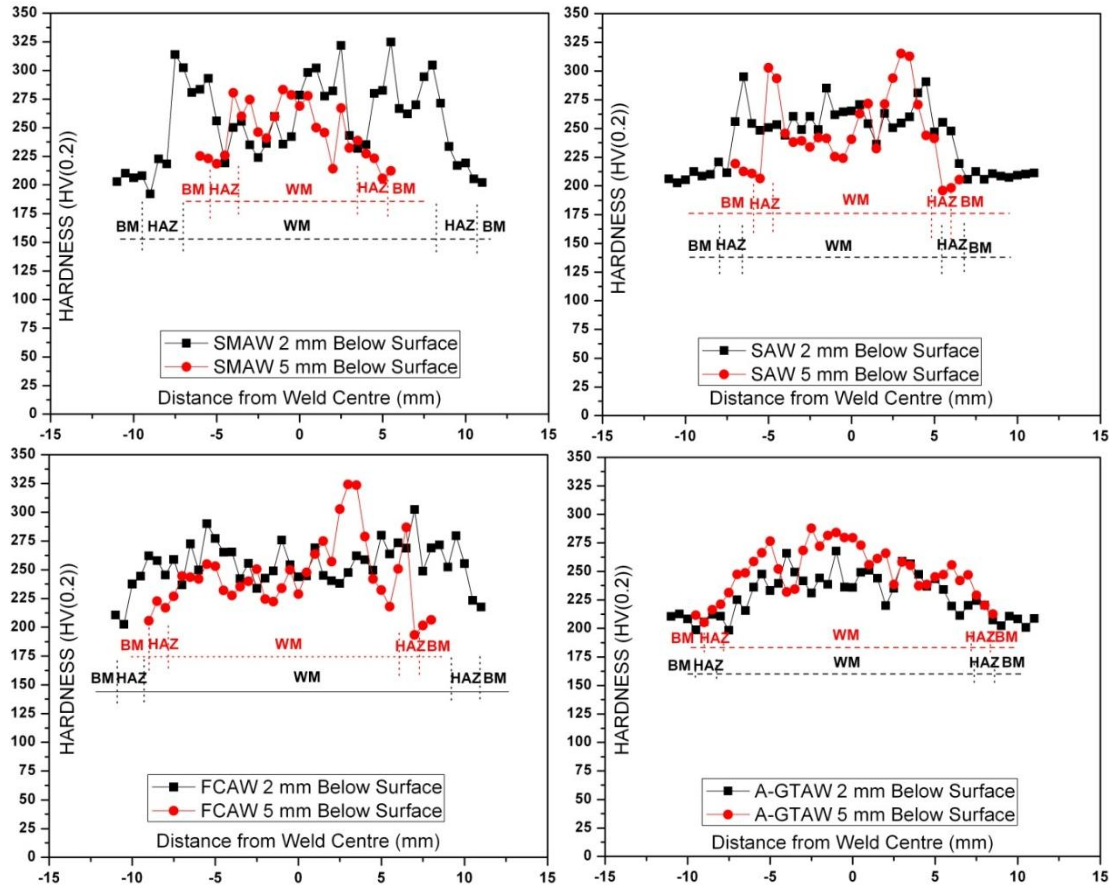

Fig. 6.15 Microhardness profiles of SMAW, SAW, FCAW and A-GTAW weld joints

The tensile test performed on cross weld specimens of the weld joints have shown yield strength of about 450 to 480 MPa, uniform elongation of 10 to 13 %, total elongation of 17 to 20% and ultimate tensile strength of 595 to 640 MPa. For DMR-249A steel (base metal) specimens, the experimentally measured values are yield strength of 435 MPa, uniform elongation of 20 %, total elongation of 30% and ultimate tensile strength of 620 MPa. The base metal specimens were observed to fracture at the centre of the specimen. The tensile fracture of the cross weld specimens of all the weld joints occurred in the base metal region away from weld metal which confirmed adequate strength for the weld metal of all the processes (Fig 6.16). The comparison of tensile properties of SMAW, SAW, FCAW and A-GTAW joints are given in Table 6.9.

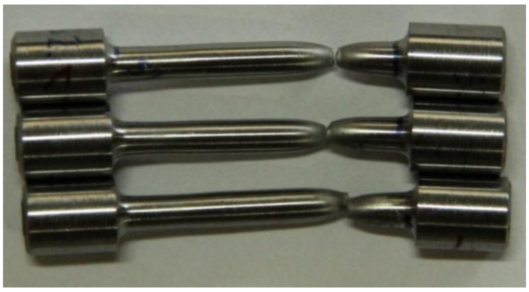

DMR-249A base steel SMAW

SAW FCAW

A-GTAW

Fig 6.16 Photos of fractured tensile specimen of DMR-249A base steel and cross weld specimen of arc welded joints (a) Base metal (b) SMAW (c) SAW (d) FCAW (e) A-GTAW

The higher micro hardness values of weld metal than the base metal substantiate that the weld metal has higher yield strength than base metal and corroborates corresponding reduction in percentage elongation. The cross weld specimen contains base metal, HAZ and weld metal in its gauge length and cannot undergo a uniform deformation in tension. The deformation accumulates and localizes faster in the weak section, which results in premature necking. For a specimen containing base metal, weld metal and the HAZ (interface specimen), the base metal section yields first, since the weld metal has a higher yield stress. The percentage reduction in area values were found to be directly proportional to the percentage elongation values with maximum reduction in area of 65% observed corresponding to percentage elongation of 30% for the base metal, DMR-249-A steel. The stress versus strain curves for DMR-249A steel base metal and arc welded joints are given in Fig 6.17.*Results of all tensile tests carried out are given in Appendix A4*.

Table 6.9 Comparison of tensile strength of DMR-249A steel and weld joints

Weld Joint	% Elongation		% RA	YS (MPa)	UTS (MPa)
	Uniform	Total			
DMR-249A	20	30	65	435	620
SMAW	12	20	63	480	610
SAW	10	17	63	450	595
FCAW	12	18	63	450	610
A-GTAW	13	20	63	480	640

The tensile test specimens fractography of base metal specimen and all the arc weld joint specimens (fracture site at base metal) revealed ductile fracture with characteristic cup and cone dimples structure. The fractography studies confirm and corroborate the measured percentage elongation of 30% for DMR-249A steel base metal and 17-20 % for the SMAW, SAW, FCAW and A-GTAW cross weld joints. The images of fractured tensile specimens and fractured surfaces are shown in Fig 6.18.

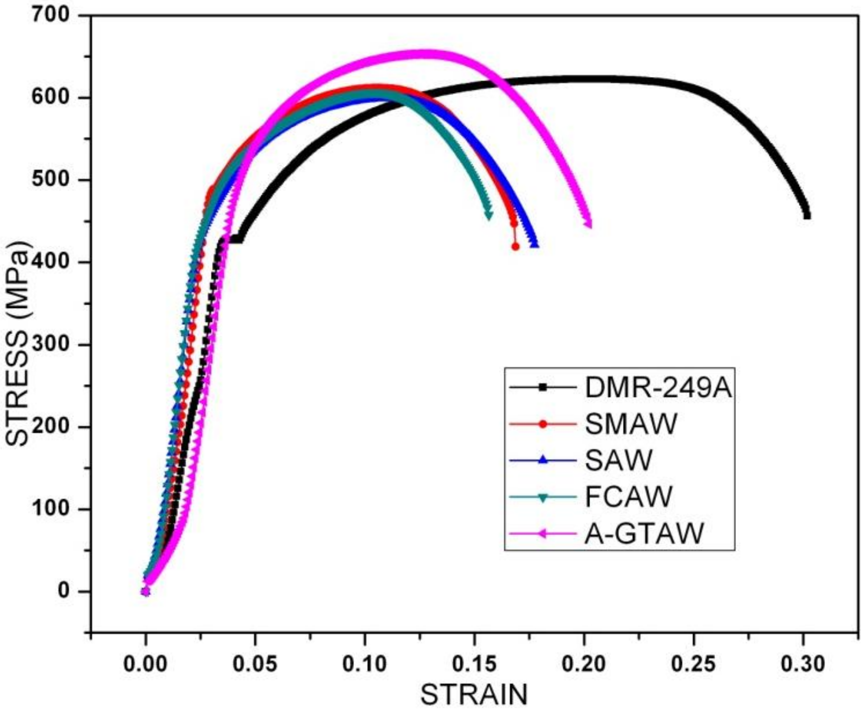

Fig 6.17 Tensile Stress Vs Strain curves for DMR-249A steel and arc welded joints

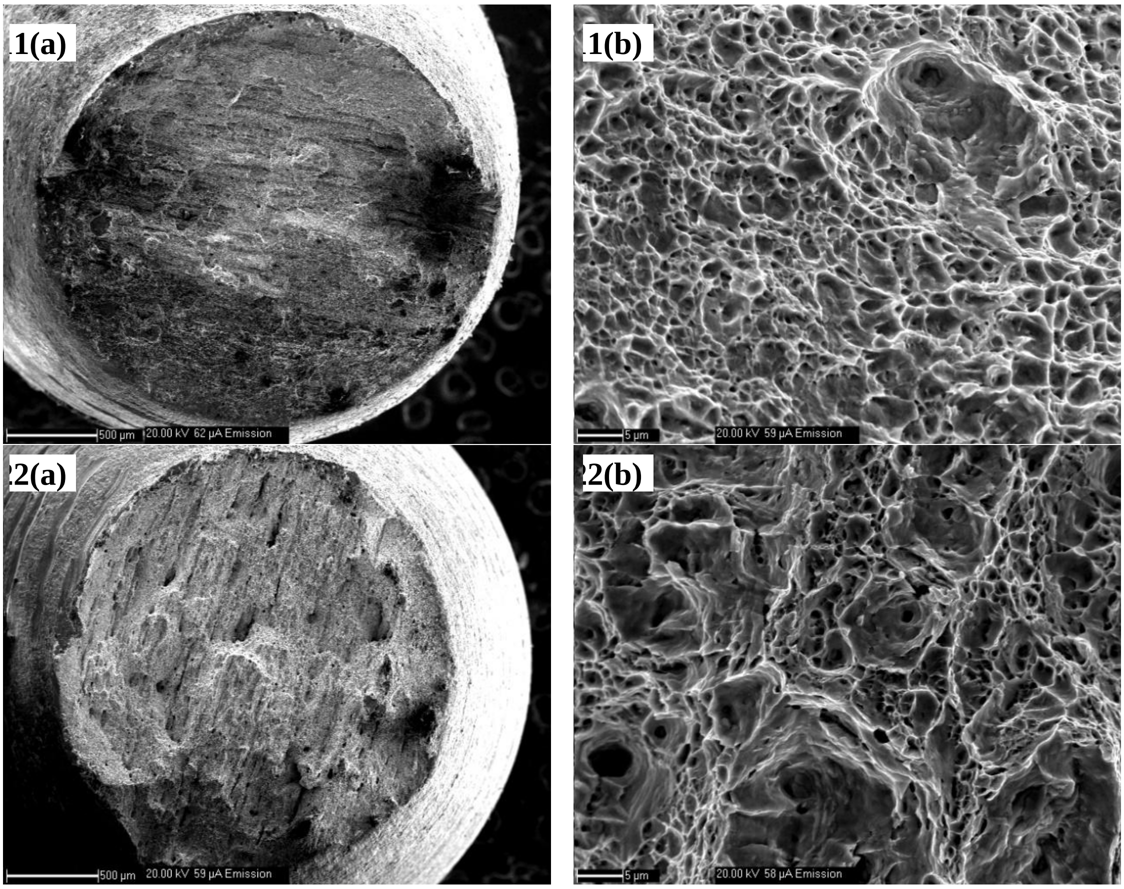

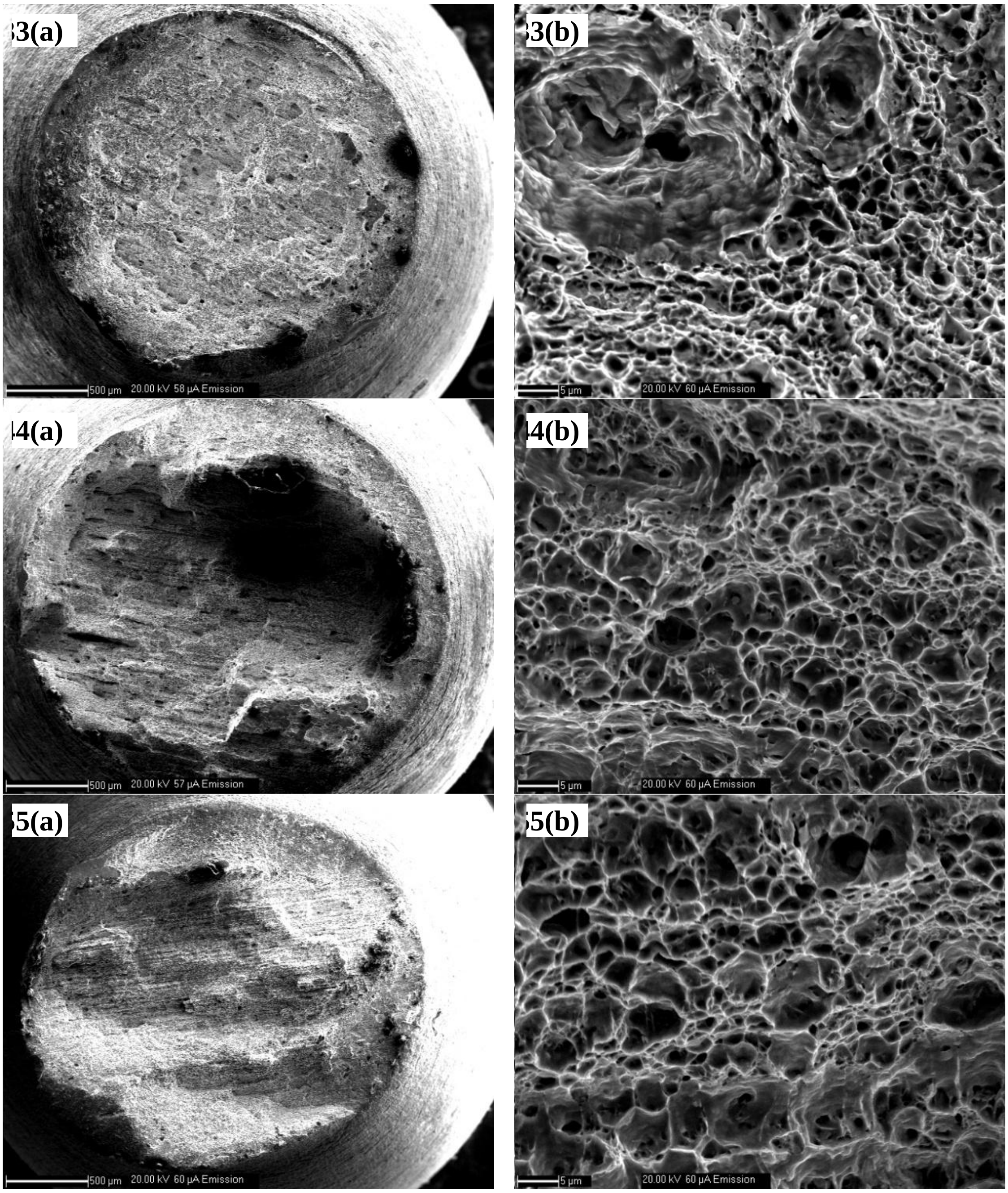

Fig. 6.18 Fractured tensile test specimen and SEM image of fracture surface for (1) DMR-249A (2) SMAW (3) SAW (4) FCAW (5) A-GTAW samples

The impact toughness tests with notch in the weld metal were carried out at room temperature and sub-zero temperature (-60°C) for DMR-249A steel and all weld joints. The impact toughness was found to be 150 J to 200 J at room temperature for all the weld joints. The impact toughness for sub-zero (-60°C) temperature is observed to be about 30-74 J for SMAW, SAW and SMAW joints. For A-GTAW joint, the impact toughness at -60°C is found to be 10 J. The DMR-249A steel (base metal) displayed superior impact toughness of greater than 350 J at room temperature and 155 J at -60°C. The comparison of impact properties of SMAW, SAW, FCAW and A-GTAW joints are given in Table 6.10.*Results of all tensile and Charpy impact tests carried out are given in Appendix A4.*

Table 6.10 Comparison of impact toughness of DMR-249A steel and weld joints

Weld Joint	V-Notch Charpy Test			
	Room Temp (~25°C)		Sub-zero (-60°C)	
	Impact Toughness (J)	Lateral Expansion (mils)	Impact Toughness (J)	Lateral Expansion (mils)
DMR-249A	>350	110	155	110
SMAW	150	90	74	45
SAW	145	110	30	24
FCAW	210	110	50	40
A-GTAW	200	100	10	19

The lateral expansion values obtained from V-notch charpy impact tests give a good indication of ductility of a material by measurement of squeezed out material on the compression side. ASME B31.3 requires lateral expansion of 0.38 mm (about 15 mils corresponding to 27 J impact toughness as per NORSOK standards)) for bolting materials and steels with UTS exceeding 656 MPa rather than specifying an impact value. ASTM E23-12c also emphasises that lateral expansion of unbroken samples may be considered as more or equal to the samples that break and provide protruded lip for measurement. The DMR-249A and all arc weld joint specimens displayed excellent ductility at room temperature with lateral expansion of 90 to 110 mils. During charpy testing at -60°C, the best ductility amongst the specimens investigated was observed in base metal DMR-249A steel. The conventional arc welded joints of SMAW, SAW and FCAW also displayed reduced ductility at sub-zero temperatures with lateral expansion values of 45, 24 and 40 mils respectively. Though A-GTAW weld joint was observed to have excellent ductility at room temperature, a sharp decrease in ductility was found at -60°C with lateral expansion value of only 19 mils.

For base metal, grain refinement is often used in conjunction with precipitation strengthening to improve toughness [13-14]. The precipitation strengthening conjoined with grain refinement for DMR-249A steel has been achieved with micro alloying additions of niobium, vanadium and titanium [13-15]. DMR-249A steel is characterized by higher strength and superior impact toughness values of more than 350 J at room temperature and 155 J at -60 °C due to fine equiaxed ferrite grains of the base metal, as seen in Fig 4(a).

The composition of filler material is generally altered to enhance the mechanical properties of weld metal [69, 237]. The chemical composition of base metal, filler material and weld metals as shown in Tables 1 and 3 show that the chemical composition of A-GTAW joint is similar to base metal (no filler metal is used except the minute quantities of activated flux) whereas the weld metals of the other three joints contain lower percentages of carbon, manganese and silicon and higher percentages of nickel as compared to base metal based on the chemical composition of the filler material. Carbon with its hardening effect increases the volume fraction of the hard microstructure and reduces impact toughness. The carbon-manganese boron free steel containing vanadium has been found to promote the formation of polygonal ferrite along the prior austenite grain boundaries, reducing reaustenization sites along the prior austenite grain boundaries during the second thermal cycle [238-241]. The high manganese content in steel enhances strength and hardness but reduces ductility and has been stated to have detrimental effect on impact toughness as it promotes the formation of weak and soft sulphides and M-A constituents, decreasing the bainite start temperature B_s [239]. Higher concentrations of silicon are detrimental to surface quality and impact toughness. Nickel, as ferrite strengthener, also improves hardenability and sub-zero impact toughness. The high proportion of acicular ferrite (AF) combined with low oxygen plus sulfur content are the primary microstructural features contributing to the superior low temperature notch toughness of the welds [238-241].

The high impact toughness of FCAW and A-GTAW at room temperature can be attributed to finer inclusions. The smaller size, lower density and lower area fraction of inclusions are associated higher impact toughness [242-243]. The lower values of impact toughness at room temperature for SMAW are attributed to large average size of inclusions.The large inclusion size along with high inclusion density results in low impact toughness in SAW weld metal, as given in Table 6.4.

The sub-zero impact toughness of A-GTAW weld metal is lower as compared to other weld joints. The micro-alloying additions through the filler material provide better sub-zero impact toughness properties for the conventional self shielding arc welded joints. Also higher notch toughness is expected at low energy inputs of SMAW, SAW and FCAW joints because of the high proportion of fine reheated (several weld beads) and higher percentage of acicular ferrite in weld metal structure as against higher percentage of grain boundary/polygonal ferrite and scattered acicular ferrites in high heat input [244] double pass A-GTAW weld joint. The coarse grains of A-GTAW weld metal are also a significant factor leading to decrease in sub-zero impact toughness.

For DMR-249A base steel and A-GTAW weld joint, the impact toughness tests with notch in the weld metal were also carried out at 0°Cand -30°C to ascertain the change in ductile brittle transition with reduction in temperature. The values of impact toughness for DMR-249A base steel and A-GTAW weld metal at various temperatures are given in Table 6.11 and Fig 6.19. The pictures of V-notch Charpy impact specimens of base steel and A-GTAW weld joint and the SEM fractography images are given in Fig 6.20 and 6.21 respectively.

Table 6.11 Impact toughness for DMR-249A base steel and A-GTAW weld metal at various temperatures

Temperature (°C)	V-Notch Charpy Test			
	DMR-249A		A-GTAW	
	Impact Toughness (J)	Lateral Expansion (mils)	Impact Toughness (J)	Lateral Expansion (mils)
25 (RT)	>350	110	200	100
0	315	110	130	90
-30	180	110	20	20
-60	155	110	10	19

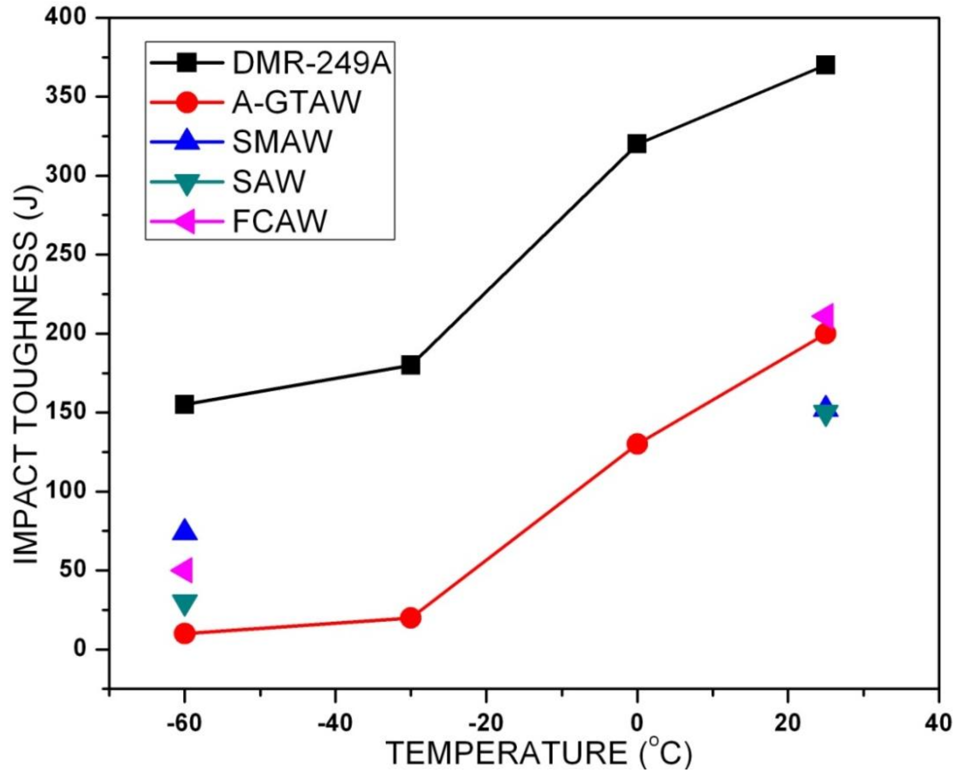

Fig 6.19 Ductile brittle behaviour of DMR-249A steel and A-GTAW joint

Fig 6.20 Pictures of V-notch Charpy impact specimens of (a) base steel (b) A-GTAW weld joint

The fractography images of V-notch Charpy impact toughness specimens of DMR-249A base metal for room temperature, zero degree and sub-zero temperatures show dull and fibrous fracture by ductile mode with cup and cone dimples corroborating the high impact toughness measured for base steel even at -60 °C. The SEM images of impact toughness specimens for A-GTAW weld metal reveal ductile fracture for room temperature and experiments conducted at zero degree. The sub-zero (-30 °C and -60 °C) temperatures specimen of A-GTAW weld metal demonstrate bright and crystalline cleavage fracture attributed to brittle fracture failure. The A-GTAW weld metal change over from ductile fracture at room temperature and 0 °C to brittle fracture surface at sub-zero temperatures is corresponding to low impact toughness values as given in Table 6.11.

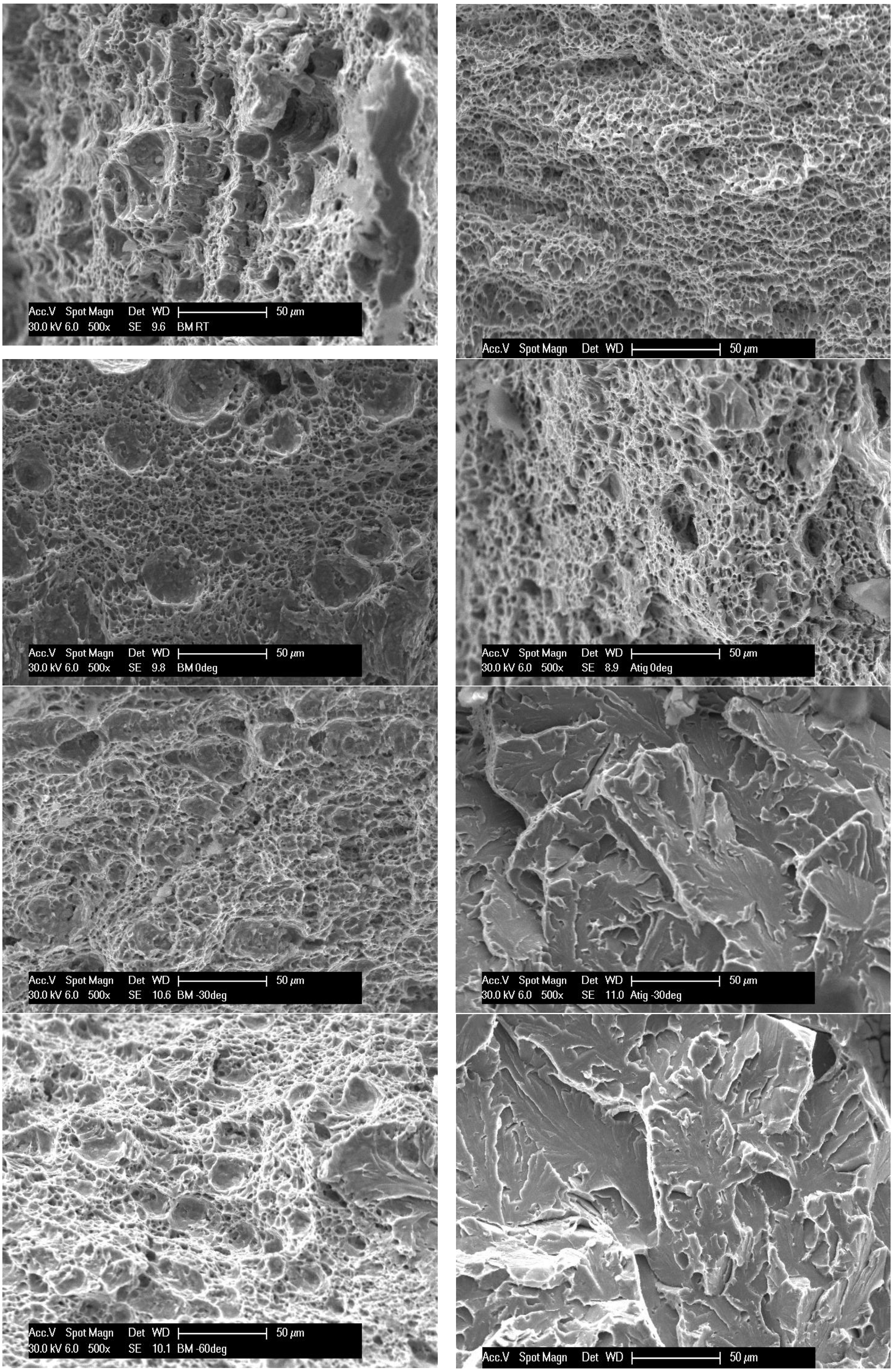

Fig 6.21SEM fractography images of V-notch Charpy impact specimens (a) base steel (b) A-GTAW weld joint at room temperature, 0 °C , -30 °C and -60 °C

The fractography images of room temperature V-notch Chapry impact toughness specimens for SMAW, SAW and FCAW welded joints show dull and fibrous fracture by ductile mode with predominant cup and cone dimples. The SEM images of impact toughness specimens for experiments conducted at sub-zero (-60 °C) temperatures reveal bright and crystalline cleavage fracture attributed to brittle fracture failure. The images of fractured impact specimens and fractured surface of SMAW, SAW and FCAW weld metal for tests carried at room temperature and sub-zero (-60 °C) temperature are shown in Fig 6.22 and 6.23 respectively.

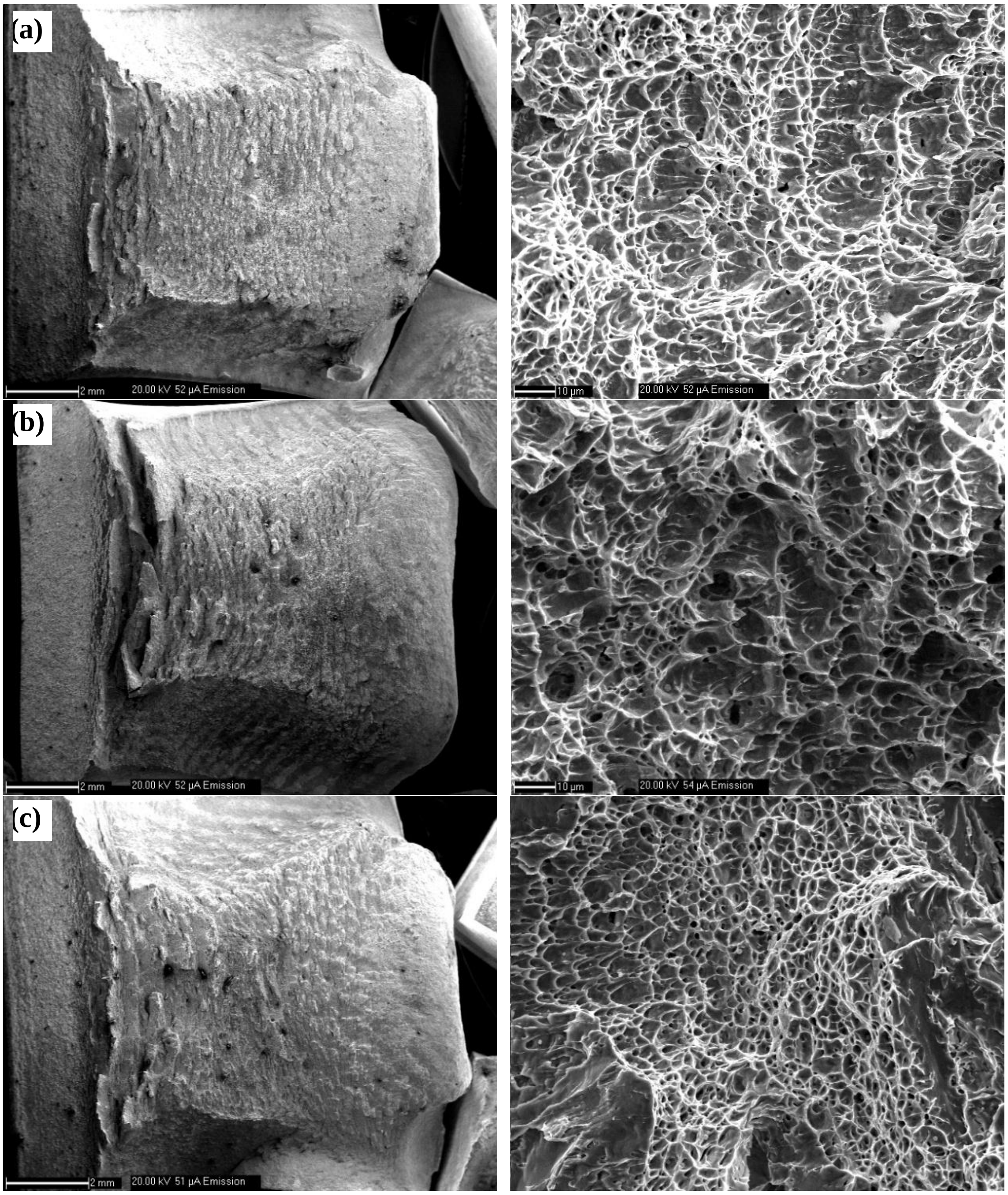

Fig. 6.21 SEM fractography of room temperature impact test specimen (a) SMAW (b) SAW (c) FCAW

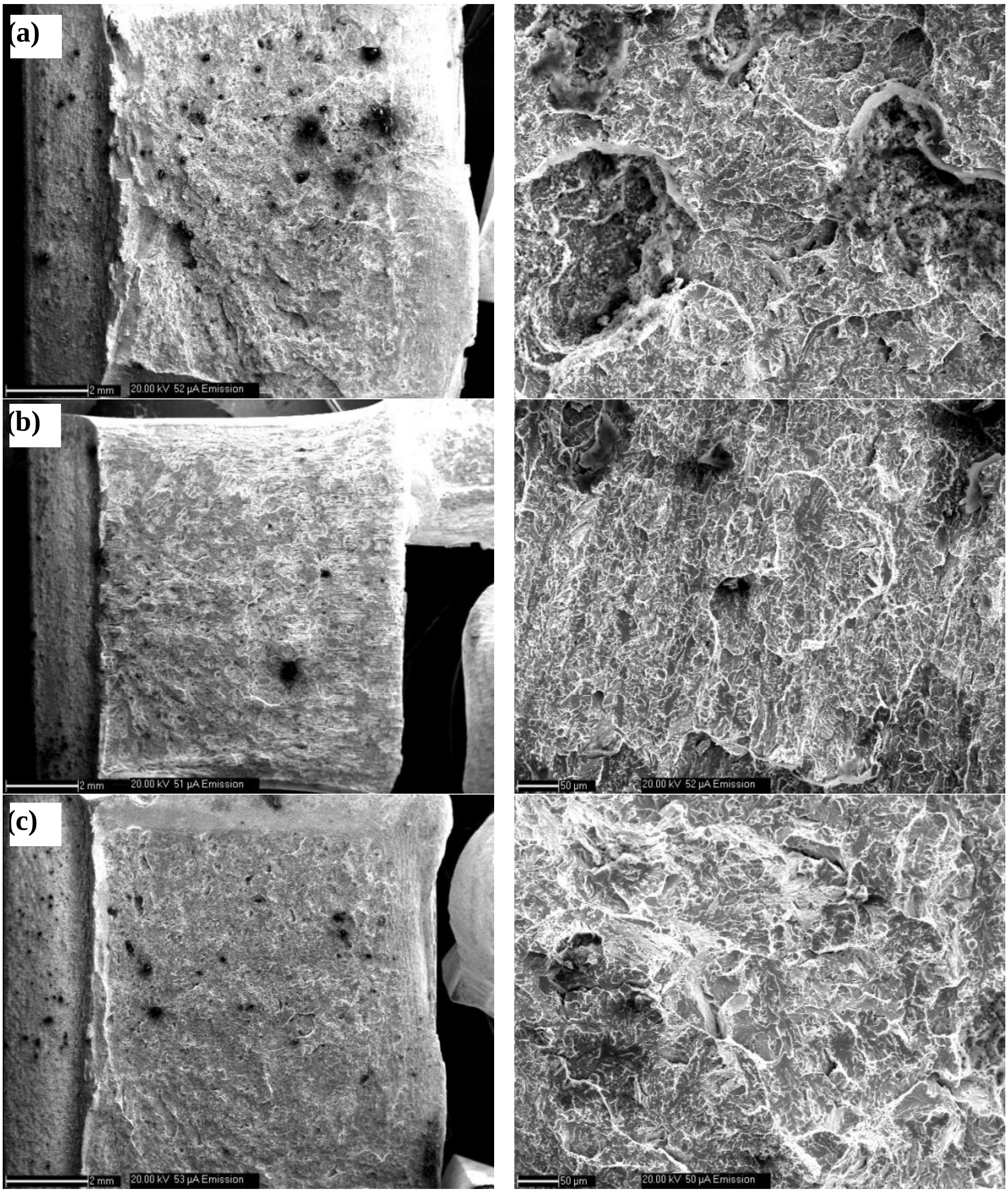

Fig. 6.22 SEM fractography of sub-zero (-60 °C) temperature impact test specimen (a) SMAW (b) SAW (c) FCAW

6.3 Conclusions

The conclusions based on the investigations to compare the effect of arc welding processes on the weld attributes of DMR-249A steel weld joints are summarized as follows:-

(a) The examination of inclusions in weld metal associated with SMAW, SAW, FCAW and A-GTAW processes indicated the presence of the least number of inclusions in the SMAW joint, of about 16.1 numbers per mm^2 and area fraction of 0.186. The SAW joint was evaluated to have numerous small and large inclusions, predominantly spherical, in clusters which are characteristic of SAW welding process due to fast solidification of weld pool leading to entrapment of more inclusions. The FCAW joint was observed to have more finer inclusions of spherical and elongated shapes. The inclusions found in A-GTAW joint were largely scattered and spherical in shape.

(b) The micro inclusions of SMAW, FCAW and A-GTAW were found to contain Al, Si, Mn and Ti oxides whereas micro inclusions in SAW weld metal were observed to be predominantly Si and Mn oxides and traces of Al or Ti were not observed. The inclusions with size greater than 2 μm in SMAW, SAW, FCAW and A-GTAW were found to be consisting of Si, Mn and Ca oxides, with inclusions in A-GTAW showing predominantly Si oxides and inclusions in SAW showing some traces of Ti oxides also.

(c) The weld joints in general exhibited microstructure consisting of grain boundary ferrite, Widmanstatten ferrite with aligned second phase along with veins of ferrite, acicular ferrite, polygonal ferrite, bainite and microphases as compared to predominantly fine grained equiaxed ferrite microstructure exhibited by DMR 249A steel. Minor changes in the percentage of volume fraction of the different ferrites (grain boundary, Widmanstatten, acicular and polygonal) were observed in the samples characteristic to the differences in heat input of the various arc welding processes.

(d) The hardness of weld metal was measured to be higher than the base metal for all the weld joints. In general, the micro-hardness values gradually increase from base metal to HAZ with a minor decrease in hardness value observed near the fusion zone followed by higher hardness values in weld metal.

(e) The weld joints were found to have minor increase in yield strength with corresponding decrease in ductility compared to base steel. The ultimate tensile strength of DMR-249A steel and arc welded joints were comparable.

(f) The V-notch Charpy impact tests confirmed that base metal possesses excellent impact toughness even at sub-zero temperatures of -60°C which is due to fine equiaxed grains. All weld joints have good impact toughness at room temperature. The toughness values for SMAW, SAW and FCAW joints were assessed to be within acceptable limits at -60°C due to presence of acicular ferrite and desirable change in weld composition by use of suitable filler material.

(g) The A-GTAW weld joint indicated good impact toughness with a measured value of 200 J at room temperature. The significant reduction in toughness of A-GTAW joint at sub-zero temperatures is attributed to a greater percentage of grain boundary ferrite in the high heat input double pass A-GTAW welding process. The coarse grains of A-GTAW weld metal is also a significant factor leading to decrease in sub-zero impact toughness.

Chapter 7. Evaluation of Mechanical Properties across Weld Joints using Automated Ball Indentation Technique

7.1 Introduction

The weld joint exhibits variation in mechanical properties across the joint due to varied microstructures in the weld metal, heat affected zone and base metal. The evaluation of variation in mechanical properties of structural components is essential for their continued safe operation. A simple, non-destructive technique, suitable for mechanical property evaluation for localized zones and requiring minimum sampling volume is useful in assessment of mechanical properties without disturbing the integrity and functional operability of the structure. One such technique is automated ball indentation (ABI) technique. Automated Ball Indentation technique employs strain-controlled multiple indentation cycles at a single penetration location on a polished metal surface by a spherical indenter with partial unloading during each cycle [245-247]. The load applied is measured using a load cell and the depth increment during the test is measured using a linear variable differential transformer (LVDT). The applied load and depth of indentation data measured during an ABI test are used to obtain the tensile properties of a material, by making use of elasticity and plasticity theories and semi-empirical relationships that govern the material behaviour under indentation loading [248-249].

Meyer [250] was the first who developed a relationship between mean pressure and impression diameter to evaluate the yield strength (YS) of materials. Tabor [251] gave an empirical relationship to find the representative strain of materials within plastic region while indentation is done through a spherical ball indenter. This technique has been used to characterize the gradient in mechanical properties of a variety of materials and weld joints of stainless steels [252-254]. The effectiveness of a laboratory scale ABI has been established at IGCAR for such applications[249, 255-256].

The present chapter evaluates the mechanical properties across SMAW, SAW, FCAW and A-GTAW weld joints of DMR-249A steel. The variations in microstructure, micro-hardness, and tensile properties obtained using automated ball indentation (ABI) technique were analysed. The ABI results were validated with standard conventional tensile test results. It was found that ABI can be effectively used to determine the mechanical properties across the weld joint by using a small amount of test materials and quite rapidly, compared to conventional test.

7.2 Theory of Automatic Ball Indentation

The photograph of ABI machine is given in Fig. 7.1(a). Here, a spherical ball with a specific rate of loading indents the test materials/components and multiple indentations in a single position are made through loading-unloading-holding-reloading sequence. It is seen that the load increases approximately linearly with the penetration depth (Fig. 7.1(b)). The two non-linear but opposing processes occur simultaneously, i.e. the non-linear decrease in the applied load with indentation depth due to the spherical geometry of the indenter and nonlinear increase of load with indentation depth due to work hardening of the test pieces. During each subsequent loading, the amount of material experiencing plastic deformation increases, so that continuous yielding and strain hardening occur simultaneously. In-contrast, for the case of a uni-axial tensile test, the plastic deformation is confined only to the limited volume of the test sample gauge section. For each loading cycle, the total depth (ht) is measured while the load is applied and the plastic depth (hp) is measured after completing unloading [255-256]. The indentation profile during an ABI test is shown schematically in Fig. 7.1(c). The computer program determines the slope of each unloading cycle. Then the intersection of this line with the zero load line determines the value of hp. The ht, hp and the corresponding loads (N) are the raw data for determining the mechanical properties like UTS, YS,n and σ_t–ε_t curve.

(a) ABI machine

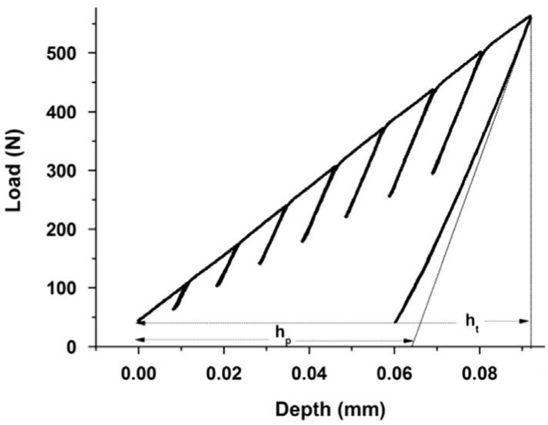

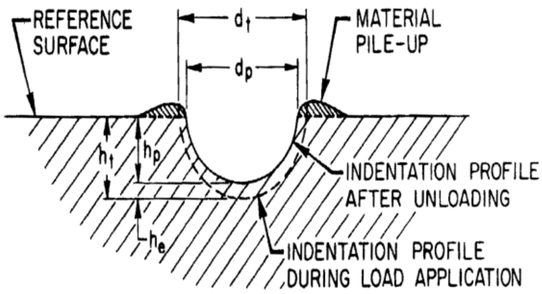

(b) ABI load vs depth plot

(c) Indentation profile during ABI

Fig. 7.1 ABI machine, typical plot and indentation profile

Fig. 7.1(c) describes the schematic showing deformed zone and recovered zone (on unloading). Corresponding to BI test set up, a number of equal depth loading cycles each followed by partial unloading is undertaken. Similarly, 'dt' and 'dp' represent the total and plastic indentation diameters, respectively. The material below the indenter flows out during plastic deformation and gets piled-up at indentation edge. The linear increase in load with increase in depth is the consequence of two non-linear and opposing processes occurring simultaneously such as: (i) the spherical geometry of the indenter resulting in increase in contact area with penetration and (ii) the increase in load required for further penetration because of work hardening of the material. In ABI test, both elastic and plastic deformations take place simultaneously during each cycle.

Plastic indentation diameter (d_p) was obtained by substituting plastic indentation depth and indenter diameter (D) values in the Hertzian equation [249, 255-256] given below:

$$d_p = \left\{ 0.5CD \left[\frac{h_p^2 + \left(\frac{d_p}{2} \right)^2}{h_p^2 + \left(\frac{d_p}{2} \right)^2 - h_p D} \right] \right\}^{1/3} \qquad \ldots\ldots\ldots\ldots \quad (7.1)$$

where,

$$C = 5.47P \left(\frac{1}{E_1} + \frac{1}{E_2} \right) \qquad \ldots\ldots\ldots\ldots \quad (7.2)$$

Where, E_1 and E_2 are the moduli of the indenter and test sample, respectively while P is applied load. Further, true plastic strain (ε_p) and true stress (σ_t) can be derived from the following equations.

$$\varepsilon_p = \frac{0.2d_p}{D} \qquad \ldots\ldots\ldots\ldots \quad (7.3)$$

$$\sigma_t = \frac{4P}{\pi d_p^2 \delta} \qquad \text{………… (7.4)}$$

Where, δ is constraint factor. During indentation, the material is constrained by the surrounding elastic material whereas the sample is free to move in tensile test. This results in high mean indentation pressure in BI as compared to flow stress in conventional tensile test. This difference is taken care by constraint factor which is a multiplication factor between the flow stress and the mean indentation pressure.The value of δ depends on the stages of plastic zone development beneath the indenter as reported in Equation 5. This factor is 1.12 at the initial stage of yielding (ϕ=1) and increased to a maximum of 2.87α_m ((ϕ>27) where $\alpha_{m=}$constraint factor index) when the plastic zone is fully developed underneath the indenter. α_m obtained by regression analysis of load-depth curve by BI software.

$$\delta = \begin{Bmatrix} 1.12 & \phi \le 1 \\ 1.12 + \tau \ln \phi 1 < \phi \le 27 & \\ \delta_{\max} & \phi > 27 \end{Bmatrix} \qquad \text{………. (7.5)}$$

Where

$$\delta_{max} = 2.87\alpha_m \qquad \text{……….. (7.6)}$$

$$\phi = \frac{\varepsilon_p E_2}{0.43\sigma_t} \qquad \text{………… (7.7)}$$

$$\tau = \frac{\delta_{\max} - 1.12}{\ln(27)} \qquad \text{………… (7.8)}$$

Yield strength calculation

The strain corresponding to yield strength of the material is beyond the minimum attainable strain by nominal size indenter, and hence the yield strength is determined from the relationship between the mean pressure and total indentation diameter (d_t).

$$\frac{P}{d_t^2} = A\left(\frac{d_t}{D}\right)^{m-2} \qquad \text{………… (7.9)}$$

Where A is the material yield parameter, m is Meyer`s index and

$$d_t = 2\sqrt{h_t D - h_t^2} \quad \ldots\ldots\ldots\ldots \quad (7.10)$$

where$h_t$is the total indentation depth

The yield strength (σ_y) and material yield parameter can be correlated with the equation

$$\sigma_y = \beta * A + B \quad \ldots\ldots\ldots\ldots \quad (7.11)$$

where β is the yield slope and B is yield offset parameter (material constants) obtained by plotting the material yield parameter across the yield strength values at different test temperatures.

Finally the plastic flow data obtained can be represented by a power law equation (Holloman equation),

$$\sigma_t = K\epsilon_p^n \quad \ldots\ldots\ldots\ldots \quad (7.12)$$

where K is the strength coefficient and n is the strain-hardening exponent.The P92 steels followed the power law. And hence the strain hardening exponent can be estimated, under this assumption, to be equal to the uniform elongation.

Evaluation of ultimate tensile strength

The ultimate tensile strength (UTS) can be calculated by the equation

$$UTS = K\left(\frac{n}{e}\right)^n \quad \ldots\ldots\ldots\ldots \quad (7.13)$$

Where, e is a constant (e=2.718).

Evaluation of hardness calculation

The Brinell hardness number can be calculated by the equation given below:

$$HB = \frac{2 \cdot P_{\max}}{\pi \cdot D \cdot \left[D - \sqrt{D^2 - d_f^2}\right]} \quad \ldots\ldots\ldots\ldots \quad (7.14)$$

WhereP_{max} is the maximum indentation load in kilograms and d_f is the final indentation diameter in millimetres.

The ABI test data is processed systematically to calculate the YS, UTS and 'n' values as given in flow chart shown in Fig. 7.2

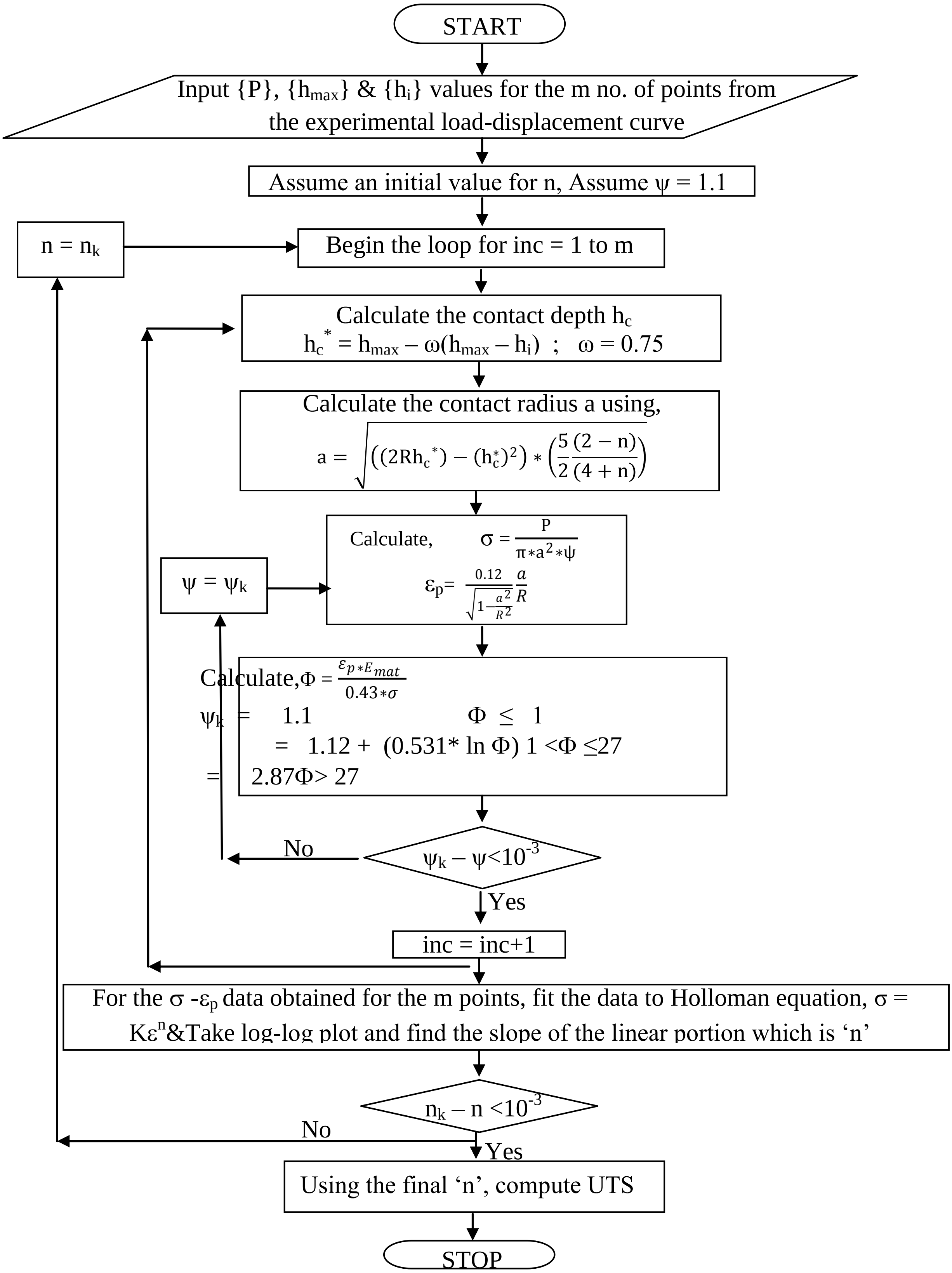

Fig. 7.2Flow chart for calculation of the true stress-strain and UTS from ball-indentation test data

7.3 Experimental details

Mechanical properties across the SMAW, SAW, FCAW and A-GTAW weld joints were determined by ABI tests at room temperature. The ABI test parameters are shown in Table 7.1. The 2D surface profiles of the indentations have been observed using stylus propeller. The settings of stylus propeller are given in Table 7.2.

Table 7.1 ABI test parameters

Material	DMR-249A	Temperature	Room Temperature
Atmosphere	Air	Indenter material	Tungsten carbide
Indenter diameter (mm)	1.0 mm	Constraint factor index	2.87
Indenter Young`s modulus (GPa)	635GPa	Material yield slope	0.228
Sample Young`s modulus (GPa)	210 GPa	Number of unloading	12-15
Indenter radius used (%)	~ 25%	Pre-load set point (N)	5
Unload (% of max. load)	40 -60 %	Indenter speed (mm/sec)	0.1 mm /min

Table 7.2 Details of stylus propeller

Profile length (μm)	2000	Force (mg)	10
Stylus dia. (μm)	12	Resolution (μm)	0.33
M Range (kA°)	2620	Profile	Hills&Valley

7.4 Results and Discussion

The true stress-strain curves were obtained from tensile testing results (Chapter 6) (Fig. 7.3).The API for base metal was carried out at three different locations and compared with the scatter obtained in the three base metal tensile tests undertaken. The true stress-strain plots for conventional tensile testing and ABI testing are shown in Fig. 7.4. The mean deviation of true stress-strain values was observed to be within the scatter of 15 MPa for conventional tensile test values and 20 MPa for ABI measurements. The variation of about 30 MPa was observed between conventional tensile and ABI based assessments.

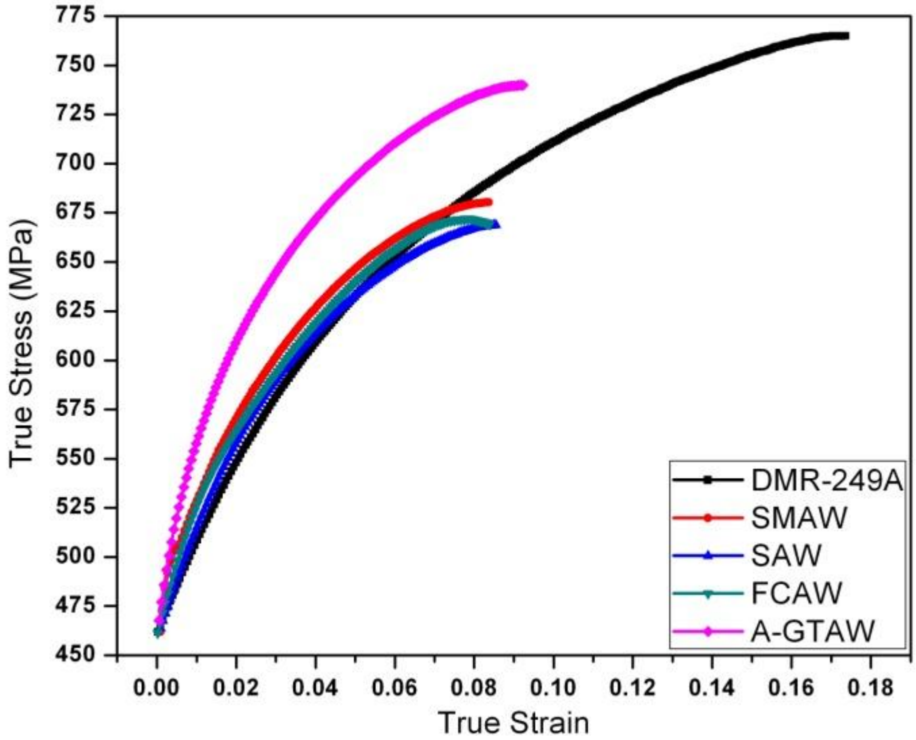

Fig.7.3 True Stress-Strain curves of DMR-249Abase metal and arc welded (cross weld) joints

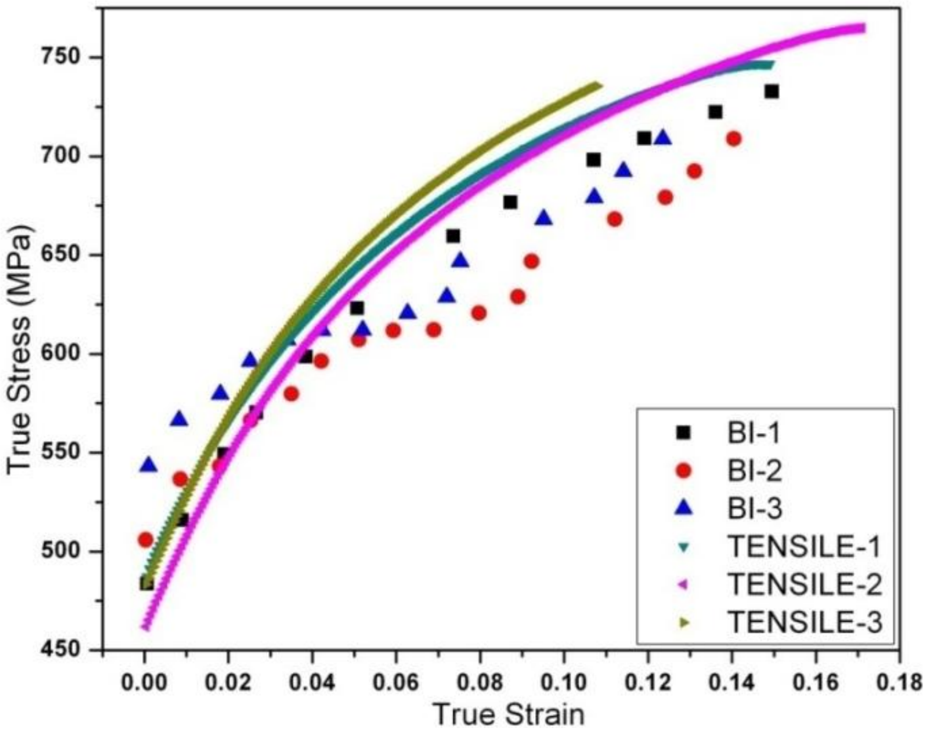

Fig. 7.4 True stress-strain curves for conventional tensile and ABI testing of DMR-249A steel

The calculated indent profiles of base metal, HAZ and weld metal in SAW specimen were compared with measured values obtained using surface profilometer. The profilometer plots obtained for weld metal, HAZ and base metal are given in Fig. 7.5. The final diameters of base metal, HAZ and weld metal as measured by surface profilometry were compared with optical measurements (Table 7.3). The optical image of a ball indentation is shown in Fig. 7.6.*The optical images of ball indentation across all weld joints is given in Appendix A5*. The comparable values obtained from measurements and calculations verified the veracity of ABI experiments conducted.

Table 7.3 Measurements of plastic diameter, plastic depth and pile up of ABI in SAW joint

SAW	Dia with Pile-up (µm)		
	Profilometer	Optical	Calculated (ABI)
BM	723	734	733
HAZ	710	702	729
WM	682	676	695

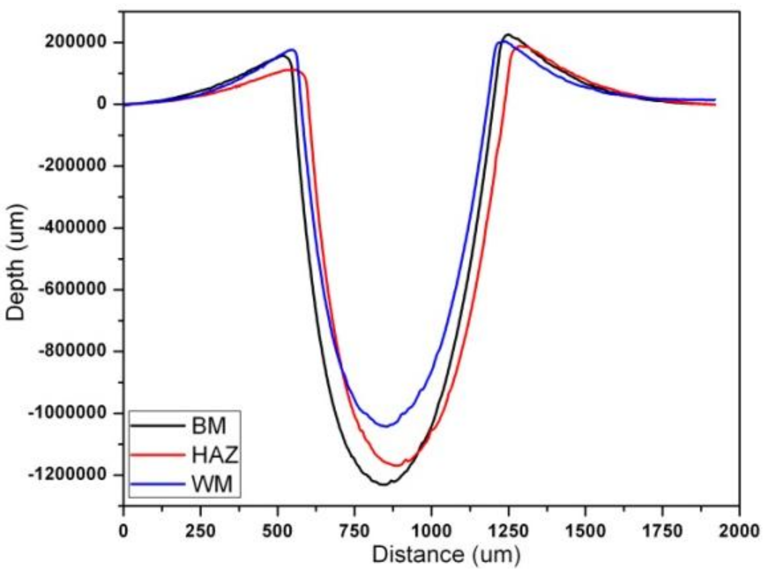

Fig.7.5 Profile of base metal, HAZ and weld metal ball indent (SAW)

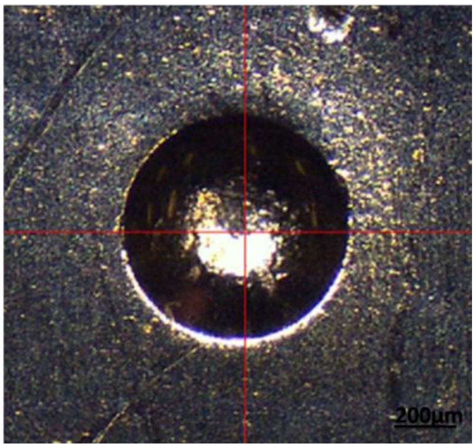

Fig. 7.6 Optical image of a ball indentball indent (SAW)

The ABI load-depth curves and derived true stress-strain curves obtained across different regions of SAW weld joint are given in Fig. 7.7. The analysis of σ-ε curves shows that the strength in the weld metal is higher as compared to HAZ followed by base metal. The high dislocation density during solidification from molten weld pool and transformation to various ferritic morphologies from equiaxed base metal resulted in increase in the hardness and strength of the weld metal. The formation of bainitic structure in HAZ results in higher values of hardness and strength to HAZ, as compared to base metal.

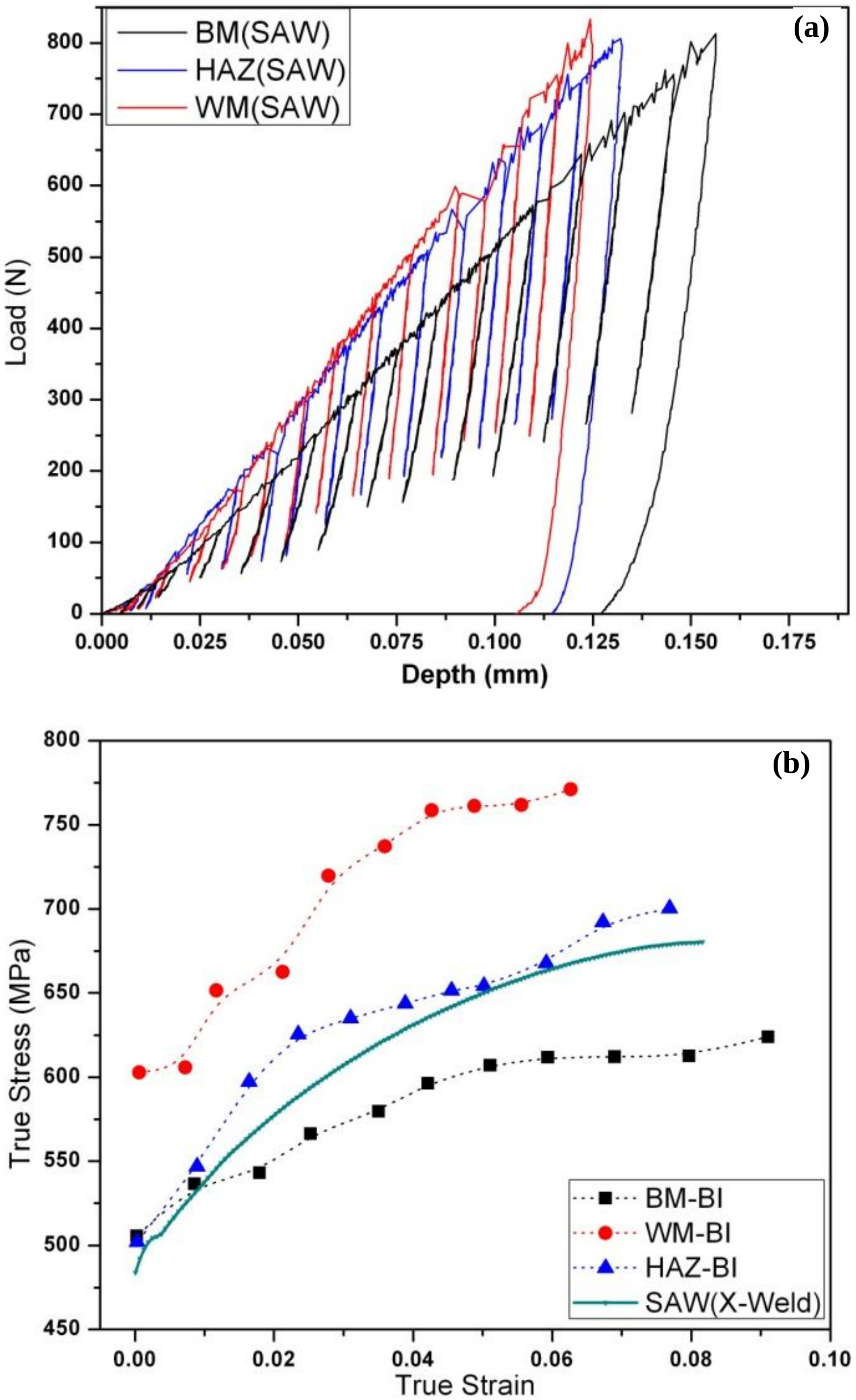

Fig. 7.7 (a) ABI load-depth curves (b) Derived true stress-strain curves across SAW weld joint

The variation of YS and UTS in theweld metal, HAZ and base metal of SAW joint is shown in Fig. 7.8. The strength values (YS and UTS) decreased systematically across the weld joint from weld metal to base metal. The weld metal was found to have highest UTS and YS of about 714 MPa and 496 MPa respectively. The UTS and YS values decreased from weld metal to HAZ. The UTS and YS values for HAZ were about 632 MPa and 428 MPa respectively.The UTS and YS values for base metal were found to be 574 MPa and 412 MPa respectively which is comparable to the strength values obtained for DMR-249A steel from conventional tensile testing (Table 6.13).

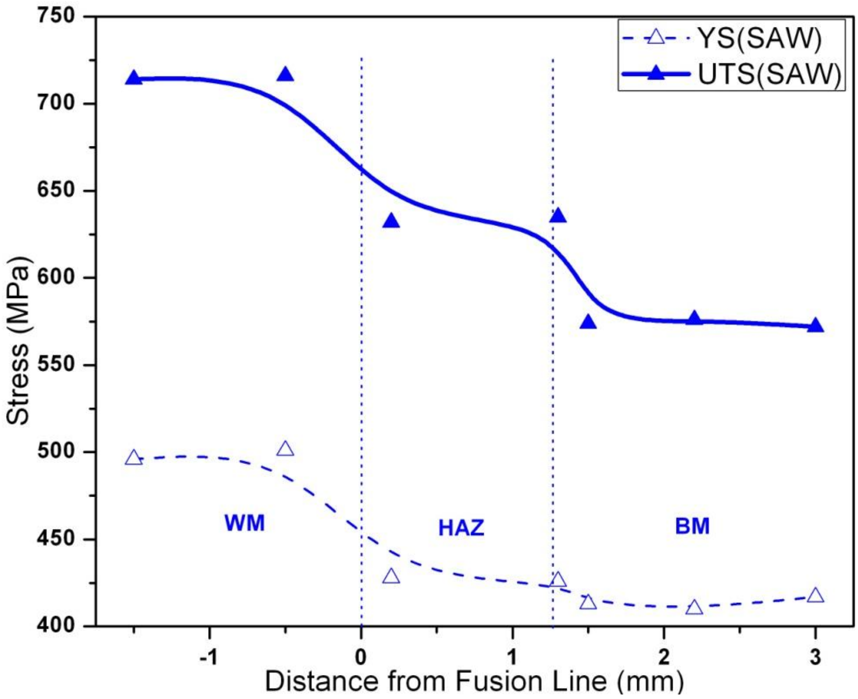

Fig. 7.8 Variation in YS and UTS in weld metal, HAZ and base metal across SAW joint

The strain hardening exponent (n) of weld metal, HAZ and base metal are 0.15, 0.20 and 0.16 respectively.The strain hardening exponent is a measure of the increase in strength of materials due to plastic deformation. The strain hardening of materials is reported to be dependent on the microstructure including grain size [257-258], temperature [259], and strain rate [260].Since strain hardening arises from the dislocation motion which is blocked at various barriers, the obstacle may be a grain boundary, subgrain boundary, tangled cell, second phase, etc. The variation of strain hardening exponents across the welded joint is essentially originated from the microstructure variation. It is observed that the weld metal and base metal have comparable strain hardening capacity. The strain hardening exponent was marginally higher for HAZ as compared to the weld metal and the base metal. While the YS and UTS in the weld metal are higher than those in the base metal and HAZ, the hardening capacity and strain hardening exponents are comparable to base metal, but lower than HAZ. The HAZ having coarser equiaxed ferritic grains shows higher strain hardening behaviour as compared to weld metal and base metal[255-256].

Similarly, the investigations of YS, UTS and ‘n’ values were carried out on SMAW, FCAW and A-GTAW weld joints. The load-indentation depth curves across weld metal, HAZ and base metal acquired by ABI (*given in Appendix A6*) were converted to true stress-strain curves (Fig. 7.9). The UTS and YS values across base metal, HAZ and weld metal obtained from API and the strengths of cross weld joint from conventional tensile testing of different weld joints are given in Table 7.4 and Fig 7.10.

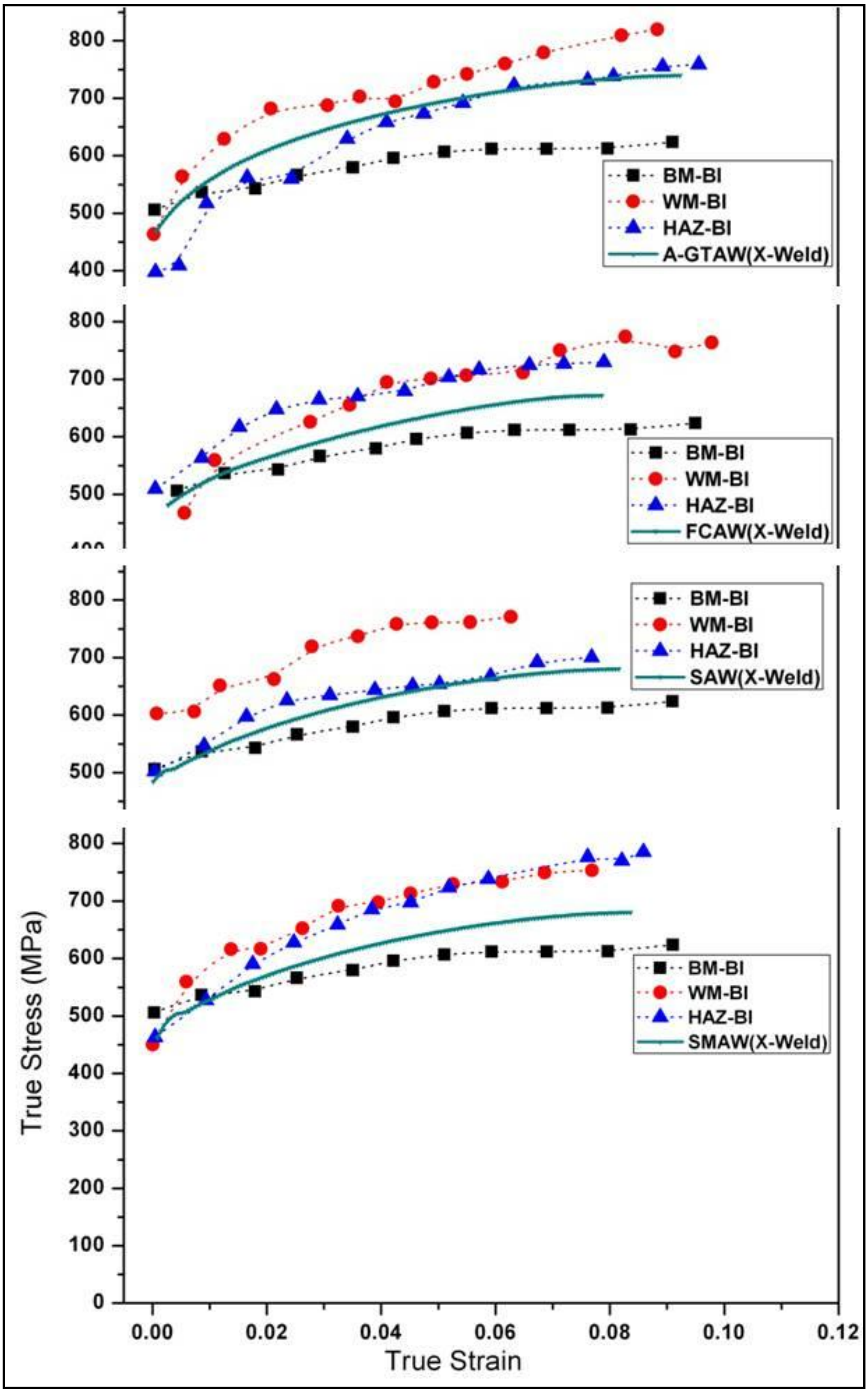

Fig. 7.9 ABI true stress-strain curves of SMAW, FCAW and A-GTAW joints

Table 7.4 UTS and YS values in MPa, across base metal, HAZ and weld metal for arc welded joints

YS	SMAW	SAW	FCAW	A-GTAW
BM	412	414	416	410
HAZ	511	428	438	496
WM	475	496	491	533
X-Weld	480	450	450	480

UTS	SMAW	SAW	FCAW	A-GTAW
BM	574	576	570	572
HAZ	744	632	668	685
WM	673	714	680	753
X-Weld	610	595	610	640

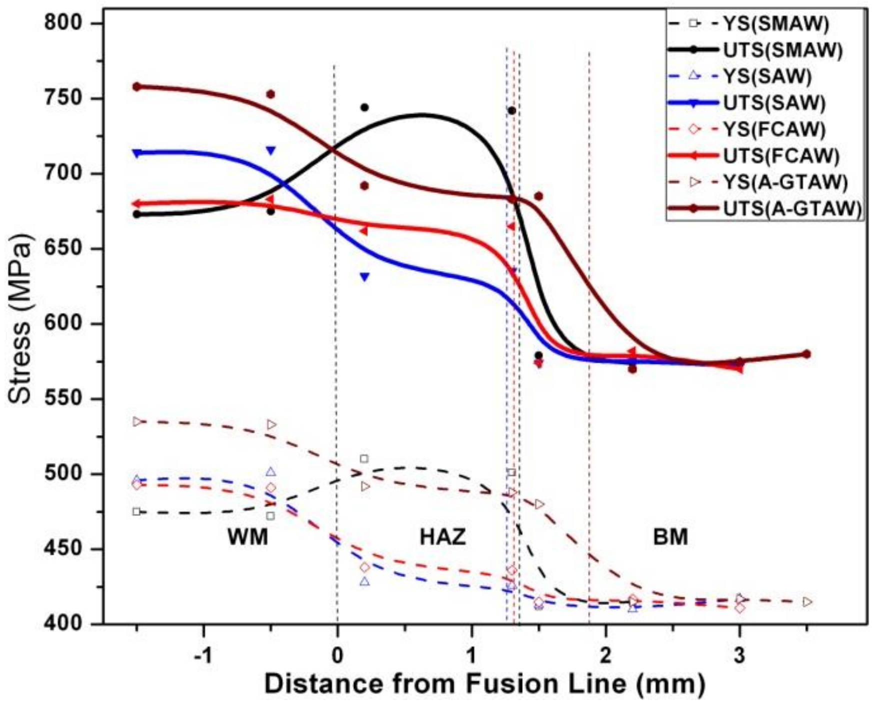

Fig. 7.10 Variation in UTS and YS values of arc values across weld joints

The strengths across the joints decreased systematically from weld metal to base metal in SAW, FCAW and A-GTAW. The strength of the SMAW HAZ was higher than the base and weld metal which is attributed to formation of higher bainitic structure in HAZ, characteristic of low heat input and higher cooling rate of HAZ associated with manual welding. The weld-metal of A-GTAW joint exhibited higher yield strength followed by SAW, FCAW and SMAW respectively. The HAZ of

SMAW joint showed higher YS followed by A-GTAW, FCAW and SAW. In all the arc welded joints, YS and UTS followed similar pattern. The SMAW and A-GTAW were observed to have the largest variation of YS and UTS across the joint.

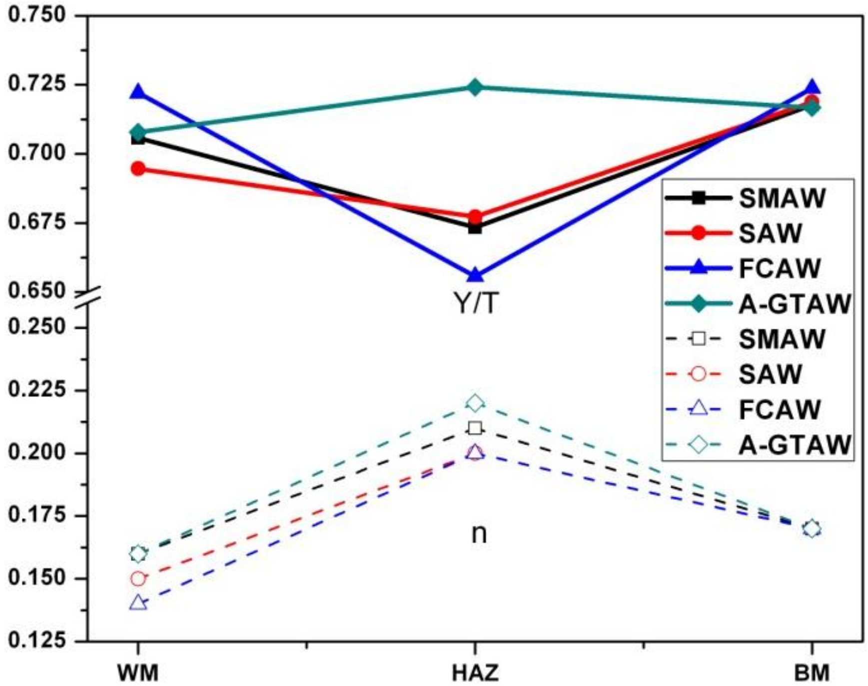

Fig. 7.11 Variation in Y/S ratio and strainhardening exponent welded joints

The strain hardening exponent for weld metal, HAZ and base metal of arc welded joints are plotted in Fig. 7.11. The ABI strain hardening exponent calculated for base material was 0.17. The strain hardening exponent calculated using ABI data was found to be comparable with strain hardening of 0.18 determined experimentally with conventional tensile testing. The strain hardening exponent was found to be comparable across the weld joints with marginally higher values for HAZ. The strain hardening exponent values of HAZ for all the weld joints was comparable. The higher strain hardening exponent values for the HAZ can be related to the coarse grain size effect. The microstructures with larger grain size accommodate more dislocations, hence higher strain hardening capacity [260-261]. Generally, the weld metal is expected to have lower strain hardening exponent due to higher dislocation density [260-261]. The strain hardening exponent is also reported to be comparable with base metal for over-matching weld joints and HSLA weld joints [262-263]. Sufficient strength in weld metal with strain hardening behaviour comparable to base metal is attributed to columnar width and higher percentage of multidirectional acicular ferrite in microstructure. It is generally accepted that the lower the ratio of YS/UTS (Y/T), the better the strain hardening capacity [264, 265]. The calculated values of strain hardening exponent were observed to correlate with Y/T values. The deviation of strain hardening exponent behavior with that of Y/T for A-GTAW HAZ is attributable to the presence of a coarse grain structure. While the coarse grains in A-GTAW HAZ contribute towards higher strain hardening exponent, the difference in the values of YS and UTS was not significant. The comparable values of strain hardening exponent for weld metal and base metal show the balanced strength and ductility of the welds. The values of strain hardening exponent across the weld joints are given in Table 7.5.

Table 7.5 ABI values of strain hardening exponent across the weld joints

Strain Hardening Exponent (n)	SMAW	SAW	FCAW	A-GTAW
BM	0.17	0.17	0.17	0.17
HAZ	0.21	0.20	0.20	0.22
WM	0.16	0.15	0.14	0.16

7.5 Conclusions

The conclusions based on investigations to evaluate the mechanical properties across the SMAW, SAW, FCAW and A-GTAW weld joint in DMR-249A steel are summarized as follows:

(a) Mechanical properties of DMR-249A steel arc welded joints were evaluated using an automated ball indentation technique. The ABI technique was found to be a simple technique for approximate characterization of mechanical properties across the weld joints by using a small amount of test materials.

(b) The YS, UTS, and strain hardening exponent for base metal as calculated using ABI data were found to be comparable to those obtained from conventional tensile testing for DMR-249A steel.

(c) The tensile strength was observed to vary significantly across the weld joints. The strength values (YS and UTS) decreased systematically across the weld joint from weld metal to base metal.

(d) The A-GTAW joint weld metal exhibited higher yield strength followed by SAW, FCAW and SMAW respectively. The HAZ of SMAW joint showed higher YS followed by A-GTAW, FCAW and SAW. In all the arc welded joints, YS and UTSfollowed similar pattern. The SMAW and A-GTAW were observed to have the largest variation of YS and UTS across the joint.

(e) The strain hardening exponent was found to be comparable across the weld joints with marginally higher values for the HAZ. The comparable values of strain hardening exponent for weld metal and base metal shows the balanced strength and ductility of the welds.

Chapter 8. Comparison of Corrosion Characteristics

8.1 Introduction

For naval structural material, the deterioration of structural strength and structural integrity is a major factor in assets management. This type of deterioration is influenced by the loss of section thickness for structural elements and by the potential for loss of integrity through corrosion; specially, where protective measures such as paint coatings, galvanizing and cathodic protection are ineffective. Various studies have been carried out to understand stress corrosion cracking, hydrogen induced cracking, microorganism induced corrosion, pitting, crevice and general corrosion behaviour of base metal and weld joints for the HSLA steels [266-272]. The corrosion processes that occur are usually a result of anodic currents. Information on corrosion rates, passivity and pitting tendencies can be obtained by measurements of current-potential relations under carefully controlled conditions. The specimen potential is scanned slowly towards positive current and therefore acts as an anode such that it corrodes or forms an oxide coating. These measurements are used to determine corrosion characteristics of a material in aqueous environments.Standard anodic polarization plot for steel is given in Fig 8.1.

This chapter discusses comparison of electrochemical properties of both DMR-249A steel and the weld metals of welded butt joints fabricated with four different welding processes: Manual process - Shielded Metal Arc Welding (SMAW) and Automatic processes - Submerged Arc Welding (SAW), Flux Cored Arc Welding (FCAW) and Activated Gas Tungsten Arc Welding (A-GTAW)by conducting potentiodynamic anodic polarization studies.The difference in OCP and corrosion rate observed in the base metal and the four different weld joints was observed to be negligible. The base metal (DMR-249A steel) and all weld joints demonstrated similar trends of corrosion within acceptable scatter band, establishing that the welding process has not deteriorated the corrosion properties of the base metal. DMR-249A steel was compared with other commercial ship building steels (ABA and D40S) of Russian origin. The corrosion characteristics of DMR-249A steel with ABA and D40S steels showed comparable and analogous trends and extent of corrosion.

8.2 Experimental details

8.2.1 Fabrication of weld joints

Welded plates were cut to fabricate five corrosion test specimens of 60x20x10 mm^3, one each for SMAW, SAW, FCAW, A-GTAW and Base Metal. Two specimens of 20x20 mm^2 sizes were fabricated from 6 mm and 16 mm plates of ABA and D40S sheets respectively. All the seven samples were polished from 80 to 2400 grit SiC papers, followed by diamond paste (1 μm) to obtain mirror finish. The polished specimens were thoroughly degreased by ultrasonic cleaning in acetone.

The material composition of the ABA and D40S steelsis given in Tables 8.1.

Table 8.1 Chemical Composition (wt.%) of ABA and D40S materials

ABA

C	S	P	Mn	Si	Al	Ni	Nb	V	Ti	Cu/Cr	N_2(ppm)
0.09	0.008	0.13	1.54	0.22	0.024	0.72	0.037	0.18	0.021	<0.020	54

D40S

C	S	P	Mn	Si	Al	Ni	Nb	V	Ti	Cu	Cr	N_2(ppm)
0.11	0.025	0.025	0.7	1.0	0.02	0.7	-	-	-	0.5	0.8	Max 0.008

8.2.2 Electrochemical Studies

A conventional three-electrode (Fig 8.2) cell assembly was used for polarization measurements. The potentiodynamic anodic polarization measurements were performed in a flat cell, which has a Teflon O-ring lined hole on one side. The polished surface of the test coupon (the working electrode) was pressed against the O ring, so that the solution in the cell could access the surface inside the O-ring. The reference and counter electrodes are fixed in slots provided on the top of the flat cell. The surface area of the working electrode was 1 cm^2. An Ag/AgCl electrode and a graphite electrode were used as reference and counter electrode respectively. Sea water from Kalpakkam (Bay of Bengal) coast (salinity – 35000 ppm, chloride – 18,981 ppm, sulfate – 2650 ppm, pH – 8.1) [273-274] and fresh water (salinity – 350ppm) were used as the electrolytes.

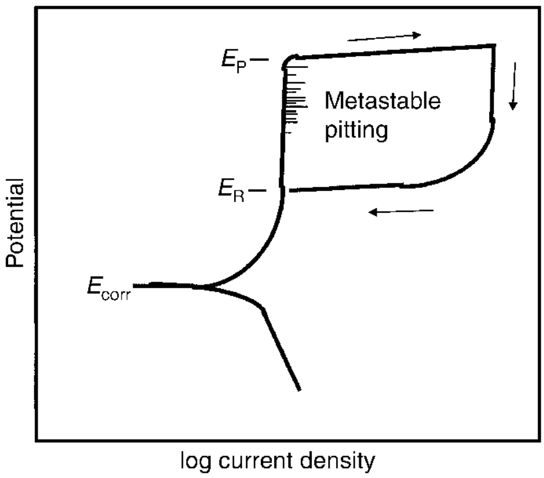

Fig 8.1 Std Anodic Polarization Plot- SS

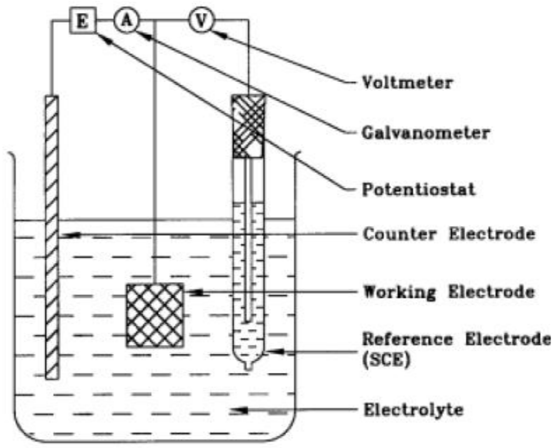

Fig8.2Electrical Circuitry For Polarization Measurement

A computer controlled potentiostat (AUTOLAB PG60, Netherlands) was used to conduct the potentiodynamic polarization experiments. The anodic polarization experiments in sea water and fresh water and cathodic/anodic polarization in Tafel region in 3.5% NaCl sea water were carried out as per ASTM standards G 3, G 5, G 59 and G 102 [275 - 278]. The anodic polarization experiments were conducted from

OCP to + 1.60 V (SCE) at a scan rate of 10 mV/min (0.167 mV/s). The tafel plot measurements were performed from -0.3 to -0.9 V (region greater than 200 mV on anodic and cathodic side of the corrosion potential).

Afterpolarization experiments, the specimens were observed under an optical microscope to study the morphology and extent of pitting attack. Further, the specimens were imaged under "SNE3000M Korea" make desktop mini-SEM for detailed pit morphological studies.

8.2.3 Surface Profile Measurements

Talysurf CLI 200, Taylor Hobson Precision, machine was used to carry out surface profile measurements. Data from pitted samples after polarization study was collected one point at a time with each point having a discrete X, Y, Z location with directional resolution of 0.5μm. The profilometry was carried out using laser gauge and CCD sensor for three of the specimens to corroborate the corrosion trends.

8.3 Results and Discussion

One simple way to study the film corrosion characteristics of steel in a solution is to monitor the open-circuit electrode potential as a function of time. The anodic polarization graphs of DMR-249A steel and four welding processes in sea water and tap water are given in Fig 8.3 and8.4 respectively. The comparative graphs of DMR-249A, ABA and D40S steels in sea water and fresh water are given in Fig 8.5.

The experiments conducted in sea water as medium to measure OCP and limiting current at 200mV for ascertaining corrosion characteristics seemed to be very similar with virtually indecisive separation in corrosion rates and trends. The OCP and limiting current values for sea water experiments are given in Table 8.2.

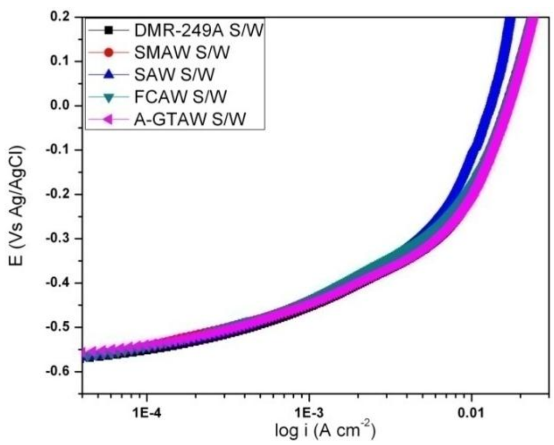

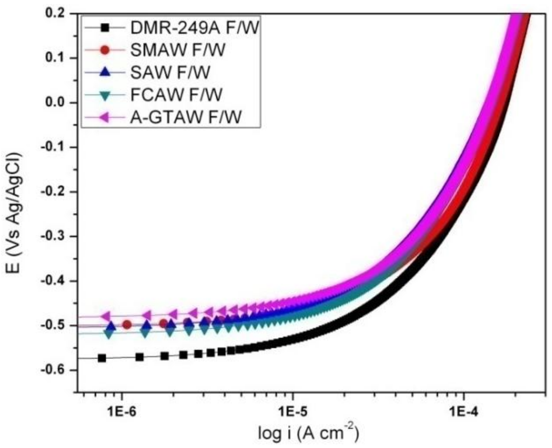

Fig 8.3Potential-Current Graph for Weld Processes(S/W) Fig8.4Potential-Current Graph for Weld Processes (F/W)

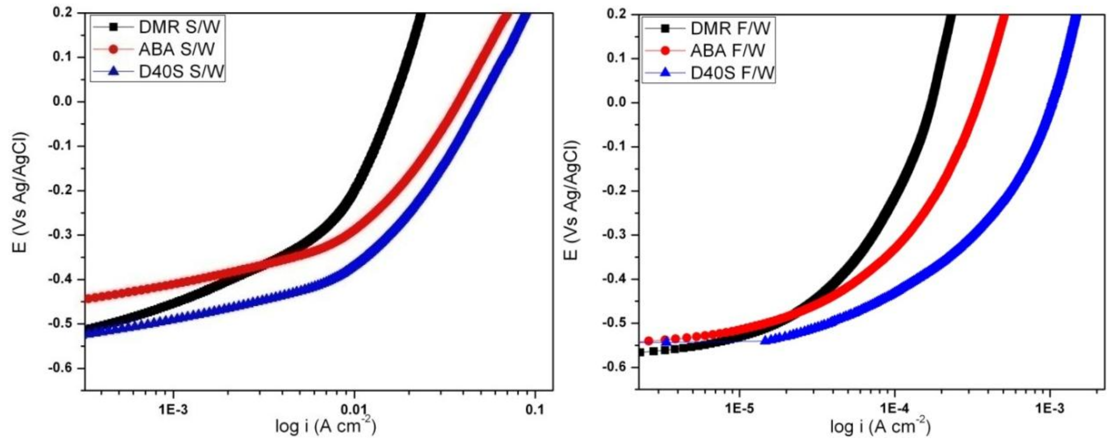

(a) Potential- Current :Steels (S/W) (b) Potential- Current G : Steels (F/W)

Fig 8.5 Comparative graphs of DMR-249A, ABA and D40S steels in S/W and F/W

Table 8.2 OCP and limitingcurrent at 200mVfor S/W

SNo.	Specimen	OCP (S/W) (V)	Limiting Current at 200 mV (S/W)(Amps)
1	A-GTAW	-0.5838	0.02433
2	SMAW	-0.5933	0.02354
3	FCAW	-0.5914	0.02356
4	SAW	-0.5917	0.01723
5	DMR-249A	-0.5983	0.02313
6	ABA	-0.5849	0.05191
7	D40S	-0.6038	0.0877

Fig 8.3 shows that corrosion characteristics in sea water seemed to be very similar with virtually indecisive separation in corrosion rates and trends. Tests in lesser aggressive environments i.e. tap water gave a better separation of corrosion

resistance (Fig 8.4). The OCP and limiting current values of DMR-249A steel and arc welded joints for fresh water experiments are given in Table 8.3.The OCP and cut off current of DMR 249A, ABA and D40S in sea water and fresh water is given inTable 8.4.It was observed that the OCP shifted to more negative values and limiting current at 200 mVwas higher in sea water as compared to experiments conducted in tap water, showing higher corrosion rate in sea water (Table 8.2-8.4).Though minor difference in OCP and limiting current at 200mV were observed in the base metal and the four different welding processes, but all specimens demonstrated values within small scatter band andsimilar trends of corrosion curves. The least negative OCP of -0.4822 was observed for A-GTAW specimen whereas most negative OCP of -0.5757 was observed for DMR-249A steel specimen. The minimum and maximum current at cut off voltage of 200mV was found to be 2.0390E-4 and 40.18E-4 for A-GTAW specimen. The characteristic current at switchover from negative to positive electrodynamic potential in fresh water and sew water medium (Table 8.5) also showed inconsequential difference for the base metals DMR 249A, ABA and D40S.

Table 8.3 OCP and Limiting Current at 200mV of Arc Welded Joints for F/W

SNo.	**Specimen**	**OCP F/W**	**Limiting Current at 200mV F/W**
1	A-GTAW	-0.5276 to -0.4822	2.0390E-4 to 40.18 E-4
2	SMAW	-0.5194 to -0.5005	2.2815E-4 to 24.32 E-4
3	FCAW	-0.5197 to -0.4911	2.0980E-4 to 36.46 E-4
4	SAW	-0.5049 to -0.5264	2.0585E-4 to 39.32 E-4
5	DMR-249A	-0.5757 to -0.5073	2.3216E-4 to 31.93 E-4

Table 8.4 OCP and Cut Off Current at 200mV of Steels for F/W

SNo.	**Specimen**	**OCP F/W**	**Cut off Current at 200mV F/W**
1	DMR 249A	-0.5757 to -0.5073	2.3216E-4 to 31.93 E-4
2	ABA	-0.5501 to -0.5200	5.104E-4 to 47.77 E-4
3	D40S	-0.5797 to -0.5333	14.6E-4 to 27.88 E-4

Table 8.5 Current at Switchover from Negative to Positive Potential

Specimen		A-TIG	SMAW	FCAW	SAW	DMR	ABA	D40S
Changeover Current (A)	S/W	0.017	0.017	0.067	0.013	0.016	0.012	0.048
	F/W	1.43E-4	1.63E-4	1.48E-4	1.39E-4	1.736E-4	3.43E-4	0.001

To clarify the differences in corrosion trends, cathodic and anodic polarization studies in the Tafel region were conducted on the specimens in 3.5% NaCl medium to determine the values of corrosion rate, polarization resistance and Tafel constants [279]. Each potentiodynamic polarisation experiment was performed three times to regularise any experimental variations and fluctuations and to obtain reliable results. The Tafel plots for the four weld metals and the three base metals are given in Fig8.6. The corrosion current (I_{corr}) was observed to be in the range of 5.535 E-5 to 9.832 E-6 Amp/cm^2 for the weld metals and 2.975 E-6 to 6.936 E-6 Amp/cm^2 for the base metals. The corrosion potential (E_{corr}) was found to be between -0.702 and -0.647 V for all the tested specimens. The density (ρ) for tested specimens was taken as 7.8 gm/cm^3, equivalent weight of corrosion products as 27.923 gm and corrosion surface area of 1 cm^2 for calculation of corrosion rate in mm per year (CR (mpy)). The corrosion rates of the weld metals varied from 6.483 E-2 to 11.67 E-2 mpy and of base metals from 3.485 E-2 to 8.124 E-2. The comparison of Tafel plot characteristics (cathodic slope b_c, anodic slope b_a and polarization resistance R_p), $I_{corr,}$ E_{corr} and CR for weld joints and base metals is given in Table 8.6. Though minor differences in Tafel characteristics and corrosion rates were observed in the three base metals and the four different weld metals, all the specimens demonstrated similar trends within the range of 0.03 to 0.1 mpy, with a small scatter band.

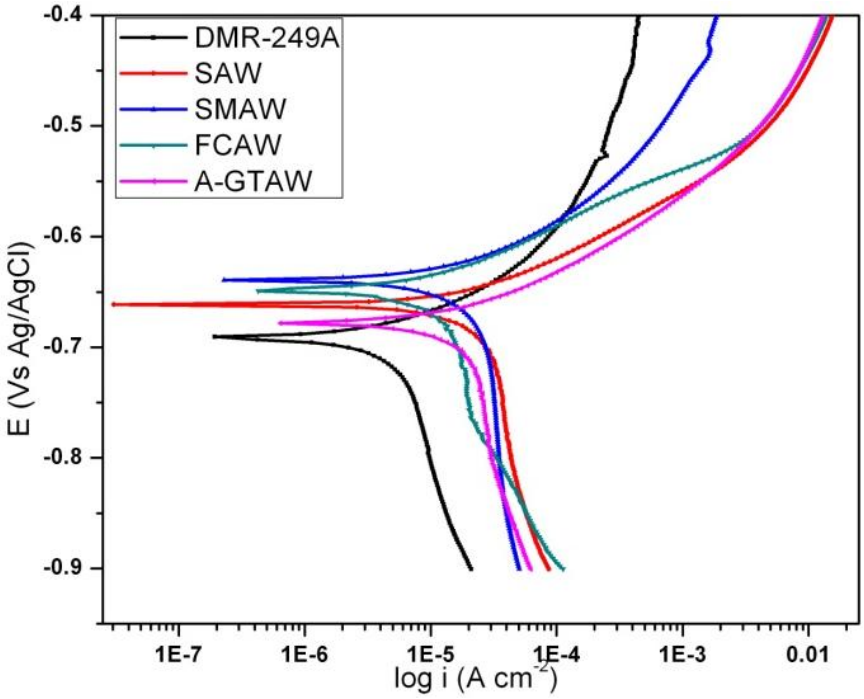

Fig 8.6(a) Tafel Plot – Weld Joints

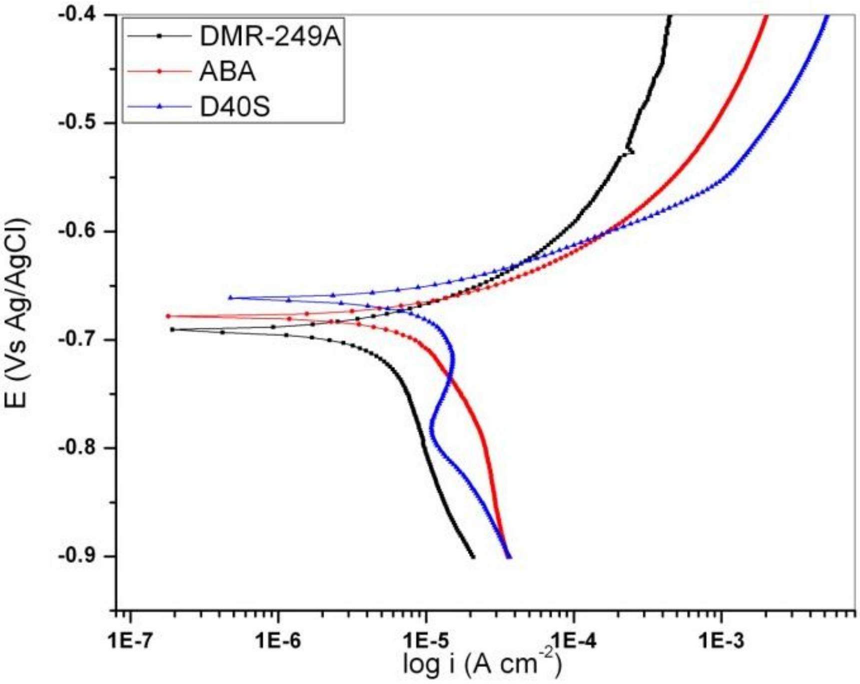

Fig8.6(b) Tafel Plot – Steels

Table 8.6 Comparison of Tafel Plot Characteristics

Specimen	b_c (V/dec)	b_a (V/dec)	R_p (E+2 Ω)	I_{corr} (E-6 Amp/cm^2)	E_{corr} (mV)	CR (E-2 mpy)
Weld Metals						
SMAW	0.062±0.007	0.058±0.005	1.88±0.3	8.296±1.0	-639±30	9.718±0.5
SAW	0.044±0.007	0.055±0.006	1.046±0.4	9.967±1.0	-671±30	11.67±0.4
FCAW	0.053±0.006	0.054±0.005	2.21±0.5	5.535±1.1	-657±30	6.482±0.6
A-GTAW	0.046±0.006	0.055±0.006	1.132±0.3	9.832±0.7	-659±30	10.31±0.3
Base Metal Steels						
DMR-249A	0.080±0.007	0.063±0.006	7.393±0.4	2.975±1.0	-692±30	3.485±0.3
ABA	0.187±0.006	0.055±0.008	6.46±0.3	6.936±1.4	-678±30	8.124±0.4
D40S	0.059±0.008	0.054±0.008	2.031±0.5	6.235±1.2	-671±30	7.303±0.6

Many corrosion studies have established that inferior corrosion resistance for weld metal as compared to base metal is due to segregation effect [280-283]. The similar corrosion characteristics observed in DMR-249A steel and weld metals of four different arc welded joints can be attributed to low Chromium content in the base metal (Refer Tables 2.1 and 6.3). Due to the low Cr content, the segregation effect does not cause much of difference in corrosion properties of the base metal and different weld metals.Earlier research work has established the effect of composition and alloying elements on corrosion behavior of this type of steel [284-288]. The studies have established the detrimental effect of carbon and beneficial effect of Nickel in steel. The marginal increase of Ni content and decrease of C in weld metals of DMR-249A steel arc weld joints (Refer Tables 2.1 and 6.3) may have also contributed to prevent any deterioration of corrosion in weld metal specimens. DMR-249A and ABA steels have similar composition. In comparison to DMR-249A and ABA steels, D40S steel has higher carbon and absence of Nb, V and Ti. However, significant amounts of Cu and Cr are present and would have compensated the detrimental effect of higher carbon content [289-290].

The photographs of specimens used for post anodic polarization experiments in fresh water and sea water are given in Fig8.7. The specimens of ABA and D40S steels used for anodic polarization studies are shown in Fig8.8.

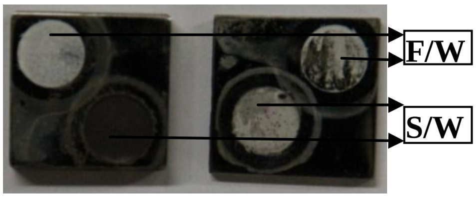

Fig8.7BM, SMAW, SAW, FCAW& S/W Polarised Samples

Fig8.8D40S and ABA S/W and and A-GTAW-F/W Specimen

Though the electrochemical polarisation studies showed similar behaviour for DMR-249A base metal and weld metals of arc weld joints, the optical microscopy and SEM observations showed different forms of pitting morphology for the specimens. The base metal showed general uniform attack all around the surface with a few pits of excessive depths. The SMAW weld joint specimen showed groups of shallow pits with small diameters, similar to base metal, which can be attributed to lesser inclusions in the weld metal. The SAW, FCAW and A-GTAW specimens showed shallow pitting with larger diameter which is attributed to the presence of inclusions in weld metals acting as corrosion initiation sites. This is similar to the observations made in published literature on effects of inclusions as sites for nucleation corrosion pits [291-294].

The weld microstructure obtained in this study was found to be refined and deleterious mixture of bainite and martensite was not observed. Is observed and analyzed from Fig6.11 & 6.12 and Table 6.3&6.5 that grain size, element composition and crystal structure all vary across the weld metals of the arc welded joints of

SMAW, SAW, FCAW and A-GTAW. It has been reported that differences in microstructure influence pit depth [295]. The variation in concentration of alloying elements in weld metal and base metal and also intra weld metal result in dissimilar metal couples that produce macroscopic galvanic corrosion. The development of localised anodic-cathodic regions and the formation of galvanic couplesleads to preferential attacked of corrosion on these areas [296-297]. In ferritic steels, the cementite lamellar of pearlite acting as cathode and the ferrite as anode also contributes towards galvanic and pitting corrosion [298].

After the polarization experiments, the specimens were examined under optical microscope and scanning electron microscope (SEM). The micrographs of the optical and SEM are given in Fig8.9 (b) and (c) respectively.The optical and SEM micrographs show general corrosion accompanied by pitting in base metal and weld joint specimens. The pits of bigger diameter were observed in weld joints (30 to 50 μm), whereas pitting observed in base metal (4 to 12 μm) was of least diameter amongst all the specimens.

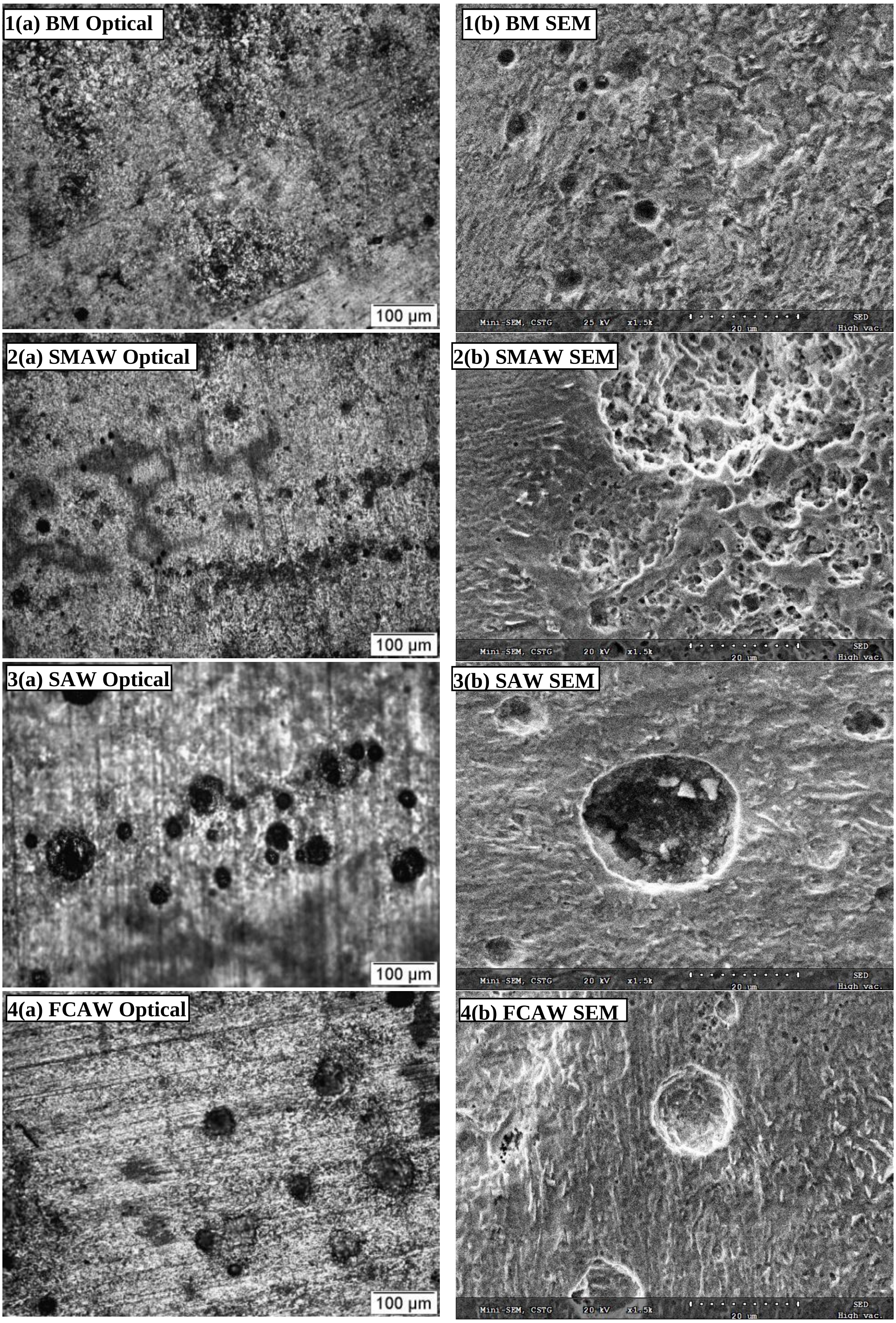
1(a) BM Optical
100 µm
1(b) BM SEM
Mini-SEM, CSTG 25 kV x1.5k 20 um SED High vac.
2(a) SMAW Optical
100 µm
2(b) SMAW SEM
Mini-SEM, CSTG 20 kV x1.5k 20 um SED High vac.
3(a) SAW Optical
100 µm
3(b) SAW SEM
Mini-SEM, CSTG 20 kV x1.5k 20 um SED High vac.
4(a) FCAW Optical
100 µm
4(b) FCAW SEM
Mini-SEM, CSTG 20 kV x1.5k 20 um SED High vac.

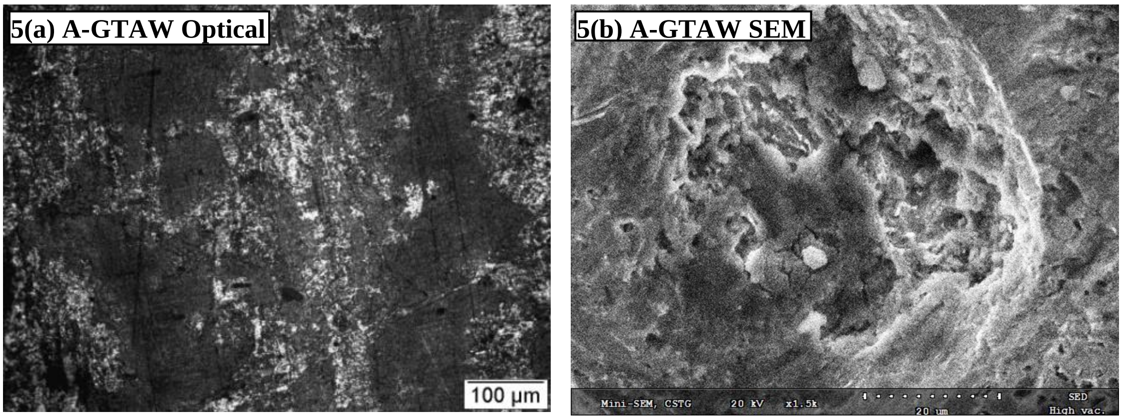

Fig 8.9Micrographs of corrosion in specimen post electrodynamic polarisation

1. BM (a) Optical (200x) and (b) SEM 1500x
2. SMAW (a) Optical (200x) and (b) SEM 1500x
3. SAW (a) Optical (200x) and (b) SEM 1500x
4. FCAW (a) Optical (200x) and (b) SEM 1500x
5. A-GTAW (a) Optical (200x) and (b) SEM 1500x

The depth of corrosion was observed to be 15 to 20 µm for fresh water as medium and 60 to 70 µm for sea water as medium of corrosion. The depth of corrosion i.e. difference between the original surface area and experimentally corroded area, as observed from surface profiling is given in Table 8.7. The depth of corrosion and pitting as seen from surface profile plots also confirm similar corrosion attack on DMR-249A steel and arc welded joints.

Table 8.7 Depth of Pitting in Surface Profiles

Specimen	A-GTAW		SMAW		BM	
Medium	F/W	S/W	F/W	S/W	F/W	S/W
Depth of Pitting (µm)	15	60	17	70	20	60

The analysis of Table 8.8 and Fig 8.10 substantiate that DMR-249A base metal and weld joints demonstrate similar corrosion characteristics. The deeper pitting observed in sea water shows higher corrosion rate as compared to fresh water.

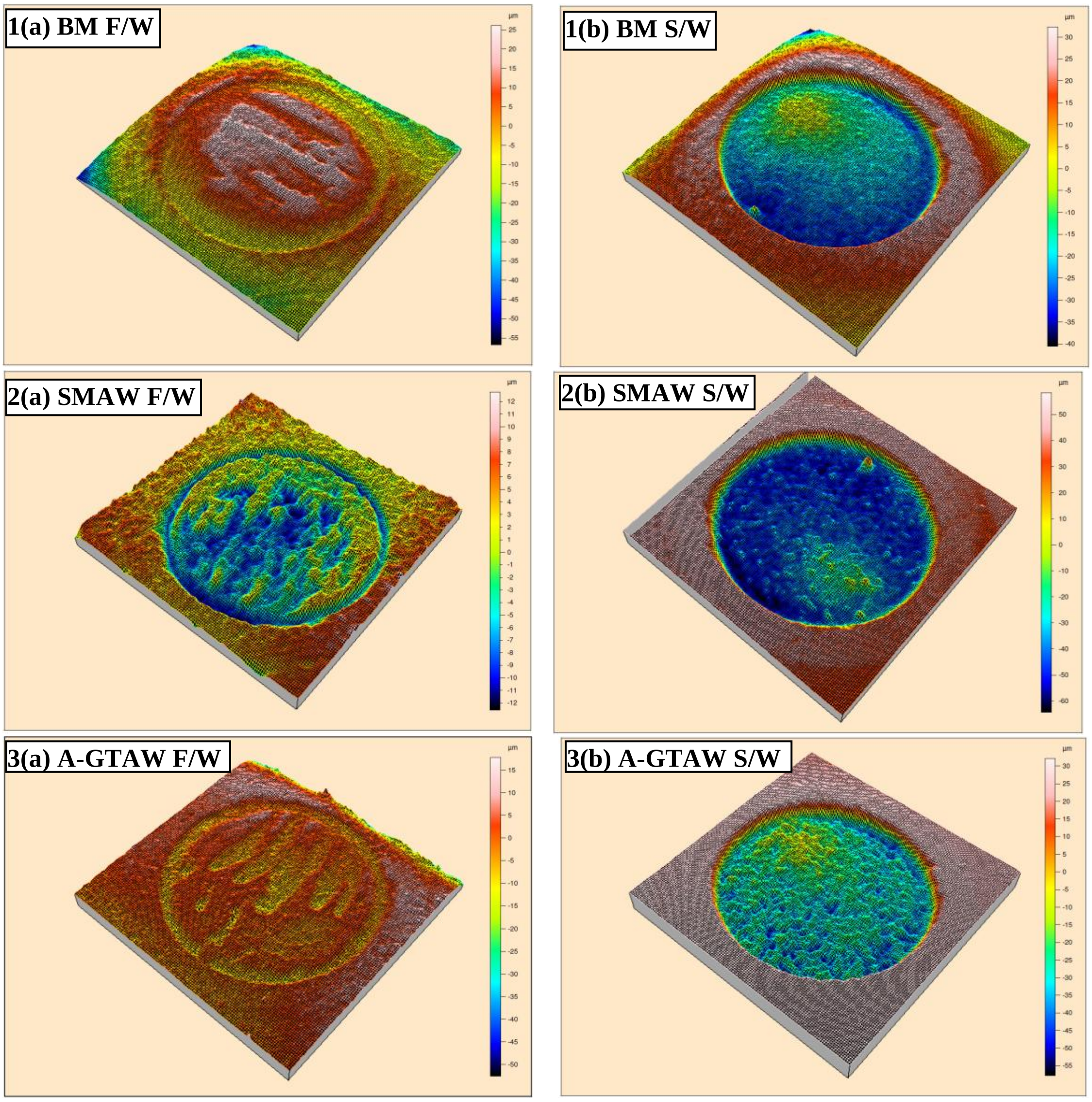

Fig8.10Surface Profile of BM, A-GTAW and SMAW in F/W and S/W

8.4 Conclusions

The results of the investigations can be summarized into following conclusions:-

(a) The base metal and weld metals of arc welded joints displayed similar corrosion characteristics for general and pitting corrosion in sea water and fresh water. It was concluded that the arc welding processes do not deteriorate the corrosion characteristics of the base metal, DMR-249A.

(c) The pitting diameter was observed to be smaller for base metal and bigger for weld specimens and attributed due to the presence of inclusions in weld metal.

(d) The experiments for corrosion characteristics of DMR-249A steel with ABA and D40S steels showed comparable trends and similar extent of corrosion in these HSLA steels being used for shipbuilding.

Chapter 9. Summary and Future Works

9.1 Summary

The objective of the research was to study the effect of arc welding processes on weld attributes of DMR-249A steel joints and development of activated flux for DMR-249A steel to achieve enhanced depth of penetration over conventional GTAW process. The feasibility of developing A-GTAW as an alternative welding technique for DMR-249A steel was examined by studying the thermomechanical behaviour, microstructure, mechanical properties and residual stresses of weld joints fabricated by the A-GTAW process. The thermal gradients and residual stress profiles of SMAW and A-GTAW process were simulated using FEM and compared with experimental results. The effect of different arc welding processes on weld attributes of DMR-249A welded joints was compared by studying the microstructure, mechanical properties, residual stresses and corrosion characteristics of the weld joints.The summary of the research findings are as follows:-

(a) An activated flux to enhance depth of penetration for weldingDMR-249A steel using a GTAW process was developed successfully.

(b) A DOP of 7.8 mm was achieved by using the developed activated flux with GTAW process in single pass compared to DOP of 3.2 mm with GTAW without flux (increase of 250% more than the conventional autogenous GTAW process).

(c) D-Optimal (RSM) and Taguchi experiment design optimization techniques confirmed the significance of current, torch speed and arc gap (in decreasing order of significance) on depth of penetration. The RSM (D-Optimal) was observed to predict optimized welding process parameters for achieving maximum DOP with better accuracy during A-GTAW process.

(d) Weld joints of DMR-249A steel were fabricated using SMAW, SAW, FCAW and A-GTAW processes for comparing microstructure, mechanical properties, residual stresses and corrosion characteristics of different arc welding processes.

(e) Numerical models for A-GTAW and SMAW were developed for prediction of residual stresses in DMR-249A steel weld joints and the results were validated using non destructive testing. There was good agreement between the measured and predicted thermal cycles and residual stress profiles for the weld joints fabricated by SMAW and A-GTAW processes.

(f) Tensile tests were undertaken to derive acousto-elastic constant (AEC) (transit time versus load relation required for measuring residual stresses using UT) for DMR-249A steel. The AEC for DMR-249A steel was measured to be 0.069 ns/MPa. The residual stresses profiles in SMAW and A-GTAW joints were found to be similar. The stress values as measured by XRD and UTwere found to be comparable.

(g) The examination of inclusions in weld metal associated with SMAW, SAW, FCAW and A-GTAW processes indicated the presence of the least number of inclusions in the SMAW joint of about 16.1 per mm^2 and area fraction of 0.186. The SAW joint was evaluated to have numerous small and large inclusions, predominantly spherical, in clusters which are characteristic of the SAW welding process due to fast solidification of the weld pool leading to entrapment of more inclusions. The FCAW joint was observed to have more of finer inclusions of spherical and elongated shapes. The inclusions found in A-GTAW joint were largely scattered and spherical in shape.

(h) The micro inclusions of SMAW, FCAW and A-GTAW were found to contain Al, Si, Mn and Ti oxides whereas micro inclusions in SAW weld metal were observed to be predominantly Si and Mn oxides and traces of Al or Ti were not observed. The inclusions with size greater than 2 μm in SMAW, SAW, FCAW and A-GTAW were found to be consisting of Si, Mn and Ca oxides, with inclusions in A-GTAW showing predominantly Si oxides and inclusions in SAW showing some traces of Ti oxides also.

(i) The micrographs of weld metals of arc welded joints exhibitedweld metal microstructure with grain boundary ferrite, Widmanstatten ferrite with aligned second phase along with veins of ferrite, acicular ferrite, polygonal ferrite, bainite and microphases as compared to predominantly fine grained equiaxed ferrite microstructure of DMR-249A steel.The minor changes in percentage of volume fraction of the different ferrites (grain boundary, Widmanstatten, acicular and polygonal) were observed in the samples characteristic to the difference in heat input of the various arc welding processes. SMAW weld metal exhibited highest percentage of acicular ferrite and high volume fraction of Widmanstatten ferrite was observed in A-GTAW weld metal.

(j) The hardness values measured across the weld joints were found within the scatter band of 200 -290 $HV_{0.2}$ as compared to values of 196-210 $HV_{0.2}$ for base metal. The hardness of weld metal was monitored to be higher than the base metal. The micro-hardness values gradually increases from base metal to HAZ and a minor decrease in the hardness value was observed near the fusion zone followed by higher hardness values in weld metal.

(k) The UTS values of DMR-249A steel and arc welded joints were found to be comparable. The weld joints were found to have minor increase in yield strength with corresponding decrease in ductility compared to base metal.

(l) The V-notch Charpy impact tests confirmed that base metal possesses excellent impact toughness even at sub zero temperatures of -60°C which is due to fine equiaxed grains. The all weld joints have appreciable impact toughness at room temperature. The toughness values for SMAW, and FCAW joints were assessed to be within acceptable limits at -60°C.

(m) The A-GTAW weld joint indicated good impact toughness value of 200 J at room temperature. A significant reduction in toughness of A-GTAW joint at sub zero temperatures is attributed to scattered acicular ferrites and embrittlement due to more percentage of grain boundary ferrite in high heat input double pass A-GTAW weld joint. The coarse grains of A-GTAW weld metal are also a significant factor leading to decrease in sub zero impact toughness.

(n) The mechanical properties across the weld joints were evaluated using an automatic ball indentation (ABI) technique.The tensile strength was observed to vary significantly across the weld joints. The strength values (YS and UTS) decreased systematically across the weld joint from the weld metal to the base metal.

(o) The strain hardening exponent was found to be comparable across the weld joints with marginal higher values for HAZ. The comparable values of strain hardening exponent for weld metal and base metal shows the balanced strength and ductility of the welds.

(p) The base metal and weld metals of arc welded joints displayed similar corrosion characteristics for general and pitting corrosion in sea water and fresh water. It was concluded that the qualified arc welding processes did not deteriorate the corrosion characteristics of the weld joints of DMR 249A steel.

The developed multi-component flux was used to achieve significant increase in depth of penetration of about 250% in joining DMR-249A steel using A-GTAW process. The UT and FEM were found to be effective tools for measurement and prediction of residual stresses in DMR-249A weld joints. The residual stresses build-up, tensile properties of cross weld joints, tensile properties across weld zones (BM, HAZ & WM) and corrosion characteristics of the weld joint fabricated by A-GTAW process were found to be comparable with that of the weld joints fabricated by other arc welding processes. The A-GTAW weld joint indicated good impact toughness value of 200 J at room temperature. The sub zero (-60°C) impact toughness was found to be 10 J. The significant reduction in toughness of A-GTAW joint at sub-zero temperatures is attributable to more percentage of grain boundary ferrite and Widmanstatten ferrite in high heat input double pass A-GTAW welding process. The coarse grains of A-GTAW weld metal is also a significant factor leading to decrease in sub-zero impact toughness. The weld attributes of phase transformation, microstructure, inclusions and mechanical properties were found to be distinctive characteristic of the different arc welding processes studied. The hardness, tensile properties and corrosion properties were found to be comparable for all weld joints. The FCAW and SMAW joints exhibited better sub-zero impact toughness followed by SAW and A-GTAW.The significant variation in sub-zero impact toughness was attributed to the microstructral transformation of equiaxed base metal to various ferrite morphologies, grain size, inclusions and variation in chemical composition of weld metals of different joints.

9.2 Future works

Based on the detailed investigations carried out on the effect of arc welding processes on weld attributes of DMR-249A steel joints and ariving at the feasibility of developing A-GTAW as an alternative welding technique for DMR-249A steel, the important issues need to be addressed in the future work are suggested below:

(a) Development of filler wires with activated flux (coating or flux cored) for enhancing welding productivity and improving mechanical properties.

(b) Computational fluid dynamics (CFD) modeling for understanding the influence of oxides based fluxes in enhancing DOP for DMR-249A steel.

(c) Characterisation of mechanical properties like fatigue crack growth and fracture toughness of A-GTAW weld joints of DMR-249A steel.

(d) Study the effect of inclusions on formation of acicular ferrite during austenite to ferrite transformation in weld joints of DMR-249A steel.

(e) Study the effect of strain rate and temperatures (sub-zero) on the strength of weld joints.

References

[1] A.C. Kneissl, C.I. Garcia, A.J. DeArdo, in: G. Tither, Z. Shouhua (Eds.), HSLA Steels, Processing, Properties and Applications, The Minerals, Metals &Materials Society, 1992, pp. 99–105.

[2] E.E. Fletcher, High Strength Low Alloy Steels: Status, Selection and Physical Metallurgy, Battelle Press, Columbus, OH, 1979, pp. 137–139.

[3] P.C.M. Rodrigues, E.V. Pereloma, D.B. Santos, Mater. Sci. Eng. A 283 (2000) 136–143.

[4] L. Meyer, C. Straßburger, C. Schneider, Proc. Int. Conf. on HSLA Steels: Metallurgy and Applications, Beijing, People's Republic of China, 4–8 November, 1985, pp. 29–44.

[5] B.K. Show, Effect of V and Cu on the structure and properties of microalloyed HSLA steel, M. Tech thesis, Indian Institute of Technology, Kharagpur, India, 2007.

[6] J. Kong, C. Xie, Mater. Des. 27 (2006) 1169–1173.

[7] Review of the performance of high strength steels used offshore Professor J Billingham, Professor J V Sharp, Dr J Spurrier and Dr P J Kilgallon School of Industrial and Manufacturing Science Cranfield University, 2003

[8] Rodgers K J, and Lockhead J C, 'The welding of grade 450 offshore structural steels', Proc Conf. on Welding and Weld Properties in the Offshore Industry, London, April 1992

[9] Webster S E, 'Structural materials for offshore structures – past, present and future', Proc.Conf. on Safe Design and Fabrication of Offshore Structures, IBC, London, Sept. 1993

[10] Healy J, and Billingham J, 'High strength steels – a viable option for offshore designs', Euroforum Conference – Latest Innovations in Offshore Platform Design and Construction, London 1996

[11] 'The influence of welding on materials performance of high strength steels offshore', Managed Programmes of University Research, Marine Technology Centre, Cranfield University, 1985-1994

[12] Sharp J V, Billingham J, and Stacey A, 'Performance of high strength steels used in jack-ups'' Journal of marine Structures, 12 (1999), 349.

[13] G. Malakondaiah. Development of Speciality Low Alloy Steels. Int. Conf. on Metals and Alloys: Past, Present and Future, Kanpur-India, 2007.

[14] B.K. Show et al. Effect of vanadium and titanium modification on the microstructure and mechanical properties of a microalloyed HSLA steel. Mater. Sci. Eng. A. 2010; 527, 1595–1604.

[15] Subrata Mallik, Biswasi S Minz and Basudev Mishra. Production of DMR 249A Steel at SAIL, Bokaro Steel Plant. Materials Science Forum 2012; 10: 149-154.

[16] Pablo Batista Guimarães et al. Determination of Residual Stresses Numerically Obtained in ASTM AH36 Steel Welded by TIG Process. Materials Sciences and Applications, 2013, 4, 268-274.

[17] S.A. Tsirkas, P. Papanikos and Th. Kermanidis. Numerical simulation of laser welding process in butt-joint specimens. Journal of Materials Processing Technology, 2003, 134, 59-69.

[18] Marc Hever et al. Modern steel-High performance material for high performance bridges. 5th International Symposium on Steel Bridges, Barcelona 2003.

[19] Konrad Laber and H. Dyja. The Effect of the Normalizing Rolling of S355J2G3 Steel Round Bars onthe Selected Mechanical Properties of Finished Product. Solid State Phenomena 2010, 165, 294-299.

[20] http://hipbuildingsteel.en.china.cn/selling-leads/detail,1160303294,a131-grade-ABS-DH40ABS-DH40-D40-steel-D40-ship-plate-abs-marine-steel-steel-for-building-ship.html

[21] Savitskii M M and Leskov G I 1980 The mechanism of the effects of electrically negative elements on the penetrating power of an arc with a tungsten cathode Avt. Svarka 9, 17–22.

[22] C. R. Heiple and 1. R. Roper: Weld. J., 1982, 61, (4), 97s.

[23] Simonik A G 1976 The effect of contraction of the arc discharge upon the introduction of electro-negative elements Svar. Proiz. 3/49–51.

[24] J. J. Lowke, M. Tanaka, M. Ushio: J. Phys. D:Appl. Phys. 38 (2005) 3438-3445.

[25] J Lu et al. (1996). Handbook of Measurement of Residual Stresses. SEM, Fairmont Press, Inc.

[26] A. Niku Lari (1987), "Advances in Surface Treatments", Vol 4, International Guidebook on Residual Stresses, p. 3.

[27] G.E. Totten (2002), "Handbook on residual stress (ASM International)", Vol 1, p. 417.

[28] I.C. Noyan, J.B. Cohen, "Residual Stress Measurement by Diffraction and Interpretation", Springer-Verlag, New York, 1987.

[29] M. Belassel, J. Pineault, M.E. Brauss, Comparison and Evaluation of Residual Stress Measurement Techniques, A Technical and Economical Study, Proto Manufacturing Limited (2009).

[30] V. Hauk, "Structural and Residual Stress Analysis by Nondestructive Methods", Elsevier, Amsterdam, 1997.

[31] D.M. Egle and D.E. Bray. Measurement of acoustoelastic and third order elastic constants for rail steel. Journal of Acoustical Society of America 1976, 60(3), 741–744.

[32] Hidekazu Murakawa , Dean Deng , Ninshu Ma, Jiangchao Wang Applications of inherent strain and interface element to simulation of welding deformation in thin plate structures Computational Materials Science 51 (2011) 43–52

[33] H. Long, D. Gery , A. Carlier , P.G. Maropoulos Prediction of welding distortion in butt joint of thin plates Materials and Design 30 (2009) 4126–4135.

[34] A. Barroso , J. Canas , R. Picon, F. Paris , C. Méndez , I. Unanue Prediction of welding residual stresses and displacements by simplified models. Experimental validation .Materials and Design 31 (2010) 1338–1349.

[35] Dean Deng , Hidekazu Murakawa Influence of transformation induced plasticity on simulated results of welding residual stress in low temperature transformation steel Computational Materials Science 78 (2013) 55–62.

[36] P. Duranton J. Devauxa, V. Robin P. Gilles, J.M. Bergheau3D modeling of multi pass welding of a 316L stainless steel pipe Journal of Materials Processing Technology 153–154 (2004) 457–463.

[37] P. Mollicone, D. Camilleri, T.G.F. Gray , T. Comlekci Simple thermo-elastic–plastic models for welding distortion simulation Journal of Materials Processing Technology 176 (2006) 77–86.

[38] D. V. Kiran, B. Basu, A. K. Shah, S. Mishra and A. De; Probing influence of welding current on weld quality in two wire tandem submerged arc welding of HSLA steel, Science and Technology of Welding and Joining (2010), Vol 15, No 2.

[39] Jazeel Rahman Chukkana et al. Simulation of Laser Butt Welding of AISI 316L Stainless Steel Sheet using Various Heat Sources and Experimental Validation. Journal of Materials Processing Technology 2015, 219, 48–59.

[40] Ganesh, K. C. et al. Thermo - Mechanical Analysis of TIG Welding of AISI 316LN Stainless Steel.Materials and Manufacturing Processes 2014.

[41] M. Zubairuddin et al. Experimental and finite element analysis of residual stress and distortion in GTA welding of modified 9Cr-1Mo steel. Journal of Mechanical Science and Technology 2014, 28 (12), 5095~5105.

[42] Ganesh, K.C. et al.Modeling, Prediction and Validation of Thermal Cycles, Residual Stresses and Distortion in type 316 LN Stainless Steel Weld Joint made by TIG Welding Process. Procedia Engineering 2014, 86, 767 – 774.

[43] M. Zuabairuddin, S. K. Albert, M. Vasudevan, V. Chaudhari, V. K. Suri. Finite Element Simulation of Weld Bead Geometry and Temperature Distribution during GTA Welding of

Modified 9Cr-1Mo Steel and Experimental Validation. Journal for Manufacturing science and Production, Volume 14, Issue 4, pp 195–207.

[44] M. Zuabairuddin, S. K. Albert, M. Vasudevan, S. Mahadevan, V. Chaudhari, V. K. Suri. Thermo-mechanical Analysis of the Preheat effect on Grade P91 Steel during GTA Welding".Material and Manufacturing processes. DOI: 10.1080/10426914.2015.1025964.

[45] M. Zuabairuddin, S. K. Albert, V. Chaudhari, V. K. Suri Influence of Phase Transformation on Thermo-mechanical Analysis of Modified 9Cr-1Mo steel.Material Procedia, Volume 5, 2014, pp 832-840.

[46] 'Investigation on Stress Corrosion Cracking Behavior of Welded High Strength Low Alloy Steel in Seawater Containing Various Dissolved Oxygen Concentrations', Huixia Zhang et.al., Int. J. Electrochem. Sci., 8 , pp 1262 – 1273, 2013.

[47] 'Hydrogen Degradation of High-Strength Steels', J. Ćwiek, JAMME, 37, 2, 2009.

[48] 'Effect of Oxygen and Biofilms on Crevice Corrosion of UNS S31803 and UNS N08825 in Natural Seawater',Laura L. Machuca et.al, Corrosion Science, 67, 242-255, 2013.

[49] 'Corrosion Fatigue Behavior of Submerged Arc Welded High Strength Steel Used in Naval Structures', H. Das and T. K. Pal, Indian Welding J , 45,2, pp 40-51, 2012

[50] 'Pitting Corrosion of Mild Steel in CO_2 Containing NaCl Brine', Z. Xia, K. Chou, Z. Smialowska, Corrosion, 45, pp 636–642, 1989.

[51] 'Electrochemical Evaluation of the Corrosion Behaviour of API-X100 Pipeline Steel in Aerated Bicarbonate Solutions', F.F. Eliyan et al., , Corrosion Science, 58, pp 181–191, 2012.

[52] 'Corrosion Behaviour of Nano Structured Sol-Gel Alumina Coated 9Cr–1Mo Ferritic Steel in Chloride Bearing Environments', G. Ruhi, O.P. Modi, I.B. Singh, Surface & Coatings Technology, 204 , pp359–365, 2009.

[53] 'A Comparison Between FSW and TIG Welding Techniques: Modifications of Microstructure and Pitting Corrosion Resistance in AA 2024-T3 Butt Joints A. Squillace', A. De Fenzo, G. Giorleo, F. Bellucci, Journal of Materials Processing Technology ,152, pp 97–105, 2004.

[54] Standard Practice for Conventions Applicable to Electrochemical Measurements in Corrosion Testing. ASTM G3 (2014).

[55] Standard Reference Test Method for Making Potentiostatic and Potentiodynamic Anodic Polarization Measurements. ASTM G5-94 (2011).

[56] Standard Test Method for Conducting Potentiodynamic Polarization Resistance Measurements. ASTM G59-97 (2014).

[57] Standard Practice for Calculation of Corrosion Rates and Related Information from Electrochemical Measurements. ASTM G102-89 (2010).

[58] Bain, E.C., Alloying Elements in Steels, ASM, Cleveland, Ohio, USA (1939).

[59] Sinha, A.K., Ferrous Physical Metallurgy, Butterworth Publishers, USA (1989).

[60] Bhadeshia, H.K.D.H, Honeycombe, R.W.K, Steels: Microstructure and Properties, Elsevier Ltd., UK (2006).

[61] ASM Handbook, Vol. 4, Heat Treating, ASM International (1991).

[62] Totten, G.E., Howes, M.A.H, Steel Heat Treatment Handbook, Marcel Dekker, Inc., USA (1997).

[63] Thelning, K.E., Steels and its Heat Treatment, Butterworth & Co. and K-E Thelning, UK (1984).

[64] Leslie, W.C., The physical Metallurgy of Steels, McGraw-Hill, Tokyo, Japan, (1981).

[65] Porter, D.A., Easterling, K.E., Phase Transformations in Metals and Alloys, CRC Press, Taylor & Francis Group, Finland (2004).

[66] N. Venkateswara Rao, B.S. Bansal, K. Ankalu, A. Dutta, M. Srinivas, K. Muraleedharan, R. Balamuralikrishnan, G. Malakondaiah, Met. Mater. Proc. 19 (2007) 261–272.

[67] T. Gladman, The Physical Metallurgy of Microalloyed Steels, The Institute of Material, London, 1997.

[68] Robert W. Messler, Principles of Welding, 2009, Wiley-VCH.

[69] Sindo Kou, Welding Metallurgy, 2003. John Wiley & Sons Inc.

[70] TWI GSP No. 5663, (1994), An evaluation of the A-TIG welding process, January, 1994.

[71] Anderson, P.C.J., and Wiktorowicz, R., (1995), A-TIG welding – The effect of the shielding gas, TWI Bulletin, July/August, p. 76-77.

[72] Anderson, P.C.J., and Wiktorowicz, R., (1996), Improving productivity with A-TIG welding, Welding and Metal Fabrication, 64(3), p.108-109.

[73] Lucas, W., Howse, D.S., Savitsky, M.M., and Kovalenko, I.V., (1996), Proc. 49th IIW annual assembly, 1996, International Institute of Welding, Document XII –1448- 96.

[74] Paskell, T., Lundin, C. and Castner, H., (1997), GTAW flux increases weld joint penetration, Welding Journal, 76 (4), p.57-62.

[75] Savitsky, M.M., Kushnirenko, B.N., and Ploeinik, O.I., (1999), Features of A-TIG welding of steels, Paton Welding Journal, p. 24-32.

[76] Modenesi, P.J., Apolinario, E.R., and Pereira, I.M., (2000), TIG welding with single-component fluxes, Journal of Materials Processing Technology, 99 (1-3), p.260-265.

[77] Tanaka, M., Shimizu,T., Terasaki. H., Ushio, M., Koshi-ishi, F., and Yang, C.L., (2000), Effects of activating flux on arc phenomena in gas tungsten arc welding, Science and Technology of Welding and Joining, 5(6), p. 397-402.

[78] Lucas, W., (2000), Activating flux – improving the performance of the TIG process, Welding and Metal Fabrication, 68(2), p. 7-10.

[79] Howse, D.S., and Lucas, W., (2000), Investigation into arc constriction by active fluxes for tungsten inert gas welding, Science and Technology of Welding and Joining, 5(3), 2000, p.189-193.

[80] Yushchenko, K.A., et al (1993), A-TIG welding of carbon-manganese and stainless steels, Intl. Conf. on Welding Technology, Paton Institute, paper 2 Cambridge, 13-14, October.

[81] Shanping Lu, Hidetoshi Fujii, Hiroyuki Sugiyama, Manabu Tanaka and Kiyishi Nogi, (2002), Weld penetration and Marangoni convection with oxide fluxes in GTA Welding, Materials Transactions, 43 (11), p. 2926-2931.

[82] Shanping Lu, Hidetoshi Fujii, Hiroyuki Sugiyama, and Kiyishi Nogi, (2003), Mechanism and Optimisation of oxide fluxes for deep penetration in gas tungsten arc welding, Metallurgical and Materials Transactions A, 34 A, p.1901-1907.

[83] Pascal Paillard and Jacques Saindrenan, (2003), Effect of activating fluxes on the penetration capability of TIG welding arc: study of fluid flow phenomena in weld pools and the energy concentration in the anode spot of a TIG arc plasma, Materials Science Forum, 426-432, p. 4087-4092.

[84] Liu, F., Yang, C., Lin, S., Wu, L., and Zhang, Q., (2003), Mechanism of increasing A-TIG penetration, Acta Metallurgica Sinica, 39(6), p. 661-665.

[85] T. Sándor , János Dobránszky : The experiences of activated tungsten inert gas (ATIG) weldingapplied on 1.4301 type stainless steel plates, Materials Science Forum Vols. 537-538 (2007) pp. 63-70.

[86] Ding Fan, Ruihua Zhang, Yufen Gu, and Ushio, M., (2001), Effect of flux on A-TIG welding of mild steels, Transactions JWRI, 30, p.35-40.

[87] Kou, S, and Wang, Y.H., (1986), Weld pool convection and its effect, Welding Journal 65 (3), p. 63s-70s.

[88] Lambert, J.A., (1991), Cast-to-cast variability in stainless steel mechanized GTA welds, Welding Journal, 70 (5), p. 41-52.

[89] Lancaster, J.F., and Mills, K.C., (1994), Recommendations for the avoidance of variable penetration in gas tungsten arc welding, Abington Publishing, Cambridge, England.

[90] Pierce, S.W., Burgardt., P., and Olson, D.L., (1999), Thermocapillary and arc phenomena in stainless steel welding, Welding Journal, 78(2), p. 45s-52s.

[91] Pollard, B., (1988), The effects of minor elements on the welding characteristics of stainless steels, Welding Journal, 67(9), p. 202s-213s.

[92] Mills, K.C., and Keene, B.J., (1990), Factors affecting variable penetration, gInternational Material Reviews, 35(4), p. 185-216.

[93] Heiple, C.R., and Roper, J.R., Stagner, R.T., and Aden, R.I., (1983), Surface active element effects on the shape of GTA, laser, and electron beam welds, Welding Journal, 62(3), p.72s-77s.

[94] ASM Handbook Volume 6: Welding Brazing and Soldering.

[95] B.J. Keene, K.C. Mills, and R.F. Brooks, Surface properties of liquid metals and their effects on weldability, Mater. Sci.Technol., Vol 1, 1985, pp 568-571.

[96] P. Burgardt and C.R. Heiple, Interaction between impurities and welding parameters in determining GTA weld shape, Weld. J., Vol 65, 1986, P 150S-155S.

[97] M.J. Tinkler, I. Grant, G. Mizuno, And C. Gluck, Welding 304L stainless steel Tubing having variable penetration characteristics, the effects of residual, Impurity, and micro-

alloying elements on weldability and weld properties, P.H.M. HART, Paper 29, The Welding Institute, Cambridge, 1984.

[98] W. S. Benneit And G. S. Mills: Weld. J., 1974,53, (12), 548s.

[99] K. Ishizaki, S. Yokoya, and T. Okada: 'Mechanism of penetration in arc welding', Report, Nippon Institute of Technology, Saitama, Japan 'Weld characteristics', NPL, Teddington,1988.

[100] An international patent "Tungsten Inert Gas Welding Flux for enhancing Penetration in Single Pass for austeniticstainless steels" (patent no. PCT/IN06/00442/dt. 8/11/06).

[101] M. Vasudevan, A.K. Bhaduri, and Baldev Raj, Microstructure and Mechanical Properties of Austenitic Stainless Steels, International Welding Congress, February 16 – 19, 2005 Mumbai.

[102] M. Vasudevan,, A.K. Bhaduri and Baldev Raj, Development and Evaluation of Activated Flux for TIG welding of Type 304 LN and Type 316 LN Stainless Steels, International Institute of Welding, International Congress 2008, January, 8-10, Chennai, 2008.

[103] T. Sakthivel, M. Vasudevan, K.S. Chandravathi, P. Parameswaran, Laha, M.D. Mathew and A.K. Bhaduri, An assessment of Creep Rupture Behaviour of Single pass A-TIG and Multi-pass TIG weld joints of Type 316 LN Stainless steel, National Welding Seminar, December, 10-13, 2009, Kolkatta.

[104] P. Sivaraman, A. Md.Mueer, M. Krishnamoorthy, R. Veluswamy, M. Vasudevan, A.K. Bhaduri and A.S.L.K. Rao, Application of Penetration Enhancing Activating Flux TIG (PEAF-TIG) Welding Process in Regular Production of stainless steel and steel components, International Institute of Welding, International Congress, January, 8-10, Chennai, 2008.

[105] P. Palanichamy, M. Vasudevan, and T. Jayakumar, Measurement of Residual Stresses in Austenitic Stainless Steel Weld Joints Using an Ultrasonic technique, Science and Technology of Welding and Joining, Vol. 14 (2), p. 166 – 171, 2009.

[106] N. Chandrasekhar, M. Vasudevan and A.K. Bhaduri, Hybrid modelling for Optimization of A-TIG Welding Process for Austenitic Stainless Steels, National Welding Seminar, December, 10-13, 2009, Kolkatta.

[107] G. Magudeeswaran , S. R. Nair, L. Sundar , N. Harikinnan, Optimization of process parameters of the activated tungsten inert gaswelding for aspect ratio of UNS S32205 duplex stainless steel welds, Defence Technology xx (2014) 1-10 [4].

[108] Sanjay G. Nayee, Vishvesh J. Badheka, Effect of oxide-based fluxes on mechanical and metallurgical properties of Dissimilar Activating Flux Assisted-Tungsten Inert Gas Welds, Journal of Manufacturing Processes 16 (2014) 137–143.

[109] Y. Zou, R. Ueji, H. Fujii," Effect of oxygen on weld shape and crystallographic orientation of duplex stainless steel weld using advanced A-TIG (AA-TIG) welding method" material characterization 91 (2014) 42-49.

[110] K.H. Tseng , K-J Chuang, "Application of iron-based powders in tungsten inert gas welding for 17Cr–10Ni–2Mo alloys" Powder Technology 228 (2012) 36–46.

[111] H-Y Huang," Effects of shielding gas composition and activating flux on GTAW weldments" Materials and Design 30 (2009) 2404–2409.

[112] T. Sakthivel , M. Vasudevan, K. Laha, P. Parameswaran, K.S. Chandravathi, M.D. Mathew, A.K. Bhaduri, "Creep rupture strength of activated-TIG welded 316L(N) stainless steel" Journal of Nuclear Materials 413 (2011) 36–40.

[113] Meng X., Qin X., Zhang Y., Fu B., Zou Z., "High speed TIG–MAG hybrid arc welding of mild steel plate" Journal of Materials Processing Technology 214 (2014) 2417–2424.

[114] Y. Ruan , X.M. Qiu , W.B. Gong , D.Q. Sun , Y.P. Li "Mechanical properties and microstructures of 6082-T6 joint welded by twin wire metal inert gas arc welding with the SiO_2 flux" Materials and Design 35 (2012) 20–24.

[115] P. Vasantharaja, M. Vasudevan, "Studies on A-TIG welding of Low Activation Ferritic/Martensitic (LAFM) steel" Journal of Nuclear Materials 421 (2012) 117–123.

[116] V. Maduraimuthu et al, “Effect of activated flux on the microstructure, mechanical properties, and residual stresses of modified 9Cr-1Mo steel weld joints” Metallurgical and Materials Transactions B 43B (2012), 123-133.

[117] B. Arivazhagan and M. Vasudevan, “A study of microstructure and mechanical properties of Grade 91 steel A-TIG weld joint” Journal of Materials Engineering and Performance (2013), DOI: 10.1007/s11665-013-0694-9.

[118] B. Arivazhagan and M. Vasudevan, “Studies on A-TIG welding of 2.25Cr-1Mo (P22) steel” Journal of Manufacturing Processes 18 (2015) 55–59.

[119] HKDH. Bhadeshia, Some phase transformations in steels, Materials Science and Technology, 1999 Vol. 15, pp 22-30.

[120] I. Madariaga, I. Gutierrez and H. K. D. H. Bhadeshia, “Acicular ferrite morphologies in a medium-carbon microalloyed steel”, Metallurgical and Materials Transactions A, Vol. 32, 2001, pp 2187-2197.

[121] LE Svensson, Control of microstructure and properties in steel arc welds, 1994, Boca Raton, FL, USA, CRC Press.

[122] HKDH. Bhadeshia, Bainite in steel, IOM Communication Ltd, London, 2001.

[123] H. K. D. H. Bhadeshia and R. W. K. Honeycombe, “Steels microstructure and properties”, Elsevier, third edittion, 2006.

[124] H. K. D. H. Bhadeshia, “The bainite transformation: unresolved issues”, Materials Science and Engineering A, Vol. 273, 1999, pp 58-66.

[125] H. K. D. H. Bhadeshia, “Modelling of steel welds”, Materials Science and Technology, Vol. 2, 1992, pp 123-133.

[126] J. Y. Suh, J. S. Byun, J. H. Shim, Y. J. Oh, Y. W. Cho, J. D. Shim and DN. Lee, “Acicular ferrite microstructure in titanium bearing low carbon steels. Metallurgical modelling of welding”, Materials Science and Technology, Vol. 16, 2000, pp 1277- 1281.

[127] Abson, D. J., and Dolby, R. E., Weld. Inst. Res. Bull., 202: July 1978.

[128] Dolby, R. E., Metals Technol. 10: 349, 1983.

[129] Classification of Microstructure in Low Carbon Low Alloy Weld Metal, IIW Doc. IX-1282-83, 1983, International Institute of Welding, London, UK.

[130] Vishnu, P. R., in ASM Handbook, Vol. 6: Welding, Brazing and Soldering, ASM International, Materials Park, OH, 1993, pp. 70–87.

[131] Onsoien, M. I., Liu, S., and Olson, D. L., Weld. J., 75: 216s, 1996.

[132] Grong, O., and Matlock, D. K., Int. Metals Rev., 31: 27, 1986.

[133] Babu, S. S., Reidenbach, F., David, S. A., Bollinghaus,Th., and Hoffmeister, H., Sci. Technol.Weld. Join., 4: 63, 1999.

[134] Bhadeshia, H. K. D. H., and Svensson, L. E., in Mathematical Modelling of Weld Phenomena, Eds. H. Cerjak and K. Easterling, Institute of Materials, 1993.

[135] Fleck, N. A., Grong,O., Edwards,G. R., and Matlock,D. K.,Weld. J., 65: 113s, 1986.

[136] Liu, S., and Olson, D. L., Weld. J., 65: 139s, 1986.

[137] Ashby, M. F., and Easterling, K. E., Acta Metall., 30: 1969, 1982.

[138] Edwards, G. R., and Liu, S., in Proceedings of the first US-Japan Symposium on Advanced Welding Metallurgy, AWA/JWS/JWES, San Francisco, CA, and Yokohama, Japan, 1990, pp. 213–292.

[139] Fox, A. G., Eakes, M.W., and Franke, G. L., Weld. J., 75: 330s, 1996.

[140] Dolby, R. E., Research Report No. 14/1976/M,Welding Institute, Cambridge 1976.

[141] Glover, A.G., McGrath, J.T., and Eaton, N. F., in S Toughness Characterization and Specifications for HSLA and Structural Steels. ed. P. L. Manganon, Metallurgical Society of AIME, NY, pp. 143–160.

[142] Dallam, C. B., Liu, S., and Olson, D. L., Weld. J., 64: 140s, 1985.

[143] Michaleris, P. and DeBiccari, A., 1997, "Prediction of Welding Distortion" Welding Journal, Welding Research Supplement, 76 (4), p 172s-181s.

[144] Feng, Zihli – "Processes and mechanism of welding residual stress and distortion" – Wood head Publishing limited, 1st Ed, Cambridge, England, 2005, Chap. 1-3, 5-9.

[145] Macherauch E, Kloos KH. Origin, measurements and evaluation of residual stresses. Residual Stress Sci Technol 1987:3–26.

[146] Hauk V (1997). Structural and Residual Stress Analysis by Non Destructive Methods. Elsevier, Amsterdam.

[147] D.S. Hughes and J.L. Kelly (1953), "Second-order elastic deformation of solids", Physical Review, Vol 92, Issue 5, pp. 1145-1149.

[148] Charles.J.Hellier (2003), "Handbook of Nondestructive evaluation" TataMcgrewHill, pp. 7.16.

[149] D.M. Egle and D.E. Bray (1976), "Measurement of acoustoelastic and third order elastic constants for rail steel", Journal of Acoustical Society of America, Vol 60, Issue 3, pp. 741–744.

[150] C.O. Ruud (1982), "A Review of selected non-destructive methods for residual stress measurement", NDT International, pp. 15-23.

[151] P. Palanichamy, M. Vasudevan and T. Jayakumar (2009), “Measurement of residual stresses in austenitic stainless steel weld joints using ultrasonic technique”, Science and Technology of Welding and Joining, Vol 14, No 2, pp. 166-170.

[152] M.Vasudevan, R. Shanmugasundaram, B. Arivazhagan, P. Vasantharaja and P. Palanichamy (2012), “Assessment of Residual stresses and Distortion in Austenitic Stainless Steel Weld joints”, Advanced Welding Processes, Monitoring and Modeling Programme.

[153] A. Joseph, P. Palanichamy, T. Jayakumar (2014), “Evaluation of residual stresses in Carbon steel weld joints by ultrasonic Lcr wave technique” Journal of Nondestructive evaluation, Vol 33, No 4.

[154] D. Gery , H. Long, P. Maropoulos Effects of welding speed, energy input and heat source distribution on temperature variations in butt joint welding Journal of Materials Processing Technology 167 (2005) 393–401.

[155] Dean Deng , Hidekazu Murakawa Numerical simulation of temperature field and residual stress in multi-pass welds in stainless steel pipe and comparison with experimental measurements Computational Materials Science 37 (2006) 269–27.

[156] Shaodong Wang , John Goldak , Jianguo Zhou , Stanislav Tchernov , Dan Downey Simulation on the thermal cycle of a welding process by space–time convection–diffusion finite element analysis International Journal of Thermal Sciences 48 (2009) 936–947.

[157] Hidekazu Murakawa , Dean Deng , Ninshu Ma, Jiangchao Wang Applications of inherent strain and interface element to simulation of welding deformation in thin plate structures Computational Materials Science 51 (2011) 43–52.

[158] H. Long, D. Gery , A. Carlier , P.G. Maropoulos Prediction of welding distortion in butt joint of thin plates Materials and Design 30 (2009) 4126–4135.

[159] A. Barroso , J. Canas , R. Picon, F. Paris , C. Méndez , I. Unanue Prediction of welding residual stresses and displacements by simplified models. Experimental validation .Materials and Design 31 (2010) 1338–1349.

[160] Dean Deng , Hidekazu Murakawa Influence of transformation induced plasticity on simulated results of welding residual stress in low temperature transformation steel Computational Materials Science 78 (2013) 55–62.

[161] Liam Gannon Yi Liu , Neil Pegg , Malcolm Smith Effect of welding sequence on residual stress and distortion in flat-bar stiffened plates Marine Structures 23 (2010) 385–404.

[162] J.J. del Coz Díaz , P. Menéndez Rodríguez , P.J. García Nieto , D. Castro-Fresno Comparative analysis of TIG welding distortions between austenitic and duplex stainless steels by FEM Applied Thermal Engineering 30 (2010) 2448e2459.

[163] L.E. Lindgren, Numerical modelling of welding Comput. Methods Appl. Mech. Engrg. 195 (2006) 6710–6736.

[164] H.M. Aarbogh, M.Hamide, H.G.Fjær, A.Mo, M.Bellet Experimental validation of finite element codes for welding deformations Journal of Materials Processing Technology 210 (2010) 1681–1689.

[165] X.K. Zhu, Y.J. Chao Effects of temperature-dependent material properties on welding simulation Computers and Structures 80 (2002) 967–976.

[166] Olivier Asserin , Alexandre Loredo , Matthieu Petelet , Bertrand Iooss Global sensitivity analysis in welding simulations—What are the material data you really need? Finite Elements in Analysis and Design 47 (2011) 1004–1016.

[167] Amin S. Azar , Sigmund K. Ås , Odd M. Akselsen , Determination of welding heat source parameters from actual bead shape Computational Materials Science 54 (2012) 176–182.

[168] M.J. Attarha, I. Sattari-Far Study on welding temperature distribution in thin welded plates through experimental measurements and finite element simulation Journal of Materials Processing Technology 211 (2011) 688–694.

[169] Benyounis K Y, Olabi A G, Hashmi M S J. Multi response optimization of CO_2 laser welding process of austenitic stainless steel. Opt. & Laser Tech 2008; 40: 76-87.

[170] Bas, D., Boyaci, I.H. Modelling and optimization-Usability of response surface methodology. J. Food Eng. 2007; 78 (3): 836–845.

[171] Myers, R.H. Response Surface Methodology 1976. Edwards Brothers, Ann Arbor, MI.

[172] Raymond H. Myers, Douglas C. Montgomery, Christine M. Anderson-Cook. Response Surface Methodology: Process and Product Optimization Using Designed Experiments. Wiley 2008.

[173] Johnson RT and Montgomery DC. Choice of second-order response surface designs for logistic and Poisson regression models. Int. J. Experimental Design and Process Optimisation 2009; 1(1).

[174] PeterGoos, Martina Vandebroek. D-optimal response surface designs in the presence of random block effects. Computational Statistics & Data Analysis 2001 ;37:433–453.

[175] Chuan-Pin Lee, Mong-Na Lo Huang. D-Optimal Designs for Second-Order Response Surface Models with Qualitative Factors. Journal of Data Science 2011; 9:139-153.

[176] Juang SC, Tarng YS. Process parameters selection for optimizing the weld pool geometry in the tungsten inert gas welding of stainless steel. J Mater Process Technol 2002;122:33–7.

[177] Neter , Kutner , Nachtseim and Wasserman (1996) Applied Linear Statistical Models 4th edition . Irwing.

[178] Freund and Littell (2000) SAS System for Regression . Third Edition . SAS Institute.

[179] Lee HK, Han HS, Son KJ, Hong SB. Optimization of Nd-YAG laserwelding parameters for sealing small titanium tube ends. J Mater SciEng 2006;A415:149–55.

[180] McElroy, J. Experimental Design Hits Detroit (A Primer on the Taguchi Method. Automotive Industries 1985;165: 48-50.

[181] Ea ley, L.. Taguchi Methods: The Thought Behind the System. Automotive Industries 1988; 168: 68-70.

[182] Wu, C.M.; Black, J.T., and Jiang, B.C. Using Taguchi Methods to Deter-mine/Optimize Robot Process Capability for Path Following. Robotics and Computer-Integrated Manufacturing 1991; 8(1): 9-25.

[183] Jiang, B.C.; Black, J.T.; Chen, D.W.H.; and Hool, J.N. Taguchi-Based Meth-odology for Determining/Optimizing Robot Process Capability. HE Transactions 1991; 23(2): 169-184.

[184] Warner, J.C., and O'Connor, J. Molding Process is Improved by Using the Taguchi Method. Modern Plastics 1989; 66: 65-66.

[185] Liu, L.; Nazaret, W.A., and Beale, R.G. Computer-Aided Design for Quality (CADQ). AT&T Technical Journal 1990; 10:103-115.

[186] Young, D.L, Teplik, J. and Weed H.D., Application of Statistical Design and Response Surface Methods to Computer-Aided VLSI Device Design: Desirability Functions and Taguchi Methods. IEEE Transactions on CAD of IC and Sys 1991. 10: 103-115.

[187] Cohen J, Multiple Regression as a General Data-Analytic System, Psychological Bulletin 1968;70(6):426-443.

[188] M. A. Bezerra, R. E. Santelli, E. P. Oliveira, L. S. Villar, and L. A. Escaleira, Response Surface Methodology (RSM) as a Tool for Optimization in Analytical Chemistry, Talanta 2008; 76(5):965–977.

[189] S. K. Gauri and S. Chakraborty, Multi-Response Optimisation of WEDM Process using Principal Component Analysis, The International Journal of Advanced Manufacturing Technology 2009, 41(7-8): 741–748.

[190] C R. Heiple, R. 1. Cluey and R. D. Dixon: in 'Physical metallurgy of metal joining', (ed. R. Kossowsky and M. E. Glicksman), 160; 1980, Warrendale, PA, Metallurgical Society of AIME.

[191] Troy Paskell, Carl Lundin and Harvey Castner, GTAW Flux Increases Weld Joint Penetration, EWI, Ohio 1997.

[192] Lu H et al. Ultrasonic stress evaluation on welded plates with L_{CR} wave. Science and Technology of Welding and Joining 2008; 13: 70-74.

[193] Gilles Pet al. Robustness analyses of numerical simulation of fusion welding NeT-TG1. International Journal of Pressure Vessels and Piping 2009; 86:3-12.

[194] Cullity BD and Stock SR. Elements of X-ray Diffraction. FistEd., Prentice Hall, New Jersey 2001.

[195] Raj B, Jaykumar T, Mahadevan S and Rai SK. X-ray Diffraction Based Residual Stress Measurement for Assessment of Fatigue Damage and Rejuvenation Process for Undercarriages of Aircraft. Journal of Non-destructive Evaluation 2009; 28 (3-4):157-162.

[196] P. J. Withers et al. Methods for obtaining the strain-free lattice parameter when using diffraction to determine residual stress. J. Appl. Cryst. 2007. 40, 891–904.

[197] ASTM E8 / E8M – 15: Standard Test Methods for Tension Testing of Metallic Materials.

[198] Egle D.M. and Bray D.E. Measurement of Acoustoelastic and Third Order Elastic Constants for Rail Steel. J Acoustical Society of America 1976; 60(3):741–744.

[199] Lu H et al. Ultrasonic stress evaluation on welded plates with L_{CR} wave. Science and Technology of Welding and Joining 2008; 13: 70-74.

[200] Gilles Pet al. Robustness analyses of numerical simulation of fusion welding NeT-TG1. International Journal of Pressure Vessels and Piping 2009; 86:3-12.

[201] Pratihar S. et al. Neutron Diffraction Residual Stress Measurements in A 316L Stainless Steel Bead-on-Plate Weld Specimen. International Journal of Pressure Vessels and Piping 2009; 86: 13–19.

[202] Belahcene F and Jian Lu. Determination of Residual Stress in Z8CDWV12 Steel using Critically Refracted Longitudinal Waves. JSME Intl J A 2000; 43-4: 367-373.

[203] Nguyen, N. T., Mai, Y. W., Simpson, S. and Ohta, A. (2004), Analytical approximate solution for double ellipsoidal heat source in finite thick plate, Welding Journal, pp.82s -93s.

[204] Chandan Kumar, Manas Das, Pankaj Biswas. “A 3-D finite element analysis of transient temperature profile of laser welded Ti-6Al-4V alloy” 5th International & 26th All India Manufacturing Technology, Design and Research Conference (AIMTDR 2014) 2014, IIT Guwahati, India.

[205] José L. Meseguer-Valdenebro et al. Experimental Validation of a Numerical Method that Predicts the Size of the Heat Affected Zone. Optimization of the Welding Parameters by the Taguchi’s Method, Trans IIM, June 2015.

[206] Dhas, J.E.R.; Kumanan, S. Modeling of residual stress in butt welding. Materials and Manufacturing Processes 2011, 26 (7), 942–947.

[207] Kohandehghan, A.R.; Serajzadeh, S.; Kokabi, A.H. A study on residual stresses in gas tungsten arc welding of AA5251. Materials and Manufacturing Processes 2010, 25 (11), 1242–1250.

[208] Rossini, N.S.; Dassisti, M.; Benyounis, K.Y.; Olabi A.G. Methods of Measuring Residual Stresses in Components. Materials and Design 2012 , 35, 572–588.

[208] ASTM E384 - 11e1: Standard Test Method for Knoop and Vickers Hardness of Materials.

[209] ASTM E23 - 12c: Standard Test Methods for Notched Bar Impact Testing of Metallic Materials.

[210] G. Krauss, S.W. Thompson, ISIJ Int. 35 (1995) 937–945.

[211] B.L. Bramfitt, Metallographer's Guide: Practices and Procedures for Irons and Steels, ASM International, Materials Park, Ohio, 2002.

[212] S.L. Shrestha et al. An automated method of quantifying ferrite microstructures using electron backscatter diffraction (EBSD) data. Ultramicroscopy 2014 137, pp 40–47.

[213] Dorschu, K. E. 1977. Factors affecting weld metal properties in carbon and low alloy pressure vessel steels. WRC 231: 1–64.

[214] Komizo, V., and Fukada, V. 1990. Toughness improvement in weld metal of carbon and HSLA steels in Japan. First United States – Japan Symposium on Advances in Welding Metallurgy, Proceedings, 358–381.

[215] K. C. Mills and B. J. Keene, International Materials Reviews 1990, 35(4), pp 185-217.

[216] Z. Zhang, R.A. Farrar. Influence of Mn and Ni on the Microstructure and Toughness of C-Mn-Ni Weld Metals Mater. Sci. Technol. 12, 1996, 237-260.

[217] F.J. Barbaro, P. Krauklis, K.E. Easterling. Formation of acicular ferrite at oxide particles in steels, Mater. Sci. Technol. 5, 1989, 1057- 1068.

[218] S.H. Nedjad, A. Farzaneh. Formation of fine intragranular ferrite in cast plain carbon steel inoculated by titanium oxide nanopowder, Scr. Mater. 57 (2007) 937-940.

[219] Shim, J.H et al. Nucleation of intragranular ferrite at Ti_2O_3 particle in low carbon steel," Acta Materialia, 1999, 2751–2760.

[220] Kanazawa, S., Nakashima, A., Okamoto, K., and Kanaya, K. Improvement of weld fusion zone toughness by fine TiN. Transactions ISII 16, 1976, 486.

[221] Koukabi, A., North, T.H., and Bell, H.B. Flux formation, sulphur, oxygen and rare-earth additions in submerged arc welding. Proc. Intl. Conf. on Trends in Steels and Consumables for Welding, London, England, The Welding Institute, 1978,281.

[222] Ito, Y,, and Nakanishi, M. Study on Charpy impact properties of weld metals with submerged arc welding. The Sumitomo Search 15, 1976, 42.

[223] Heintze, G.W., and /McPherson, R. Grain refinement of steels by titanium innoculation during submerged arc welding. Australian Welding lournal 28, 1983, 37.

[224] Mori, N., Homma, H., Okita, S,, and Asano, K. The behavior of B and N in notch toughness improvement of Ti-B bearing weld metals. IIW DOC IX-1980, 1158-80.

[225] Pargeter, R. Investigation of Submerged Arc Weld Metal Inclusions. The Welding Institute, Cambridge, England. 1981.

[226] Devillers, L, Kaplan, D., Marandet, B., Ribes, A., and Riboud, P.V. The effect of low level concentrations of some elements on the toughness of submerged arc welded C-Mn welds. Proc. Intl. Conf. on The Effects of Residual, Impurity and Micro-alloying Elements on Weldability and Weld Properties, London, England, The Welding Institute, 1983,1.

[227] Cochrane, R.C, Ward, J.L., and Keville, B.R. The influence of deoxidation and/ or desulphurisation practice on the weld metal toughness of high dilution welds. Proc. Intl. Conf. on The Effects of Residual, Impurity and Micro-alloying Elements on Weldability and Weld Properties, London, England, The Welding Institute, Paper 16,1983.

[228] Saggesse, M.E., Bhatti, A.R., Hawkins, D.N., and Whiteman, J.A. Factors influencing inclusions chemistry and microstructure in submerged arc welds.. Proc. Intl. Conf. on The Effects of Residual, Impurity and Microalloying Elements on Weldability and Weld Properties, London, England, The Welding Institute, Paper 15,1983.

[229] Harrison, P.L., and Farrar, R.A. Influence of oxygen-rich inclusions on the austenite to ferrite phase transformation in high-strength low-alloy (HSLA) steel weld metals, Journal of Materials Science 16, 1981, 2218.

[230] Yang J.R. and Bhadeshia H.K.D.H., "The Dislocation Density of Acicular Ferrite in Steel Welds," The Welding Journal, vol. 69, 1990, 305s-307s.

[231] Liu, S., and Olson, D. L. The role of inclusions in controlling HSLA steel weld microstructures. Welding Journal 65(6), 1986, 139s-149s.

[232] Tweed J.H. and Knott J.F., "Effect of Reheating on Microstructure and Toughness of C-Mn Weld Metal," Metal Science, vol. 17, no. 2, 1983, 45-54.

[233] Almond E.A., Timbres D.H., and Embury J.D., "Influence of Second Phase Particles on Brittle Fracture," Proceedings of the Second International Conference on Fracture, 1969,253-264.

[234] Avner S.H. Introduction to Physical Metallurgy. Tata McGraw-Hill Education 1997.

[235] H. K. D. H. Bhadeshia. Application of Phase Transformation Theory to Welding. POSCO Lectures, 16th February 2008.

[236] W.W. Bose-Filho, A.L.M. Carvalho, M. Strangwood. Effects of alloying elements on the microstructure and inclusion formation in HSLA multipass welds. Materials Characterization 2007; 58, 29–39.

[237] Fox, A.G., Clarke, A.L. and Franke, G.L. The Effect of Small Changes in Flux MnO Content on the Microstructure and Mechanical Properties of Navy HY-100 Steel. Welding Journal, 1998.

[238] Keehan, E., Karlsson, L., and Andren, H.-O. Influence of C, Mn and Ni on strong steel weld metals: Part 1, effect of nickel content. Science and Technology' of Welding and Joining 2006. 11, pp 1-8.

[239] Keehan, E., Karlsson, L., Andren, H.-O., and Bhadeshia, H. K. D. H.. Influence of C, Mn, and Ni on strong steel weld metals: Part 2, impact toughness gain from manganese reductions. Science and Technology of Welding and Joining 2006,11, pp 9-18.

[240] Keehan, E., Karlsson, L., Andren, H.-O., and Bhadeshia, H. K. D. H. Influence of C, Mn and Ni on strong steel weld metals: Part 3, increased strength from carbon additions. Science and Technology of Welding and Joining 2006, 11, pp18-24.

[241] N. J. Smith et al. Microstructure/Mechanical Property Relationships of Submerged Arc Welds in HSLA 80 Welding Research Supplement 1989, pp 112-120.

[242] Tianli Zhang et al. Effect of inclusions on microstructure and toughness of deposited metals of self-shielded flux cored wires. Materials Science and Engineering: A 2015, Volume 628, pp 332–339.

[243] Warren M. Garrison Jr and Andrzej L. Wojcieszynski. A discussion of the effect of inclusion volume fraction on the toughness of steel. Materials Science and Engineering: A2007, Volume 464, Issues 1–2,pp 321–329.

[244] D. J. Abson and R. J. Pargeter, "Factors influencing the as deposited strength, microstructure and toughness of manual metal arc welds suitable for C-Mn steel fabrication", International metals Review, 1986, Vol.31, No 4, pp 141-194.

[245] F. M. Haggag. In-situ measurements of mechanical properties using novel automated ball indentation system. American Society for Testing and Materials. [ASTM STP 1204].

[246] F. M. Haggag, R. K. Nanstad, J. T. Hutton, D. L. Thomas and R. L. Swain: Use of automated ball indentation to measure flow properties and estimate fracture toughness in metallic materials. American Society for Testing and Materials. [ASTM 1092].

[247] K. H. Kim, Y. C. Kim, E. C. Jeon and D. Kwon: 'Evaluation of indentation tensile properties of Ti alloys by considering plastic constraint effect', Mater. Sci. Eng. A. 2011; 528, 5259–5263.

[248] T.C.Totemeier,H.Tian,J.A.Simpson. Effect of normalization temperature on the creep strength of modified 9Cr-1Mo steel. Metall.Mater.Trans.A 2006; 37(5), 1519–1525.

[249] V. Karthik, Analysis and improvements in small specimen test techniques for evaluating the mechanical properties of steels,University of Madras,2011 (Ph.D. Thesis).

[250] E. Meyer, Z. Ver, Dtsch. Ing. 1908; 52 (645), 740– 835.

[251] D. Tabor, The Hardness of Metals, 1951, 1.

[252] D.R. Barbadikar et al. Investigation on mechanical properties of P92 steel using ball indentation technique. Materials Science & Engineering A 2015; 624, 92–101.

[253] G. Das, M. Das, S. Sinha, K. K. Gupta, S. Chakrabarthy and A. K. Ray: 'Characterisation of cast stainless steel weld pools by using ball indentation technique', Mater. Sci. Eng. A. 2009; 51, (3–514), 389–393.

[254] F. M. Khoshnaw and I. A. Hamakhan: 'Determination of the mechanical properties of austenitic stainless steel weldments by using stress strain microprobe', Mater. Sci. Eng. A. 2006; 426, 1–3.

[255] V.Karthik et al. Finite element analysis of spherical indentation to study pile-up/sink-in phenomena in steels and experimental validation. Int.J.Mech.Sci. 2012; 54(1), 74–83.

[256] V.Karthik et al. Small Specimen Test Techniques for Estimating the Tensile Property Degradation of Mod 9Cr-1Mo Steel on Thermal Aging. J. Test. and Eval. 2007; 35 (4), 1-11.

[257] Simar A, Bréchet Y, de Meester B, Denquin A, Pardoen T. Sequential modeling of local precipitation, strength and strain hardening in friction stir welds of an aluminum alloy 6005A-T6. Acta Mater 2007;55:6133–43.

[258] Bani Mostafa Arab N, Ayaz M, Mirahmadi Khaki D. Statistical modeling of strain-hardening exponent and grain size of Nb-microalloyed steels using a two-level factorial design of experiment. J Mater Eng Perform 2013;22:3337–47.

[259] Choudhary BK, Christopher J, Rao Palaparti DP, Isaac Samuel E, Mathew MD. Influence of temperature and post weld heat treatment on tensile stress–strain and work hardening behaviour of modified 9Cr–1Mo steel. Mater Des 2013;52:58–66.

[260] M.-L. Zhu, F.-Z. Xuan. Effect of microstructure on strain hardening and strength distributions along a Cr–Ni–Mo–V steel welded joint. Materials and Design 2015; 65: 707–715.

[261] Sun PL, Cerreta EK, Gray III GT, Bingert JF. The effect of grain size, strain rate, and temperature on the mechanical behavior of commercial purity aluminum. Metall Mater Trans A: Phys Metall Mater Sci 2006;37:2983–94.

[262] M. Rakin et al. Modelling of ductile fracture initiation in strength mismatched welded joint. Engg. Frac. Mech. 2008; 75(11): 3499–3510.

[263] Aleksandar Sedmak et al. Ductile Fracture Resistance of the Weld Metal and Heat Affected Zone in a HSLA Steel Welded Joint. http://www.structuralintegrity.eu.

[264] Afrin N, Chen DL, Cao X, Jahazi M. Strain hardening behavior of a friction stir welded magnesium alloy. Scr Mater 2007; 57:1004–7.

[265] Luo J, Mei Z, Tian W, Wang Z. Diminishing of work hardening in electroformed polycrystalline copper with nano-sized and uf-sized twins. Mater Sci Eng A 2006; 441:282–90.

[266] 'Key issues related to modeling of internal corrosion of oil and gas pipelines – A review', S. Nesic, Corros. Sci, 49, pp 4308–4338, 2007.

[267] 'Investigation on Stress Corrosion Cracking Behavior of Welded High Strength Low Alloy Steel in Seawater Containing Various Dissolved Oxygen Concentrations', Huixia Zhang et.al., Int. J. Electrochem. Sci., 8 , pp 1262 – 1273, 2013.

[268] 'Hydrogen Degradation of High-Strength Steels', J. Ćwiek, JAMME, 37, 2, 2009.

[269] 'Effect of Oxygen and Biofilms on Crevice Corrosion of UNS S31803 and UNS N08825 in Natural Seawater',Laura L. Machuca et.al, Corrosion Science, 67, 242-255, 2013.

[270] 'Corrosion Fatigue Behavior of Submerged Arc Welded High Strength Steel Used in Naval Structures', H. Das and T. K. Pal, Indian Welding J , 45,2, pp 40-51, 2012

[271] 'Electrochemical Evaluation of the Corrosion Behaviour of API-X100 Pipeline Steel in Aerated Bicarbonate Solutions', F.F. Eliyan et al., , Corrosion Science, 58, pp 181–191, 2012.

[272] 'Corrosion Fatigue behavior of Submerged Arc Welded high strength steel used in Naval Structures' H. Das and T. K. Pal. Indian Welding J (2012), Vol45(2) (40-51)

[273] 'Desalination of Seawater Using Nuclear Heat', M.S. Hanra, Desalination, 132, pp263-268, 2000.

[274] ‘Studies on Breakdown of Passivity of Titanium Covered with in Vitro Biofilms’, B. Anandkumar, Nanda Gopala Krishna, R.P. George, N. Parvathavarthini and U. Kamachi Mudali, Journal of Corrosion Science and Engineering, 16, 26,2013.

[275] Standard Practice for Conventions Applicable to Electrochemical Measurements in Corrosion Testing. ASTM G3 (2014).

[276] Standard Reference Test Method for Making Potentiostatic and Potentiodynamic Anodic Polarization Measurements. ASTM G5-94 (2011).

[277] Standard Test Method for Conducting Potentiodynamic Polarization Resistance Measurements. ASTM G59-97 (2014).

[278] Standard Practice for Calculation of Corrosion Rates and Related Information from Electrochemical Measurements. ASTM G102-89 (2010).

[279] ‘The Polarization Resistance Technique for Measuring Corrosion Currents’, Fontana MG, Staehle RW, Mansfeld F, Advances in Corrosion Science and Technology, 6, Plenum Press, 1976.

[280] ‘Corrosion Behaviour of Welded Stainless Steel’, Gooch TG, J. Welding, Welding Research, AWS, 135-154, 1996.

[281] ‘Pitting and Stress Corrosion Cracking Behaviour in Welded Austenetic Stainless Steel’, Lu BT et.al, Electrochemica Acta, 50, 6, pp 1391-1403, 2005.

[282] ‘Effect of TIG welding on Corrosion Behaviour of 316L Stainless Steel’, Dadfar M et.al, Materials Letters, ,61, 11-12,pp 2343-2346, 2007.

[283] ‘Effect of Composition Profiles on Metallurgy and Corrosion Behaviour of Duplex Stainless Steel Weld Metals’, Ogawa T and Koseki T, Welding Research Supplement, WRC Bulletin, s181-191, 1989.

[284] ‘The Corrosion Resistance of Low Alloy Steels’, J.C. Hudson, J.F. Stanners,J. Iron Steel Inst.,180, pp 271–284, 1955.

[285] ‘Corrosion of Metals in Tropical Environments—Part 3—Underwater Corrosion of Ten Structural Steels ‘,B.W. Forgeson, C.R. Southwell, A.L. Alexander,Corrosion (NACE),16, 3, pp 105–114, 1960.

[286] ‘Influence of Alloying Elements on the Marine Corrosion of Low Alloy Steels Determined by Statistical Analysis of Published Literature Data’, W.A. Schultze, C.J. van der Wekken, British Corros. J, 11, 1,pp 18–24,1976.

[287] ‘Verhalten Von Grossbaustahlen in Meerwasser ‘J. Petersen, Das, Werkstoffe und Korrosion 28, pp 748–754, 1977.

[288] ‘Development of High Strength Low Alloy Steels for Marine Applications, Part 1: Results of Long Term Exposure Tests on Commercially Available and Experimental Steels’, F. Blekkenhorst, G.M. Ferrari, C.J. van der Wekken, F.P. IJsseling, Br. Corros. J. 21,3,pp 163–176, 1986.

[289] ‘Effects of Alloying Elements on the Corrosion of Steel in Industrial Atmospheres ‘, H. E. Townsend ,Corrosion, 57, 6, pp. 497-501. 2001

[290] ‘Effects of Cr, Cu, Ni And Ca on the Corrosion Behavior of Low Carbon Steel in Synthetic Fresh Water’,Yoon-Seok Choi, Jae-Joo Shim and Jung-Gu Kim ,Journal of Alloys and Compounds, 391,1-2, pp162-169, 2005.

[291] ‘Corrosion Mechanisms in Theory and Practice’, P. Marcus, J. Oudar,Marcel ,Dekker, second ,pp. 243-349, 2002.

[292] ‘ Influence of Microstructure and Non Metallic Inclusions on Sulphide Stress Corrosion Cracking in Low Alloy Steels’, V.I. Astafjev, S.V. Artamoshkin, T.V. Tetjueva, Int. J. Pressure Vessels Piping, 55, pp 243-250 ,1993.

[293] ‘The Influence of Non Metallic Inclusions on the Corrosion Fatigue of Mild Steel’, G.P. Ray, R.A. Jarman, J.G.N. Thomas, Corros. Sci, 25, pp 171-184, 1985.

[294] ‘Effect of Ti-Based Inclusions and Acicular Ferrite on the Corrosion Performance of Multipass Weld Metals’ M. Fattahi et al., Materials Chemistry and Physics, 146, pp 105-112, 2014.

[295] N. M. A. Eid: Proc. World Cong. on ‘Desalination and water reuse’, Kuwait, November 1989, Elsevier Science Publications, Paper 78.

[296] R. W. Revie: ‘Uhlig’s corrosion handbook’, 2nd edn; 2000, New York, John Wiley & Sons.

[297] I. A. Chaves and R. E. Melchers. Long term localised corrosion of marine steel piling welds. Corrosion Engineering, Science and Technology 2013, 48, 6, 469-474

[298] Y.T Zhao et al. The mechanical properties and corrosion behaviors of ultra-low carbon microalloying steel. Materials Science and Engineering A 454–455 (2007) 695–700.

[299] D. Rosenthal, 1946, The Theory of moving heat and its applications to metal treatments Trans. ASME Vol. 68, pp. 849-865.

[300] R. R. Rykalin, 1974, Energy sources of welding, Welding in the World Vol. 12 No. 9/10, pp. 227-248.

[301] J. A. Goldak, A. Chakravarti, M. Bibby, 1984, *A finite element model for welding heat sources*, Metallurgical Transactions B, Vol. 15B, pp. 299-305.

[302] Withers PJ, Bhadeshia HKDH. Residual stress: Part 1. Mater Sci Technol2001;17:355-65.

[303] Withers PJ, Bhadeshia HKDH. Residual stress: Part II. Mater Sci Technol2001;17:366-75.

[304] Bhadeshia HKDH. Effect of materials and processing–ASM handbook of residualstress and deformation of steel. Materials Park, OH: ASM International,c2002; 2002.

APPENDIX

A1 A-GTAW Joint Bend Test

(*Refers to para 3.3.3 page 95*)

The face, root and side bend test for A-GTAW weld joint was carried out as per ASTM E290. The details of samples and test set up are given in Table A1.1. The pictures of U-Bend test set up and side, face and root bend test samples of A-GTAW joint are given in Fig A1.1. No cracks observed on application of dye penetration testing confirmed adequate ductility of A-GTAW weld joint.

Table A1.1 Details of samples and test set up for U-Bend test

Specimen	Dimension (mm^3)	Thickness (t) (mm)	Mandrel Size (4t)(mm)	Gap (4t+1/8”)
Side Bent	160x10x10	10	40	43.175
Face and Root Bend	160x20x10	10	40	43.175

(a) U-Bend test set up (b) Side bend specimens (c) Face and root bend specimens
Fig A1.1 Pictures of U-Bend test set up and side, face and root bend test samples of A-GTAW joint

A2 Changes in thermal and mechanical properties with respect to temperature

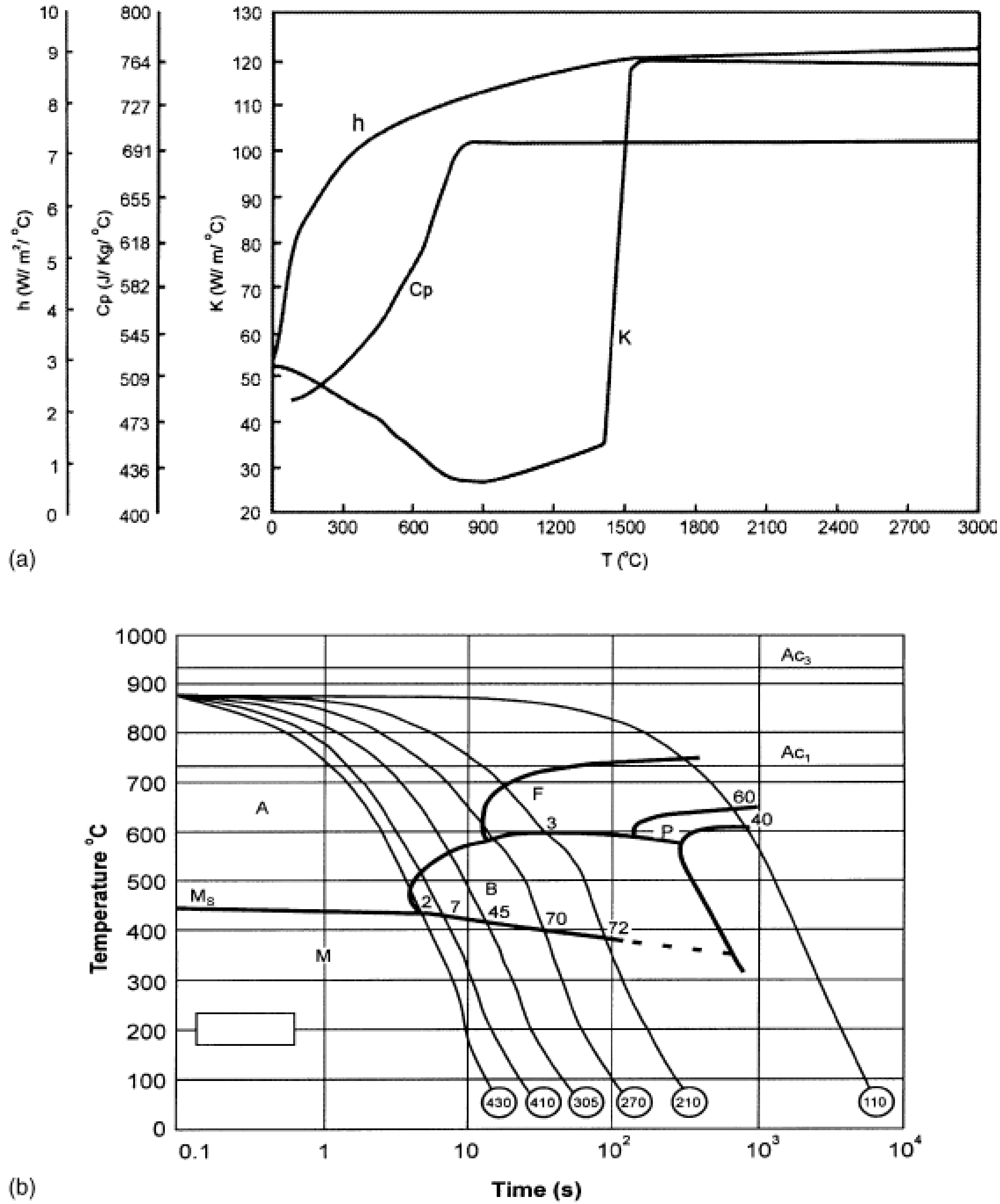

Fig A2.1 (a) Variation of thermal material properties with temperature (b) CCT diagram

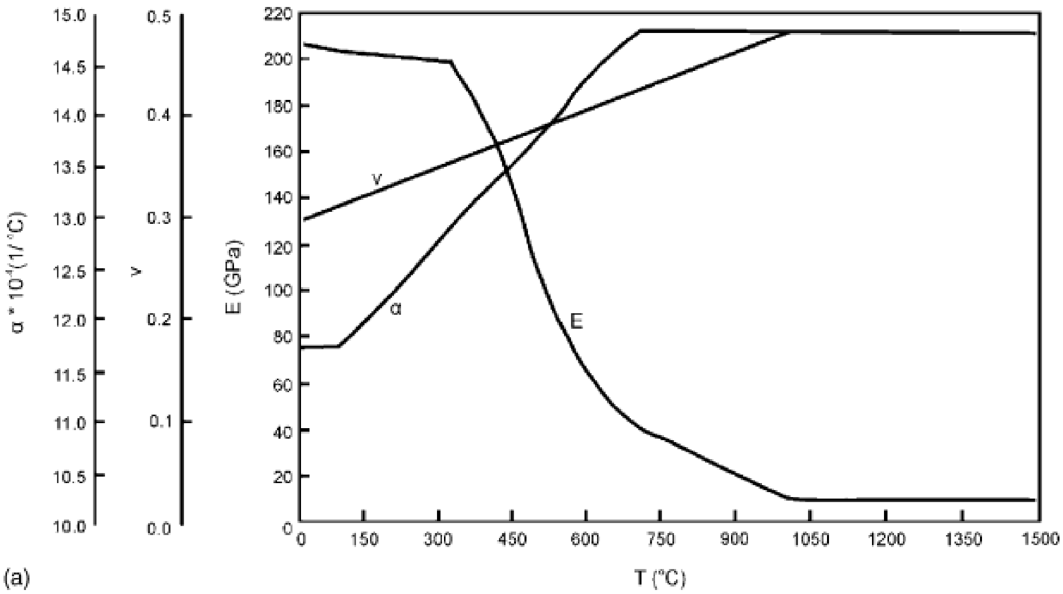

(a)

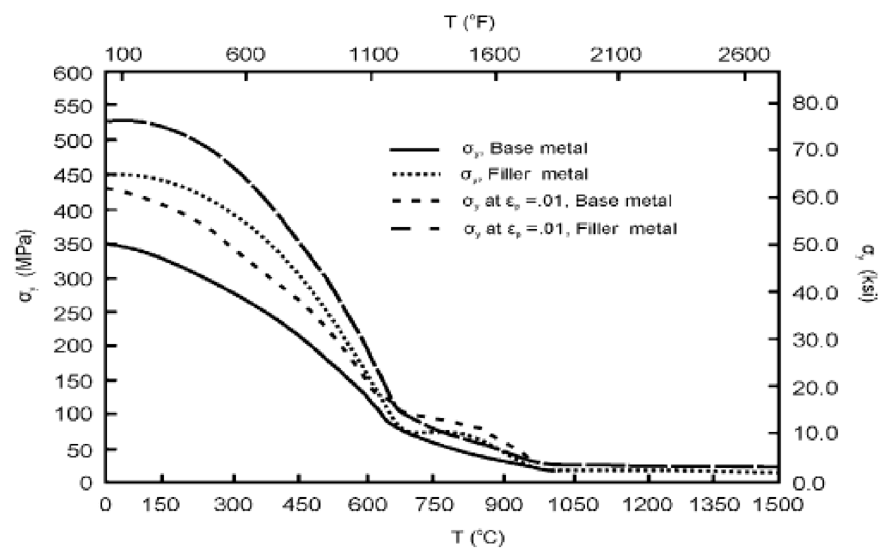

(b)

Fig A 2.2 Variation of mechanical material properties with temperature:
(a) Young's modulus (E), Poisson's ratio ( ) and thermal expansion coefficient (α)
(b) Yield strength of material (σ)

A3 SEM and EDS of Inclusions

(*Refers to para 6.2.2 page 14795*)

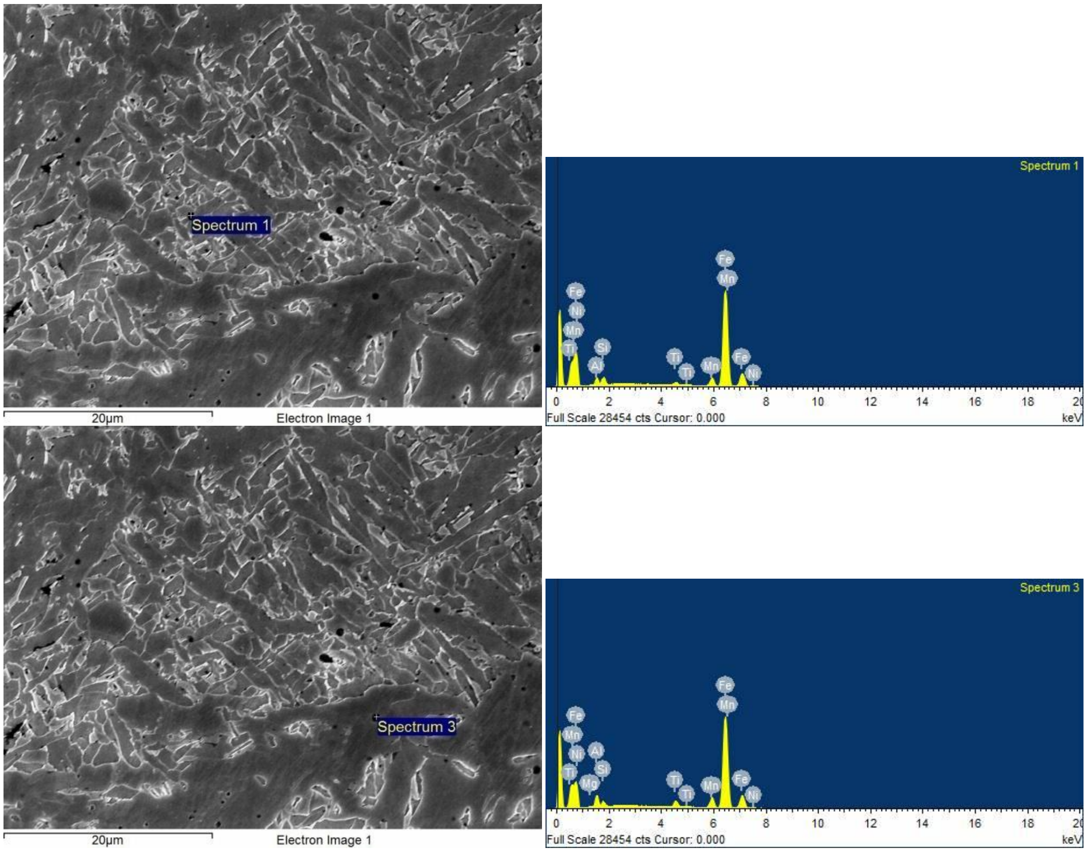

(a) SMAW SEM and EDS micrographs of inclusions (i) source of acicular ferrite (ii) without acicular ferrite

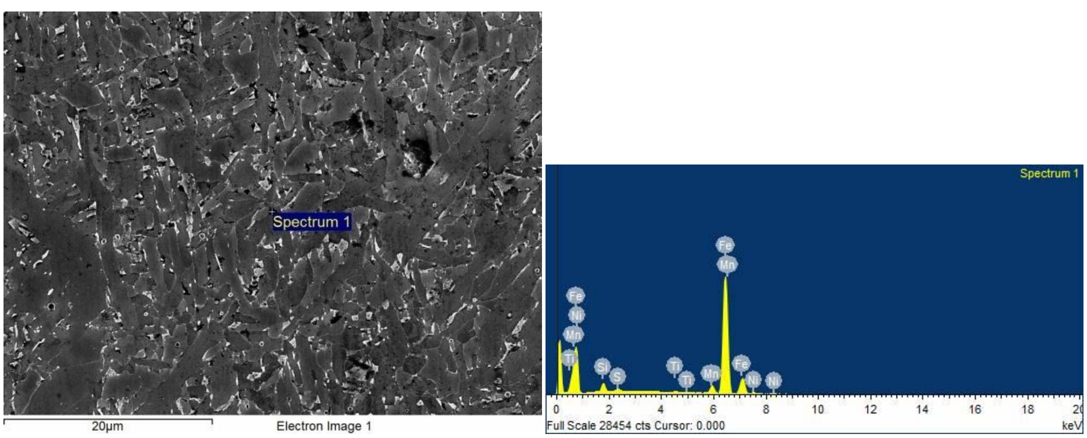

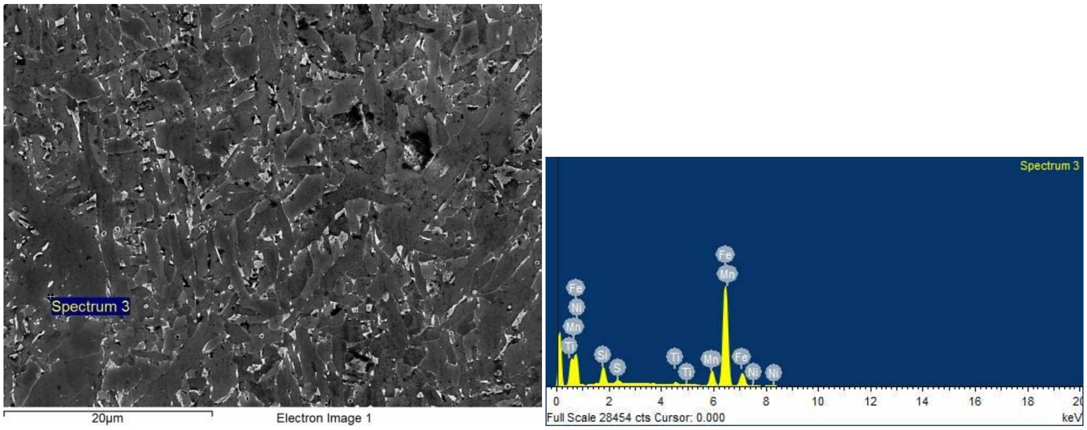

(b) SAW SEM and EDS micrographs of inclusions (i) source of acicular ferrite (ii) without acicular ferrite

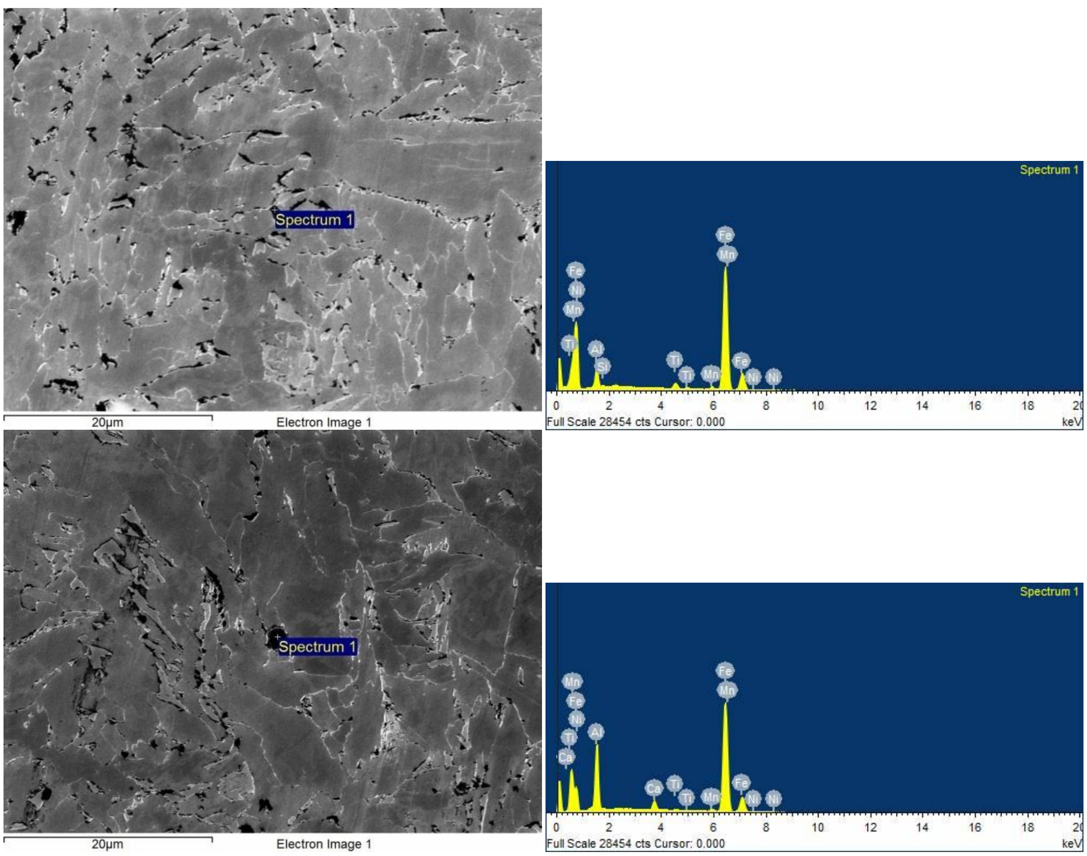

(c) FCAW SEM and EDS micrographs of inclusions (i) source of acicular ferrite (ii) without acicular ferrite

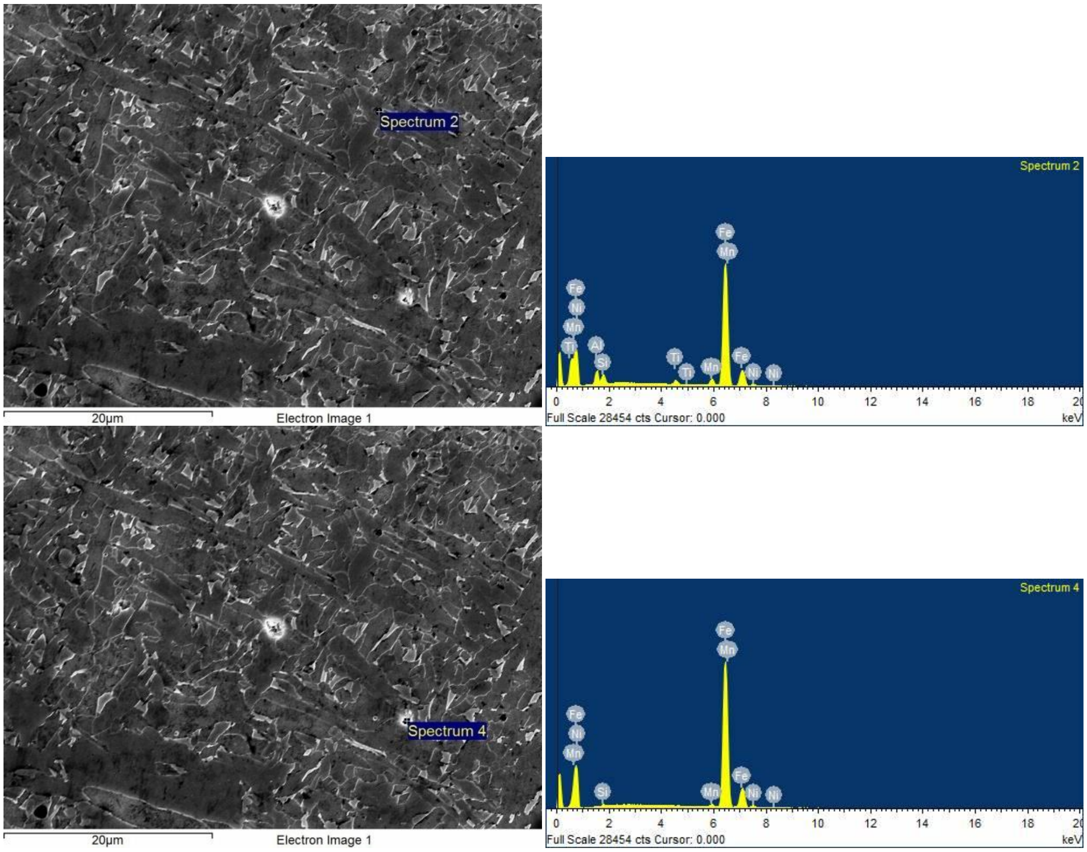

(c) FCAW SEM and EDS micrographs of inclusions (i) source of acicular ferrite (ii) without acicular ferrite

Fig A2.1 SEM and EDS micrographs of inclusions in weld metals as source of acicular ferrites and without acicular ferrite

A4 Tensile and Impact Tests Data of Base Metal and Weld Joints

(*Refers to para 6.2.4 page 165& page 168*)

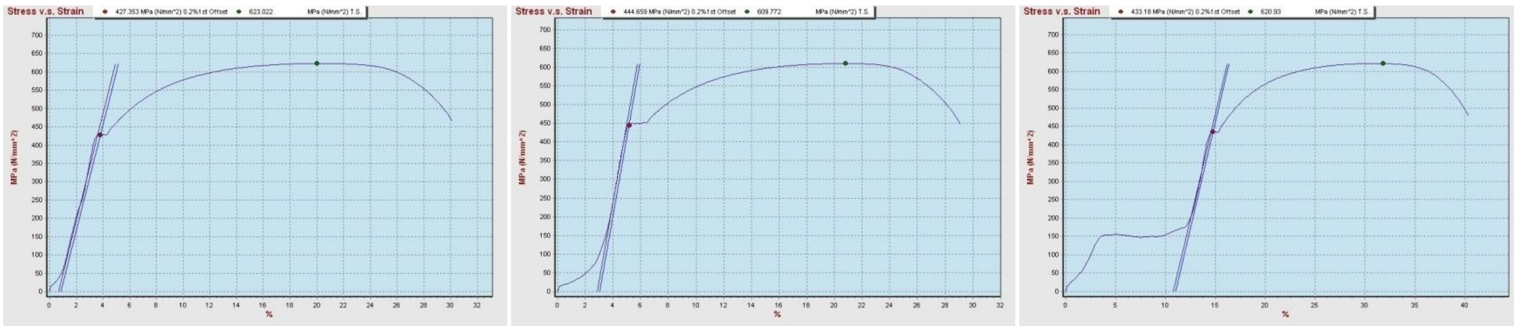

(a) Tensile tests – Base Metal DMR-249A

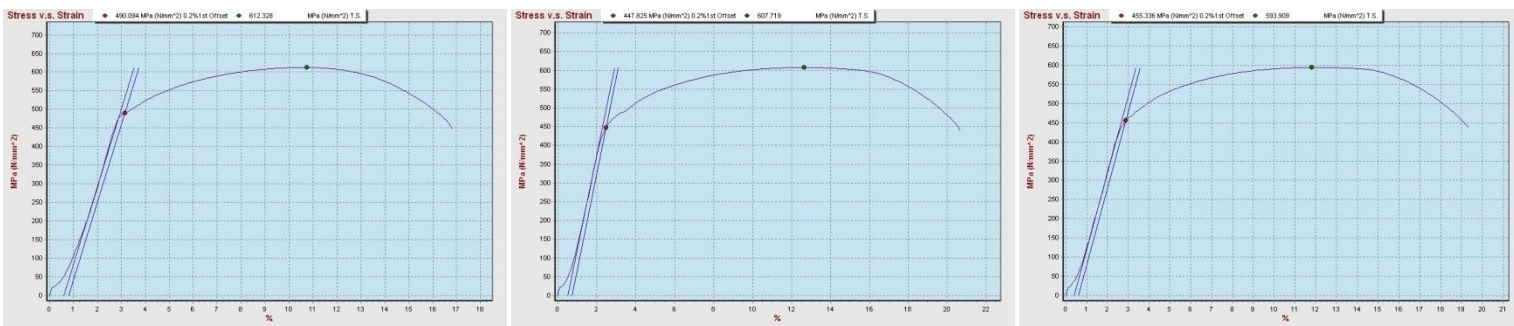

(b) Tensile tests – SMAW

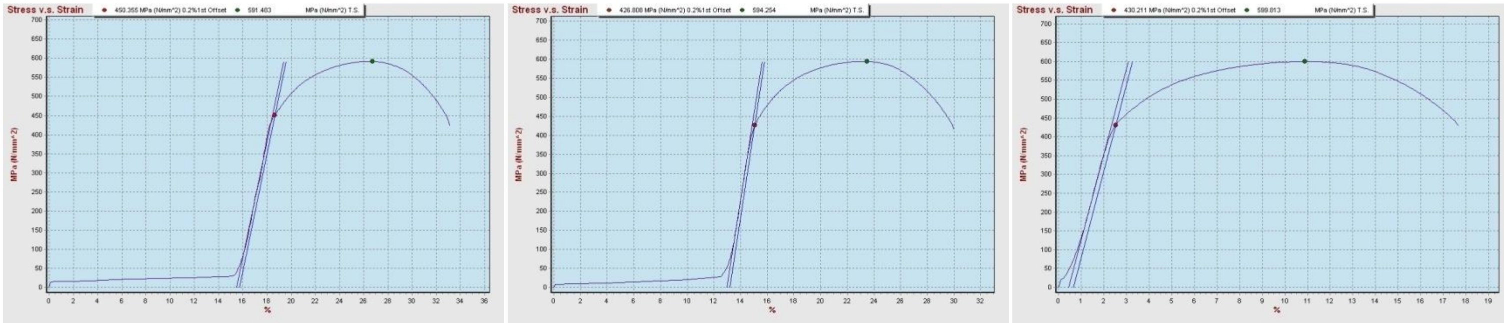

(c) Tensile tests – SAW

(d) Tensile tests – FCAW

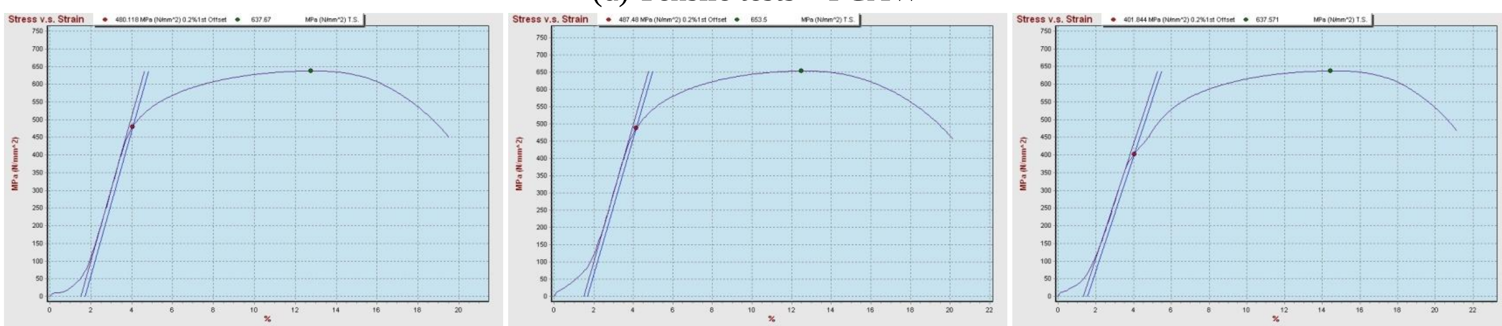

(e) Tensile tests – A-GTAW

Fig A3.1 Tensile test graphs of base metal and weld joints

Table A3.1 Tensile Test Data

OVERALL LENGTH	GAUGE LENGTH	FINAL LENGTH	GAUGE DIA	FINAL DIA	%UNIFORM ELONGATION	%ELONGATION	% AREA REDUCTION	YS	UTS
BASE METAL DMR-249A									
49.9	25.6	33.0496	3.94	2.33	20.82	29.1	65.02809	444.66	609.77
49.74	25.62	33.33674	3.93	2.36	20.02	30.12	63.93891	427.35	623.02
49.73	25.6	32.99072	3.98	2.34	20.13	28.87	65.43269	433.18	620.93
SMAW									
50.01	26.04	30.41732	3.89	2.32	10.75	16.81	64.43058	455.37	593.91
49.76	26.44	31.56143	3.96	2.49	11.83	19.37	60.46258	447.83	607.72
50.55	26.14	31.54052	3.88	2.27	12.57	20.66	65.77147	490.09	612.33
SAW									
50.24	26.28	30.9263	3.96	2.39	10.89	17.68	63.57451	430.21	599.81
50.29	26.16	30.75893	4.01	2.41	10.93	17.58	63.8802	426.81	594.25
50.18	26.8	31.46856	4.01	2.39	11.21	17.42	64.47721	450.36	591.48
FCAW									
50.26	26.14	30.76939	4.01	2.41	12.09	17.71	63.8802	498.39	610.48
49.99	25.83	29.8569	4	2.44	10.57	15.59	62.79	424.57	606.78
50.29	25.95	31.12962	3.97	2.36	15.07	19.96	64.66192	444.04	643.05
A-GTAW									
49.29	25.55	30.68555	3.96	2.39	12.5	20.1	63.57451	487.48	653.5
49.64	26.21	31.32357	3.96	2.49	12.76	19.51	60.46258	480.11	637.67
49.98	26.38	31.95937	3.92	2.38	14.45	21.15	63.13776	401.84	637.57

Table A3.2 Impact Test Data

	ROOM TEMP	LE 1	LE2	TOTAL LE	-60DEG(J)	LE 1	LE2	TOTAL LE	0 DEG (J)	LE 1	LE2	TOTAL LE	-30 DEG(J)	LE 1	LE2	TOTAL LE
DMR 249A	>350	UNBROKEN		~110	150	48,50	11,53	50+53=103	315	UNBROKEN		~110	190	UNBROKEN		~110
	>350	UNBROKEN		~110	153	11,54	44,47	54+47=111	317	UNBROKEN		~110	172	46,56	59,51	56+59=117
					152	54,10	42,57	54+57=111					181	UNBROKEN		~110
ATIG	172	44,30	36,23	44+36=80	10	6,7	12,11	7+12=19	134	40,42	58,22	42+58=100	14	8,7	12,11	8+12=20
	200	UNBROKEN		~110	7	4,4	7,11	4+11=15	127	48,56	11,40	56+40=96	24	4,6	7,11	6+11=17
	226	43,36	26,44	43+44=87	12	6,8	16,11	8+16=24	132	48,40	20,19	48+20=68	19	6,8	16,11	8+16=24
SMAW	150	50,42	68,22	50+68=118	78	16,19	21,31	19+31=50								
	150	58,56	11,50	58+50=108	72	17,18	27,25	18+27=45								
	156	48,50	20,29	50+29=79	70	12,14	16,18	14+18=32								
SAW	160	48,06	59,11	48+59=107	29	12,10	9,12	12+12=24								
	159	46,41	62,65	46+65=111	24	12,10	11,10	12+11=12								
	140	51,48	56,51	51+56=107	33	12,11	12,12	12+12=24								
FCAW	217	UNBROKEN		~110	55	11,25	20,22	25+22=47								
	208	56,56	59,61	56+61=117	49	24,9	21,21	24+21=45								
	209	UNBROKEN		~110	44	11,14	14,9	14+14=28								

A5Optical Images of Ball Indents across Weld Joints

(*Refers to para 7.4 page 189*)

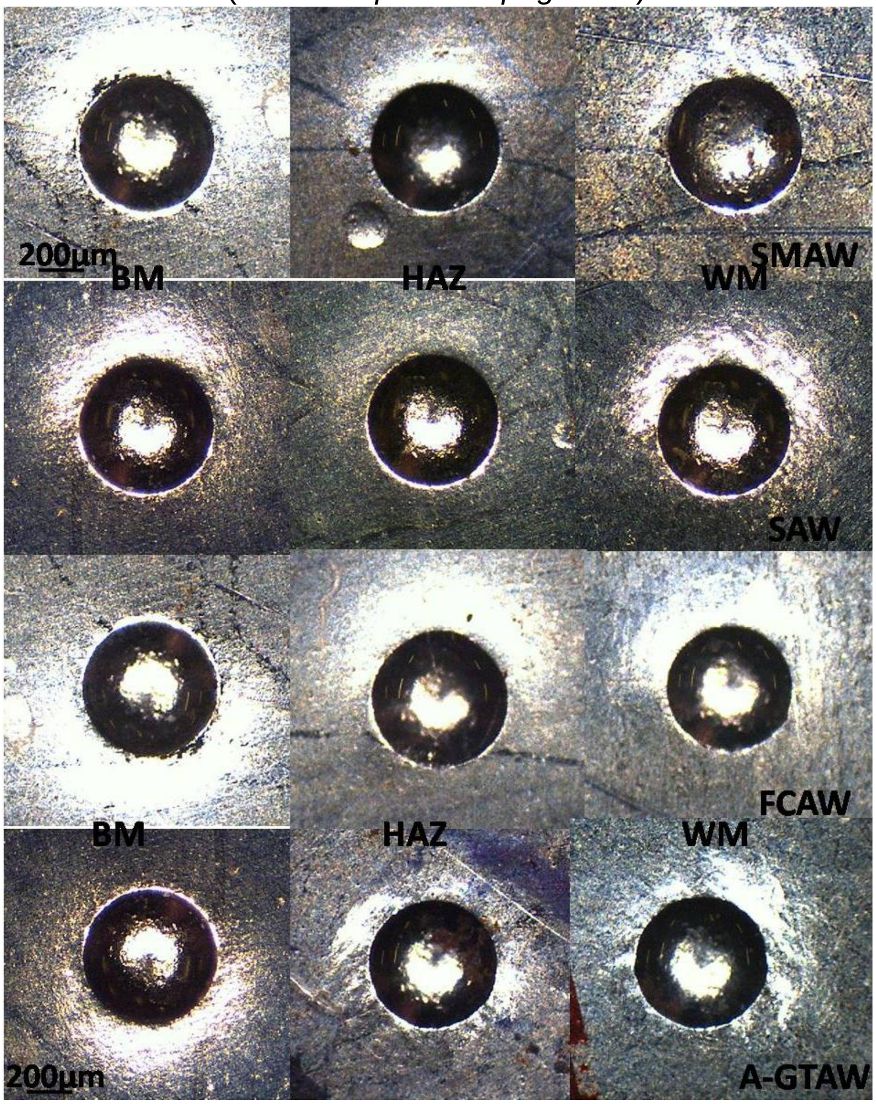

Fig A 4.1 Optical images of ball indents across weld joints

Table A 4.1 Diameters of ball indents across weld joints measured using optical images

Radius (µm)	BM				HAZ				WM			
	I	D	L	n	I	D	L	n	I	D	L	n
SMAW	361	734	373	0.17	344	527	183	0.21	352	731	379	0.16
SAW	367	692	325	0.17	351	562	211	0.20	338	678	340	0.15
FCAW	359	729	370	0.17	350	658	308	0.20	338	685	347	0.14
A-GTAW	371	706	336	0.17	343	561	218	0.22	343	635	292	0.16

I:Indentation radius, D:Max.Deformed Radius, L:Length of Deformation(D-I), n:Strain Hardening Exponent

Deformation length (L) for BM and WM were comparable whereas 'L' for HAZ was found to be lesser than BM and WM corresponding to higher 'n' in HAZ.

A6Load-Depth Curves of Automatic Ball Indentation Technique

(*Refers to para 7.4 page 193*)

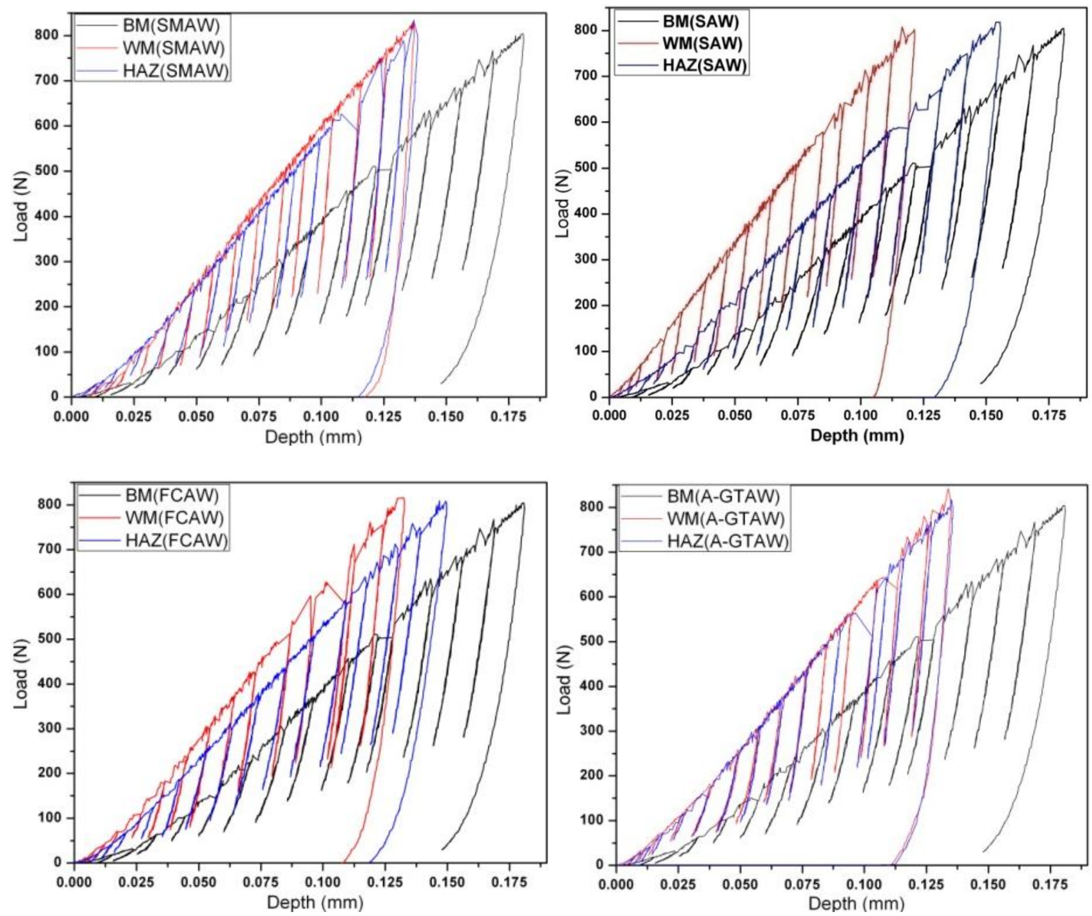

Fig A5.1 Load-Depth curves of automatic ball indentation technique